Synthesis of Bi O CO nanosheets by electrical discharges in liquids for photocatalytic and nanoelectronic applications

Anna V. Nominé

DISSERTATION

submitted in accordance with the requirements of the University of Lorraine

for the degree of Doctor of Philosophy

Specialty: Physics

by

Anna NOMINE (BEZZUBOVA)

Synthesis of $Bi_2O_2CO_3$ nanosheets by electrical discharges in liquids for photocatalytic and nanoelectronic applications

14th of December 2023

Jury

Supervisor:	**Th. BELMONTE,** Research Director, IJL, CNRS, **France**
President:	**N. FRESSANGEAS,** Professor, LMOPS, Lorraine University, **France**
Reviewers:	**U. CVELBAR,** Professor, Jozef Stefan Institute, **Slovenia**
	A. BOUSQUET, Assistant-Professor, ICCF, Clermont Auvergne University, **France**
Examiners:	**D. DUDAY**, Project Leader, LIST, **Luxembourg**
	S. BRUYERE, Assistant-Professor, IJL, Lorraine University, **France**
Invited members:	**V. MILICHKO,** Junior Professor, IJL, Lorraine University, **France**
	F. MONTAIGNE, Professor, IJL, Lorraine University, **France**

To my dearest son, Raphael

Preface

This dissertation is submitted for the degree of Doctor of Philosophy at the Lorraine University. The research described herein was carried out by myself in the period from November 2020 to September 2023, under the supervision of Professor T. Belmonte, in the Chemistry and Physics of Solids and Surfaces Department (CP2S) of Institut Jean Lamour.

I hereby declare that, except where specific reference is made to the work of others, the contents of this dissertation are original. No part of this dissertation, or any similar to it, has been, or is currently being submitted for consideration for any other degree or qualification at any other University or similar institution. This dissertation is the result of my own work and includes nothing which is the outcome of work done in collaboration except where specifically indicated in the text and Acknowledgements. It is fewer than 49000 words in length.

Anna V. Nomine (Bezzubova)

Abstract

This work presents information on the synthesis of $Bi_2O_2CO_3$ ultrathin nanosheets, hereafter referred to as BOC, utilizing the rapid and straightforward technique known as Electrical Discharges in Dielectric Liquids (EDDL). To ensure synthesis reproducibility, a pre-treatment method involving the etching of bismuth electrodes with Nital was applied. The selected process involves the initiation of electrical discharges between these electrodes submerged in either liquid nitrogen or water. Notably, both liquids yielded identical nanostructures, a similarity corroborated by Optical Emission Spectroscopy (OES), which confirmed the metallic nature of the discharge in both environments. Subsequent to this stage, the nanosheets undergo rapid oxidation, and carbonation upon exposure to air.

The proposed growth mechanism closely relates to the ledge mechanism, taking into account the presence of kinks and jogs that are distinctly visible along the edges of the nanosheets. These two-dimensional nanostructures initially form on the cathode's surface and then grow vertically, aided by ion assistance, in regions resembling comb-like patterns generated during the chemical etching step, which is a prerequisite for the discharge process.

Detailed crystallographic characterization of BOC nanosheets was achieved through a range of techniques, including Transmission Electron Microscopy (TEM), Scanning Transmission Electron Microscopy (STEM), High-Resolution TEM (HRTEM), Energy-Dispersive X-ray Spectroscopy (EDX), Selected Area Electron Diffraction (SAED), Convergent Beam Electron Diffraction (CBED), Energy Filtered TEM (EFTEM), and Electron Energy-Loss Spectroscopy (EELS). The investigation reveals that the crystallographic structure of BOC conforms to the space group I4/mmm, with lattice parameters of a=3.91 Å and c=13.77 Å, a determination that was confirmed by X-ray Diffraction (XRD).

The study also elucidates the potential nature of satellite spots consistently observed in SAED patterns along the [001] zone axis. In this study, these spots were attributed primarily to two phenomena: multiple diffraction and local disorder-to-order transformations within the BOC crystal structure. This transformation involves a shift from a body-centered tetragonal structure to a primitive Bravais lattice.

To assess their practical utility, the catalytic performance of BOC nanosheets synthesized via the EDDL method was evaluated, finding it to be consistent with BOC obtained through alternative methods. Additionally, the electronic performance of BOC was explored, aiming to uncover their potential in nanodevice applications.

Keywords: plasma in liquid ; EDDL Synthesis ; $Bi_2O_2CO_3$ nanosheets ; ledge mechanism ; satellite spots ; carbonation in air

Acknowledgements

The research presented in this thesis has been carried out in the Institut Jean Lamour at the University of Lorraine. The path towards this thesis spans three years of a multidisciplinary research covering materials engineering, crystallography, photocatalysis and nanoelectronics. From the outset, many people have been involved and have contributed to the presented ideas and making their technical realization possible. I gratefully acknowledge those who have helped along the way and influenced the formation of the understanding and the approach to representation of concepts presented in this thesis.

Special appreciation goes to Prof. Thierry Belmonte, my supervisor, for his advice, guidance, patience and continuous support throughout this project. His scientific supervision, marked by stimulating discussions and a profusion of ideas, has significantly enriched this work.

I would like particularly to thank Dr. Jaafar Ghanbaja for his extensive expertise and support during all that time, to providing me with cutting-edge TEM techniques and characterizations. I truly appreciate the generous amount of time he devoted to this endeavor, and have significantly contributed to the depth of my work.

Prof. Valentin Milichko's bright ideas and involvement in the process are gratefully acknowledged.

I wish to express my warm and sincere appreciation to Prof. Abdelkrim Redjaïmia, for his valuable interpretations and comments on crystallographic matter, and Dr. Thomas Gries for introducing me to the realm of photocatalysis.

Furthermore, my gratitude extends to Prof. François Montaigne and Dr. Sébastien Petit-Watelot for their constructive contributions, providing ideas on nanoelectronic device fabrication, guiding me through electrical characterizations, and offering insightful comments. Special thanks are due to members of CC Minalor, Demba Ba, and Laurent Badie, whose efforts were instrumental in translating the device concept into technical reality.

I would like to thank the rest of my thesis committee: Prof. Nicolas Fressangeas, Prof. Uros Cvelbar, Dr. Stephanie Bruyère, Dr. Angelique Bousquet, Mr. David Duday for their valuable comments on this research.

Elsewhere in the department there have been a number of people who have helped make this project possible, particularly Cédric Noel, Frédéric Brochard, Alexandre Nominé, Ghouti Mejahdi, Sebastien Hupont, Regis Peignier, Sylvie Migot, Erwan Etienne, and all the workshop personnel. Special appreciation is extended to Jean-Luc Audisio and all members of CC Ermione for their unwavering technical support.

Special mention goes to Patric Grysan at LIST for his assistance with breakdown field measurements, and ITMO students Ekaterina Gunina, Yurii Mezenov, Pavel Alekseevsky, Anastasia Efimova and Sergey Rzhevsky for their personal and scientific contributions.

I recognize that this research would not have been possible without the financial assistance of the French PIA (Programme d'Investissements d'Avenir) Project Lorraine Université d'Excellence (Ref. ANR-15-IDEX-04-LUE).

I thank my hard-working students Mikhail Nazarov, Jose Chamorro, Anton Glavatskih for their productive cooperation.

Acknowledgments are extended to the committed members of the PPS (Plasmas, Processes, and Surfaces) group, namely Grégory, Gérard, Stéphane, as well as the PhD students Corentin, Ronny, Majed, Arthur, Dimitry, Aiman, Lucas, postdocs Lucile, Anna Paula, and Benjamin, along with the entire team.

My endless appreciation goes to my family, my mother, my father, and my sister, people who were always there for me despite the distance between Russia and France, who always endow me with infinite support, wishes, continuous love, encouragement, and patience.

Last but not least, I would like to thank my son Raphael. I dedicate this dissertation to him not just because he has been so kind, understanding and supportive little man during all those years especially at the moments when it wasn't easy, but for being a truly wonderful friend the entire amazing journey with me.

Anna V. Nomine (Bezzubova)

Contents

Introduction

Problem Statement

Materials with lamellar structure hold significant promise in advancing the energy transition due to their unique properties and applications:

- Efficient Energy Storage: Lamellar materials, like graphene and transition metal dichalcogenides, offer high surface areas for energy storage in batteries and supercapacitors, enhancing their energy density and performance.
- Catalysis Enhancement: They can serve as catalyst supports, accelerating reactions crucial for renewable energy technologies, such as fuel cells and electrolysis, thus improving energy conversion efficiency.
- Solar Energy Harvesting: Lamellar materials can be utilized in photovoltaic devices, like perovskite solar cells, to enhance light absorption and charge carrier transport, contributing to more efficient solar energy conversion.

but we could also add lightweight structural materials, heat management, gas separation, enhanced lubrication, energy-efficient lighting, improved energy storage devices, sustainable materials, etc.

Their abundance and potential for recyclability make lamellar materials eco-friendly choices, aligning with the sustainability goals of the energy transition.

$Bi_2O_2CO_3$ (CAS #5892-10-4), also known as bismuth oxycarbonate or subcarbonate (or BOC in short), is a lamellar material with several intriguing properties. Bismuth is relatively abundant, and $Bi_2O_2CO_3$ is considered non-toxic compared to some other semiconducting materials, making it a more sustainable and environmentally friendly option for various applications. It is also a semiconductor with a bandgap of 3.1-3.5 eV that makes it suitable for electronic applications. It can be used in electronic devices, sensors, and energy-efficient electronics, supporting advancements in energy-efficient technologies. $Bi_2O_2CO_3$ exhibits excellent photocatalytic activity, particularly in degrading organic pollutants and purifying water. This property is valuable for environmental remediation and wastewater treatment in the context of the energy transition, aligning with the goal of cleaner water resources.

Currently, the practical applications of $Bi_2O_2CO_3$ are scarce and there are few literature sources available. Its crystallographic structure is not accurately known. Its growth mechanisms

are poorly documented. Determination of many of its properties are still lacking, like its permittivity, its breakdown field and even its density. It is noteworthy that BOC can also be regarded as a carbon dioxide (CO_2) sink, which, evidently, does not lack practical significance.

Motivation and Challenges

In 2018, a noteworthy discovery was reported by Hamdan *et al*. [Hamdan2018] concerning the use of liquid discharges for synthesizing bidimensional materials. Specifically, it was possible to generate PbO_2 nanosheets, ranging in thickness from 4 to 20 nm, through the erosion of lead electrodes submerged in liquid nitrogen, oxidation being due to the air once the liquid is evaporated. In the case of bismuth electrodes, we also observed the formation of similar structures when the applied voltage exceeded slightly the breakdown voltage. However, the reproducibility of these experiments was consistently low, preventing us from gaining control over the process to create Bi-containing nanosheets as needed.

Due to the considerable interest surrounding BOC, it was decided to embark on a research endeavor aimed at achieving control over the synthesis of these nanosheets, delving into the growth mechanism of these entities, and uncovering some of their elusive properties.

The overarching strategy employed to address the inquiries prompted by this undertaking involved several key objectives: attaining control over the reproducibility of Bi-containing nanosheet synthesis, comprehending their growth mechanism, precisely ascertaining their structural and compositional attributes, and exploring their catalytic and electronic properties. To fill in the gaps in knowledge on these specific aspects we employed a set of characterization techniques accessible within our laboratory. Consequently, the subsequent thesis structure was established accordingly.

Thesis Outline

The thesis is composed of six chapters, including background information (introduction and literature review), experimental results (three chapters) and conclusion, the details of which are illustrated as follows:

• **Chapter 1** – Literature Review

This chapter, which draws from a previously published review, primarily focuses on three key areas: the synthesis of nanomaterials through electrode erosion using liquid discharges, the synthesis of 2D materials via this method, and providing an overview of the $Bi_2O_2CO_3$ material.

To maintain clarity, the process description has been condensed compared to the published text. Finally, the main objectives of the thesis are presented.

• **Chapter 2** – Synthesis and growth mechanism of $Bi_2O_2CO_3$ nanosheets by pulsed discharges in liquids

Chapter two places its focus on three key aspects: the experimental setup, the synthesis method, and the prerequisites necessary to achieve highly reproducible outcomes. It also delves into the growth mechanism responsible for the anisotropic growth of nanosheets within the discharge volume.

• **Chapter 3** – Detailed crystallographic study of $Bi_2O_2CO_3$

Bi_2O_3 was initially anticipated to yield nanosheets in a similar manner as experiments with lead resulted in the formation of PbO_2. However, we discovered that instead of Bi_2O_3, BOC (Bismuth Oxycarbonate) was formed. The structure of BOC was not well-documented in the literature, as diffraction patterns did not entirely align with the proposed data. Therefore, a comprehensive investigation was imperative to elucidate its true nature.

• **Chapter 4** –Photocatalytic Activity of $Bi_2O_2CO_3$ Semiconductor

BOC is a widely recognized photocatalytic material; however, previous experiments made with this material did not involve ultrathin nanosheets like those generated through our unique process. Consequently, we found it intriguing to explore the photocatalytic potential of these ultrathin BOC nanosheets to assess whether they exhibit enhanced properties due to quantum confinement effects. To showcase the behavior of BOC, we selected degradation studies of Rhodamine B and methyl orange as illustrative examples.

• **Conclusions and Perspectives**

The main conclusions based on experimental results are summarized and future work is recommended.

Let's mention that result chapters are presented in form of peer-reviewed articles in scientific journals. We kindly request the reader's patience regarding occasional repetitions, particularly in relation to the experimental method sections.

The document is supplemented by two sections: one containing additional information essential for supporting specific results presented in the main text, and an **appendix** detailing our efforts to assess the electronic properties of $Bi_2O_2CO_3$. This endeavor necessitated the fabrication of a specialized device and subsequent testing.

Chapter 1

State of the art

1.1 Synthesis of nanomaterials by electrode erosion using discharges in liquids

Partly extracted from our published article:

A. V. Nominé, Th. Gries, C. Noel, A. Nominé, V. Milichko, T. Belmonte, Synthesis of nanomaterials by electrode erosion using discharges in liquids. Journal of Applied Physics, 2021, 130 (15).

Discharges in liquids are very efficient to synthesize nanoparticles by electrode erosion. This simple process is only simple in appearance. Mechanisms responsible for the production of nanoparticles are several, depending on the choice of process parameters. They determine size distributions, shapes, composition and defects of produced particles. They also control their possible assembly into more complex structures. This chapter describes some basic phenomena associated with nanoparticles synthesis by discharges in liquids using electrodes. It also gives a summary of the research efforts that have been devoted to the understanding of this process. Although a complete picture is not available yet, huge progress has been made and offers new capabilities for a better control of this kind of processes. Finally, among important challenges that are still to tackle, the possibility of forming nanoalloys from immiscible elements or achieving unimodal monodisperse size distributions is questioned from the current mastery reached in this field.

1.1.1 Experimental approaches

There are two main ways to generate a direct current (DC) discharge in a liquid to synthesise nanoparticles. A low-voltage generator (typically below 1 kV) can be used, which requires to put the two electrodes in contact, the discharge being created when the gap between the electrodes increases, either by material erosion or by mechanical separation. The current [Karahaliou2012], [Bera2006] or the voltage [Horváth2006] are, most often, used as closed-loop feedback signals to keep the inter-electrode gap distance, measured with a detector, as constant as possible. For instance, Bera *et al.* [Bera2005] developed an optoelectronic system made of three main components to maintain constant a preselected distance between the electrodes (**Fig. 1.1**):

a photosensor for an optical emission diagnosis, a feedback loop which is composed of analogue electronics and a computing unit, and a servo-unit for axis translation of the anode.

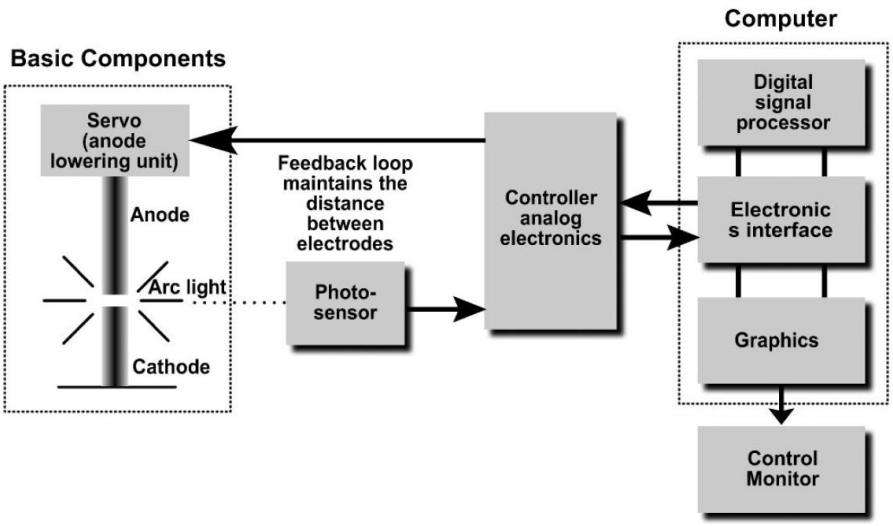

Fig. 1.1: Block diagram showing the concept and major components of the optoelectronic feedback control of the electrode feeding system that is implemented in the present ADS process. *Reproduced from Rev. Sci. Instrum. 76, 033903 (2005), with the permission of AIP Publishing* (Fig. 3 in [Bera2005]).

Resorting to high-voltage discharges (typically beyond 1 kV) enables breakdown at short gaps (*i.e.* from 100 µm to 1 mm typically, depending to the strength of the dielectric liquid). If one electrode is insulating, AC or radiofrequency (RF) excitation can also be used. **Table 1.1** presents selected examples of discharges in liquids for the synthesis of nanoparticles of simple metals. It is useful to compare conditions and have practical values of parameters. For carbon materials, a thorough review is available [Arora2014].

Experimentally, reactor designs are many (**Fig. 1.2**), even though it is relatively simple to set up a process, as only a power generator, two electrodes and a vessel containing the liquid are required. Indeed, the power source can be used to generate a DC, AC (low frequency), radio frequency, microwave, unipolar pulsed discharge or bipolar pulsed discharge. The electrodes can be a pin, a plate or even materials granules. The shape of the vessel can be a cylinder or a cone to prevent the drift of particles from the discharge zone. The process can be assisted by ultrasound [Mizukoshi2017], [Bulychev2019]. One electrode can vibrate to facilitate electrical breakdown and mix the treated solution [Vanraes2016].

Liquid (Volume)	I(A)	V_{appl} (V)	T_{on} (µs)	T_{off} (µs)	Gap (µm)	Gap control	Particles*	Electrodes**	Comments	Ref.
Liquid nitrogen	70	DC: 10000	0.1–2.5	3.3×10^5	100	Hand	Ag NPs, Cd NCs and NWs Ag: (30-50 nm) Cd: (5-10 nm)	2: Ag or 2: Cd	Self-assembly of Cd NCs into NWs	[Trad2019]
Deionized Water (200 mL)	11.5	DC: 140	5–1000	1000–5	30	Servo	Ag or AgO (1–200 nm) NPs Trimodal (1,5 / 6 / 80 nm)	2: Ag	Cathode is twice larger than anode	[Tseng2013]
Distilled water	50–150	DC: 27			1000	Yes	Oxidized Al, Cu and Al–Cu composite NPs and MPs	2: Al or 2: Cu or 1:Al + 1 Cu	1 Al electrode and 1 Cu electrode	[Rebollo2014]
Liquid ammonia at 100°C and n-heptane at 25°C	Current frequency: 1–2 Hz	DC: 11000 for NH_3 DC: 7500 for heptane			No gap	-	AlN, TiN, Fe, Cr_2N in NH_3 Al_4C_3, TiC, Fe, Fe_2C and Cr_7C_3 in heptane. (1–10 µm)	2: Al (for AlN and Al_4C_3) or 2: Ti	Pellets of Al, Ti, Fe and Cr as starting material and put between 2 eletrodes	[Sato1992]
$HAuCl_4$ solution	15	DC: 3			Adjusted to set current	Hand	Au NPs (8 ± 3 nm)	2: Ti	Electrode in contact for ignition	[Ashkarran2009] [Ashkarran2013]
0.01 M $HAuCl_4$-xH_2O		DC: -1000	0.02			Single electrode	Au NPs Unimodal (36 ± 9 nm)	200 nm carbon nanopipettes	Single pulse applied	[Bhattacharyya2009]
100 mL deionized water or pure ethanol	2-12	DC: 3200	1	999	unknown	1 movable electrode	Au NPs Unimodal (20 ± 15 nm)	2: Au wires	Ultrasound assistance	[Ghomi2013]
$HAuCl_4$-$3H_2O$ (0.5mM), distilled water (200		DC: 2000			500		Au NPs Unimodal (23 ± 9 nm)	2: W wires		[He02010]

ml) + 2.0mM KOH										
$HAuCl_4$-$4H_2O$ (37mM) + Sodium dodecyl sulfonate (0.01 mol) added to 150 ml of water		DC: 1600 and 3200	2	64.6	300	Constant	Au NPs with exotic shape Unimodal (25-50 nm) and (10-20 nm)	2: W wires	Utilization of SDS as surfactant	[Hieda2008]
Deionized water	4	DC: 70–100V (2–3µs) and 20–40V pulse	10	50	A few µm	Servo	Au NPs Unimodal (15-30 nm)	2:Au wires		[Lung2007] [Tien2010]
Hexane	Unknown	Single pulse (0.05 J)	Unknown	Unknown	Unknown	Unknown	Fusiform Au NPs after reduction with sodium citrate from Au nano-dispersion L: 50-150 nm D: 5 to 15 nm	2: Au (V-shape configuration)	Post-treatment: exposed to aqua regia for 20 min and next 1% sodium citrate dispersion.	[Sulaimankulova2019]
Ethanol	6.4	DC: 135V and 18V after breakdown	50	50	20-40	Servo	Au NPs Unimodal (8 ± 6 nm)	2: Au		[Tseng2009]
Liquid nitrogen	~100	DC: 10000	0.1	10^5	100	Hand	Cu, Ag, Cu_xAg_y alloys Trimodal (2-10 nm / 30-50 nm / large)	2: Cu or 2: Ag or 2: $Cu_{28}Ag_{72}$	x < 8.8 wt% or x > 92wt%	[Kabbara2018a]
Liquid nitrogen	~100	DC: 10000	0.075	10^5	100	Hand	Cu NPs, Zn NPs and NSs, Cu@Zn NPs Trimodal	2: Cu or 2: Ag or 1: Cu + 1:Zn	Cu NPs are wrapped in Zn NSs.	[Kabbara2018b]

							(2-10 nm / 30-50 nm / large)			
Water + 0.007 wt% NaCl	Unknown	DC: Unknown (High Voltage)	1–2	99–98	300–500	Hand	Fibre-shaped (CuO) NPs and flower-shaped ZnO NPs Bimodal (15–25 / 50–60 nm)	2: Cu or 2 : Zn		[Hu2014]
Deionized Water (150 mL)	0.5–25	DC: 90–220	2–2400	2400–2		Servo	CuO NPs (20–200 nm) (68 nm ± 33 nm)	2: Cu	Fluid cooled between 2 and 25°C. Pressure [20–760 Torr]	[L02005]
5 mM $CuCl_2$, 10 mM ascorbic acid in 1% by weight gelatin solution (130 ml deionized water).	0.002	DC: 900	12.5–35	15–37.5	500	Constant	Cu NPs (around 25 nm) with shape changing vs treatment time. sphere/ cube / hexagon / triangle (33.7 ± 5.8 nm) / (19.2 ± 3.3 nm) / (20.3 ± 2.9 nm) / (35.1 ± 7.6 nm)	2: W		[Pootowang2013]
0.1 mol/L $NaNO_3$ solution		AC: 150					CuO colloidal reduced chemically to Cu_2O and Cu NRs After 30 min (1-2 nm)	2: Cu	Chemical reduction: 0.1 mol/L ascorbic acid and 1 mL hydrazine hydrate (35 wt%)	[Ya02005]
Deionized Water (0.5 L)	1.5	DC: 220	12	2	7	Servo (current)	TiO_2 NPs (a few 100s of nm)	2: Ti		[Chen2004]

							Unimodal (80 nm)			
Deionized Water (3 L)	50	DC: 28–34	-	-	1000	Hand	$Cd(OH)_2$ NPs and NWs D: 5–40 nm	2: Cd	NWs formed by NPs assembly	[Eskizeybek2011]
Liquid nitrogen	30	DC: 10000	0.3	$3.3x10^5$	100	Hand	PbO_2 NSs D=several µm	2: Pb		[Hamdan2018]
Ethyl alcohol (60 mL)	120	DC: 0, 300, 500	20	9980	Unknown	No	W, Ni, C, Steel NPs and MPs D: 15–20 nm	2: W, Ni, C or Steel		[Parkansky2005]
Liquid nitrogen	70	DC: 8000–12000	0.1–2.5	$3.3x10^5$	100	Hand	Co, Ni, CoNi alloy NPs Trimodal (4-15 nm / 30-60 nm / large)	2: Co or 2: Ni or 1: Co + 1:Ni		[Trad2020]

* NPs: Nanoparticles – MPs: Microparticles – NWs: Nanowires – NSs: Nanosheets –NCs: Nanocubes – NRs: Nanorods

** 0, 1+1 or 2 means no electrode, 1 electrode made of a given material and 1 electrode made of another material or 2 electrodes made of the same materials.

Table 1.1: Submerged discharges in liquids used to synthesize nano-objects.

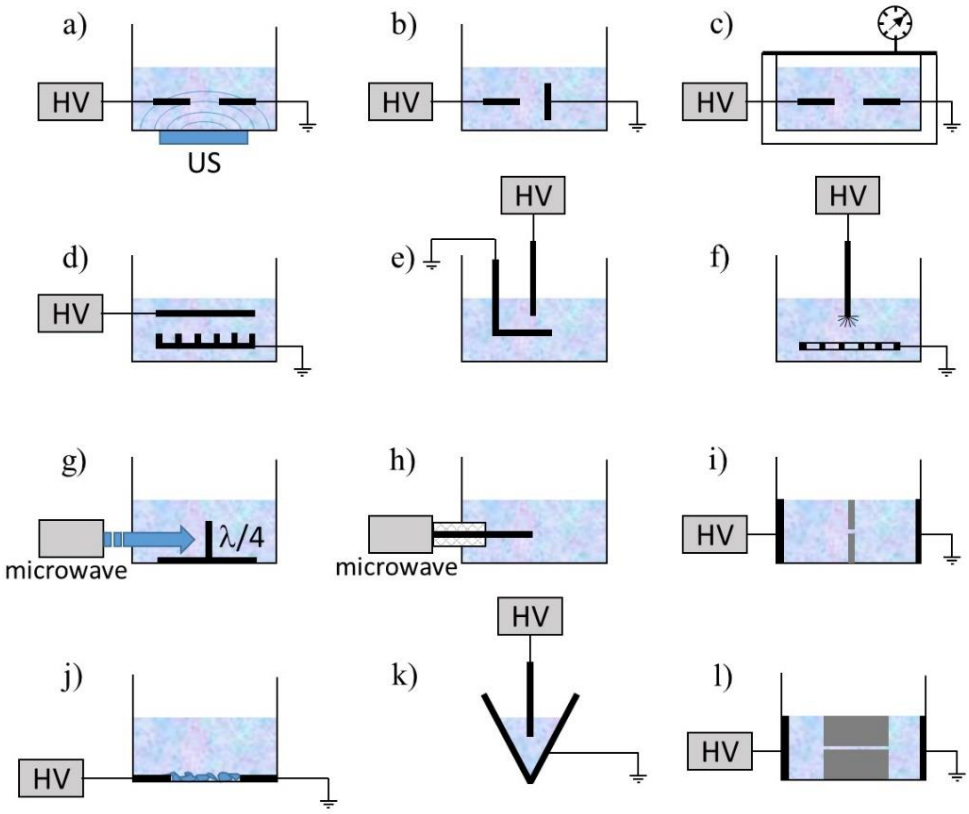

Fig. 1.2: Selected examples of submerged discharge processes. a) pin-to-pin spark discharge with ultrasound assistance [Bulychev2016], b) pin-to-plate [Hamdan2013a], c) supercritical or cryogenic fluids [Hamdan2018], [Shizuno2011], d) multi-pin-to-plate [Vanraes2016], e) pulsed arc with vibrating electrode [Parkansky2008], f) brush-to-plate [Vanraes2016], g) microwave discharge with quarter-wavelength antenna [Lebedev2018], h) microwave discharge with coaxial line [Lebedev2018], i) diaphragm discharge [Kozáková2019], j) spark discharges between metal chunks [Shiyan2015], k) funnel-type reactor [Mardanian2013], l) capillary discharge [Baerdemaeker2005].

1.1.2 Simplified sketch of events

The fastest voltage rise time used to generate discharges in liquids is around 150 picoseconds [Starikovskiy2011]. For the synthesis of nanoparticles, it is always beyond 2 nanoseconds (*i.e.* within the so-called *short* time scale) and can extend to the second time scale. This means that typical phenomena found in target ablation by femtosecond and even picosecond lasers (leading to the so-called *ultra-short* interactions) are beyond the scope of this work.

The synthesis of nanoparticles by electrode erosion using discharges in liquids can be described by the following simplified chronological sketch of events (**Fig. 1.3**).

Before plasma ignition, charges are injected into the liquid during the pre-breakdown phase. Either electrons are injected at the cathode or impurities (and even the liquid itself if it is aprotic) can be split into ion pairs of opposite charges at the anode. Charge injection drives the electrohydrodynamic movement of the liquid, possibly leading to turbulent flows. Once charges

are injected in the liquid, breakdown occurs when the liquid density becomes low enough to enable charge multiplications.

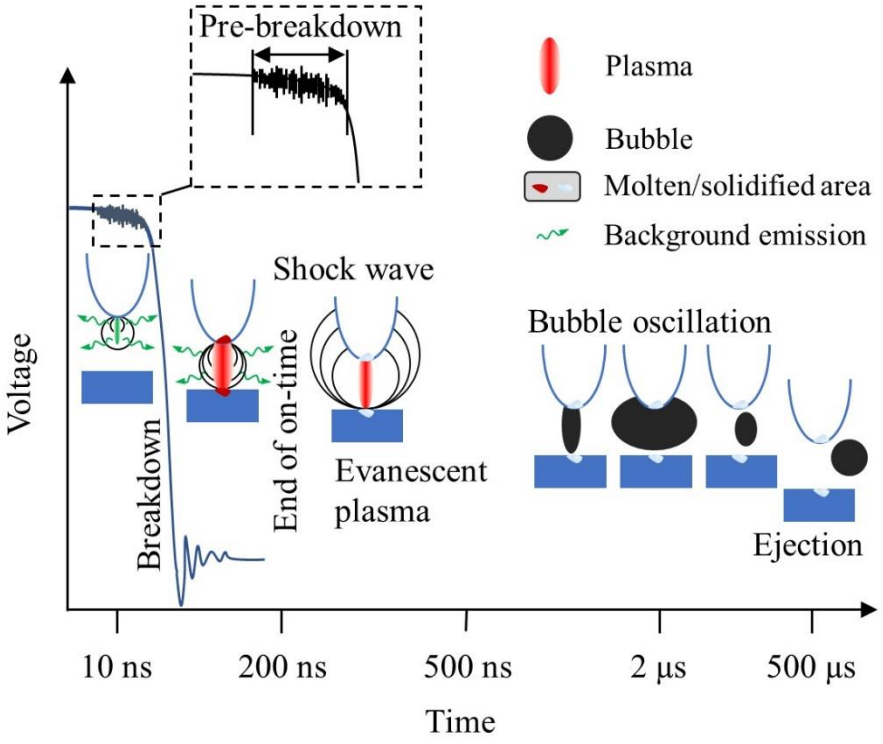

Fig. 1.3: Simplified sketch of events occurring in submerged discharge processes. *After J. Appl. Phys. 113, 213303 (2013), with the permission of AIP Publishing* (Fig. 1 in [Hamdan2013b]).

When the discharge ignites, if the dissipated power is high enough, a shockwave can be emitted. The current flows back and forth across the electrode-liquid interfaces. Both electrodes are submitted to these current oscillations that can be described by a damped RLC circuit. The discharge volume extends towards the ground electrode under the electric field, forming an ionized channel that crosses the inter-electrode gap, typically in several nanoseconds for sub-millimetric gap distances, a bit like streamers in dielectric barrier discharges. When the channel reaches the ground electrode, the voltage drops suddenly, transforming the discharge channel into an arc discharge. The electrodes, on contact with the high-temperature arc discharge, start melting after a few hundred nanoseconds, releasing a metallic vapour in the discharge. Once the metallic vapour is emitted, nanoparticles are synthesized by condensation.

Other erosion processes may also be involved, depending on the conditions, leading to different size distributions of nanoparticles. Produced particles are next transferred into the liquid phase. Once the discharge phase stops, the gas volume it occupied expands and collapses several times within the millisecond time scale, leading to bubble oscillations. An energy balance is useful at this stage [Qotba2005]. Basically, the largest part of the energy delivered by the source is used to create the plasma (~95%). Electrode erosion consumes only about one percent of the

total energy (~1%), whereas the bubble dissipates a few percent (~5 %). The amount of energy spent in the shockwave is almost negligible (<0.1%). Of course, these figures are affected by the type of discharge used, the inter-electrode gap distance, the nature of the liquid, etc. However, we readily understand that the overall yield of nanoparticles production is a key issue in this kind of process, even though large quantities of nanoparticles can be produced because of high production rates (typically ~100 mg h^{-1} and up to 10 g h^{-1}) [Horikoshi2017].

1.1.3 Electrode erosion

Electrodes can be eroded by different mechanisms. This produces impacts with complex shapes. As mentioned previously, some recently identified ablation mechanisms in laser processes with ultra-short time scale (from a few femtoseconds to a few picoseconds) will not be considered [Wu2014, Wu2016].

1.1.3.a Erosion mechanisms

At short pulses, thermal processes must be considered, which is not true for ultra-short processes. The melting of the electrodes by the discharge is the most important mechanism that leads to particles synthesis. The modelling of the process is generally attuned to those developed for the description of arc–surface interaction in domains like welding or circuit-breakers [Fan2004a], [Ushio2004], [Gonzalez2009]. However, several other mechanisms are possible, depending on experimental conditions. Whatever the conditions, the mean energy of ions in these high-pressure discharges is too low to promote any sputtering effect as it is too often claimed.

1. Melting and vaporization (evaporation and sublimation)

The discharge pressure at ignition is typically beyond hundreds of bars. It is still around a few tens of bars 200–250 ns after ignition, at the end of a nanosecond-pulsed discharge [Hamdan2014]. This means that the energy of most particles in the ionized gas is certainly too low for sputtering. The melting of metal electrodes is not due to the Joule effect either, the resistivity of the material being too low until dissolved gases start forming bubbles, which affects the material conductivity. Following Hamdan *et al.* [Hamdan2013b], electrodes melt essentially by irradiation from the blackbody emission of the high-temperature discharge. The maximum temperature reaches a fraction of eV (typically around 5000 K), discharges being close to local thermodynamic equilibrium. As radiation is emitted similarly on either side of the discharge channel, erosion spots are similar on either electrode. The time to melting is of the order of 100 ns for a micrometric erosion spot on an aluminium electrode.

Local melting of the electrode leads to the formation of a liquid well. The bottom of the well is in contact with a mushy region if the electrode is an alloy and not a simple metal. The interface between the surface of the liquid well and the discharge is not clearly described for several reasons: the time evolution of the pressure is not well known, the existence of a plasma sheath is contentious as it should be extremely thin, the surface is likely to be unstable, etc.

The heated electrode emits a vapour either by evaporation from the molten electrode or by sublimation from the solid electrode, and this vapour condensates in colder parts where nanoparticles form. This mechanism together with nucleation (described hereinafter) is responsible for the synthesis of the smallest particles generated by discharge in liquids. Vaporization at the surface of the molten pool can be estimated as follows [Xu2002]. The rate of the atomic flux (m^{-2} s^{-1}) leaving the surface during normal evaporation and due to a pressure gradient is given by the Knudsen-Langmuir equation:

$$\dot{m}_p = \alpha \sqrt{\frac{M}{2\pi RT}} (P_s^{\infty} - P), \qquad \text{(Eq1.1)}$$

M is the molar mass of the evaporating molecule or atom. The factor α (<1 and depends on temperature) is called the efficiency coefficient. R is the ideal gas constant. P is the vapour phase pressure and P_s^{∞} the saturation pressure at the temperature T of the liquid surface. These quantities are related by the Rankine form of the Clausius-Clapeyron equation, assuming the latent heat of vaporization L_v constant:

$$P_s^{\infty} = P_0 \, exp\left(-\frac{L_v}{R}\left(\frac{1}{T} - \frac{1}{T_b}\right)\right), \qquad \text{(Eq1.2)}$$

P_o is the ambient pressure and T_b is the equilibrium boiling temperature at the ambient pressure (the normal boiling temperature). L_v is either the heat of sublimation or the heat of evaporation. If L_v cannot be considered as constant, other expressions (like Dupré or Riedel's formulas) are required.

Vaporization can also occur because of a concentration gradient [DebRoy1991]. The diffusive vaporization rate $\dot{m}_d$ is expressed in terms of a phase change at the surface and the subsequent transport of the vaporized species to the bulk gas phase through the mass transfer boundary layer surrounding the pool. The vaporization rate is then defined as:

$$\dot{m}_d = K \frac{M P_s^{\infty}}{R T_b}, \qquad \text{(Eq1.3)}$$

where K is the mass transfer coefficient given by similarity laws.

2. Spallation

What is referred to as "spallation" corresponds to material ejection driven by relaxation of the stress induced by the treatment [Kanitz2019] [Povarnitsyn2013]. Basically, the spallation of a liquid phase in contact with its mother solid phase is due to a drift in the phase diagram where the following thermodynamic pathway crosses the liquid branch of a binodal domain and enters a metastable region. This leads to the nucleation, growth, and coalescence of voids. This induces the formation of a transient foamy structure of interconnected liquid regions, and eventual separation (or spallation) of a thin liquid layer from the bulk of the target. Material spallation occurs at the liquid–solid boundary, where the spall strength is lower than that in the solid phase. However, the tensile wave is strong enough to cause the cut-off in the liquid phase, according to the applied criteria of nucleation (**Fig. 1.4a**).

In a liquid – the situation under vacuum being different –, the particles produced by this mechanism exhibit distribution sizes that are around 10 nm [Wu2014]. The foamy structure coarsens with time and eventually decomposes into individual droplets on the time scale of nanoseconds. The top liquid layer loses stability because of Rayleigh-Taylor instability and decomposes into large droplets, estimated to have diameters from hundreds of nanometers to tens of micrometers [Shih2017].

3. Phase explosion, also called explosive boiling

What is referred to as "phase explosion" or "explosive boiling" is a process where a superheated surface region, expanding rapidly, undergoes a fast decomposition into a mixture of vapour and liquid droplets (**Fig. 1.4b**). Thermodynamically, it means that solid matter is rapidly superheated up to the thermodynamic critical temperature, at which the spinodal decomposition in vapour and liquid phase in the irradiated material occurs by homogeneous nucleation. This is typically what can be observed when a very clean glass of water (*i.e.* without surface defects to promote nucleation of steam bubbles) is heated in a microwave oven without boiling.

The superheated metastable liquid can undergo an explosive liquid-vapor phase transition when a massive homogeneous nucleation of vapor bubbles starts, by simply touching the surface of the liquid, for instance. This phenomenon appears at much higher energy than spallation and occurs within the nanosecond time scale [Shih2020]. As for spallation, on the time scale of nanoseconds, vapor, small nanoparticles (~10 nm), and large liquid droplets are produced.

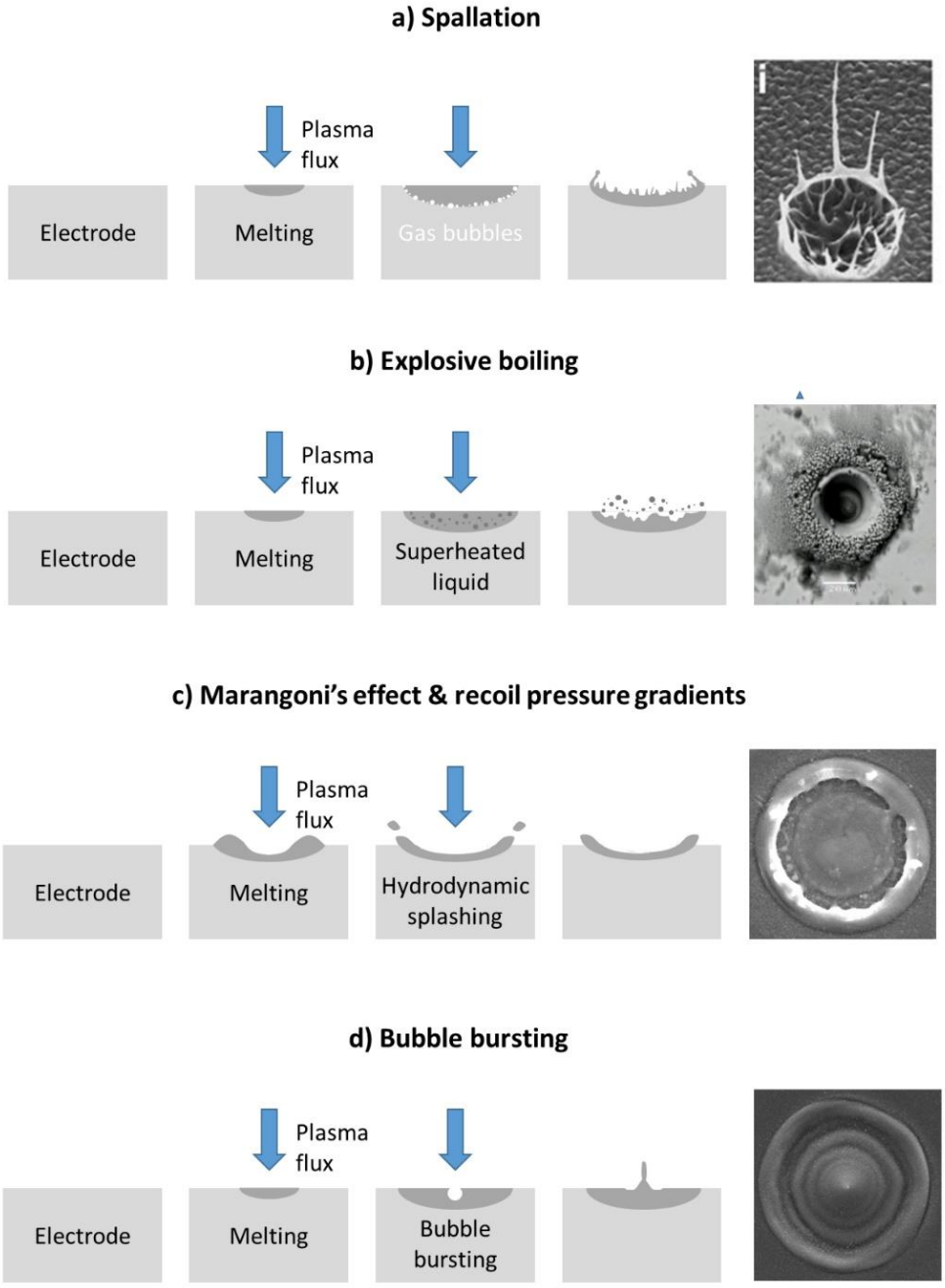

Fig. 1.4: Typical shapes of impacts and related underlying mechanisms leading to the production of large particles. Pictures in a) and b) are *reproduced with permission from Elsevier – Physics Procedia* (Fig. 1 in [Kuchmizhak2017]) and *from Elsevier – Materials Research Bulletin* (Fig. 4 in [Knotek2013]). Other pictures are current authors' credits. All spot sizes are around 10-20 µm in diameter.

4. Droplet emission due to surface temperature gradients

Non-homogeneous distribution of surface temperature is caused by radial temperature gradients in the discharge. It can also be amplified if the discharge channel is not oriented perpendicularly to the liquid well. Because of this non-homogeneous distribution, two driving forces responsible for expulsion of the molten liquid are generated: one emanating from the recoil

pressure effect caused by evaporation, and the other one from the Marangoni effect. Large (beyond 100 nm in diameters and up to hundreds of μm) droplets are produced by both mechanisms (sometimes called hydrodynamic splashing [Shih2018]) and emitted radially (**Fig. 1.4c**).

Recoil pressure gradient

Expulsion of large liquid droplets can be driven at sufficiently high power by the vapour recoil. This phenomenon induces a pressure that splashes the melt and residual recoil pressure redistributes the metallic melt [Ra02014]. The melt expulsion by the recoil pressure is caused by the spatial variation of the normal stress exerted by vapour pressure within the hot spot. The gradient of vapour pressure makes the melt flow outwards, from the high-pressure spot centre to the low-pressure periphery [Volkov2017].

Marangoni's effect

The Marangoni or thermocapillary effect creates a strong tangential stress on a surface submitted to large gradients. The liquid movement within the molten pool is affected by this boundary condition that is due to the dependence of the surface tension on temperature. The surface tension of liquid pure metals decreases with increasing temperature [Sarou-Kanian2003] and then, Marangoni's force acts in the opposite direction of the surface temperature gradient. As the temperature usually peaks at the centre of the well, the liquid flows from the centre to the spot edge, which contributes to the expulsion of the melt. At high heating rates and small thicknesses of the molten layer, Marangoni's stresses can lead to the rupture of the molten layer [Ajaev2003], melt spattering, and formation of droplets [Willis2000].

5. Bursting bubbles

The emission of droplets from the molten well is possible via bursting of bubbles formed in the liquid. Bubbles within the molten well can be created from boiling of the liquid metal or from absorption of discharge gases [Hassanein1997]. Blisters are thus formed on the surface of the well [Balden2013]. A liquid film, covering the surface of the bubble, bursts and releases very fine droplets [Bird2010]. The subsequent collapse of the bubble forms a rising jet of liquid that pinches, according to the Rayleigh-Plateau instability, and produces a spray of micron-scale droplets within tens of microseconds (**Fig. 1.4d**). The effect of the electric field on the ejection of droplets from bubbles bursting at the liquid surface was considered by Holgate and Coppins [Holgate2019].

1.1.3.b Shapes of eroded areas

The different shapes of eroded areas, produced by the mechanisms described previously, are depicted in **Fig. 1.4**. Of course, these mechanisms can combine over sufficiently large time scales, and give more complex structures. However, most of the eroded areas exhibit these shapes that are the most commonly encountered. Roughly, the size of a crater is a linear function of the square root of the electrical charge dissipated during the discharge process [Hamdan2013c].

1.1.3.c Limited erosion

It is possible to strongly limit electrode erosion by using materials with high melting points (usually tungsten) and low current density [He02010, Hieda2008]. When nanoparticles are synthesized from a liquid precursor, this point is critical to keep the as-produced nanofluid with high purity.

1.1.4 Particles aggregation and stability of dispersions

Proper conditions are sometimes encountered for particles to aggregate, which depends on physicochemical processes at stake. Then, particles may settle, as they get bigger, on the bottom of the vessel in which they are contained. Because water is often used as primary solvent, the specific case of oxidative processes in liquid has to be specifically emphasized. Indeed, the stability of solutions is a key point in the synthesis of nanofluids. It is usually estimated by resorting to the zeta potential that derives of the electric double layer that forms around particles.

1.1.4.a Aggregation of nanoparticles

Aggregation of nanoparticles, which leads to the formation of highly porous structures, is of primary importance as it generates multi-modal distributions that can compromise the application of synthesis processes of nanoparticles [Letzel2017]. Irreversible aggregation of nanoparticles is well understood. The fractal formation in colloidal aggregation and the general underlying mechanism have been extensively investigated. They are well known and they can be appropriately applied on the nanoscale. Conversely, reversible aggregation still deserves to be deepened and it is only touched upon in this thesis.

1. Irreversible network formation

Irreversible aggregation will be described briefly since many reference works provide comprehensive pictures of this phenomenon [Everett2007], [Markutsya2010], [Matijevic2012], [Cosgrove2005].

The formation of colloidal structure and the irreversible nanoparticle aggregation are well described by the diffusion-limited cluster aggregation (DLCA) model [Kolb1983], [Meakin1983], a more accurate version of the diffusion-limited aggregation (DLA) model [Witten1981]. The latter considers the existence of a primary particle acting as a seed for the formation of a cluster, to which other individual particles diffuse and attach. The former describes how all particles bind to each other, and diffuse as clusters that can also attach together when in contact.

To account for the compactness of agglomerated structure, often estimated less dense than observed, the reaction-limited cluster aggregation (RLCA) model was proposed [Kolb1984], [Meakin1988]. It relies on the idea that approaching particles aggregate with a probability less than one. This probability is defined by the distribution of situations where the strength of the repulsion between the particles is inferior to the strength of the attraction force at shorter distances, which enables aggregation. The repulsion force is given by the Derjaguin–Landau–Verwey–Overbeek (DLVO) theory [Derjaguin1941], [Verwey1955]. It accounts for van der Waals interactions and electrostatic forces arising between the double layers around the particles. This supplementary degree of freedom favours non-binding collisions between clusters, which increases their interpenetration, and produces denser structure once binding occurs. This approach was used for instance by Ziashahabi *et al.* [Ziashahabi2017] to study the formation mechanism of bead-chain-like ZnO nanostructures prepared via DC arc discharge in liquid.

In colloidal solutions, an appropriate change of the conditions destabilizes the nanoparticle suspension, and induces the aggregation of particles. The particles interact differently because their surface state changed in the new situation [Jungblut2019]. Forces exerted on a single particle are modified and the former balance is affected in such a way that aggregation is enabled. This results in chemical bonding, non-covalent bonding being conventionally restricted to self-assembly.

2. Reversible network formation

Aggregation of nanoparticles is expected to proceed reversibly, and the general macroscopic laws describing the irreversible network formation process are not directly useable on the nanoscale. Reversible network formation is a complex emerging topic, an example of which is as follows.

It is possible to account for the many-body van der Waals interactions on the nanoscale with so-called “many-body dispersion (MBD)” models [Ambrosetti2016], [Kim2006]. Van der Waals forces between polarizable non-metallic nanostructures can be understood by collective interactions between wavelike charge density fluctuations. A simple summation over pairwise

interactions between instantaneous particle- or fragment-like dipolar fluctuations is not as meaningful. The collective wavelike fluctuations are responsible for the emergence of nontrivial modifications of the power laws that govern non-covalent interactions.

Practically, there are several ways in which the modelling of the formation of nanoparticle networks is approached. A practical review on reversible network formation is available in [Jungblut2019]). Nonetheless, a theoretical framework accounting for the reversibility of the clustering process is still pending.

1.1.4.b Oxidation in liquids

Discharges are often created in liquids with different oxidation capabilities. Notoriously, water is more oxidizing than ethanol, and ethanol than ethylene glycol [Xia2009]. In general, alcohols, glycols, and hydrazine can all serve as reductant source. The choice of the liquid is also known to affect the shape of the nanoparticles [Chen2015], [L02005], [Ya02005].

Discharges in liquids make these effects even more complicated to explain than other processes as liquids are transformed by discharges. Indeed, by-products resulting from liquid-discharge interactions are likely to play a role on the nucleation and growth of nanoparticles.

In the case of water, where air gases dissolve, chemistry is extremely complicated. It includes as main species H_2O, O_2, N_2, $OH^\bullet$, $H^\bullet$, $O^\bullet$, $N^\bullet$, H_2O_2, NO_x, O_3, HNO_2, HNO_3, $NO^\bullet$, ONOOH, and ions [Lukes2012]. Species responsible for oxidation are likely to be several, but the way oxidation occurs is still unclear.

Simple description explaining how ethanol molecules scavenge OH radicals, and generate reducing species (H and H_2) [Ke2011], [Wang2008]:

$$OH + C_2H_5OH \rightarrow H_2O + C_2H_4OH \quad \text{(R1.a)}$$

$$e_{aq}^- + C_2H_5OH \rightarrow H + C_2H_5O^- \quad \text{(R1.b)}$$

$$H + C_2H_5OH \rightarrow H_2 + C_2H_4OH \quad \text{(R1.c)}$$

is put forward to explain how non-oxidized metal nanoparticles can be produced by discharges in ethanol. Similar reasoning can be applied to ethylene glycol as metallic nanoparticles can be produced as well (see *e.g.* [Khezri2012], [Khezri2013]).

More complex mechanisms are certainly at stake, as in the case of carbonaceous liquids or liquids containing carbonaceous additives like surfactants, where nanoparticles are often coated by a few layers of carbon [Chen2015]. Lee *et al.* [Lee2014] showed by dissolving WCl_6 in ethanol

that they could synthesize spherical tungsten nanoparticles. By adding an anionic surfactant (SDS) at 30% and 50% (the surfactant/WCl_6 molar ratio), spherical particles are no longer agglomerated. A weak fraction of triangular and hexagonal-shaped nanoparticles are also found. The presence of carbon is not studied but is very likely. Generally, the balance between a too large quantity of surfactant, leading to carbon contamination and a too small quantity, leading to no effect, can only be determined by a trial and error procedure.

1.1.4.c Stability of dispersions

Because of the importance of nanofluids in many industrial applications, it is essential to ensure a high stability of the dispersion in order to maintain the fluid properties constant in time. The physicochemistry of nanoparticles in liquids is a complex topic, and the examples of gold and silver will be taken to illustrate this aspect. Next, the concept of electrical double layer will be introduced to explain how the zeta-potential is defined, a useful quantity to evaluate the stability of dispersions.

1.1.5 Particles' life

Particles' life starts by nucleation, nuclei becomes seeds, and seeds nanocrystals. What is meant by seeds is an intermediate object between a nucleus and a nanocrystal, in which no structure fluctuation (*i.e.* changes of bond-orientational order [Li2014]) is possible. From their formation to their transfer into the liquid phase, nanoparticles are submitted to complex environments where huge gradients prevail. Even though discharges in liquids are often close to equilibrium, nanoparticles can adopt complex shapes.

1.1.5.a Shape control

The shape and structure of Au or Ag nanocrystals strongly affect their spectroscopic properties (like localized surface plasmon resonance LSPR [Wiley2006], surface-enhanced Raman scattering (SERS) [Kottmann2001], Surface Enhanced Fluorescence [Muniz-Miranda2011], plasmon enhanced optically stimulated luminescence [Isikawa2021], etc.), enabling Enhanced Spectroscopies, reviewed for example in the following contributions [Henry2011, Bonyár2018, Li2017].

1. From atoms to nuclei

Classical nucleation theory stipulates that the formation of nuclei in supersaturated homogeneous solution is governed by the balance between the bulk and surface energy of the new phase.

$$J_{nucl} = A\, exp\left(-\frac{E_a}{k_B T}\right) exp\left(-\frac{\Delta G_{ex}}{k_B T}\right), \quad \text{(Eq1.4)}$$

The first exponent ($-E_a$ / k_BT) is related to the kinetic barriers with an overall activation energy E_a, while the second exponent ($-\Delta G_{ex}$ / k_BT) represents the thermodynamic barrier. The parameter A is a pre-exponential factor that depends on the properties of the investigated material. It is possible to predict nucleation rates from this equation for any material at a given level of supersaturation.

However, as discussed by Gebauer *et al.* [Gebauer2014], values calculated accordingly can differ by orders of magnitude from experimentally measured data. Non-classical nucleation theories are then needed but are beyond the scope of this work.

2. From nuclei to seeds

The shape of a single crystal at equilibrium in an inert gas at low temperature (rigorously 0 K) or vacuum can be determined by the Wulff construction. For a fcc metal, possible shapes correspond to polyhedrons. However, the final shape adopted by a fcc nanocrystal can differ a lot from Wulff's shapes. This deviation can be attributed to several reasons [Xia2009]:

- nucleation and/or growth are far from equilibrium,
- surface energies are modified by a capping agent, impurity, or solvent,
- twin defects affect nucleation and growth and lead to new shapes such as decahedron and icosahedron with a total free energy lower than that of Wulff's polyhedrons,
- the synthesis temperature is high.

There are three main ways to control the shape of nanoparticles.

Interfacial energy

Discharges in liquids are often near thermodynamic equilibrium. The shape of nanoparticles is then controlled by the interfacial free energy, γ. It can be defined as the energy needed for creating a unit area of new surface:

$$\gamma = \left(\frac{\partial G}{\partial S}\right)_{n,T,P} = \frac{1}{2} N_b \varepsilon \rho_s, \quad \text{(Eq1.5)}$$

where G is the free energy and S the surface area. For a given surface, N_b is the number of broken bonds, ε the bond strength, and ρ_s the atom surface density. For an fcc structure with a lattice constant of a, one finds easily that:

$$\gamma_{111} = 4.24 \times \frac{\varepsilon}{a^2} < \gamma_{100} = 4 \times \frac{\varepsilon}{a^2} < \gamma_{110} = 3.36 \times \frac{\varepsilon}{a^2}, \quad \text{(Eq1.6)}$$

Then single-crystal seed takes an octahedral or tetrahedral shape in order to maximize the expression of {111} facets and minimize the total surface energy. These inequalities can be modified by the introduction of twin defects. The fcc structures, like Au and Ag mentioned before, are twinned along (111) plane, the s.c. ∑3 twin boundary. The local atomic structure on a twin boundary is hcp, and in a simple single twin there is no strain. The strain is affecting the structure only in the case of 5-fold twinning (still the same, along (111) plane) and the well-known fcc gap of ≈7°. The strain energy caused by twin defects greatly increases as the seed grows in size. This critical dependence on size is also sensitive to reaction kinetics, which offers a possibility of control.

Kinetics limitation

If the reaction that forms the atoms building the particle is slow, nuclei and seeds form through random hexagonal close packing (rhcp), together with the inclusion of stacking faults [Germain2003]. This limitation by a kinetically controlled step makes seeds adopt shapes that depart from those favoured by thermodynamics. In ideal equilibrium there is no possibility to grow anisotropic particles (like rods, plates etc.), as particles would be the same as calculated Wulff shapes. Inclusion of stacking faults and/or twin boundary is needed to induce anisotropic growth.

The key is to ensure an extremely low concentration of metal atoms, so the nuclei will not be able to grow auto-catalytically into polyhedral structures. Instead, the atoms will add to the edges of a planar cluster to generate a plate-like seed. This was observed ([Hamdan2018], [Kabbara2019]) by forming plate-like lead oxide particles using discharges in liquid nitrogen (**Fig. 1.5**).

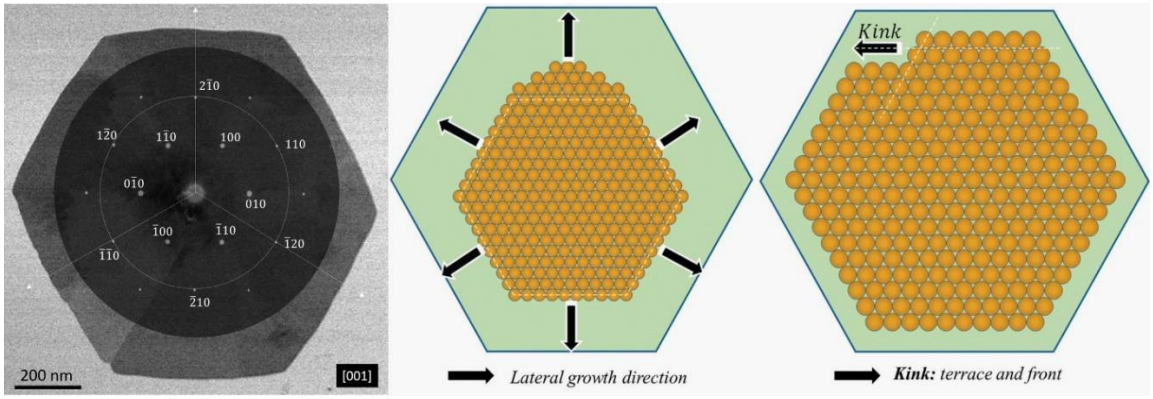

Fig. 1.5: Left: Diffraction pattern of a PbO_2 single crystal superimposed on the TEM bright field micrograph. Oxidation occurred after air exposure but growth corresponds to Pb in liquid nitrogen. The arrows show directions that are perpendicular to the growth of the hexagon faces. The zone axis is [001]. *Reproduced with permission from Elsevier – Particuology* (Fig. 7 in [Hamdan2018]). Middle and right: Schematic representation of the radial growth of the lead nanosheet. *Reproduced with permission from IUCr – Journal of Applied Crystallography* (Fig. 8 in [Kabbara2019]).

Oxidative etching

Hieda *et al.* [Hieda2008] produced gold nanoparticles whose shape was progressively etched and decreased in size during the treatment beyond 5 min by changing the composition of the colloidal solution (initially water containing $HAuCl_4 \cdot 4H_2O$ and sodium dodecyl sulfonate). Successive discharges create H_2O_2 species and lower the pH value, leading to new conditions where nucleation stops, and etching is enabled. This is also what Saito *et al.* [Saito2018] observed in similar experiments (**Fig. 1.6**).

Xia *et al.* [Xia2009] give a more accurate view of oxidative etching. The distribution of single-crystal versus twinned seeds can be further modified by oxidative etching, in which zero-valent metal atoms are oxidized back to ions. If a ligand for the metal ion is also present in the same solution, a combination of the ligand and O_2 can result in a powerful etchant for both the nuclei and seeds.

Consequently, we can readily understand how discharges in colloidal dispersions contribute to the shaping of nanoparticles. As the discharge runs, production of oxidizing species (among which H_2O_2) progressively modifies the liquid composition by reacting with ligands and by forming etching agents. However, these mechanisms have not been clarified yet in the case of discharges in liquids.

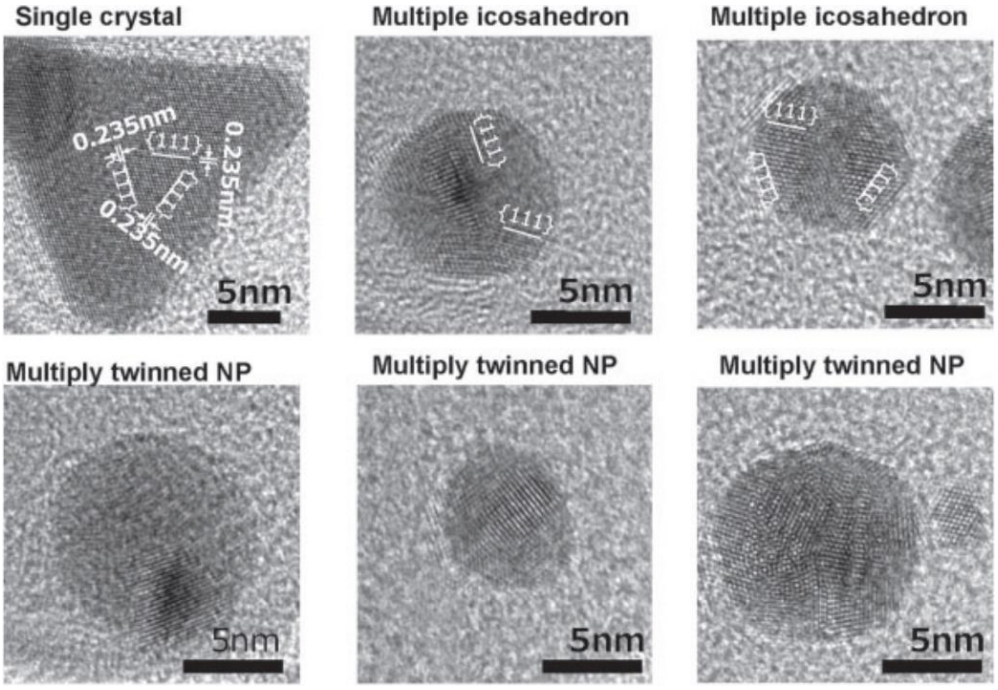

Fig. 1.6: HRTEM micrographs of gold nanoparticles synthesized by discharges in reverse micelle solution. The synthesized gold nanoparticles have different crystal features like fcc single-crystalline particles, multiply twinned particles, and incomplete multiply twinned particles (single-nanotwinned fcc configuration). *Reproduced with permission from IOP Science – Japanese Journal of Applied Physics* (Fig. 7 in [Saito2018]).

3. From seeds to nanocrystals

The condensation mechanism for the growth of nuclei, *i.e.*, deposition of atoms or molecules on the surface of growing particles, the condensation rate can be approximated by the collision rate of monomers with the nucleus [Gouriet2009]:

$$v_{cond} = v_{th}\rho(r_0 + r_n)^2, \quad \text{(Eq1.7)}$$

The average thermal velocity of the monomers in the gas is given by $v_{th} = (8k_BT/\pi M)^{1/2}$, where ρ is the monomer density, r_0 and r_n are the hard sphere equivalent radii of a monomer and a cluster. In this expression for the condensation rate, the cross section is taken as the surface area of a sphere of radius r_n and the sticking probability upon collision is equal to 1.

Consequently, if this probability is not 1 but dependent on facet orientation, the shape of a crystal can change if there is a mix of different facets on the surface. For example, when metal atoms add to the {100} faces of a nanocube, they migrate to the edges of the face resulting in the elongation of the {111} facets. Progressively, the cube transforms into a cuboctahedron and eventually an octahedron. This shape evolution process is known as overgrowth.

The introduction of a capping agent can alter the growth rates of the different facets, thus dramatically altering the final nanocrystal shape. In discharges in liquids, sodium citrate [Ashkarran2013], [Sulaimankulova2019], reverse micelle solution (sodium bis (2-ethylhexyl) sulfosuccinate in dodecane) [Cho2011], sodium dodecyl sulfonate [Hieda2008], cetyltrimethylammonium bromide (CTAB) [Sun2016], among many other capping agents, are used, from recipes developed for chemical processes.

It is important to mention that surfactants and capping agents are very difficult to decompose completely, which results in poor catalytic activities. Discharges in liquids are often presented as efficient methods to synthesize nanoparticles without any surfactant.

1.1.5.b Other phenomena affecting size

Nanoparticles within the discharge can melt, be vaporized or coalesce, leading to changes in size distributions.

1. Melting

The melting point of a spherically symmetric nanoparticle decreases as the radius decreases, which is only observed at very low radius (typically below 10 nm) [Font2013]. This effect can be described down to about 1 nm for gold [Font2013] or nickel [Teijlingen2020] by using a

continuum model (**Fig. 1.7**). Melting point depression is often accounted for by the generalized Gibbs–Thomson implicit relation:

$$L_m\left(\frac{T_m}{T_m^*}-1\right)+\Delta c_p\left[T_m\, ln\left(\frac{T_m}{T_m^*}\right)+T_m^*-T_m\right]+2\frac{\sigma_{sl}}{\rho_s}\kappa=\left(\frac{1}{\rho_l}-\frac{1}{\rho_s}\right)(p_l-p_a), \qquad \text{(Eq1.8)}$$

L_m is the latent heat [J kg^{-1}], T_m the temperature at which the phase change occurs [K], T_m^* the bulk phase change temperature [K], c_p is the specific heat [J kg^{-1} K^{-1}], $\Delta c_p = c_l - c_s$, σ the surface tension [N m^{-1}] and κ the mean curvature. ρ is the density [kg m^{-3}]. p is the pressure [Pa]. Subscripts a, s and l indicate ambient, solid and liquid, respectively.

Surface atoms are less strongly bound to the cluster than bulk atom. Then, melting proceeds by separation of surface atoms from the bulk. This separation is paid for with the latent heat. With a sufficiently large cluster, the energy required is relatively constant since each surface molecule is affected by the same quantity of bulk molecules. However, as the cluster decreases in size, surface molecules are less and less influenced by the bulk, and less and less energy is required for separation. The change in the ratio of surface to bulk energy may also lead to a structural transition and a reduction in surface tension.

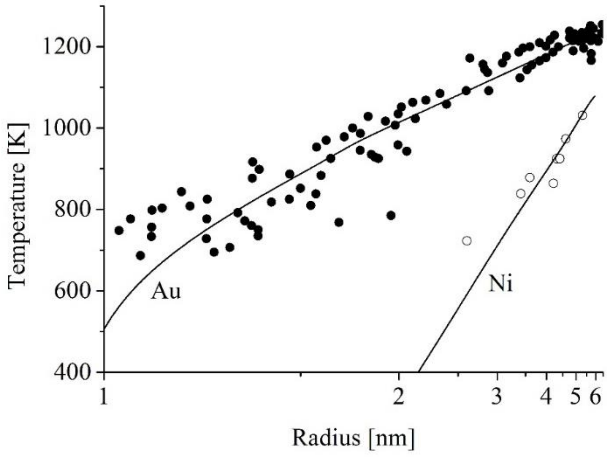

Fig. 1.7: Experimental data and Gibbs-Thomson curves established from Eq. (1) showing the size dependence of the melting temperature of gold [Font2013] and nickel [Teijlingen2020] nanoparticles in an (Y – 1/X) graph. The behaviour is almost linear beyond 2 nm in this graph and follows a reciprocal law.

2. Vaporization

Once the vapour is emitted from the electrode, it condensates farther in colder regions into droplets that are still prone to vaporization along their path. Vaporization of a nanodroplet is affected by the particle size. The equilibrium pressure at the surface of the droplet (**Eq. 2**) must be corrected [Samples1970], [Samples1971]. The correction is:

$$P_s^r = P_s^\infty\, exp\left(\frac{2\sigma M}{\rho RT}\times\frac{1}{r}\right), \qquad \text{(Eq1.9)}$$

P_s^r is the saturation pressure for a droplet of radius r. σ the surface energy and ρ the density.

3. Coalescence

Coalescence affects the size distribution of nanoparticles by merging primary particles, *i.e.* those produced by condensation, into a larger single nanoparticle (see **Fig. 1.8**). This is a very complex phenomenon between nanocrystals that can be decomposed into elementary steps [Grammatikopoulos2019]:

1) *Coagulation* refers to the attraction and contact between primary particles. In the discharge, it is due to in-flight collisions after which particles remains stuck together. This phenomenon is often referred to as Smoluchowski ripening [Stoldt1999].

2) *Rigid body reorientation* occurs once the primary particles are close enough to start interacting. An interface forms that is usually misoriented, because of the randomness in the coagulation geometry. Thus, a number of interface layers are shorn. Eventually, the particles rotate as rigid bodies, driven by mutual torques, maximizing the contact area. A more coherent interface with a larger area is then produced.

3) *Formation of defects* results from the very fast (few ps) reorientation stage. If primary particles cannot be perfectly aligned because of their geometry, which is the most probable situation, a twin boundary forms, as rotation is hindered by the newly formed bonds.

4) *Heat release* results from free-surface annihilation due to bond formation. As the surface/volume ratio decreases, the part of the surface energy remaining after the creation of the interface transforms into thermal energy [Lehtinen2002].

5) *Temporary melting of interface* has been proposed by Grammatikopoulos *et al.* [Grammatikopoulos2014]. If the heat release essentially contributes to the temperature rise of the child particle (case of an adiabatic system), it can be sufficient to reorganize it at the atomic level. A wave that originates at the interface between the primary particles, propagates along the body of the child particle, resulting in its full crystallization. Concurrently, a temporary disordering of the atoms at the interface and a "softening" of their bonds is observed.

6) *Neck growth* is all the more fast as local curvature is high, which speeds up atomic surface diffusion. A neck is formed on either side of the interface when primary particles coagulate. However, the neck only reaches substantial dimensions if it is promoted by the temporary melting of the interface that enhances the transport of atoms from the core of primary particles to the neck.

7) *Plastic deformation*. Even after neck formation, the system can still behave within the elastic limit (~0.8 nm after Averback and Zhu [Averback1996]) as a coupled-oscillator (with possible rotation of the two primary particles). Thermal vibration makes each particle pulsate around the initial contact locus. Plastic deformation is then possible by relaxation of accumulated internal shear stress, possibly assisted by the heat, which enables the glide of misfit dislocations and their annihilation at the surface. Protrusions can thus be formed.

8) *Consolidation*. The neck thickens at a growth rate that slows down, because the difference in curvature between the neck and the primary particles becomes smaller. The two-particle system gets stiffer, which hinders its pulsation, and makes it behave as a single particle. Consolidation takes about 100–200 ps. Free-surface annihilation becomes negligible, and so the heating it induces. Oftentimes, experimentally grown nanoparticles are trapped in a metastable steady state due to quenching upon deposition. Coalescence is often considered as achieved at this point in theoretical approaches.

9) *Slow aging*, however, extends the coalescence process and favours a "sphericization" of the system, as referred to by Lewis *et al.* [Lewis1997], a process that lasts for hundreds of ns up to a few μs. This means that the ratio of the surface area of the particle tends toward the surface area of a sphere of the same volume as the particle. Here, the neck acts as a sink for diffusing atoms.

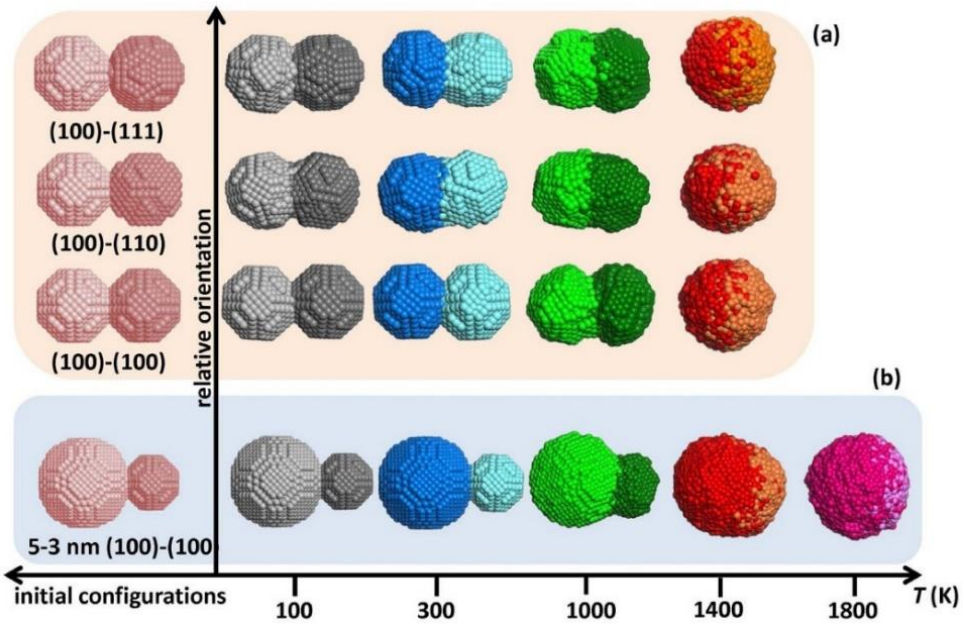

Fig. 1.8: Parameters affecting nanoparticle coalescence. (a) Effect of temperature and relative orientation on the coalescence of 2 crystalline Pd nanoparticles, 3 nm in diameter. (b) Effect of temperature and size on the coalescence of 2 crystalline Pd nanoparticles of different sizes (5 and 3 nm in diameter), with touching (100)-type facets. Note that (b) is not to scale with (a). (For clarity, temperatures are represented by shades of colours). *Reproduced with permission from Springer Nature – Scientific Report* (Fig. 2 in [Grammatikopoulos2014]).

4. Oxidation in air

Except for gold, nanoparticles produced by submerged discharges are prone to be oxidized either in air, when they are floating on or taken out of a non-oxidizing liquid. They can also be oxidized on purpose but this aspect is deemed to be beyond the scope of this thesis. Oxidation of sub-micrometric objects has been studied thoroughly [Atkinson1985]. Only oxidation in dry air at room temperature is described here. This process changes the size of the pristine nanoparticles because of the change of molar volume between the metal and its oxides.

Basically, when the particle is less than 1 µm in diameter, electrical neutrality, assumed in Wagner's theory for thick films [Wagner1933], within the oxide layer is not satisfied, and when less than 20 nm, the Nernst-Einstein relationship is no longer appropriate. Thus, theories of thin film growth must consider atom jumps in the presence of large electric fields and the possibility of large space charges.

Cabrera and Mott's [Cabrera1949] theory assumes that electrons can freely pass from the metal to ionize adsorbed oxygen atoms or molecules at the oxide/gas interface, so that the electron electrochemical potential (Fermi level) is equal in the metal and the adsorbed gas layer. The general picture is based on the injection of defects into the oxide at one of the film interfaces (with gas or metal). This process is assumed to be rate-controlling. Using the Kröger-Vink notation, and taking the example of chromium oxidation, one notices that, depending on the temperature and O_2 partial pressure, either triply charged chromium vacancies are injected at the gas/oxide interface and diffuse inward:

$$\frac{3}{2}O_2 \rightarrow 3O_O^x + 2V_{Cr}^{'''} + 6h^{\bullet}, \qquad \text{(R1.4)}$$

(p-type $Cr_{2-x}O_3$) – gas/oxide interface

or triply charged interstitial chromium atoms are created at the metal/oxide interface and diffuse outward:

$$Cr_2O_3 \rightarrow 2Cr_i^{\bullet\bullet\bullet} + 6e' + \frac{3}{2}O_2, \qquad \text{(R1.5)}$$

(n-type Cr_2O_{3-x}) – metal/oxide interface

In both cases, the accumulation of vacancies at the metal/oxide interface induces the development of Kirkendall porosity. Such a porosity is not observed if the oxide growth is driven by two other types of mechanisms, observed with other metals: oxygen atoms, injected at the gas/oxide interface, diffuse inward (p-type MO_{1+x}) and oxygen vacancies, injected at the

metal/oxide interface, diffuse outward (n-type $M_{1+x}O$). This explains why oxidation of some nanoparticles leads to core-shell structures and/or hollow particles.

For very thin (*i.e.* where tunnelling can no longer be neglected) films, Fromhold [Fromhold1980] showed that the assumption of electronic equilibrium is reasonable. In the case of nanoparticles, quantum confinement effects should also intervenes, but to best of our knowledge, no study has been done on this topic yet.

Finally, it is also important to mention that reduction of nanoparticles after oxidation does not lead to a complete recovery of the initial metallic state. For instance, after oxidation in O_2, ZnCu clusters (< 10 nm) transform into a polycrystalline cluster consisting of separate CuO and ZnO nanocrystals. Subsequent reduction in H_2 converts CuO into Cu with ZnO nanocrystal covering its surface. Then, H_2 dissociates onto metallic Cu to form H atoms that partially reduce ZnO into CuZn [Holse2015].

These theories are based on point defects but oxidation is also affected by the presence of structural defects that play a tremendous role at low temperature, as volume diffusion is strongly limited because of high-energy barriers of jump processes. These barriers can be lowered by stress to a certain extent, which is also an important effect to take into account in order to predict correctly how oxidation occurs in these specific conditions. Finally, in air, not only oxygen but also water vapour can intervene as oxidation agents. The reader is referred to a number of seminal papers illustrating these phenomena in the case of different elements: *e.g.* oxidation at room temperature of reduced iron oxide nanoparticles by Wang *et al.* [Wang2005], air oxidation of monodisperse cobalt nanoparticles by Varon *et al.* [Varón2013], the first stage of air oxidation by Chen *et al.* [Chen2005], or the evolution of the oxide thickness and oxidation rate of Si nanoparticles in air and at room temperature by Yang *et al.* [Yang2005].

The effect of the spherical geometry on metal oxidation driven by mobile charged point defect was also studied by Fromhold [Fromhold1988]. The electric potential developed across the oxide is the same as for planar geometry, but the time, for complete oxidation for spherical particles of a given diameter, can be as much as a factor of 3 shorter than that for planar samples of the same thickness.

1.1.5.c More complex structures

Discharges in liquids can be used to synthesize nanoparticles made of, at least, two different materials that can be organized in different structures depicted in **Fig. 1.9**. Both

materials are made immiscible, either because thermodynamics imposes it (**Figs. 1.9a to e**), or because they are synthesized successively (**Figs. 1.9a, b or c**).

Bi-particles (**Fig. 1.9a**) have been synthesized by different groups: *e.g.* Pt-Pd [Kim2014], Ni-Cu [Sun 2016], Ag-Pt [Pootawang2012], Ag-Cu [Rahaghi2015], etc. This kind of structures results from coalescence of particles that are synthesized either simultaneously (from electrodes made of different materials) or separately (in space and/or time). Tsukanov *et al.* [Tsukanov2019] showed by molecular dynamics that immiscible nanoparticles can interpenetrate if they collide with sufficiently high relative velocities.

Core-shell structures (**Fig. 1.9b**) are usually obtained by chained treatments where seed nanoparticles of one material are coated by another material in a second step. The best way to coat nanoparticles already present in a liquid is to decompose a precursor that deposits onto the nanoparticles surface. This is easy to achieve by discharges in contact with liquids for instance.

Conversely, discharges in liquids rather form attached nanoparticles in sequenced treatment. The expansion of the discharge repels nanoparticles added in the liquid from emitted species by the electrodes. Then, one-step synthesis is only possible by mixing intimately the two elements in a crucible: *e.g.* CuO@Ta_2O_5 [Karahaliou2012]. For a carbon shell, one-step synthesis is also possible with a carbonaceous liquid, like benzene or hexane: *e.g.* (Co, Ni, Fe)@C. [Sergiienko2007], [Abdullaeva2012], [Xu2006]. Then, using a liquid precursor (like $HAuCl_4$) in a aqueous colloidal dispersion containing nanoparticles, say Pt, should give Pt@Au nanoparticles in one step. But to the best of our knowledge, no experiment of that kind has ever been done yet.

Pulsed laser ablation also provides similar capabilities. For instance, the introduction of *ad hoc* solvents lead to the creation of carbon shell or structures [Zhang2018]. Even more interestingly, the possibility of using CO_2 sub-products in solution with NaOH was showed to be efficient for the production of gold-carbon nanocomposites [Del Ross02016, Del Ross02018].

Kabbara *et al.* [Kabbara2017] showed that it is also possible in two steps, by wrapping one type of particle (Cu) into an ultra-thin foil made of another one (Zn) synthesized beforehand, this mechanical way of forming core-shell nanoparticles requiring no deposition.

Decorated nanoparticles (**Fig. 1.9c**) are usually obtained by depositing one phase of small size onto another phase of large size. Usually, this is a two-step process. This has been achieved in one step by discharges in liquids for the Si-Sn system [Kabbara2015]. The mechanism relies on grain detachment of a sintered Si-Sn electrode, where Si and Sn are well separated, leading to tin nanoparticles attached to silicon grains.

Nanoparticles with multiple domains (**Fig. 1.9d**) are either made of one phase inlaid into another or made of one phase segregated at the grain boundaries of another. These particles, as Janus particles (**Fig. 1.9e**) – a special type of nanoparticles with surfaces exhibiting two or more distinct physical properties – have only been synthesized by PLAL but not by discharges in liquids.

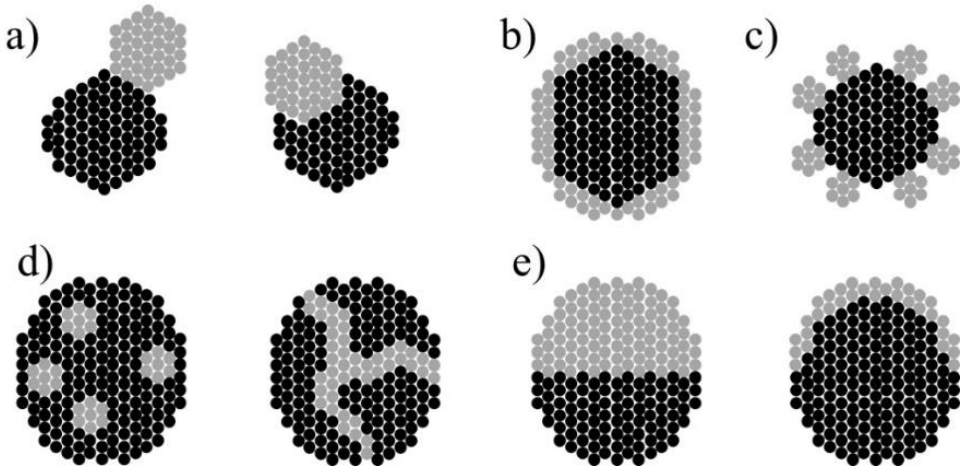

Fig. 1.9: Possible structures associated with bi-particles. a) bi-particles (more or less interpenetrated); b) core-shell; c) decorated; d) multiple domains; e) Janus.

1.1.6 Particles' size distribution

As discharges in liquids most often produce particles with broad size distribution, it is essential to describe how to measure them, which requires to master the techniques used in order to get convergent results. It is also possible to change size distributions by fragmenting nanoparticles.

1.1.6.a Size distributions

Ashkarran *et al.* [Ashkarran2009] (**Table 1.1**) obtained almost monodisperse (*i.e.* with a geometric standard deviation of a log-normal distribution < 1.25) gold colloidal dispersion (mean size: 8 ± 3 nm) by creating discharges between two titanium electrodes in a $HAuCl_4$ solution. This process behaves as an electrochemical process, similarly to discharges in contact with liquids. Submerged discharges in liquids where nanoparticles are produced by electrode erosion produce multimodal size distributions (**Fig. 1.10**) [Hamdan2013d], [Sergiienko2010], [Chen2004].

At most, three distributions coexist. Large particles (*i.e.* > 100 nm and up to tens of µm) are only a few and spread all over the substrate. Nanoparticles of intermediate size (*i.e.* from 20 to 100 nm) are found either as necklace-like or fractal agglomerated structures or as isolated particles. Nanoparticles of small size (*i.e.* from 2 to 10 nm) are primary particles.

However, this approach is not satisfactory as the various populations are not associated with their mechanisms of formation. From the list of erosion mechanisms established hereinabove, it is easy to understand that the origin of the largest population of nanoparticles is due to ejection of droplets from the liquid well but there are several possible mechanisms that may be involved. The origin of the smallest distribution can only be due to the rapid condensation of the vapour phase. On the contrary, the origin of the intermediate-size population can be multiple. The smallest nanoparticles can continue growing if they stay within the discharge region, reacting with the emitted vapour that is not homogeneously distributed within the interelectrode gap. They can also grow by coarsening with other particles and then, the distribution of the particles themselves also matters.

Consequently, we could expect 4, 5 or even more contributions in a multimodal size distribution. This statement is corroborated by several works where trimodal distributions are proposed (see for instance [Tseng2013] and [Trad2020] in **Table 1**) but with very different mode positions. The issue lies in the possibility for distinguishing accurately all the modes in a distribution of nanoparticles.

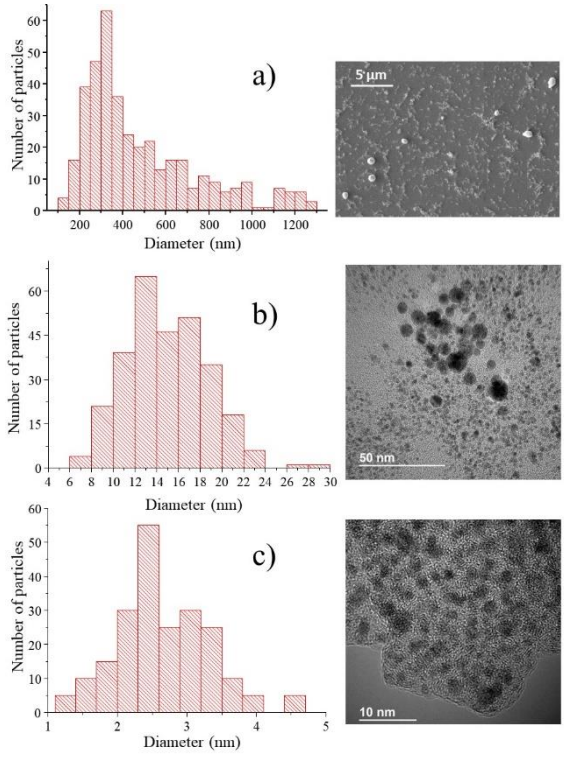

Fig. 1.10: Size distributions of particles produced by discharges in liquid. Three distributions are commonly found. The two lowest distributions can overlap, leading to two main distributions, as it is described in some other processes like pulsed laser ablation in liquid. *Reproduced with permission from Elsevier – Materials Chemistry and Physics* (Fig. 4 in [Hamdan2013d]).

In LASiS (Laser Ablation Synthesis in Solution), nanosecond pulsed laser ablation is known to give more or less narrow monomodal distributions that are described by a log-normal distribution, ablation being principally driven by thermal processes. On the other hand, pico and femtosecond ablation may lead to multimodal distributions, due to the multiple ablation mechanisms. In this latter case, size distributions can also be sometimes by described by a log-normal distribution. Therefore, caution must be taken to interpret these particle size distributions.

Logically, the existence of several erosion mechanisms must lead to an identical number of distributions. However, one reads commonly that two populations are to be distinguished: small and large. In recent studies based on molecular dynamics simulation, Shih *et al.* [Shih2018], [Shih2020] investigate the origin of bimodal nanoparticle size distributions produced by laser ablation in liquids. They establish that three distinct nanoparticle generation mechanisms operating at different stages of the ablation process and in different parts of the emerging cavitation bubble exist. Two of them produce large nanoparticles (spallation and explosive boiling) and one of them small nanoparticles (nucleation at the very front of the emerging cavitation bubble). They conclude that the coexistence of the three distinct mechanisms of the nanoparticle formation at the initial stage of the ablation process can be related to the broad nanoparticle size distributions commonly observed in nanosecond PLAL experiments. To the best of our knowledge, no attempt was made to fit with a multimodal approach, size distributions of nanoparticles produced by ns laser pulses that can be described by a monomodal log-normal function.

The confusion also exists because only the smallest nanoparticles are collected for analysis. For instance, it is possible to proceed as follows [Mardanian2014]. In a discharge-based process, when heavy particles settle at the bottom of the vessel that contains the synthesized colloid suspension, this latter can be cleared from its sediments by pouring carefully the upper part of the solution into another beaker. Then, small quantities of the new solution containing only its lightest particles can be collected with a pipette for further characterization.

There are several techniques that can be used to evaluate the mean diameter of a set of well-defined nanospheres: DLS (dynamic light scattering), AFM (atomic force microscopy) in tapping mode, UV-Visible spectroscopy and two-colour SPR (Surface Plasmon Resonance) spectroscopy. Several papers [Zaman2019], [Georgiev2013] showed that estimates of the mean diameter of well-controlled nanospheres synthesized by wet chemistry and evaluated by the previously-cited techniques are very close, demonstrating the convergence of these methods for

almost ideal spheres. On the other hand, for other types of nano-objects, caution must be taken to interpret results produced by these different diagnostics, as discussed by Tomaszewska *et al.* [Tomaszewska2013]. For example, differences between TEM and UV-Vis spectroscopy often arise due to:

- possible agglomeration of nanoparticles during deposition on the grid, especially in colloidal dispersions in water;
- non-spherical shape of nanoparticles;
- a non-representative sampling of nanoparticles for TEM analysis;
- nanoparticles are oxidized, which affects the effective dielectric constant to be used in the Mie fit required by UV-Vis spectroscopy.

The existence of an intermediate size distribution is not clearly understood yet, likely because it probably results from distinct phenomena:

- the duration of the nucleation process may strongly vary if the vapour is emitted at the very beginning of the process, when the pressure is high, or much later, when it is reduced;
- it is also true for the vapours emitted by the cathode and by the anode;
- coalescence of particles certainly affects the size distribution, and smear out transitions between modes, etc.

To conclude about particle size distribution analysis, it is important to mention that even though it is a useful concept to describe the population of nanoparticles produced by a given process, it cannot be used usually to correlate observations on size modes with underlying growth mechanisms.

1.1.6.b Fragmentation of nanoparticles

Until now, fragmentation of nanoparticles has not been observed with electric discharges, but this process might exist as well for sufficiently fast electric fields (picosecond-pulsed discharges). Indeed, Giammanco *et al.* [Giammanco2010] fragmented Au nanoparticles by interaction with the second and the third harmonics of a Nd:YAG picosecond laser. However, laser and discharge treatments are already associated in that purpose [Tarasenka2020].

The photothermal mechanism responsible for nanoparticle fragmentation relies on the way temperature rise in response to the laser excitation. At moderate fluences, heating, melting, and evaporation of irradiated nanoparticles enables size reduction of primary nanoparticles, creating a new population of smaller ones by nucleation and growth from the evaporated atoms.

At higher fluences, nanoparticles can be either fully evaporated or fragmented by explosive decomposition into vapor and liquid droplets when superheated up to the limit of thermodynamic stability of the molten material Garrison.

According to Huang and Zhigilei, [Huang2021] the detailed analysis of the nanoparticle fragmentation mechanisms reveals two distinct pathways of the formation of the fragmentation products: (1) the direct generation within ~100–200 ps of relatively large nanoparticles with diameters ranging from ~2.5 to 4 nm and (2) the much more gradual growth of smaller nanoparticles formed by agglomeration and coalescence of atomic clusters on the timescale of tens of nanoseconds. These two pathways are responsible for the early appearance of a bimodal mass-weighted particle size distribution.

1.1.7 Crossing interfaces

1.1.7.a The discharge-liquid barrier

The discharge-liquid interface is very difficult to probe but interesting results could be obtained thanks to original experimental works. Sano *et al.* [Sano2008] recorded under microgravity conditions the development of an arc discharge submerged in water. They notice, from images of the reactor falling freely in a column under vacuum for about 4 s, that a transparent gas film was generated in the gas phase zone adjacent to the gas–liquid interface. The authors concluded that chemical reactions involving water were possible inside the bubble and not only at the water-gas interface.

The behaviour of nanoparticles in discharge bubbles is much better understood thanks to recent results obtained with synchrotron facilities on pulsed laser ablation in liquid [Reich2017], [Letzel2017], [Letzel2018]. It has been shown, with SAXS (Small-angle X-ray Scattering) experiments, that the bubble interface is a quite impervious boundary for the primary and secondary particles. In PLAL, they cross the interface barrier by jet-like emission after the collapse of the first rebound. These two statements must also apply for submerged discharges created between two electrodes. Indeed, bubbles oscillations produce many different kinds of instabilities [Menon1998] like Rayleigh-Taylor, Kelvin-Helmholtz, Landau-Darrieus or Birkhoff, leading to jet-like emission (**Fig. 1.11**).

Basically, the discharge-liquid barrier is rather nanoparticles tight. The transfer from one phase to the other is limited. This is also the case of the liquid-air barrier.

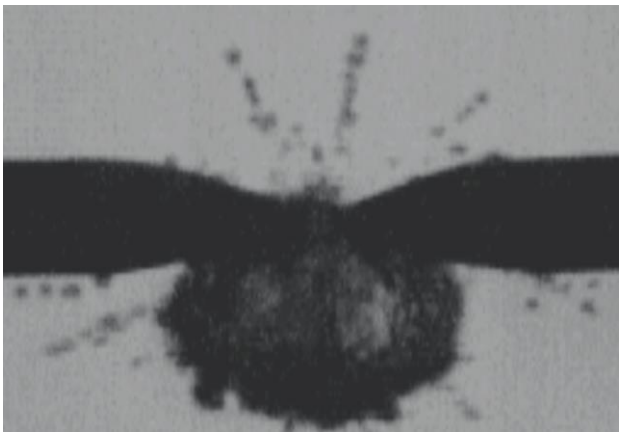

Fig. 1.11: Example of jet-like emission after the collapse of the first rebound of a bubble formed by nanosecond-pulsed discharge in heptane. Jets fragment into groups of aligned bubbles forming threads that point toward the center of the interelectrode gap [Hamdan, lab files].

1.1.7.b The liquid-air barrier and safety aspects

Sano *et al.* [Sano2001], [Sano2002] synthesized carbon nanomaterials by erosion of graphite electrodes submerged in water. They noticed that nanoonions (average diameter : 25-30 nm) were majorly present as floating powder on the water surface, the other nanocarbons being rather found located on the bottom of the vessel.

Even though the liquid evaporates, this mechanism does not transport any nanoparticles in air [Chon2007]. This is why the dewetting of a colloidal dispersion concentrates nanoparticles at the moving front of the liquid fingers that form upon demixing of the two phases [Thiele2009]. However, evaporation is affected by the presence of nanoparticles [Chen2010].

As long as nanoparticles are left in the liquid, nanofluids in containers can be considered as safe. However, they also face public concerns about their safety in use as they can be spilled by accident. The lack of legal framework for their handling and recycling is a key issue [López2018]. It would be prudent to pursue green designs by choosing nontoxic or biodegradable nanoparticles [Choi2009].

1.1.8 Outlook and new applications

In this pedagogical review, emphasis is put on specificities of discharges in liquids in nanoparticles' synthesis. As colloids and nanofluids are generated by these processes, application related to these biphasic systems is extremely large. For instance, they can be used:

- to replace water and ethylene glycol as conventional coolants in an automotive car radiator [Leong2010];

- to produce hydrogen via their use as working fluid in solar parabolic trough collectors [Toghyani2019];
- to recover oil more efficiently in rock pores by depositing a wedge film making rock surfaces more dewettable [Choi2017];
- to decrease by several orders of magnitude bacterial activity including Gram-negative, Gram-positive and spore bacteria [Jalal2010];
- to serve as a new reaction media in the preparation of chemicals, like amides via direct amidation of aliphatic carboxylic acids [Tamaddon2011];
- to enable sensing like, for instance, those magnetically polarizable nanoemulsions used for imaging internal defects in materials [Mahendran2012]; etc.

There is a number of challenges that deserve to be tackled:

- Recently, nanoalloys, *i.e.* single solid solution, made of immiscible elements have been synthesized by PLAL [Swiatkowska2013, Swiatkowska2015]. Producing them by discharges in liquids has been showed to be possible too [Yang2019a]. Mechanisms leading to nanoalloying of immiscible elements are still to be clarified.

These new results open up the way to the study of optical properties of metallic nanoalloys [Swiatkowska2015, Larin2020]. Engineering of nanoalloys for optical properties consists in controlling defects, element distributions, oxidation and surface functionalization processes.

- Chemistry driven by discharges in liquids is a very complex topic, still in its infancy. Discharges in carbonaceous liquids for instance are responsible for the deposit of a carbon layer onto nanoparticles, but they also produce unusual chemical by-products like polyynes [Cataldo2004]. This is also true for the synthesis of uncommon nitrogen polymer [Senthilnathan2013] or diamondoids [Oshima2012].

Chemistry driven by discharges in liquids is extremely complex and capable of producing rare by-products. The possibility of a better control of chemical reactions in the liquid phase is an important stake. It is a major challenge for discharges in contact with liquids [Lukes2014] but also for discharges in liquids.

- Multimodal size distributions are still an issue for large scale production of well-controlled nanoparticles but huge progress made recently on erosion mechanisms gives promising outlook to achieve unimodal monodisperse size distributions.

The possibility of controlling size distributions in a one-step process is not an easy task. If unimodal distributions have been produced by several groups (see **Table 1.1**), none of them

achieved to get monodisperse distributions. Discharges in liquids containing precursors are more suited to this goal than processes based on electrodes erosion.

- Control of defects to control properties.

Engineering of defects (twin defects, vacancies, edges, doping, etc.) in nanoparticles is a key topic to better control optical [Ahmed2016] and catalytic properties [Ortiz2019]. Controlling defects in nanoparticles by discharges in liquids remains hitherto a dare to take. This is could be a way to develop low-cost catalysts based on non-rare chemical elements or to tune non-linear effects in nanoparticles for optics.

- Control of surface physicochemical states.

Controlling the grafting of selected chemical functional groups on nanoparticles remains a challenge. It is essential anyway to set the stability of nanoparticles in colloidal dispersion. It also control their activity, not only catalytically but also optically. It may even affect the chemical homogeneity of very small nanoparticles. As seen before, discharge-enhanced post-treatments can be used to functionalize nanoparticles, but resorting to these processes cannot be generalized to any situation.

1.2 2D materials by discharges in liquids

Intense research efforts have focused on 2D materials due to their exceptional properties and potential to unveil novel phenomena [Geim2013, Butler2013, Geng2018]. However, the utilization of discharges in liquids for nanosheet production is uncommon for most materials (except for carbon), which are often absent from comprehensive reviews in the field [Belmonte2014, Saito2015, Burakov2015, Chen2015, Horikoshi2017]. Notably, while significant progress has been made in generating various types of nanocarbons through experiments with arc discharges in gas, the synthesis of nanosheets composed of non-carbon materials has remained relatively limited, following the pioneering work by Sano *et al*. [Sano2001, Sano2004].

Nanosheets growth through nanosecond-pulsed discharges in liquids has proven successful for various materials such as ZnO [Kabbara2017], AgO [Kabbara2018a], and PbO_2 [Kabbara2019]. Hamdan *et al*. [Hamdan2021] achieved the formation of 2D mesoporous CuO agglomerates by assembling elementary nanocrystals with sizes in the range of a few nanometers. Saito *et al*. [Saito2012] generated SnO plates through a discharge initiated in a 0.001 M K_2CO_3 solution, utilizing a biased Sn wire operating at 400 V. The anisotropic nature of these nanostructures is attributed to differential growth rates, resulting in the formation of $Sn_6O_4(OH)_4$

octahedrons that assemble into plate-like skeleton crystals. In these studies, the electrodes contribute the necessary material for the formation of nanoobjects through their erosion.

Similarly, Chen *et al*. [Chen2012a] utilized a gas-liquid interface discharge at atmospheric pressure between two tungsten electrodes. One electrode was positioned above a 0.1 mol/L $NaNO_3$ solution, while the other was immersed in the liquid. They successfully synthesized ultrathin single-crystal WO_3 nanosheets consisting of six monolayers. This achievement was accomplished through the lateral attachment of small WO_3 nanocrystals. In a similar setup, Furuya *et al*. [Furuya2007] synthesized gold nanoplates; however, the metal source was not the electrodes but rather $HAuCl_4$ (0.33 mM) added to an aqueous solution containing 1.33 mM $NaHCO_3$. These structures formed on the surface of the solution, rather than within the solution itself. Recently, a rapid synthesis of Mn_3O_4 nanosheets was achieved through a one-step liquid plasma discharge deposition. This process involved orienting a titanium foil perpendicularly to the electric field created between two electrodes placed in an electrolyte. The electrolyte consisted of 0.01 M $C_4H_6MnO_4{\bullet}4H_2O$, 0.5 M NaCl, 9 mg of (1-Hexadecyl) trimethylammonium bromide as a surfactant, and 50 mL of deionized water mixed with 30 mg of polyvinylpyrrolidone as a stabilizing agent [Xiu2023]. Notably, no nanosheets could be grown when the electric field was parallel to the surface of the foil.

1.3 Introduction to $Bi_2O_2CO_3$ Nanosheets

$Bi_2O_2CO_3$ nanosheets represent a fascinating class of nanomaterials that have garnered significant attention in recent years due to their unique properties and promising applications in various scientific and technological domains. These nanosheets are characterized by its layered crystal structure.

The bismutite ($Bi_2O_2CO_3$) first reported by Grice's group [Grice2002] is a typical "sillén" phase, in which Bi–O layers and (CO_3) layers are intergrown with the plane of the (CO_3) group orthogonal to the plane of the Bi–O layer.

$Bi_2O_2CO_3$, a nanostructured material with unique layered structures, is composed of alternate stacking of $(Bi_2O_2)^{2+}$ sheets interleaved by CO_3^{2-} groups [Ding2020]. It exhibits exceptional photocatalytic properties when exposed to UV–vis light irradiation [Dong2011] [Chen2012b]. Consequently, $Bi_2O_2CO_3$ has garnered considerable attention in the field of photocatalysis until recently [Zha02011, Cheng2010, Dong2012, Lu02016, Ni2016, Tian2022, Chen2023]. It can be hybridized with various elements or cocatalysts such as Bi [Liang2023, Liu2018], Br [Zhang2019a], Ni [Amadu2021, Han2023], BiOCl [Zhang2014], g-C_3N_4 [Zhang2017,

Hu2021, Yang2019b], RGO [Kang2019], polyaniline [Zha02015], Ag_2CO_3 [Li2016], Bi_2MoO_6 [Zhang2019b], Bi_2WO_6 [Liu2018], MoS_2 [Hu2018], Mo_2S_3 [Li2022a], Co_3O_4 [Gu02018] or Fe_2O_3 [Hu2014].

$Bi_2O_2CO_3$ nanosheets can be synthesized using various methods, including hydrothermal and solvothermal processes [Liu2010a] [Ding2020], sonochemical synthesis with liquid phase exfoliation of Bi [Gupta2022], electrochemical exfoliation of bismuthene [Qin2021], or controlled reconstruction of SN-BiOx immersed in a 0.5 M $KHCO_3$ solution [Zhang2023]. Among these methods, the production of nanoobjects through pulsed discharges in liquids stands out as a versatile one-pot synthesis process, capable of anchoring nanoparticles and generating hierarchical nanostructures [Belmonte2023, Saito2019]. Furthermore, it can be highly efficient, enabling the production of tens of milligrams of nanoobjects per hour [Jedsukontorn2018].

Chapter 2

Synthesis and growth mechanism of $Bi_2O_2CO_3$ nanosheets

2.1 Synthesis and growth mechanism of $Bi_2O_2CO_3$ nanosheets

The growth of $Bi_2O_2CO_3$ nanosheets through nanosecond-pulsed discharges in liquid environments has been achieved by applying voltages slightly above the breakdown voltage. This growth process involves surface modification of the cathode electrode following pre-treatment with chemical etching. Remarkably, the choice of liquid medium, whether water or liquid nitrogen, does not significantly affect the interaction between the electrodes and the metallic discharge that forms during the initial stages of synthesis. This process is fast and template-free. The anisotropic growth of these two-dimensional objects is attributed to ion-assisted deposition via the ledge mechanism, supplemented by the presence of surface defects. Prior to the growth treatments, chemical etching is essential to enhance the probability of nanosheet formation from virtually zero to almost a hundred percent. This step is crucial in eliminating native oxide layers and exposing surface defects, which are present as parallel planes forming combs within polishing scratches. The detachment of nanosheets from the cathode and their release into the liquid is facilitated by the sweeping of the liquid-bubble interface, which breaks the nanosheets away from their substrate. As the electrodes undergo aging, nanosheets are formed by outward diffusion of bismuth and reaction with water and CO_2 in the air. By gaining a better understanding of this growth mechanism, exciting opportunities arise for the design and large-scale production of 2D nanostructures.

2.1.1 Experimental details

The experimental setup (**Fig. 2.1**) involved a solid-state switch (Behlke HTS-301-03-GSM) connected to one pin-electrode, while the other pin-electrode was grounded. The switch was supplied by a high DC voltage power generator (Technix SR15-R-1200-15 kV-80 mA). The voltage

rise time was approximately 20 ns. Pulses of positive voltage, with a duration of 75 ns, were applied at a frequency of 10 Hz to the power electrode (anode) for a duration of 30 minutes. The influence of the applied voltage was investigated in the range of +4 to +10 kV. Nanosheets were formed only when the voltage was slightly higher than the breakdown voltage, around +4 kV for liquid nitrogen and milli-Q water. Specifically, nanosheets were synthesized at +4 and +5 kV, with the highest production observed at +5 kV. Beyond this voltage, nanoparticles are synthesized and all the more numerous as the voltage increases. At +10 kV, nanosheets are no longer synthesized. All results presented in this study were obtained at +5 kV.

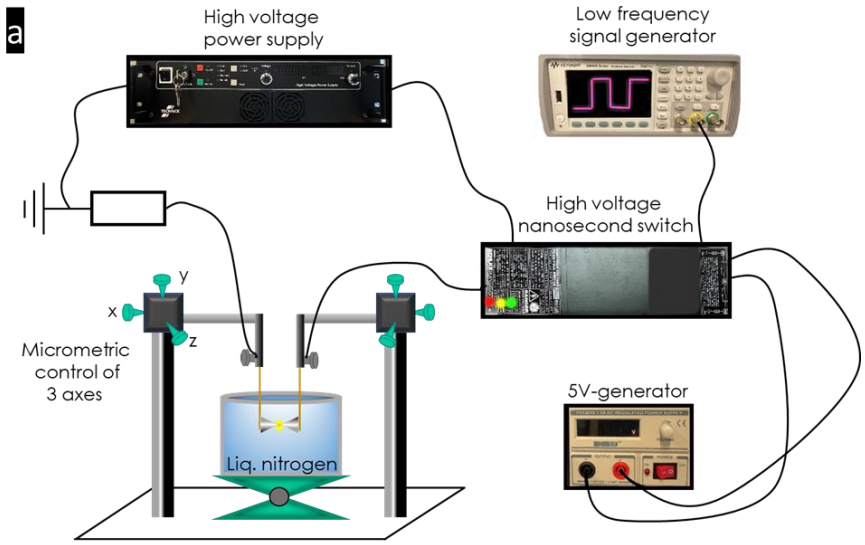

d

Solution	Composition
Nital 4%	96 ml C_2H_5OH + 4 ml HNO_3 (>70 wt.%)
Nital 5%	95 ml C_2H_5OH + 5 ml HNO_3 (>70 wt.%)
Chloric-based solution	30 ml HCL + 2 g $FeCl_3$ + 100 ml H_2O

Fig. 2.1: a) Schematic of the experimental setup, here presented in the case of liquid nitrogen. b) Pre-treatment of the electrodes leading to a cone-shaped pin etched in one of the chemical solution presented in d). c) Picture of the electrodes in milli-Q water. d) Composition of the four chemical solutions tested in this work.

The experimental setup involved immersing the two electrodes, configured in a pin-to-pin arrangement, in a 100 ml Dewar flask. The distance between the electrodes was maintained at a constant 100 µm throughout the process using micrometric screws for continuous adjustment. This setup allowed for repeated breakdown to occur. Nanosheets were prepared using either liquid nitrogen (99.9998% purity) or milli-Q water (with a resistivity of 18.2 MΩ·cm). The synthesis process involved an ultra-facile and rapid procedure consisting of the following steps:

- Pre-treatment: The electrodes underwent chemical etching in a selected etching solution.
- Treatment: The electrodes were subjected to erosion using nanosecond-pulsed discharges in either liquid nitrogen or water.
- Exposition to air: For liquid nitrogen, once the liquid had evaporated, the nanosheets were exposed to air. For water, the nanosheets were collected in the solution and exposed to air.

The bismuth rods used as electrodes were obtained from Goodfellow Ltd. They had a diameter of 10 mm and were of high purity, with a 99.999% purity level. To prepare the electrodes, they were first sharpened to form conical tips (see **Fig. 2.1b-c**). Then, they were polished using a 1200-grit sanding disk and rinsed with tap water. Subsequently, the electrodes underwent chemical etching in a selected etching solution for a duration of 20 minutes. After etching, they were rinsed with distilled water, mounted on holders, and immersed either in liquid nitrogen or milli-Q water.

Various etching solutions (see **Fig. 2.1**) were prepared using Nitric Acid (70%) from Sigma-Aldrich Co., ethanol (99.8%, AR) from VWR International LLC, acetic acid, chloric acid, and iron (III) chloride. Comparable results were obtained using all of these solutions. The results presented in this study were obtained after etching using the Nital-5% solution.

After the treatment process and complete evaporation of the liquid in the case of liquid nitrogen, nanosheets were collected through sedimentation. A TEM (Transmission Electron Microscopy) Cu-supported holey carbon grids was placed on a silicon wafer at the bottom of the vessel to capture the nanosheets. These collected nanosheets on the TEM grids and silicon wafer were then available for further analysis. In the case of liquid nitrogen, nanosheets underwent oxidation only when exposed to air, and this oxidation process was uncontrolled. However, when synthesized in water, the oxidation occurred in the liquid phase. The resulting nanosheets had a lamellar structure. With exposure to air, carbonation occurred through the reaction of CO_2, transforming the bismuth oxide into $Bi_2O_2CO_3$. This process has not to be confused with the aging of the electrode material as discussed hereafter. Carbonation is very fast as it is occurs after a few seconds whereas aging takes days. The former is only observed on the cathode, whereas the latter affects both electrodes.

To investigate the structure and composition of the nanosheets, high-resolution transmission electron microscopy (HRTEM) was conducted. The characterization was performed using a JEOL ARM 200F cold FEG TEM/STEM equipped with a GIF quantum ER model 965, operating at 200 kV. High-angle annular dark-field scanning transmission electron microscopy (HAADF-STEM)

and two-dimensional elemental mapping using energy-dispersive X-ray (EDX) spectroscopy were employed to determine the chemical composition of the nanoparticles. Additionally, scanning electron microscopy (SEM) observations were carried out using an FEI Quanta 600 FEG SEM in SE and Inlens modes at 2-5 kV.

An ultrafast camera FASTCAM SA5 (model 1000K-M3) was used to observe the discharge bubble and the release of nanosheets in the case of water. Videos were recorded at a rate of 75 000 frames per second with a pixel resolution of 12.3 µm.

Slow-mode recording at 60 images per second was also used to observe the liquid flow.

2.1.2 Results and discussion

The pre-treatment of electrodes is not mandatory for obtaining nanosheets, but this step significantly enhances the likelihood of obtaining them, increasing the probability from nearly zero to nearly 100%. As previously mentioned, it has been observed that the applied voltage should not be excessively high, but rather slightly higher than the breakdown voltage. All etching solutions appear to yield similar outcomes, making them indistinguishable. The process is relatively fast as 30 min of treatment are sufficient to synthesize nearly 0.5 mg of nanosheets.

2.1.2.a Characterization of nanosheets

The most remarkable discovery regarding nanosheets is their consistent characteristics (shapes, compositions, structures, etc.) regardless of whether they are synthesized in liquid nitrogen or water (see **Fig. 2.2**). Bismuth oxide nanosheets exhibit various shapes depending on their thickness, regardless of the liquid medium. When they are sufficiently "thin" (*i.e.*, below ~5 nm, otherwise considered "thick"), they can appear flat, crumpled, or rolled due to stress (**Figs. 2.2a-c** in liquid nitrogen and **Figs. 2.2e-g** in water). On the other hand, thicker nanosheets maintain a flat configuration (**Fig. 2.2d** and **h**). Single nanosheets (see circles in **Figs. 2.2a, d, e** and **h**) distinctly show the presence of kinks.

Scanning electron microscopy images in the **Supplementary Material S2.1** provide an overview, revealing the presence of crumpled nanosheets. Upon closer examination at high magnification, small fragments similar to those depicted in **Figs. 2.2a** and **e** can be easily observed around the crumpled nanosheets. Additionally, thick nanosheets, such as those shown in **Figs. 2.2d** and **h**, can be seen broken due to stress.

This stress can be induced by oxidation and the uptake of CO_2 from the air. Remarkably, the nanosheets presented in this study exhibit identical size, shape, composition, and

crystallographic features as those reported by several authors [Lv2017, Lui2010, Qin2021, Yang2020, Zhang2014] (refer to **Supplementary Material S2.2**). They consist of stacked layers with a zig-zag structure, constituting a 2D material. As explained by Zhang *et al.* [Zhang2014], CO_2 can convert BiOOH into $Bi_2O_2CO_3$. This aspect will be discussed in detail hereinafter.

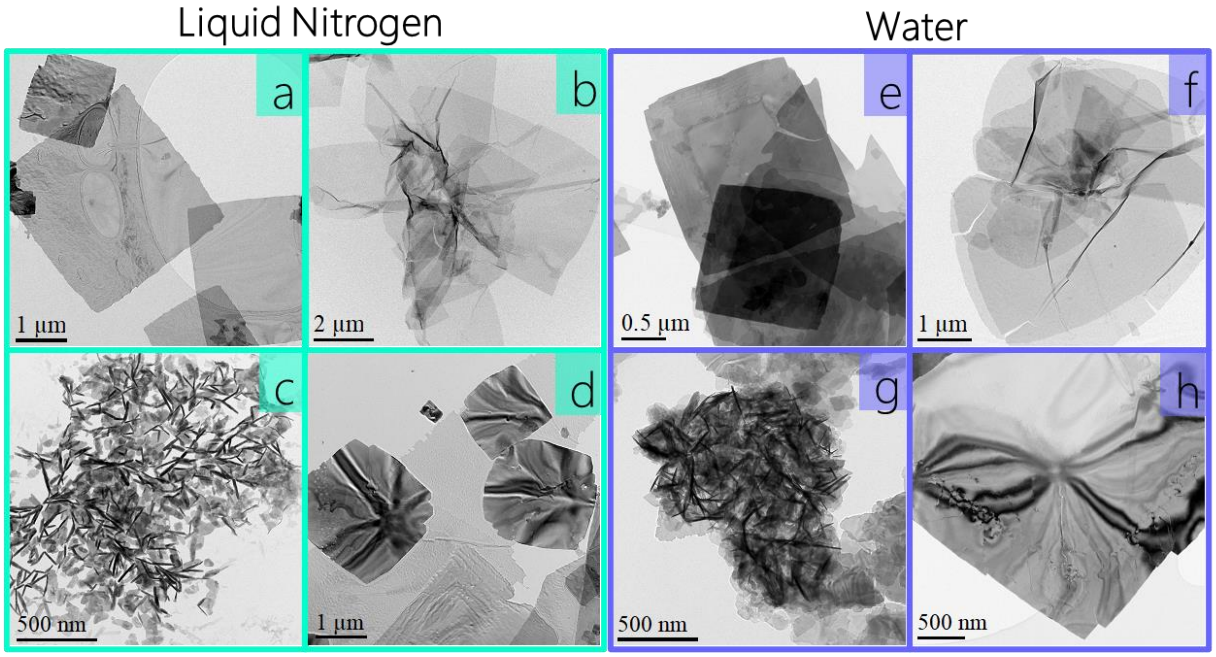

Fig. 2.2: Bright Field TEM micrographs showing the different shapes of nanosheets synthesized in liquid nitrogen and in water. a) and e) thin flat nanosheets. b) and f) thin crumpled nanosheets. c) and g) thin rolled nanosheets. d) and h) thick flat nanosheets.

2.1.2.b Metallic character of discharges

The ability to use either water or liquid nitrogen equivalently can be attributed to two possibilities: either different growth mechanisms are at play, or if the mechanisms are the same, similar discharge conditions are being implemented. To compare the emission spectra obtained from time-resolved optical emission spectroscopy in the two liquids, refer to **Fig. 2.3**. It should be noted that the data collected in water were slightly noisier compared to those obtained in liquid nitrogen (as mentioned in a previous work [Nominé2021]). The optical fiber used for these measures was not directly plunged in the liquid like it was done in LN_2, which is more insulating than water. Despite this difference, the presence of bismuth lines (indicated by "o" in **Fig. 2.3**) is clearly observed and identified from the time-resolved spectra (refer to **Supplementary Material S2.3**, where the absence of H_α emission at 656 nm is also noted). Furthermore, the lack of OH emission, as demonstrated in **Supplementary Material S2.4**, provides strong evidence of the metallic nature of the discharges.

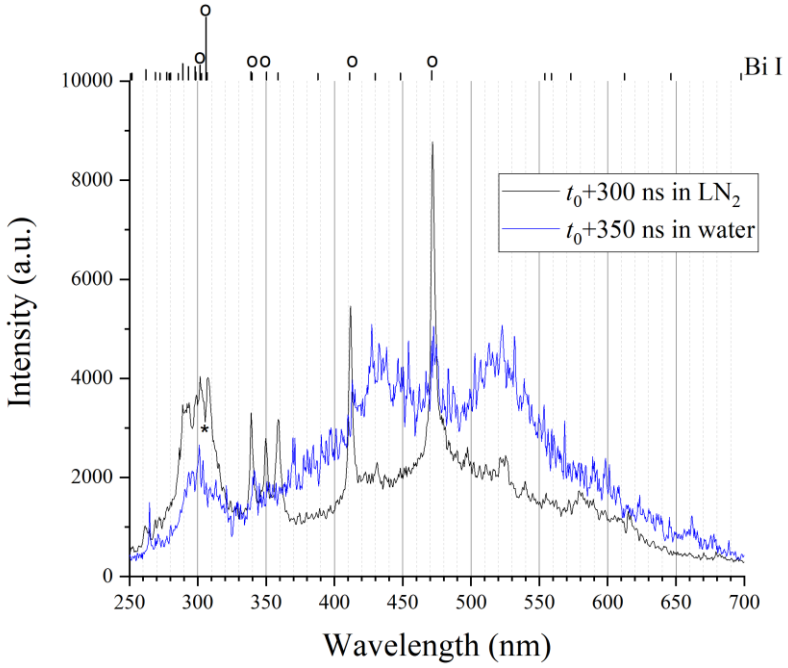

Fig. 2.3: Comparison of low-resolution emission spectra recorded by time-resolved optical emission spectroscopy in water and in liquid nitrogen at almost the same times after breakdown (t_0). Before 300 ns in water, only continua are observed (150 ns in liquid nitrogen). Spectra in water are much noisier than in liquid nitrogen. For this reason, Bi I lines that are identified for certainty are depicted by an "o" above the expected wavelengths of the possible transitions showed by bars on the top of the graph. * shows an absorbed line due to absorption of photons emitted by the continuum. Data in liquid nitrogen were taken from [Nominé2021]. Wavelengths of Bi I transitions are taken from NIST [NIST2023].

The absence of H and OH emissions in the spectra obtained in water, even long after breakdown when the medium is optically thinner, indicates that the discharge is predominantly metallic and arises from the emission of metal vapor resulting from electrode erosion. The emitted vapor displaces the water, leading to a discharge that closely resembles what is observed in liquid nitrogen.

2.1.2.c Aging in air

Following the treatment, the electrodes were subjected to aging in ambient air for 6 days. Let's mention first that the aging of $Bi_2O_2CO_3$ nanosheets from the solution does not change these objects at all. On the contrary, the surface states of both electrodes change as BOC nanosheets grow by this process. Thus, the colour of the electrodes turns to white.

The results are shown in **Fig. 2.4.** After 6 days, the surfaces of the electrodes were found to be completely covered with ultra-large nanosheets, measuring approximately up to 100 µm in width (**Fig. 2.4a**). The trenches resulting from the polishing process were barely visible as they were concealed by the nanosheets (**Fig. 2.4b**). The kinetics of the direct oxidation of bismuth in air, both in dry and moist conditions, as well as in superheated steam, have been investigated at temperatures above 500 K [Tahboub1979, George1986]. However, these oxidation processes are

too slow to be measured at room temperature. Hence, it is presumed that an alternative mechanism is responsible for the observed phenomenon in the present study.

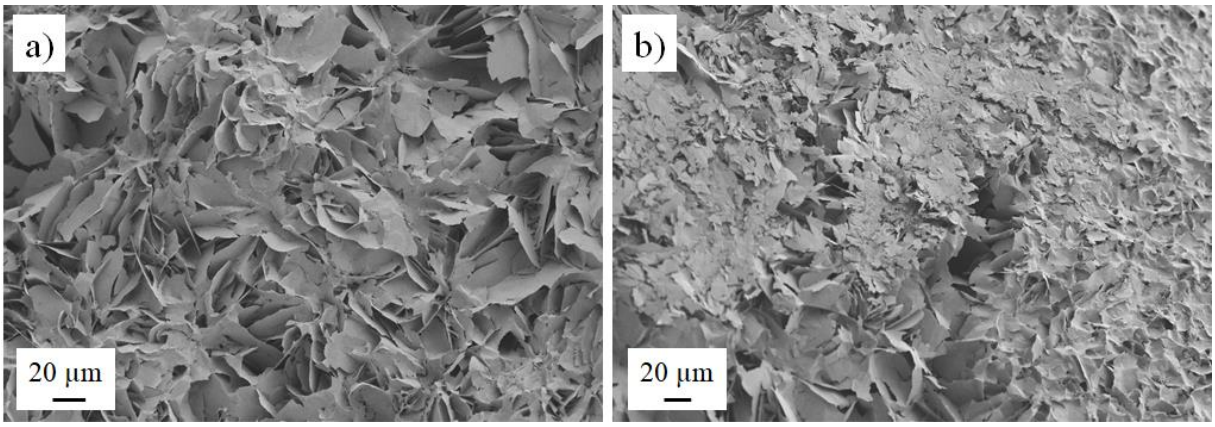

Fig. 2.4: $Bi_2O_2CO_3$ nanosheets formed in the air after 6 days. a) Detail of the basal nanosheets. b) SEM micrograph showing two trenches and nanosheets covering the gap between them.

Subsequently, experiments were conducted to examine whether similar outcomes could be achieved without in-liquid discharge treatment. These experiments involved electrode polishing, Nital etching, and exposing the electrodes to air for a duration of 6 days as well. The result shows undoubtedly that no nanosheets were synthesized without in-liquid discharges (**Supplementary Material S2.5**).

2.1.2.d Surface states of the electrodes

After the treatment, the electrode tips exhibit two distinct regions: one covered by impacts and the other covered by trenches resulting from the polishing and etching steps (refer to **Supplementary Material S2.6**). Following the polishing process (**Figs. 2.5a-c**), the scratches on the surface appear as flat streaks that are almost connected, with minimal spacing between them. Upon etching (**Figs. 2.5d-f**), clear trenches with widths ranging from 0.5 to 1 µm become visible. The chemical etching of the electrodes facilitates the formation of these trenches on the surface. The dissolution of the native bismuth oxide, which may have varying thickness locally, leads to differential erosion of the surface, increasing its roughness. In **Fig. 2.5f**, one can observe the presence of closely spaced parallel planes forming comb-like structures, which are a result of the chemical etching process. This feature is also evident in **Figs. 2.5h** and **i**. After the treatment (**Figs. 2.5g-i**), the trenches are still observable, measuring approximately 3-5 µm in width. Within these trenches, numerous localized and aligned nanostructures consisting of entangled nanosheets form flower-like patterns, but only on the cathode. No flowers are observed on the anode, and this observation holds true for both liquids (refer to **Supplementary Material S2.7**). The random distribution of these nanostructures along the scratches is attributed to the presence of localized

defects, likely the planes of the comb structures, which promote their growth. This mechanism is a result of a deposition process rather than a solid-diffusion process like oxidation, as observed in both water and liquid nitrogen. It can be concluded that the bismuth forming the flower-like structures can only originate from the vapor produced by the erosion of the electrode tip.

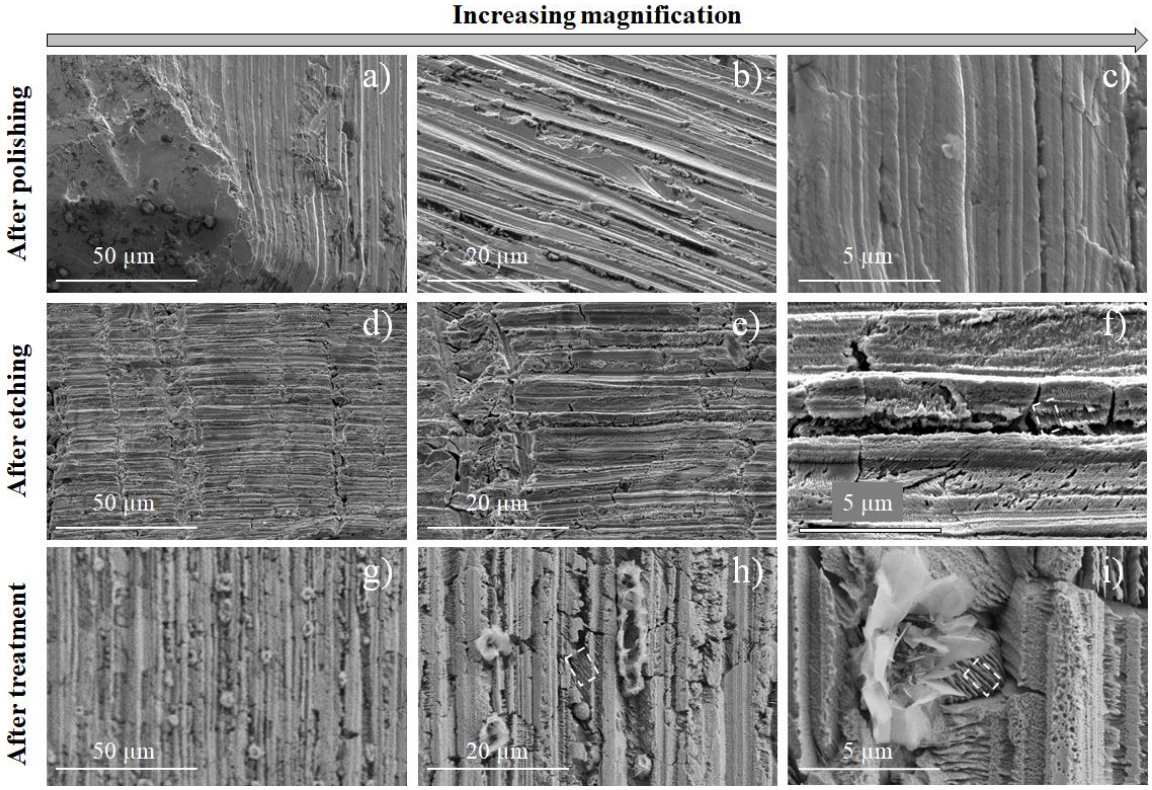

Fig. 2.5: SEM micrographs of surface states of the bismuth cathode at different magnifications after: polishing, chemical etching and discharge erosion (here in liquid nitrogen). Areas enclosed by rectangles with dashed lines in f), h) and i) show the presence of tight parallel plans forming combs (see also Fig. 2.6 for higher resolution images).

Figs 2.6a-e illustrate examples of flower-like structures formed within the trenches. These structures are composed of entangled nanosheets. Upon close observation, it is evident that the largest and thinnest nanosheets do not stand upright but spread out over the surface (**Fig. 2.6a** and **e**). The flowers grow perpendicular to the surface within the trenches (**Fig. 2.6c**) and on the comb structures (**Fig. 2.6b**). This growth pattern suggests that the process involved is deposition rather than etching. Notably, the growth of nanosheets on the comb structures appears to be influenced by the orientation of the underlying planes (**Fig. 2.6d**), as the nanosheets align accordingly.

2.1.2.e Possible growth supports

Within the present process, several surfaces are involved, including the liquid-air interface, the interface between the gas bubble and the liquid, and the surfaces of the electrodes. While it

is occasionally possible to observe nanosheets floating on the surface of water, it remains uncertain whether this phenomenon is also applicable to liquid nitrogen, as the surface of the liquid is typically rough. However, in most cases, nanosheets are denser than the liquid and tend to collect at the bottom of the vessel. The ability of nanosheets to float is attributed to changes in the buoyancy force resulting from an increase in liquid uptake within the nanostructures [Eckert2021]. Depending on the sign of the buoyant mass, which may vary over time, colloidal particles either sediment towards the bottom or rise towards the surface. In both cases, gravity creates a density gradient of particles in the vertical direction. Sedimentation-diffusion equilibrium is achieved when the particle flow induced by gravity is balanced by the diffusive flow driven by the density gradient and interparticle interactions. Therefore, at initial stages, nanosheets do not grow at the air-liquid interface. This observation is supported by slow-mode videos that reveal the trace left by erosion products in the liquid (refer to **Supplementary Material S2.8**). Consequently, this mechanism can be ruled out as the primary mode of nanosheet growth at the air-liquid interface.

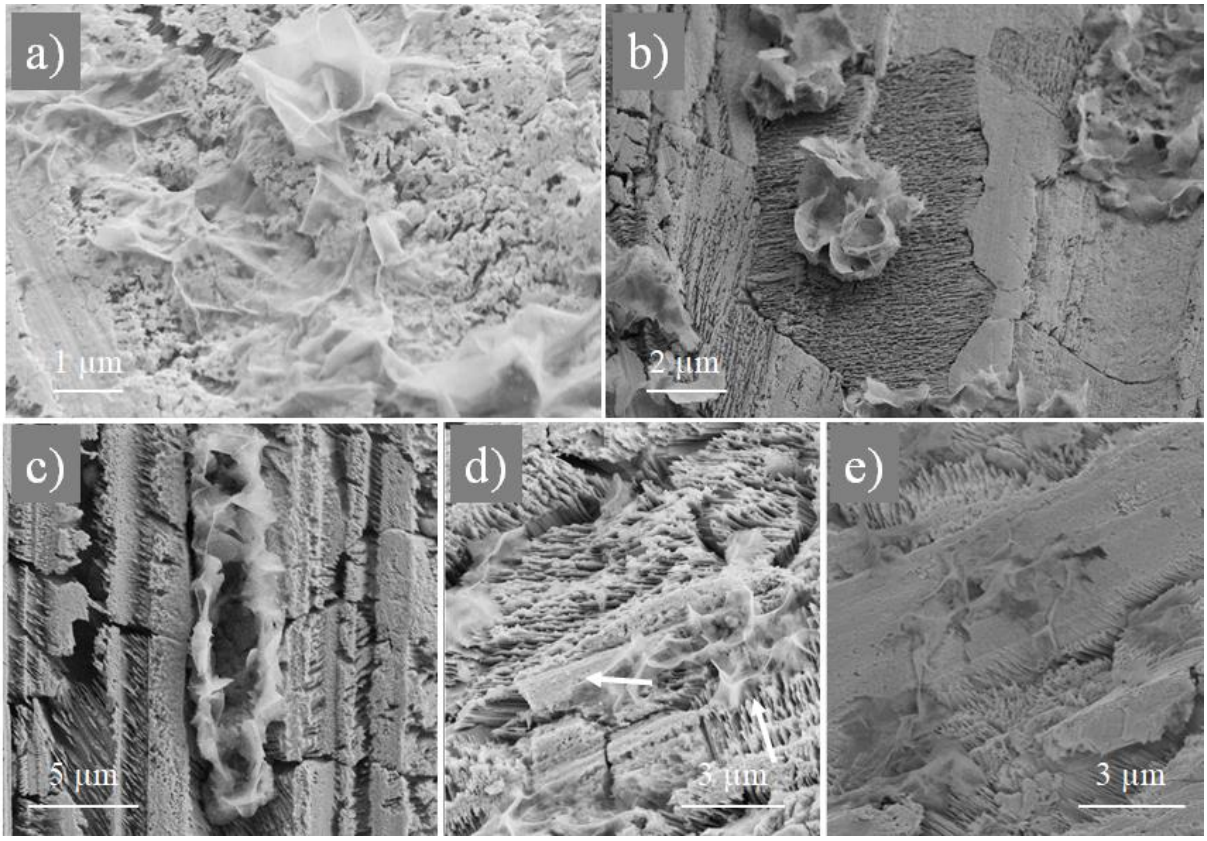

Fig. 2.6: SEM micrographs showing example of flowers nanosheets observed on the surfaces of cathodes. a) Network of nanosheets with one flower. Note that no nanosheets stand on the smooth surface on the left-hand side of the image. b) Flowers are located on rough areas like combs. c) flower growing along walls in one trench. Note the orientation of the combs on either side of the trench. d) Nanosheets on combs with two different orientations (given by arrows). e) Nanosheets spreading from a trench on a smooth surface.

The possibility of nanosheet growth at the interface between the gas bubble and the liquid can also be ruled out. If nanosheets were synthesized at this interface, there would be no need for a pre-treatment step. The emission of vapor from the electrodes, heated by the discharge, would remain unchanged regardless of whether a pre-treatment was performed or not. Consequently, condensation of vapor atoms on the bubble-liquid interface would occur consistently. However, it should be noted that the erosion process of the electrodes caused by the arc discharge is not influenced by the thickness of the native oxide layer, which is typically a few nanometres thick at room temperature. This thickness is significantly smaller compared to the depth of the crater left by the discharge under the present conditions, which is approximately 1 µm [Hamdan2013d].

Therefore, it can be concluded that nanosheets can only grow on the surface of the electrodes, and it is observed that this mechanism exclusively occurs on the cathode.

2.1.2.f Transfer to the liquid

Through the utilization of an ultrafast camera with high resolution (refer to **supplementary material S2.9**), we were able to observe that the transfer of nanosheets from the surface of the cathode to the liquid is facilitated by the mechanical sweeping action of the bubble-liquid interface (**Fig. 2.7**). This phenomenon occurs during an event where the bubble undergoes a single expansion and collapse (**Fig. 2.7a**), and the release of nanoobjects can be witnessed following the collapse phase (**Fig. 2.7b**). The velocity distribution of the released nanoobjects narrows around the mean fluid velocity, indicating a deceleration of their movement after being ejected from the bubble.

Indeed, this mechanism of mechanical sweeping by the bubble-liquid interface is responsible for the fragmentation of nanosheets into smaller pieces. It explains the presence of small fragments alongside flowers or parts of flowers. However, the precise factors that control the thickness of the nanosheets remain to be fully understood. Recently, Gupta *et al*. [Gupta2022] successfully synthesized 2D $Bi_2O_2CO_3$ nanoobjects through a sonochemically-assisted exfoliation method. By employing various suspension media such as water, methanol, isopropanol, ethanol, and an isopropanol:water (4:1) mixture, they were able to manipulate the lateral sizes of the nanoobjects, ranging from micrometer-sized nanosheets to nanoflakes measuring tens of nanometers.

Experimenting these liquids with the present process could be useful for comparison with Gupta *et al*.'s results, even though the use of liquid nitrogen and water already demonstrates the lack of sensitivity of the present process to the chosen liquid. Further research is needed to

confirm the underlying mechanisms that govern the thickness of nanosheets in Gupta *et al.*'s process, but the lack of electrode in their case and the much longer processing times that are needed pleads in favour of another growing mechanism.

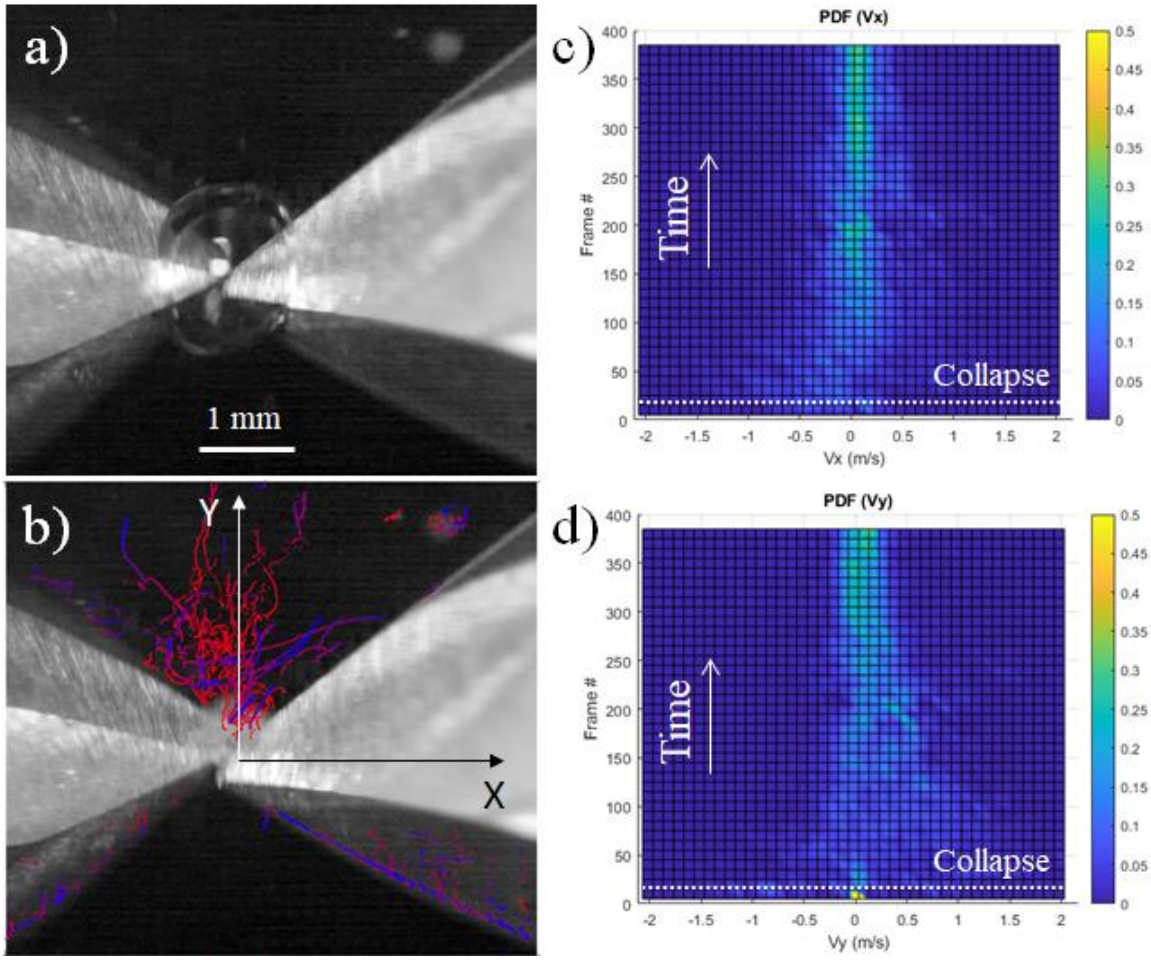

Fig. 2.7: a) Image of the bubble collapse 53 µs after breakdown. b) Trajectory of nanoobjects tracked after the collapse in the liquid (integration over 990 frames recorded every 13.3 µs, *i.e.* 13.2 ms). The red-to-blue scale corresponds to the first 400 frames where changes are the most significant. c) and d) Normalized Probability Density Function (PDF) of the velocities of the tracked nanoobjects projected onto the horizontal and vertical axes, respectively. The end of the bubble collapse is shown by a dotted line. The velocity distribution strongly narrows around the mean value of the fluid velocity, which is slow and close to 0. This evolution shows the slowing down of movement of the nanoobject after ejection from the bubble.

2.1.2.g Growth mechanism

Nanosheets commonly exhibit kinks, which can be easily observed in **Figs. 2.2a**, **d-f**. This observation led us to consider the "ledge" mechanism, which is well-known for describing the growth of plate-like precipitates within solid matrices [Porter2009]. In this context, the matrix is either replaced by the liquid itself, which acts as an isotropic medium, or by a suitable surface capable of supporting the growth of 2D objects.

In the case of precipitation within solids, the growth of the precipitate via the ledge mechanism is driven by the coherency of the interfaces between the precipitate and the matrix where the growth occurs. The development of the precipitate is more significant for incoherent interfaces than for coherent ones. Additionally, the lateral growth of the precipitate typically outpaces its thickening [Porter2009]. In the present case, the possibility of replacing the solid matrix with the liquid medium must be ruled out because it would not align with the observed phenomenon of using either water or liquid nitrogen.

Under conditions that are thermodynamically unfavourable, vapor cannot adsorb and adhere to surfaces without additional energy provided by surface defects such as emerging dislocations or atom vacancies. This explains why nucleation on electrodes occurs randomly, where defects are present. Similarly, nucleation on nanosheets is possible as long as these surface defects are present within the nanosheets themselves [Meng2013]. **Fig. 2.8** demonstrates this phenomenon, where a BOC nanosheet serves as a substrate for the growth of a nanopyramid from an emerging dislocation. It is worth noting that these types of objects are rare, as nanosheets are typically single crystals.

Based on the ledge mechanism, nanosheets grow through the deposition of bismuth emitted by the electrodes during the discharge, specifically on surface defects. The remarkable contribution of ions, known to promote the 2D growth of nanoobjects [Levchenko2007, Zhuang2013], is evident, as only the cathode surface is covered in nanosheets, while no nanoobjects are visible on the anode surface.

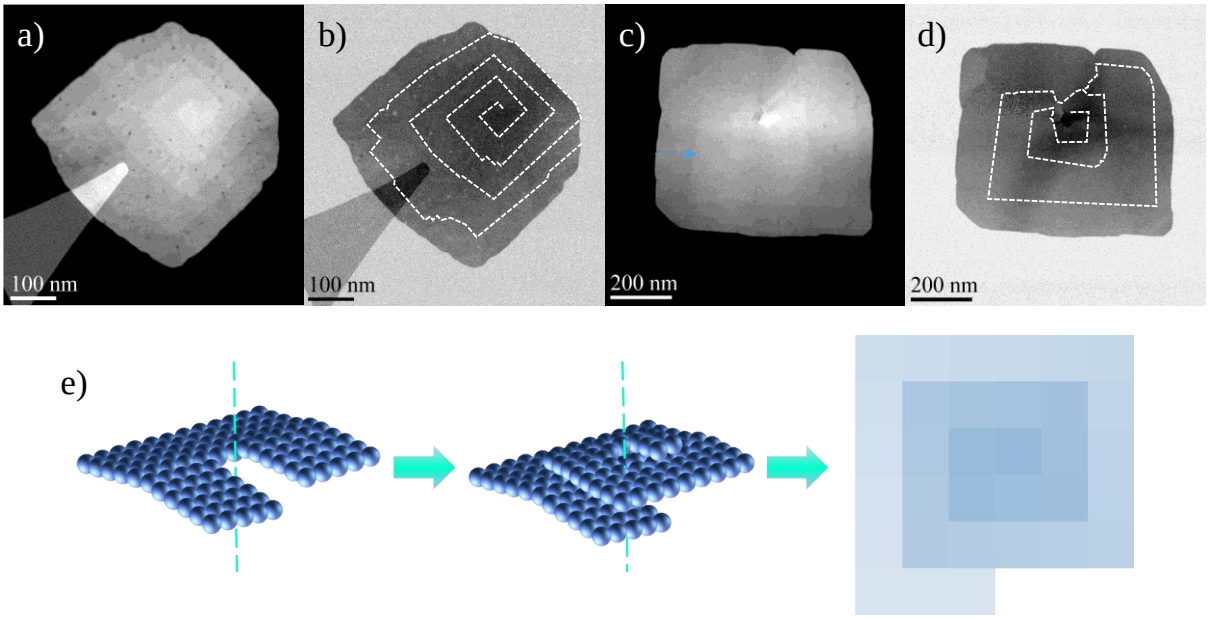

Fig. 2.8: a) and b): bright field and dark field STEM images of a nanopyramid. c) and d): another example. Dotted lines reproduce the spiralling edge of the pyramid. e) 3D view of steps leading to 3D-growth.

This observation partially explains why overvoltage beyond the breakdown voltage should not be excessively high, as strong ion irradiation is known to hinder the formation of nanosheets [Hori2011]. It is also important to mention that ions here are bismuth ions. As the discharge is metallic, negative charges are electrons and those do not act the same on the anode. If ions where those of the liquid, H_3O^+ and OH^-, the main negative charge carrier in water, should play similar roles on either electrode, which is not what is observed. This mechanism is very different from Fan *et al.*'s mechanism, for instance, which is based on the ripening of dendritic nanostructures [Fan2004b].

In general, the electric field streamlines are perpendicular to the electrode surfaces, favouring growth perpendicular to the surface unless influenced by local charge accumulation or space charge field effects. Although ions are known to promote anisotropic growth [Levchenko2007], it has been suggested that planar defects are necessary in a discharge environment to form arrays of nanosheets [Zhuang2013]. This finding aligns with the present study, as these planar defects correspond to the planes of combs formed during the etching step.

Thin nanosheets are believed to grow through deposition assisted by ions with moderate energy. In the early stages of the discharge, ions are highly concentrated, as the medium is considered a spark (or arc) discharge, with concentrations reaching up to 10^{17} cm^{-3} under the present conditions [Nominé2021]. The mean energy of these ions is low (~0.35 eV), making sputtering by these ions highly unlikely. The ions become neutralized upon reaching the cathode surface and adhere to surface defects or edges, where kinks serve as surface defects in the ledge mechanism, through surface diffusion. These defects provide the necessary excess energy for chemical bonding. Consequently, the observed vertical growth of the nanosheets is the result of the interplay between the discharge's electric field and surface defects. A schematic representation of this mechanism is depicted in **Fig. 2.9a**.

As elucidated by Levchenko and Ostrikov [Levchenko2007], nanostructures formed in discharge environments, in contrast to neutral gas-based processes, exhibit a wide range of dimensionalities and shapes, higher surface density, desired geometrical parameters, and narrower size distribution functions. This effect is primarily attributed to the strong ion focusing resulting from irregular electric fields in the nanopatterns. This focusing effectively redistributes the influx of discharge-generated building units, allowing selective control of their delivery to the growing nanostructures. As a result, the contribution of neutral atoms produced by electrode erosion is likely to be minimal. These neutral atoms are emitted outward from the electrode tip, and it is unlikely that they reach the counter-electrode with sufficiently high concentrations to

compete with ions at the cathode, even though the gap between the electrodes is only 100 µm, otherwise deposition at the anode would be possible too. It is also important to note that these neutral atoms tend to form nanoparticles when the applied voltage is sufficiently high. In the present case, nanosheets are sometimes formed with minimal or very low concentrations of nanoparticles. Consequently, the atomic ratio of metallic neutrals to ions is likely to be low as well. However, experimentally supporting this statement is challenging due to the optical thickness of the medium [Kabbara2017].

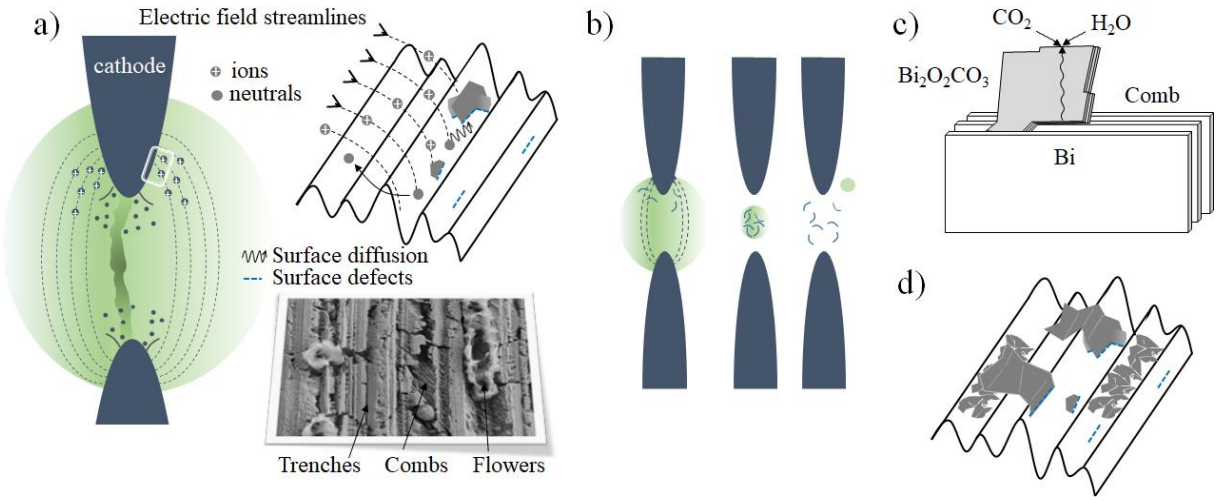

Fig. 2.9: Scheme of the growth mechanisms inferred from present results. In the liquid: a) When ions are neutralized at the cathode, they can diffuse on the surface and desorb if they do not encounter any defect. Otherwise, they contribute to growth of nanosheets. Neutral species, emitted outward from the electrode tip, do not contribute to the growth. b) Collection and ejection of nanosheets are caused by the movement of the gas-liquid interface of the discharge bubble. In the air: c) Bi atoms from the electrode core diffuse outwards and reach the surface where they react with H_2O and CO_2 to form $Bi_2O_2CO_3$. d) This process is activated at room temperature and kinetically slow but nanosheets can grow significantly to cover the trenches.

Once nanosheets are formed on the cathode, their collection and release in the liquid is ensured by the movement of the gas-liquid interface of the discharge bubble whose oscillations sweep the electrode surface (**Fig. 2.9b**). The present mechanism relies on surface processes at the cathode, providing a significant advantage by minimizing the influence of the liquid phase. This comprehensive approach paves the way for synthesizing nanosheets using different materials.

Aging in the air of electrodes leads to the synthesis of nanosheets (**Figs. 2.9c and d**) and modify the electrode colour from metallic to white (**Supplementary Material S2.10**, **Figs. S10a** and **S10b**). This growth mechanism does not occur directly after the etching step but after the in-liquid discharge step. This means that air oxidation is activated by the discharge treatment.

Hu *et al.* [Hu2016] formed $Bi_2O_2CO_3$ nanosheets by simple hydrolysis of bismuth nanopowders through a 3-step mechanism:

$$2Bi + 6H_2O \rightarrow 2Bi(OH)_3 + 3H_2 \quad \text{(R2.a)}$$

$$Bi(OH)_3 \rightarrow BiOOH + H_2O \quad \text{(R2.b)}$$

$$2BiOOH + CO_2 \rightarrow Bi_2O_2CO_3 + H_2O \quad \text{(R2.c)}$$

The two last steps are the same as those proposed by Zhang *et al.* [Zhang2014] for the synthesis from BiOCl, this compound being transformed into $Bi(OH)_3$ by reaction with H_2O and OH^-. This process operates at low temperature and for treatment durations that are compatible with the present observed kinetics: 60 °C and 12 h. As $Bi_2O_2CO_3$ is a semiconductor, we suggest that the aging process is simply governed by the outward diffusion of bismuth ions supplied by the electrode volume through the $Bi_2O_2CO_3$ nanosheets and their further oxidation by water from the air according to Zhang *et al.*'s mechanism. A schematic of this mechanism is presented in **Fig. 2.9c**. The process is then limited by diffusion and nanosheets, which grow longer and longer, bend mechanically and conceal the trenches as shown in **Figs. 2.4b** and **2.9d**.

The previous process assumes that discharge activation provides access to the bismuth reservoir, which is formed by the core of not only the cathode but also the anode. Then, this step cannot be related to the ions. Discharge activation modifies the surface states of combs (**Supplementary Material S2.10**, **Figs. S2.10c** and **d**) and the early stage of nanosheet growth makes the surface fuzzier due to the presence of small nanosheets.

The exact role of discharges as an activation step for the air oxidation of electrodes still needs clarification. However, it is evident that an in-liquid discharge treatment is essential for this specific growth mechanism. Presumably, the discharges play a role in creating defects on emerging plans forming combs, which enable bismuth to easily access the surface. However, further experiments are required to confirm this suggestion.

This mechanism will be elucidated from a crystallographic perspective in the next chapter.

2.2 Conclusion and perspective

The synthesis of nanosheets with similar characteristics can be achieved through nanosecond-pulsed discharges in both water and liquid nitrogen. To ensure successful synthesis, a low applied overvoltage slightly above the breakdown threshold is required, and the process is significantly enhanced by a suitable chemical etching pre-treatment. The selectivity of the process can be excellent, with nanosheets being the predominant nanoobjects produced without the presence of other types of nanostructures.

Nanosheets grow through localized deposition assisted by ions on the defects created by the chemical etching of the cathode electrode. Planes of combs, primarily found in trenches created by the polishing process but not limited to them, provide the necessary support for nanosheet growth. The nanosheets form flower-like structures that are randomly distributed along the trenches. The sweeping action of the bubble-liquid interface over the cathode surface collects the nanosheets, often leading to their fragmentation, and releases them into the liquid during the collapse of the bubble. This mechanism facilitates the transfer of nanoobjects to the liquid, where they can be subsequently collected.

Aging of electrodes in air after in-liquid discharge treatment makes nanosheets grow on both electrodes but with much slower rates than by discharges in liquids. Nanosheets grow by outward diffusion of bismuth from the electrode core but the way the discharge treatment activates this mechanism is still unclear. It should imply creation of defects on emerging plans in combs on both electrodes. Carbonation in the air is not fully understood and would deserve a specific study to be clarified.

This study does not clarify why certain materials with low-melting points as bismuth (545 K), such as tin (melting point = 505 K) or indium (melting point = 430 K), do not form nanosheets. One possible reason for the limitation of nanosheet growth in these cases could be the absence of emerging defects. Further investigations are now required to fully understand these limitations and to extend the synthesis of nanosheets to a wider range of metals.

Chapter 3

Structural characteristics of $Bi_2O_2CO_3$ nanosheets

3.1 Structural characteristics of $Bi_2O_2CO_3$ nanosheets

A comprehensive analysis of $Bi_2O_2CO_3$ nanosheets, which were synthesized using nanosecond-pulsed discharges in water between bismuth electrodes, was conducted in order to investigate the crystallographic features of this material. Analyses, employing electron diffraction, XRD and EELS techniques, revealed the presence of a stoichiometric tetragonal $Bi_2O_2CO_3$ structure, labelled BOC in this study. This structure crystallizes in body centred tetragonal Bravais lattice and belongs to the I4/mmm space group (139), with the following lattice parameters: a = 3.91 Å and c = 13.77 Å.

The nanosheets adopt squared shapes when synthesized in water, considered as an isotropic medium. This shape is dictated by the symmetry elements of its point group 4/mmm under the prevailing local conditions. From the energetic point of view, this shape, dictated by the 4/m2/m2/m point group, therefore a pinacoid, corresponds to an absolute extremum, an indicator of the stability of this BOC nanosheets.

Most nanosheets are crossed by equal inclination fringes or bend contours. These bend contours reflect the fact that the BOC nanosheets are so thin and/or contain crystal defects that they bent elastically leading to rotation of the lattice planes towards diffracting Bragg position. The diffracted beams coming from the intersection domains of the bend-contours lead to ⟨*uvw*⟩ zone axis diffraction patterns.

In this study, the diffraction patterns corresponding to bend-contours intersecting along [001] zone axis attracts attention. Satellite diffraction lattices are superimposed on the diffraction pattern of the BOC crystallographic structure. The origin of these lattices is essentially attributed to two phenomena: multiple diffraction and local disorder-order transformations of the BOC crystal structure, passing from a body centered tetragonal to a primitive Bravais lattice.

A mechanism related to the ledge mechanism (kinks and jogs), explaining the formation of nanosheets in metallic matrix, has been adapted and proposed for the formation of the BOC nanosheets in water. When the nanosheets are removed from water, they get carbonated once in the air, leading to formation of BOC, inheriting the nanosheet morphology.

3.1.1 Introduction

Nanoscale materials have garnered substantial interest owing to their distinctive properties and potential applications across various domains. Among these, bismuth oxycarbonate (BOC) $Bi_2O_2CO_3$, also known as bismutite or bismuth subcarbonate, and sometimes represented as $(BiO)_2CO_3$, has emerged as an exceptional material. BOC exhibits diverse morphologies, including sponge-like hierarchical microspheres, nanoflowers, nanosponges, and nanoplates, as reported in various studies [Zheng2010, Madhusudan2013, Zha02011, Tian2022, Ni2016]. These morphologies are efficiently used as a visible-light-driven photocatalyst for the degradation of organic dyes such as Rhodamine B, Methylene Blue, and Methyl Orange. This material also has captured significant interest due to its remarkable electronic, optical, and sensing properties [Wang2017, Huang2014, Umar2016].

Numerous methods have been documented in the literature for synthesizing this subcarbonate material. These methods encompass hydrothermal processes [Zheng2010], solution precipitation techniques [Chen2012b], and a template-free approach involving Ostwald ripening [Dong2011]. These methods primarily yield three-dimensional morphologies or thick plates. Nevertheless, achieving extremely thin, free-standing nanosheets with a thickness below 10 nm has proven to be a formidable challenge. A recent groundbreaking study by Gupta *et al.* introduced an innovative strategy to overcome this challenge. They successfully produced laterally large, atomically-thin 2D $Bi_2O_2CO_3$ nanosheets using a sonochemically-assisted template-free synthesis method through liquid-phase exfoliation (LPE) treatment of bulk Bi powder [Gupta2022].

In addition, Qin *et al.* reported on $Bi_2O_2CO_3$ nanosheets with a remarkable thickness of 4-5 nm [Qin2021]. These nanosheets were obtained spontaneously through the transformation of two-dimensional bismuthene nanosheets via electrochemical exfoliation. Remarkably, after exposing the bismuthene nanosheets to ambient air for a few days, they underwent a transformation into thin $Bi_2O_2CO_3$ nanosheets.

In this context, our study introduces an innovative approach that enables the creation of free-standing $Bi_2O_2CO_3$ nanosheets with an average thickness below 10 nm. This method employs

nanosecond-pulsed discharges occurring between two bismuth electrodes submerged in water, resulting in nanosheet formation through electrode erosion. Initially, metallic nanosheets are generated via the erosion of the Bi electrodes. The metallic state of these initial nanosheets was demonstrated thanks to optical emission spectroscopy measurements and further comparison with submerged discharges in liquid nitrogen [Nominé2021]. Subsequently, these nanosheets undergo oxidation in the water, transforming into Bi_2O_3. Upon exposure to air, these nanosheets undergo carbonation, leading to their conversion into tetragonal $Bi_2O_2CO_3$.

A mechanism akin to the ledge mechanism, which elucidates the generation of thin plates within a metallic matrix, has been adapted and proposed to account for the formation of tetragonal $Bi_2O_2CO_3$ nanosheets in other studies [Kabbara2019, Porter2009, Morin2011]. When water is removed, the nanosheets experience carbonation, resulting in the formation of tetragonal $Bi_2O_2CO_3$, while retaining their nanosheet morphology. As far as our knowledge extends, this marks the inaugural endeavor in synthesizing such layered $Bi_2O_2CO_3$ nanosheets through nanosecond-pulsed electrical discharges in liquids, followed by carbonation in the atmosphere.

The produced nanosheets typically display widths ranging approximately from 1 to 10 µm and thicknesses ranging from 3 to 20 nm. Since this represents the first instance of $Bi_2O_2CO_3$ synthesis through this particular technique, a comprehensive investigation was undertaken to characterize these nanosheets in great detail. Various techniques, including, X-ray Diffraction (XRD), Electron diffraction (SAED, CBED and Microdiffraction modes), Transmission electron Microscopy imaging (HRTEM-High-Resolution Transmission Electron Microscopy, STEM-Scanning Transmission Electron Microscopy, HAADF-High Angle Annular Dark Field), Spectroscopies (EELS-Electron Energy-Loss Spectroscopy, EDS-Energy Dispersive Spectroscopy microanalysis), FIB (Focused Ion Beam), and AFM (Atomic Force Microscopy), were employed to elucidate the crystal structure in which these squared nanosheets crystallize.

It turns out that important features, actually observed by TEM in some previous reports about $Bi_2O_2CO_3$ [Gupta2022, Li2022b], and other Bi-containing nanosheets [Xu2013, Zhou2010], were not discussed. For instance, additional spots on electron diffraction patterns were reported but the origin of these interesting features remains unclear. The purpose of this work is to provide a complete description of the structural characteristics of $Bi_2O_2CO_3$ nanosheets. Simulated of the crystal structure of the BOC has been conducted under different software, more particularly, by Vesta [Vesta2011] and CrystalMaker® [CrystalMaker2023], *etc*.

3.1.2 Experimental setup

Bismuth oxycarbonate nanosheets were synthesized through the electrical discharges in dielectric liquids (EDDL) process. Initially, bulk bismuth rod electrodes underwent chemical etching, followed by erosion through nanosecond-pulsed discharges in MilliQ water. The procedure began by shaping the Bi rod into a conical structure featuring a 10 mm base diameter. Then, the electrodes were meticulously polished using 1200-grit paper and subsequently rinsed with tap water. Following this, the electrodes were immersed in a 5% Nital chemical etching solution for a duration of 20 minutes.

After the etching phase, the Bi electrodes underwent rinsing, were securely positioned in electrode holders, and were immersed in a 30 ml glass beaker filled with ultra-pure water (conductivity: 0.055 $\mu S\ cm^{-1}$) chosen as the dielectric liquid. The distance between the electrodes was consistently maintained by precise adjustments using micrometric screws. A high positive voltage was supplied by a DC power source (Technix SR15-R-1200) to a solid-state switch (HTS-301-03-GSM), which was under the control of a function generator, generating high voltage pulses.

In this setup, the power electrode received the electrical signal, while the second electrode acted as the cathode and remained grounded during the process. Pulses with a voltage of +5 kV, frequency of 10 Hz, and pulse width of 75 ns were applied to the power electrode over a duration of 90 minutes. This process aimed to achieve a concentration of 15 mg within a water volume of 30 ml.

For characterizing the products resulting from the electrode erosion, carbon and holey carbon grids were utilized as substrates for electron microscopy analysis. The nanosheets were collected by immersing a TEM grid in a solution containing the synthesized $Bi_2O_2CO_3$ nanosheets.

3.1.3 Results and discussion

3.1.3.a Morphology of the BOC

Throughout the synthesis process, the electrodes undergo erosion. Through the comparison of electrode weights before and after a series of discharges, we calculated an average erosion rate of approximately 0.2 µg per discharge. **Fig. 3.1** presents low magnification SEM images showcasing the as synthesized BOC nanosheets at different magnifications (**Figs. 3.1a-c**). These figures are accompanied by lateral size distribution data (**Figure 3.1d**). Typically, our synthesis process yields nanosheets with lateral dimensions around 4-5 µm, as consistently observed in numerous experiments. However, it is worth noting that on occasion, larger

nanosheets, approximately 20 µm in size, have also been observed, as indicated in our **Supplementary Material S3.1**.

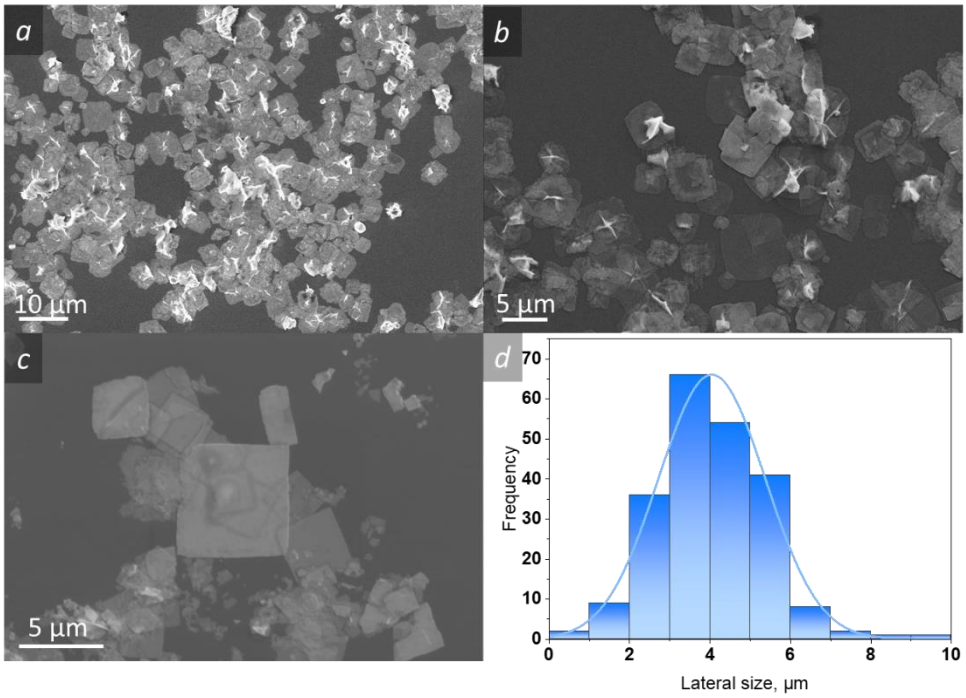

Fig. 3.1: Low-magnification SEM images of a) nanosheets deposited on a Si substrate, b) magnified view of the nanosheets, c) enlarged depiction of a squared sheet, d) lateral size distribution of synthesized nanosheets.

Fig. 3.2 showcases TEM, STEM images of the synthesized nanosheets after 30 min of treatment. The most commonly encountered nanosheet morphologies are squared nanosheets with sizes ranging from 1 to 10 µm (**Figs. 3.2a-c**). To elucidate the lamellar arrangement of the nanosheets, cross-sectional view of the BOC nanosheet was attained through the application of the Focused Ion Beam (FIB) technique along [100] zone axes utilizing the HAADF STEM mode, which provides a Z-contrast image (**Fig. 3.2d**).

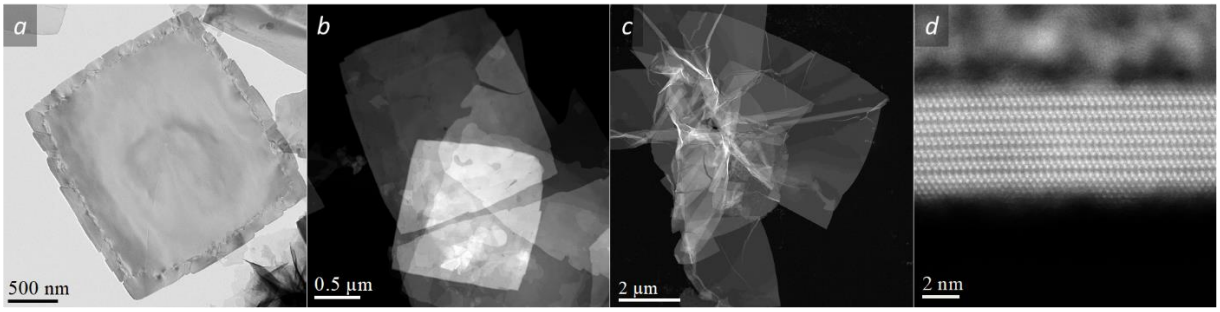

Fig. 3.2: a) BF TEM and b-c) HAADF STEM micrographs showing $Bi_2O_2CO_3$ with most commonly encountered nanosheet morphologies, d) high resolution STEM FIB cross section micrograph of a BOC nanosheet along [100] zone axes.

Importantly, these structures exhibit remarkable stability under ambient air conditions, and observations conducted over a span of more than a year consistently yielded identical outcomes.

AFM (**Fig. 3.3**) and EELS (**Fig. 3.4 and Supplementary Material S3.2**) analyses were conducted to ascertain the thicknesses of the produced nanosheets.

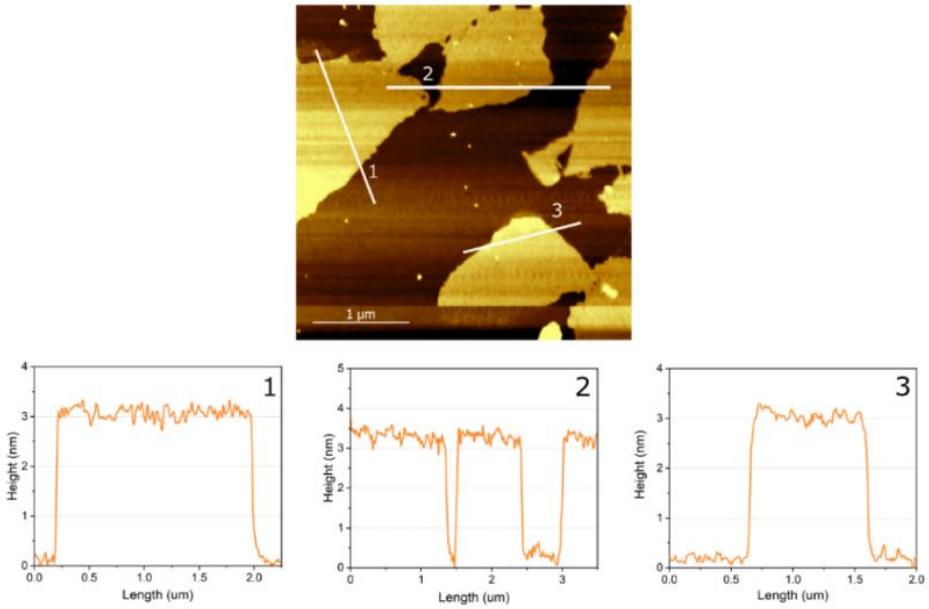

Fig. 3.3: AFM height-sensor micrograph depicting an individual BOC nanosheet. This micrograph provides a one-dimensional step height profile along the white lines labeled as 1-3. Corresponding cross-sections accompany these profiles, offering additional visual information.

The thickness estimation of a single layer was carried out by considering the t/λ ratio obtained from EFTEM (Energy Filtered Transmission Electron Microscopy), which ranged from 0.03 (**Fig. 3.4a, b**) to 0.24 (**Supplementary Material S3.2**). The value of λ, representing the mean free path in nanometers, was theoretically calculated using the formula [Carter2009, Oh-Ishi2020]:

$$\lambda = \frac{106 \times F\left(\frac{E_0}{E_m}\right)}{\ln\left(2\beta\frac{E_0}{E_m}\right)} \qquad \text{(Eq3.1)}$$

where λ is the mean free path, E_o is the energy in kilo-electron volts (keV), β is the collection angle in milliradians (mrad), F is the relativistic correction factor, and E_m is the average energy loss in electron volts (eV). For a material with an average atomic number Z, E_m is given by:

$$E_m = 7.6 \times Z^{0.36} \qquad \text{(Eq3.2)}$$

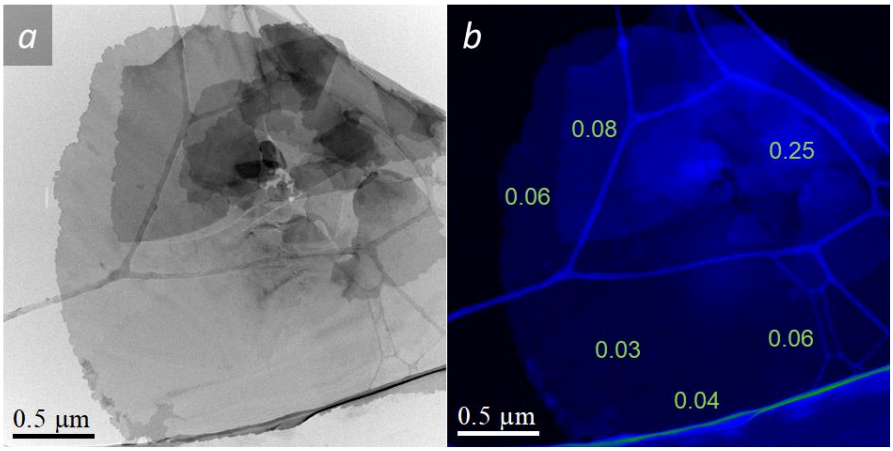

Fig. 3.4: Example of the thin nanosheet a) BF STEM micrograph of a BOC nanosheet deposited on a holey carbon TEM grid with b) corresponding EELS thickness mapping. These mappings indicate the values of the t / λ ratio needed for thickness estimation.

Considering the specific material $Bi_2O_2CO_3$ with an average atomic number *Z* of 32.25, the calculated mean free path is 86.5 nm. With this calculated value, the estimated thickness of a thinnest nanosheets falls within the range of 3-5 nm (**Figs. 3.4a-b**). For the thickest nanosheets present on a substrate after synthesis (as shown in **Supplementary Material S3.2**), this estimation extends up to 20 nm. Significantly, this estimation aligns exceptionally well with the AFM measurements presented either in subsequent sections (see **Fig. 3.3**) or in the earlier discussion, substantiating the reliability of our thickness estimation technique.

3.1.3.b Crystal structure identification

In TEM, the microdiffraction pattern corresponds to the intersection of the Ewald sphere with the zeroth and first reciprocal lattice layers recorded along the ⟨*uvw*⟩ direction, a zone axis of the phase that we are attempting to identify. To these zeroth and first layers correspond the zero-order Laue zone (ZOLZ) and to the first-order (FOLZ) order Laue zone, respectively. The analysis of microdiffraction is based on the net and ideal symmetries of the ZOLZ and of the entire pattern, which is represented as WP = (ZOLZ + FOLZ). The net symmetry primarily pertains to the position of the reflections in the pattern, while the ideal symmetry encompasses not only the positions but also the intensities of these reflections. These symmetries, observed along specific zone axes, are connected to the crystal systems and to the point groups.

Figure 3.5a shows an experimental microdiffraction pattern recorded along the ⟨*uvw*⟩ zone axis of the BOC particle. Taking into account both the position and the intensity of the reflections of this zone-axis pattern (ZAP), it is clear that the highest ideal symmetry for this phase is {(**4mm**), **4mm**}. This symmetry is recorded along ⟨*uvw*⟩ = ⟨001⟩ or ⟨*uvw*⟩ = [001] for the cubic or the tetragonal systems, respectively.

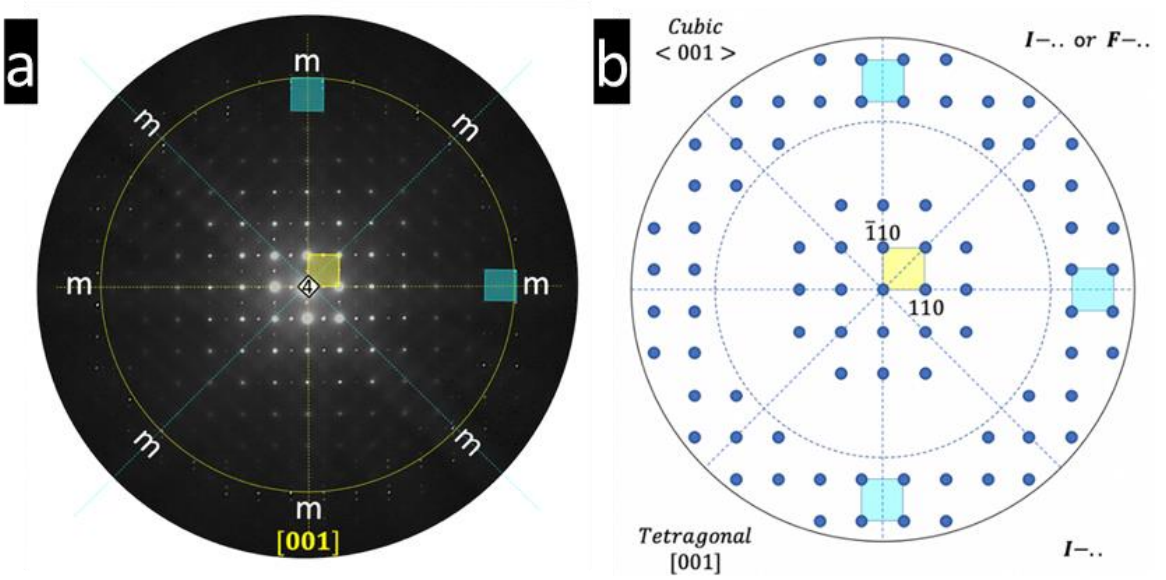

Fig. 3.5: a) Experimental electron microdiffraction patterns recorded along the <001> or [001 zone axis, showing the {4mm), 4mm} ideal symmetry for the whole pattern WP = (ZOLZ + FOLZ). One can notice the half shift between the reflection nets of the ZOLZ and the FOLZ along the horizontal and orthogonal mirrors. b) Simulated microdiffraction patterns along <001> or [001], highlighting the partial diffraction symbol, common to both crystal systems, cubic and tetragonal, respectively

By taking into account the relative positions of the reflections belonging to the ZOLZ and to the FOLZ, it comes out that the partial diffraction symbol is $I-..$ for the tetragonal system and $I-..$ or $F-..$ for the cubic system (**Fig. 3.5b**). The extra reflections forming a square net in the ZOLZ are not taken into account for the determination of the partial diffraction symbol. The origin of these satellite reflections will be treated in detail in paragraph 3.6.

The simulated diffraction pattern (**Fig. 3.5b**) highlights the partial diffraction symbol, common to both cubic and tetragonal systems. The identified partial diffraction symbol asserts that there is no glide plane along ⟨001⟩ or [001] if the BOC crystallizes in cubic or tetragonal system, respectively.

The diffraction symbol will be completely identified if the partial diffraction symbols are identified along the [100] and [110] zone axes for the tetragonal system and along the ⟨110⟩ axis for the cubic system. Unfortunately, it is quite difficult to record microdiffraction patterns along the latter axes due to the fact that the nanosheet are always flat and almost never edge-on.

To identify the crystal system (cubic or tetragonal), we measured the R_{FOLZ} (the radius of the FOLZ) of the diffraction pattern recorded along ⟨001⟩ (**Figs 3.6** and **3.7a**) and consequently the layer parameter $P_{\langle uvw \rangle}$ which is none other than the parameter a for the cubic system or c for the tetragonal system. The layer parameter $P_{<uvw>}$ is related to R_{FOLZ} by the following equation [Thomas1979]:

$$P_{<uvw>} = 2\frac{(L\lambda)^2}{(\lambda)R_{FOLZ}^2} \quad \text{(Eq3.3)}$$

where:

- $P_{<uvw>}$ is the row parameter,
- λ = 2.51 10^{-3} nm is the wavelength of electrons under accelerating tension, $V = 200$ kV,
- $L = 92.79$ cm is the chamber length of the microscope, working at 200 kV and
- $R_{FOLZ} = 5.6$ mm is the measured radius of the FOLZ (**Figs. 3.6** and **3.7a**)

The deduced lattice parameter a from the ZOLZ of the diffraction pattern recorded along ⟨001⟩ or [001] is $a = 0.391$ nm for both the two crystal systems, cubic or tetragonal.

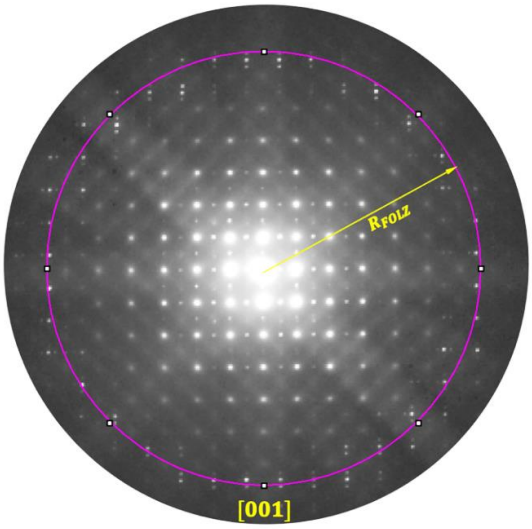

Fig. 3.6: Experimental diffraction pattern recorded along $< 001 >$ for the cubic system or [001] for the tetragonal system pointing out the R_{FOLZ}, the radius of the FOLZ. The latter is related to the range parameter $P_{<001>}$ ($P_{<001>}$ for the cubic system or $P_{[001]}$for the tetragonal system)

Following the procedure previously mentioned, the calculated row parameter is $P_{<001>} = 1.378$ nm, which is completely different from $a = 0.391$ nm and which, in addition, is not its multiple. If the lattice parameter c is a multiple of a ($c = ka$), this would indicate that we have a reflection extinction induced by the presence of a helicoidal axis parallel to c ($c // < 001 >$).

Through this characterization, we can conclude that the BOC crystallizes in the tetragonal system with a body-centred Bravais lattice. The cubic system is thus eliminated.

Based on the {(4mm), 4mm} ideal symmetry of the diffraction pattern recorded along [001], the BOC belongs either to the 4mm or to the 4/mmm point groups, and it would belong to one of the four following space groups, ranked in **Table 3.1**:

Table 3.1: Possible space groups, candidates for BOC characterization

Point groups	Space groups
$4mm$	$I4mm$ (107) I4cm (109)
$4/mmm$	$I\frac{4}{m}mm\ or\ \left(I\frac{4}{m}\frac{2}{m}\frac{2}{m}\right)\ \left(I\frac{4}{m}\frac{2}{m}\frac{2}{m}\right)$ (139) $I\frac{4}{m}cm\ \ or\ \ \left(I\frac{4}{m}\frac{2}{c}\frac{2}{m}\right)$ (140)

One can notice that the space groups belonging to the body centred tetragonal and having helicoidal axes along [001] are removed. We are left only with two space groups per point group.

Based on the Buxton *et al.* method [Buxton1976], we can achieve the same result by considering the symmetry characteristics of the diffraction pattern obtained in CBED mode (convergent beam electron diffraction) along the zone axis [001]. The symmetries, we are concerned with, are those of the Bright field and of the whole pattern.

The symmetry of the whole pattern is 4mm (**Fig. 3.7a**). To this symmetry, correspond the diffraction group groups $4mm$ and $4mm1_R$. The diffraction group $4mm1_R$ is connected to the holo-symmetric point group $4/mmm$ ($\frac{4}{m}\frac{2}{m}\frac{2}{m}$) or m$\bar{3}$m ($\frac{4}{m}\bar{3}\frac{2}{m}$) while the diffraction point group $4mm$ is connected to the point group $4mm$. The point groups $4/mmm$ and $4mm$ belong to the tetragonal system while the $m\bar{3}m$ belongs to the cubic system.

One of the special features of this method is the precision of the R_{FOLZ} measure (**Fig. 3.7a**) and therefore of the row parameter and in our case of the lattice parameter c.

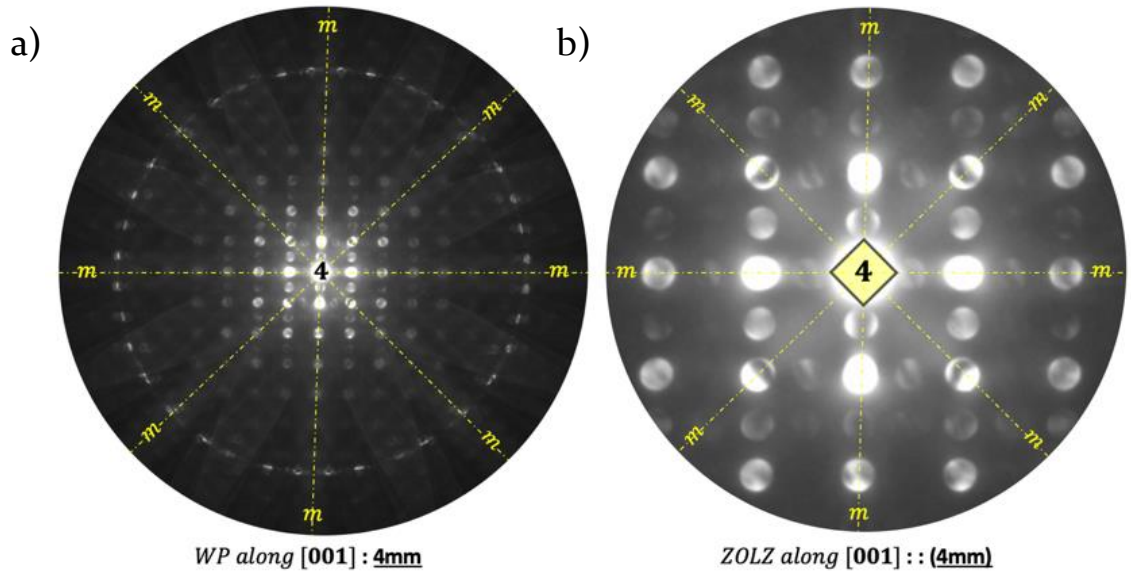

Fig. 3.7: Convergent beam electron diffraction (CBED) pattern recorded along [001] zone axis, a) the whole pattern ideal symmetry is 4mm, b) the ZOLZ pattern ideal symmetry is also (4mm).

In order to access the single space group, it is necessary to consider the symmetries of the diffraction patterns (CBED or microdiffraction) along the zone axes <100] and/or <110]. This operation is somewhat delicate because the nanosheets are always flat and it is difficult to orient them edge-on.

Another very elegant method to refine the characterization of the BOC is to consider the symmetry of the nanosheet form. This is what we will address in the following paragraph 3.3.3

3.1.3.c Symmetry analysis and morphology

It is firmly established in materials science, through the principles of group theory, that the morphology of phases presents in any medium, whether it be solid, liquid or gas, is of great importance. Extensive efforts have been made to comprehend both the equilibrium shape and the habit plane adopted by these phases within a specific medium [Cahn1982]. It is a well-acknowledged fact that the shape of a crystallographic precipitate developing within a solid matrix is determined by the point group, whose elements are shared between the precipitate and the matrix [Cahn1982, Redjaïmia1993, Van Landeghem2015, Skiba2018, Ozturk2020]. On the other hand, the shape of a phase occurring in an isotropic medium is solely imposed by the symmetry element of its point group [Buerger1978, Kabbara2019].

We will apply this group theory, based on the symmetry analysis, to explain the shape developed by the BOC nanosheets.

A trace analysis derived from the electron diffraction pattern recorded along [001] (**Fig. 3.8b**), superimposed on its corresponding TEM image (**Fig. 3.8a**), reveals that the BOC particles adopt a square shape. The lateral faces parallel to the c-axis – *i.e.*, parallel to [001] –, and bounding the square shape are parallel to the following crystallographic planes: (110)), ($\bar{1}$10)) and their opposites.

On the basis of the electron diffraction pattern, we can assert that the BOC particles, belonging to the point group 4mm or 4/m2/m2/m, develop a square shape (through the origin) [Phillips1971]. The latter, pedion or pinacoid, are both open forms dictated by the symmetry elements belonging to the hemihedral point group 4mm or to the holo-symmetric 4/mmm point group, respectively. The pedion is a singled face form parallel to (001) or (00$\bar{1}$) while the pinacoid is a pair of faces parallel to (001). These open forms must also have at least one additional (any) form in order to completely enclose the space surrounding the pedion or the pinacoid. These two shapes, belonging to 4mm or 4/mmm corresponding both to an absolute extremum [Cahn1982],

indicate that the development of the BOC particles is energetically favorable, *i.e.*, a stable BOC nanosheet.

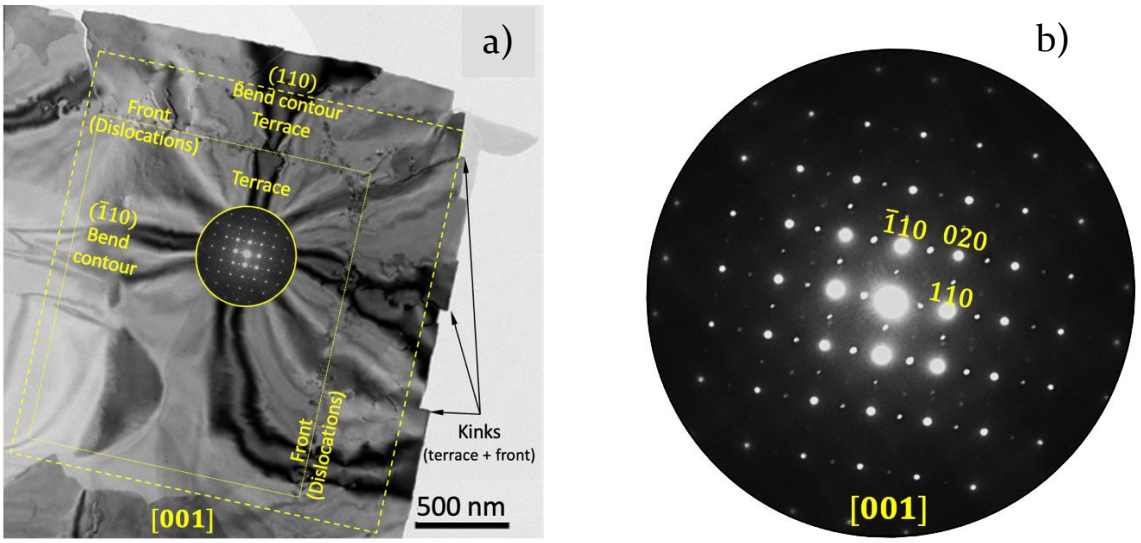

Fig. 3.8: a) Electron diffraction pattern recorded along the [001] zone axis superimposed on the corresponding bright field TEM image of a BOC nanosheet; one can notice the indexed Bend contours. Focus on one of the kinks shown at the right side of the nanosheet Fig. 3.8a. The characteristics of this kink are its terraces (110), (1̄10) and the corresponding front along [1̄10] and [110] directions, respectively. b) Corresponding SAED pattern recorded along [001] zone axis.

On close inspection of **Fig. 3.8a**, the convexity of the faces of the BOC nanosheet and the presence of kinks (terrace and front) on lateral faces of the square nanosheet of the BOC particle are apparent.

In **Fig. 3.8a**, the kinks terraces are parallel to the (110), (1̄10) nanosheet faces and their fronts move parallel to the [1̄10] and [110] directions, respectively.

The HRTEM image recorded along the [100] direction **(Fig. 3.9)**, presenting the edge of the square nanosheet, points out two perfectly parallel faces. This geometry goes against that of the pedion, a single face orthogonal to the [001] direction, and fits perfectly with that of the pinacoid (pair of parallel planes). Consequently, it is clear that the BOC nanosheet belongs to the point group 4/mmm and not to the 4mm one.

The combination of structural and morphological analyses by electron microscopy leads us to, ultimately, affirm that the BOC nanosheet is described by a centred tetragonal Bravais lattice belonging to the point group 4/*mmm* and crystallizing either in the spatial group *I*4/*mmm* (139) or in the spatial group *I*4/*mcm* (140). The comparison of the theoretical simulations of the diffraction patterns recorded along the [100] zone axis of the space groups *I*4/*mcm* and *I*4/*mmm* with the FFT of the HRTEM image obtained along the same zone axis [100] (**Fig. 3.10**), makes it

possible to deduce without ambiguity that the space group describing the structure of the BOC is indeed $I4/mmm$ or $I\frac{4}{m}\frac{2}{m}\frac{2}{m}$, in its full notation.

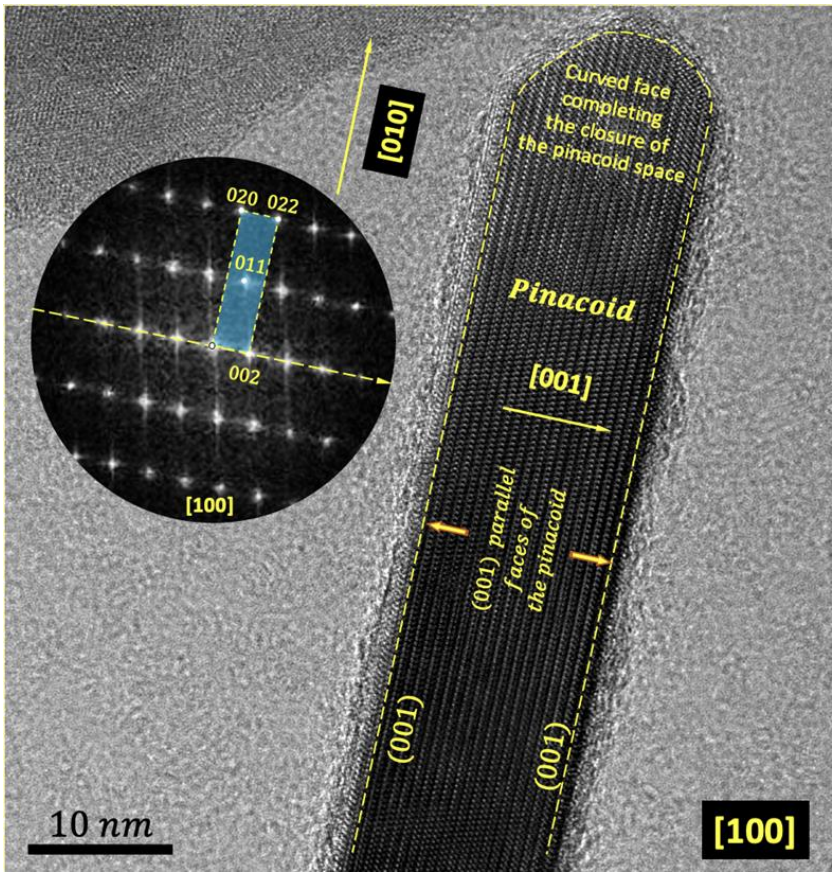

Fig. 3.9: HRTEM image of the BOC nanosheet observed edge-on along the [100] direction. Corresponding FFT along [100] zone axis with the centred tetragonal unit cell. One can notice that the edge-on faces of the nanosheet are parallel to (001) plane as pointed out by the corresponding FFT. This geometric information indicates that we are in the presence of a pinacoid (a pair of parallel faces Supplementary Material S3.3).

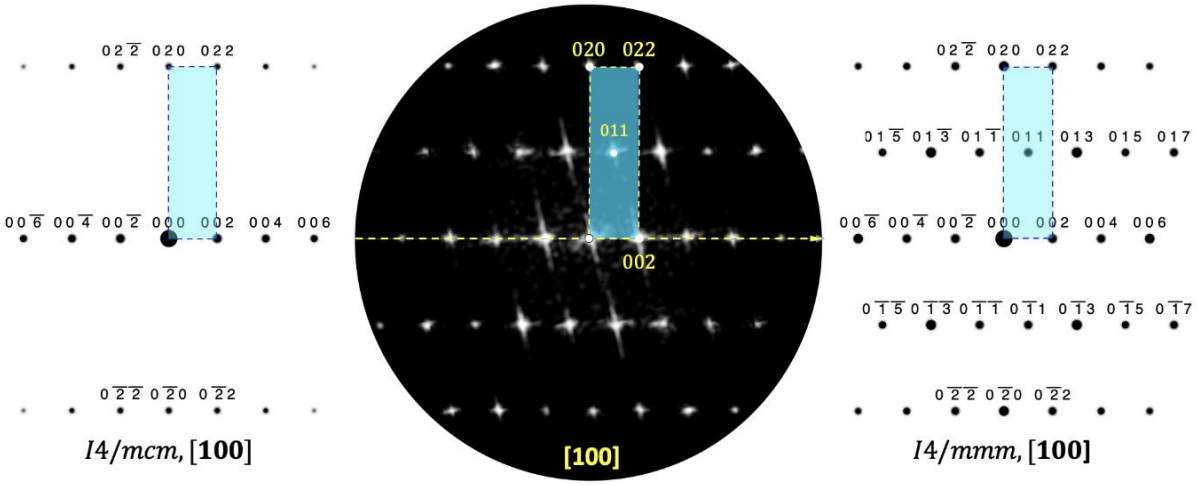

Fig. 3.10: Parallel between the simulations of the diffraction patterns of the space groups I4/mcm and I4/mmm obtained along the zone axis [100] and the FFT of the HREM image of the BOC nanosheet recorded along the same zone axis [100]. We can point out the similarity between the simulation corresponding to the space group I4/mmm, and the FFT of the experimental HREM of the BOC nanosheet obtained along the same zone axis [100].

To provide additional validation for this deduction, structural characterization was performed by TEM/SAED and further confirmed by XRD measurement (**Figs 3.11** and **3.12**) in Bragg-Brentano geometry. The XRD data exhibits a flawless alignment with the body centred tetragonal $Bi_2O_2CO_3$ structure, oriented along the [001] direction, further reinforcing this conclusion.

The lattice parameters obtained from SAED patterns recorded along different zone axes ([001] **Figs 3.7a, 3.8b** and [100] **Fig. 3.10b**), are in adequacy with those obtained by X-rays diffraction describing the BOC (**Fig. 3.12**) and the SAED pattern recorded on a zone with many nanosheets differently oriented (**Fig. 3.11**), are:

$$a = 3.91\ \text{Å and } c = 13.77\ \text{Å}.$$

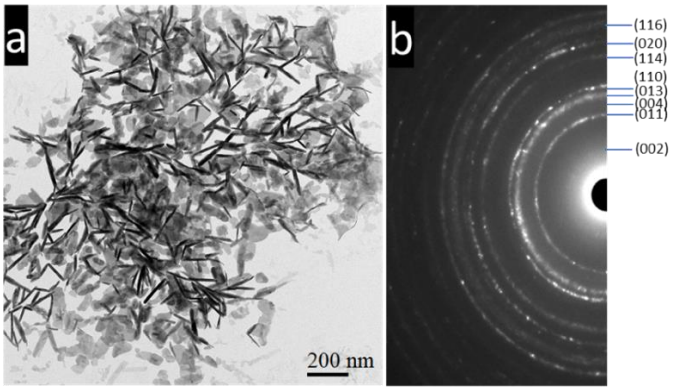

c

d-spacing exp, nm	d-spacing, nm PDF 41-1488	hkl
0.6888	0.6841	002
0.3788	0.3720	011
0.3460	0.3420	004
0.2989	0.2952	013
0.2754	0.2734	110
0.2138	0.2135	114
0.1913	0.1933	020
0.1729	0.1750	116

Fig. 3.11: a) TEM micrograph of nanosheets with b) corresponding SAED pattern and c) d-spacings indexed to $Bi_2O_2CO_3$ (JCPDS card 41-1488)

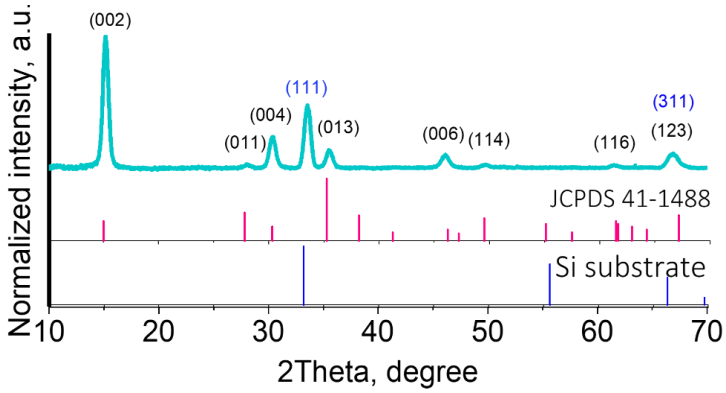

Fig. 3.12: XRD pattern of the nanosheet measured in Bragg-Brentano geometry. Comparison is made between the experimental pattern obtained with λ_{Co} = 1.78897 Å and the reference data from JCPDS 41-1488, corresponding to $Bi_2O_2CO_3$ with the space group I4/mmm.

We have clearly established, by electron diffraction (SAED, CBED) in combination with symmetry theory, that the crystallographic structure of the BOC is described by the space group I4/mmm ($a = 3.91\ A\ and\ c = 13.77\ A$). This result was confirmed on the atomic scale by TEM images obtained in HAADF-STEM mode (**Fig. 3.13**) along the zone axes [001], [100] and [110].

The atomic organization along these 3 zone axes thus obtained is in perfect agreement with the simulations carried out with Vesta [Vesta2011] and CrystalMaker softwares [CrystalMaker2023].

To elucidate the arrangement of the nanosheets at the atomic scale, additional to **Fig. 3.9**, investigations were conducted utilizing the HAADF STEM mode, which provides a Z-contrast image. These findings are presented in **Fig. 3.13**.

To achieve this visualization, cross-sectional views of the nanosheets were attained through the application of the Focused Ion Beam (FIB) technique along two zone axes: [100] and [110]. The resulting images in **Figs. 3.13b** and **c** exhibit high-resolution STEM cross-section views. Additionally, a top view of a nanosheet is presented in **Fig. 13a**.

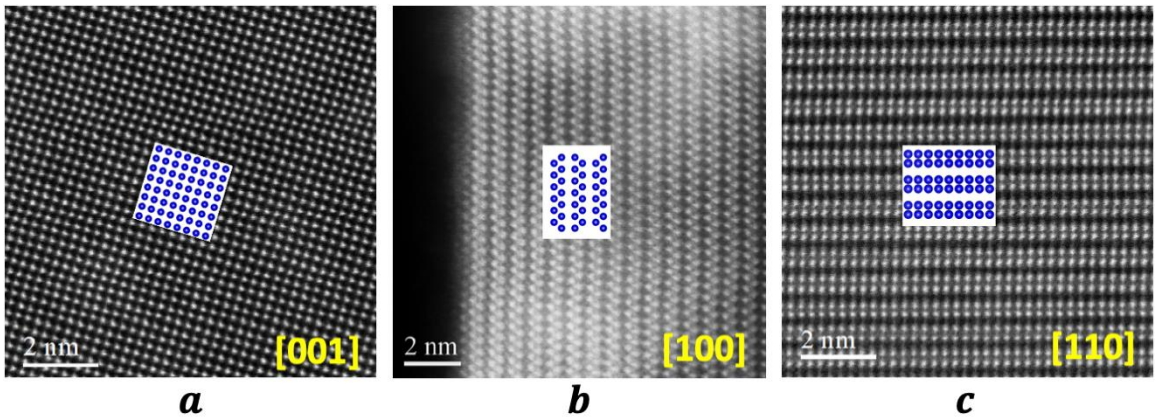

Fig. 3.13: High Resolution images of the BOC nanosheet and simulation a) HAADF micrograph recorded along [001] zone axis b) and c) STEM FIB cross section micrographs recorded along [100] and [110], respectively. Inserted the corresponding simulated images of the BOC nanosheet using the Vesta Software [Vesta2011]. Only the Bismuth atoms (High Z) are highlighted in the three simulations.

3.1.3.d Spectroscopy analysis of BOC nanosheet

To confirm that Bi_2O_3 nanosheets synthesized in water undergo carbonation upon exposure to air, resulting in their conversion into the tetragonal phase of $Bi_2O_2CO_3$, EELS analysis was conducted specifically on the carbon C-K edge, as depicted in **Fig. 3.14a**.

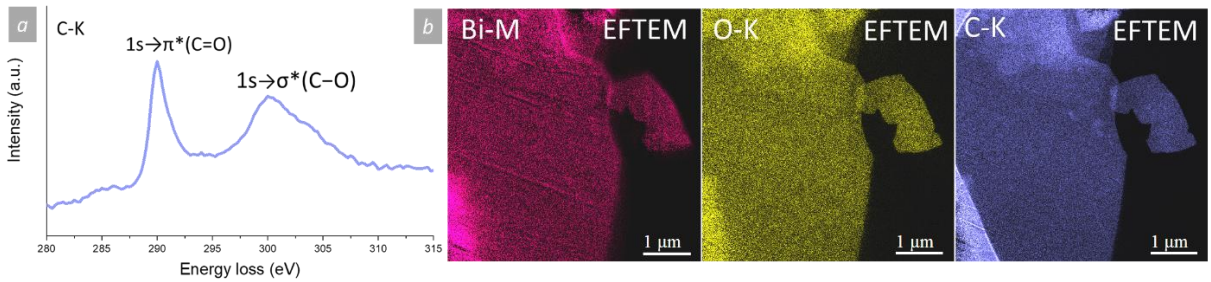

Fig. 3.14: a) EELS spectrum showing the presence of carbonate functional groups, b) EFTEM elemental mapping of $Bi_2O_2CO_3$ nanosheets deposited on a holey carbon TEM grid.

EELS analysis provides further confirmation, as the fine structure observed in the spectrum at the C-K edge corresponds to the carbonate signal (**Fig. 3.14a**). Additionally, EFTEM elemental mapping was conducted, revealing a consistent and uniform dispersion of the Bi, O, and C elements within the nanosheets, as illustrated in **Fig. 3.14b**.

Furthermore, this analysis strongly supports the idea that the synthesized nanosheets have undergone not only oxidation but also carbonation, resulting in the formation of $Bi_2O_2CO_3$. This carbonation process is attributed to exposure to air following the synthesis. The presence of C=O and C-O functional groups indicates additional reactions with carbon dioxide from the ambient environment, ultimately leading to the formation of $Bi_2O_2CO_3$.

For the EDX analysis results, please refer to **Supplementary material S3.4.**

The comprehensive data collected from TEM/SAED, XRD, EDX, EELS and EFTEM collectively offer compelling evidence supporting the categorization of the EDDL-synthesized nanosheets of $Bi_2O_2CO_3$ within tetragonal centred Bravais lattice and belonging to the *I*4/*mmm* (139) space group.

3.1.3.e Growth mechanism of the BOC

The BOC-phase is formed by oxidation and carbonation (reaction with carbon dioxide) of bismuth nanosheets, in contact with water first and air next, after evaporation of the liquid. It is therefore important to understand which mechanism is involved in the formation of bismuth nanosheets in water. In this section, we will try to describe this mechanism. The square shape and the particular dimensions of the particles lead us to question the formation mechanism of these bismuth nanosheet in water, which can be considered as an isotropic medium.

To answer this question, special attention to the diffraction pattern and its corresponding TEM image (**Fig. 3.9**) is required.

From these figures, further characteristics can be drawn:

- Most of the particle faces are decorated by kinks. The latter are characterized by their terraces and their fronts (**Fig. 3.8a**).
- The particle lateral faces are at least flat (**Figs. 3.8, 3.15a-b, 3.16a**) or convex (**Figs. 3.4a, 3.17**) but never concave.

This behavior indicates that the development of the nanosheet proceeds by lateral expansion of the kinks (terrace and front): the front move in the <110] directions parallel to the terrace plane (001). The front can move in opposite direction and sometimes leading to collisions

of the fronts and also to the creation of pores having the same geometry as the fronts give rise to them. If the porous zone is continuous (**Fig. 3.16a**), this leads to a fracture of the nanosheet and the consecutive detachment of the central part of the nanosheet. The later collapses, leaving in the nanosheet a scared area, empty of matter (**Fig. 3.16b**).

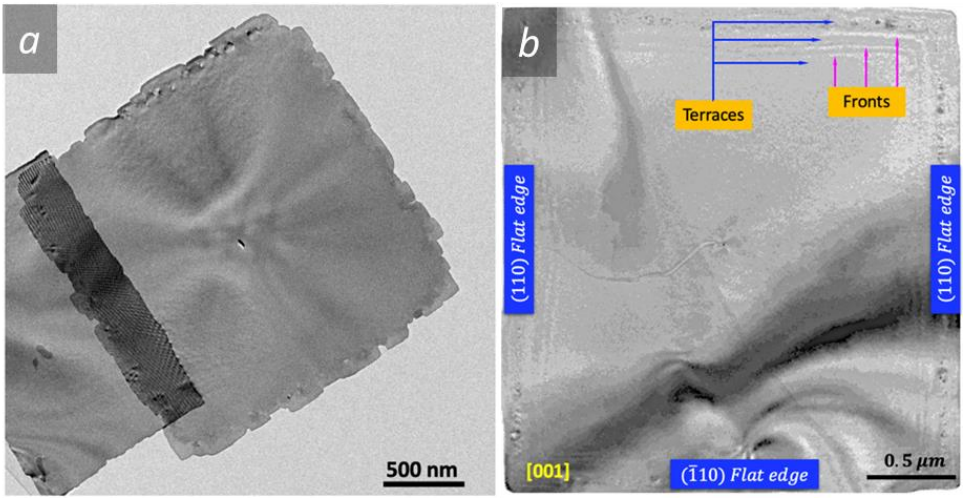

Fig. 3.15: Bright Field TEM images showing squared shape of BOC nanosheets with a) serrated edges by kinks (terraces and fronts) and b) flat edges (with no apparent kinks). One can notice the presence of terraces and fronts on the projected surface.

Under specific conditions, which may be linked to production parameters, it is possible for the lateral growth of the four faces to fade or diminish, only to resume under the same crystallographic orientation conditions. This interruption gives rise to a semi-coherent interface. This semi-coherent interface is marked by the presence of dislocations that introduce slight deviations from the initial terrace coherence, ultimately ensuring continuity, as illustrated in **Fig. 3.8a**.

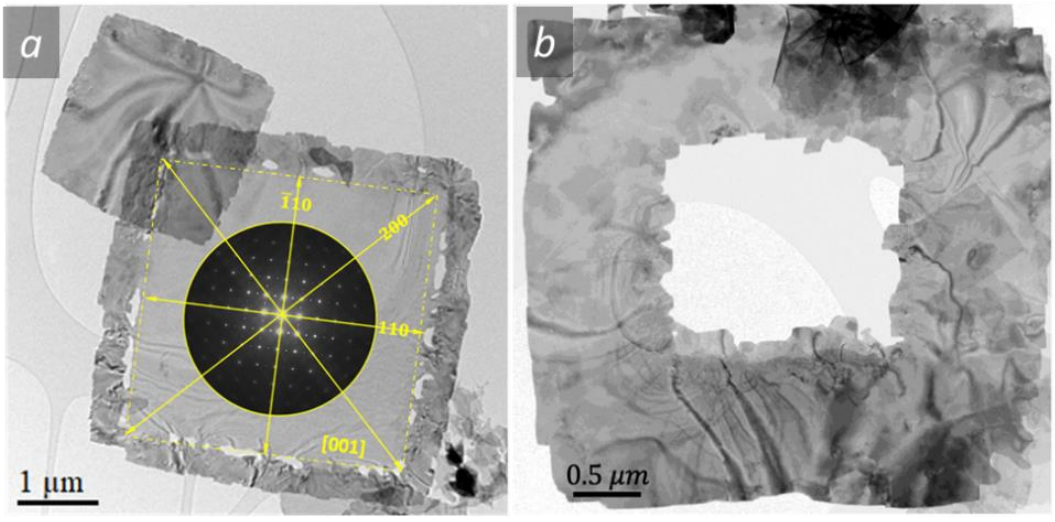

Fig. 3.16: a) Collision between kinks, whose terraces are offset from each other and fronts are of different heights, leading to a porous zone. b) If the porous zone is continuous, this leads to a fracture of the nanosheet; the centre of the nanosheet collapses, leaving in the nanosheet a scared area, empty of matter.

In some instances, certain BOC nanosheets exhibit jogs, both on the terraces and fronts, which give the impression of a spiral-like development, as depicted in both STEM BF and HAADF modes in **Figs. 3.17a** and **b**. In this case, the terraces run parallel to the nanosheet plane, while the corresponding fronts are perpendicular to the nanosheet plane, aligning with the c-axis (// [001]) of the unit cell. This particular geometric arrangement bears resemblance to the development of phase particles along dislocations. It is worth noting that the process of thickening through these jogs, where terraces are parallel to the nanosheet plane while fronts are perpendicular to it, progresses relatively slowly.

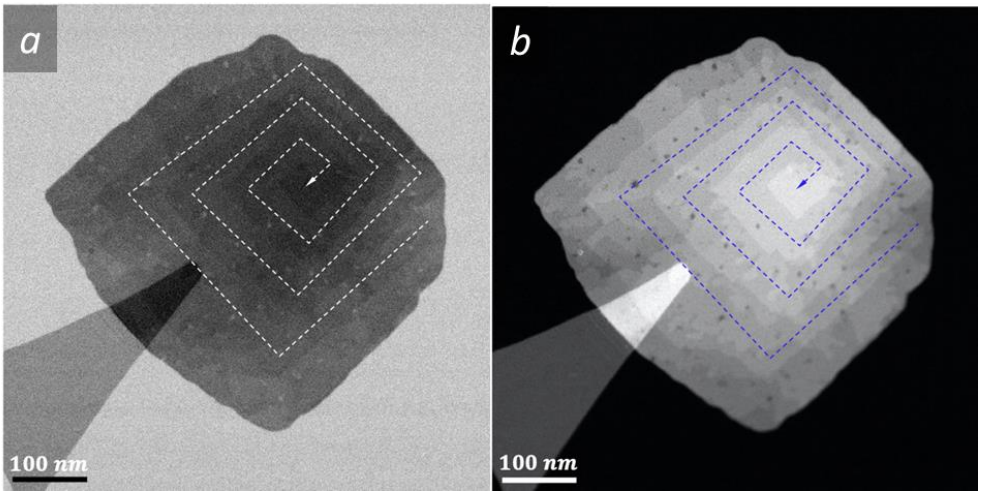

Fig. 3.17: a) TEM-Bright Field micrography showing the BOC nanosheet developed by jog (terrace // (001) and front // [001]) effect reminiscent of a spiral development. b) Corresponding TEM-Dark field. The dashed lines point out the spiral effect.

3.1.3.f Origin of satellite spots recorded along [001]

1. Bend contours

Most nanosheets are crossed by equal inclination fringes or bend contours (**Fig. 3.18**). These bend contours are change in image contrast indicating that the crystallographic orientation of $(hkl)_i$ planes are equal with respect to the incident beam along $\langle uvw \rangle$ direction. They correspond to exact Bragg diffraction position. When some of these bend contours intersect, they indicate that the corresponding planes $(hkl)_i$ are in relation to zone $\langle uvw \rangle$ *i.e.*, $h_i u + h_i v + h_i w = 0$.

The bend contours reflect the fact that the nanosheets are so thin and/or contain crystal defects that they bent elastically leading to rotation of the lattice planes towards diffracting Bragg position. The diffracted beams coming from the intersection domains of the bend-contours lead

to ⟨*uvw*⟩ zone axis diffraction patterns. This bend contour phenomenon has been reported by different authors [Viswanath2008, Suito1965, Marczewska2010, Coughlan2018].

The TEM micrograph (**Fig. 3.18**) recorded along the [001] zone axis is decorated by intersecting bend contours. The latter can successively move from one area to another (a, b or c) when the specimen under observation is slightly tilted.

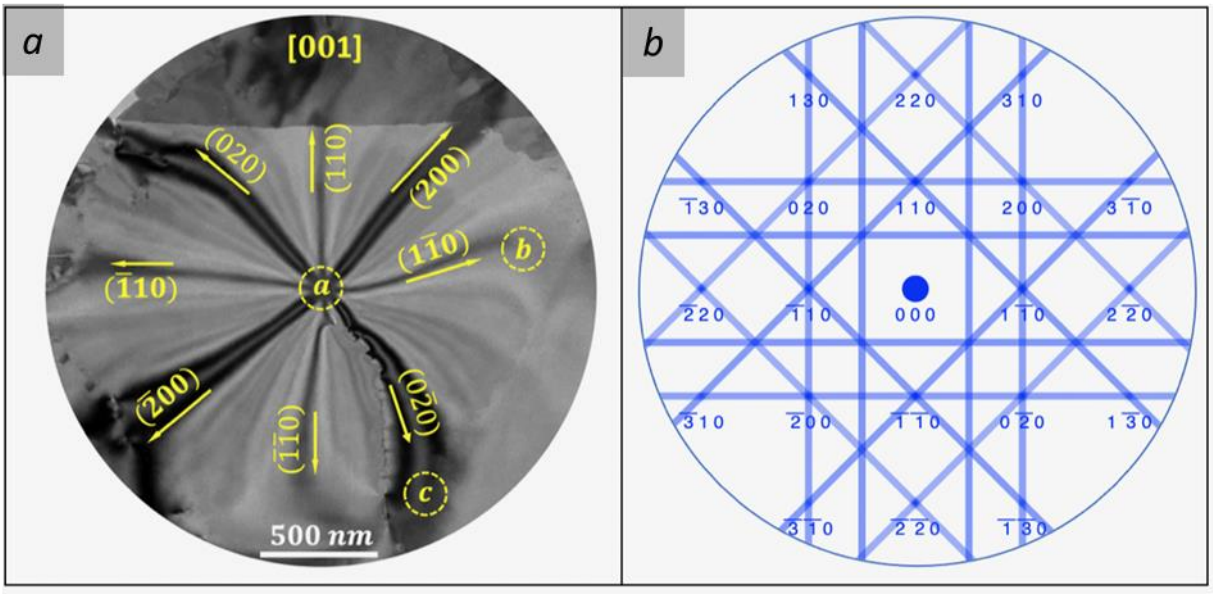

Fig. 3.18: a) BF-TEM micrograph recorded along [001] zone axis decorated by intersecting bend contours. The intersection of the bend contours can move from one area to another one (a, b or c) when the specimen under observation is slightly tilted. b) Diffraction pattern recorded along [001] zone axis and the corresponding Kikuchi bands diagram.

Bright-field Transmission Electron Microscopy (TEM) images of these nanosheets (as depicted in **Figs. 3.8a, 3.15, 3.16a** and **3.18**) reveal numerous contrast contours, particularly when the objective aperture is positioned exclusively over the zero beam.

Such features are common in materials with thin plate morphologies [Viswanath2008, Suito1965]. These contours frequently correspond to bend contours [Marczewska2010, Coughlan2018], stemming from the adaptation of thin nanoplates to the uneven surface of the TEM grid. They can also manifest as spider contours. Spider contours can result from strain fields originating from screw dislocations, indicating the presence of these dislocations within the nanoplates [Morin2011].

2. Satellite, the extra spots

All electron diffraction patterns obtained from the $Bi_2O_2CO_3$ nanosheets exhibit additional satellite reflections, notably along the [001] direction **(Figs. 3.5-8, 3.16a)** . These satellite reflections are supplementary spots or diffraction peaks that emerge between the primary

diffraction spots. Satellite diffraction lattices are superimposed on the diffraction pattern of the BOC crystallographic structure.

The occurrence of satellite (extra) spots around the reflections of the electron diffraction patterns can occur due to the presence of planar defects such as stacking faults and twins, point defects like oxygen vacancies, line defects such as dislocation arrays, spinodal decomposition, multiple (double) diffraction, order-disorder transformation, *etc*. The extra spots have been reported by different authors ([Rodríguez-González2006, Ou2008, Shi2019, Xu2013, Zhou2010].

For reasons outlined below, the origin of these lattices is essentially attributed to two phenomena: multiple diffraction and local disorder-order transformations of the BOC crystal structure, passing from a body centered tetragonal to a primitive Bravais lattice.

The extra-spots in the experimental diffraction patterns (**Fig. 3.19**), we are interested in, are recorded from the area labelled a, b and c (**Fig. 3.18**). Due to the low intensity of the extra spots, surface plots are drawn around the reflections of the diffraction patterns recorded along [001] (**Fig. 3.19**). One can notice that the aspect of the extra lattice depends on the area where the incident electron beam is focused. Based on this aspect, the extra spots can be grouped in two lattices in relation to their origins.

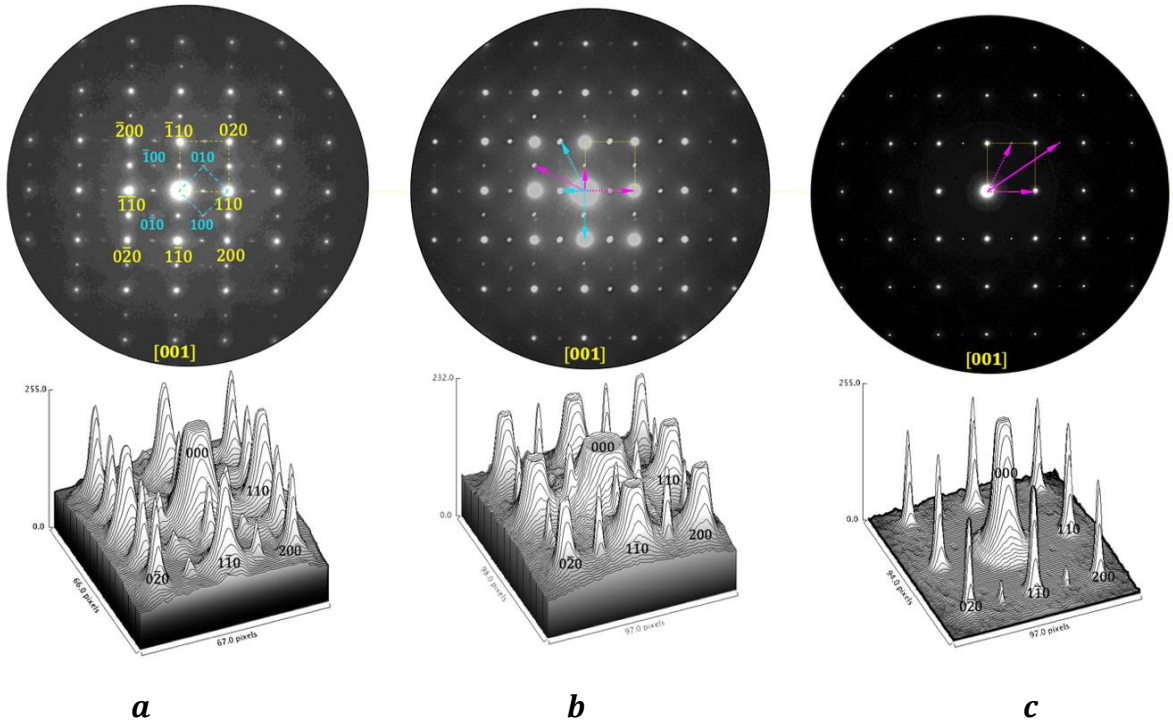

Fig. 3.19: Origin of the extra reflections on the electron diffraction pattern recorded along [001] on different area under the electron beam: a) order-disorder transformation (unit cell coloured in cyan), b) and c) multiple diffraction pointed out by vectors coloured in cyan and/or in magenta.

- The origin of the first one (dashed line colored in cyan, **Fig. 3.19a**) may come from the disorder-order microstructural transformation of the BOC. The latter loses its centred tetragonal symmetry ($I4/mmm$) and operates a transition towards a structure described by a simple tetragonal ordered cell ($P4/mmm$). The spots are indexed taking into account the simple tetragonal unit cell. One can notice that theses reflections occupy the forbidden position of the centred tetragonal unit cell of the BOC. The lattice parameter of the ordered unit is identical to that of the disordered phase.

- The second group of extra spots is due to multiple diffraction. This phenomenon occurs when two very thin crystals overlap, which have slightly different lattice parameters to each other. The diffracted beam (diffracted wave) by the upper crystal is further diffracted by the lower crystal. In addition to the acquired diffracted patterns belonging to the two crystals, appear extra spots due to the multiple (double) diffraction. The latter could be organized in reflections lattice. It often happens that multiple (double) diffraction spots appear, among others, in diffraction sites (position) prohibited by the structure of the studied crystal(s). This phenomenon is illustrated by the **Fig. 3.19**. Multiple diffraction paths are indicated by basis vectors colored in cyan (**Fig. 3.19b**) and/or magenta (**Fig. 3.19c**).

3.2 Conclusion

Through this study, we have demonstrated that the synthesis of Bismuth OxyCarbonate (Bismutite) (BOC) nanosheets (labelled in this study BOC) originates from nano-second pulsed discharges in water, followed by oxidation and carbonation in air. This BOC crystallizes in the body centred tetragonal Bravais lattice (a = 3.91 Å and c = 13.77 Å) nm and belongs to the $4/m2/m2m$ holosymmetric point group and to the $I4/mmm$ space group (or $I4/m2/m2/m$ in its full notation).

Based on the group theory (symmetry analysis), the BOC nanosheets exhibit a pinacoid shape, characterized by a pair of parallel planes parallel to (001). This particular shape is unique to the $4/m2/m2/m$ point group and is inherited from the bismuth nanosheets formed in water. Bismuth crystallizes in the trigonal system, and described using a hexagonal unit cell (with lattice parameters: $a = 3.77$Å et $c = 11.38$Å). It belongs to the point group $\bar{3}\frac{2}{m}$ (scalenohedron) and the space group $R\bar{3}\frac{2}{m}$. Energetically, the BOC shape is described by the symmetry element of the 4/mmm point group, which corresponds to an absolute extremum, resulting in a stable state of the nanosheet.

A mechanism, similar to the ledge mechanism (kinks and jogs) initially proposed to explain the formation of thin plates in metallic matrix, was showed to be relevant in this work. However, unlike the plane coherency in the ledge mechanism, the plane compactness plays an important role in the development of the bismuth nanosheets in water, before their subsequent oxidation in the liquid and carbonation in air.

To the best of our knowledge, this study is the first instance of synthesizing Bismuth OxyCarbonate by the spark discharge, identifying its crystallographic structure, explaining its morphology, and proposing a mechanism for its growth.

It is interesting to report that the Bismuth OxyCarbonate $Bi_2O_2CO_3$ has been identified by Grice [Grice2020] as crystallizing in the body centred orthorhombic crystal system and belonging to the $Imm2$ (44) space group with the following lattice parameters $\boldsymbol{a = 3.865(2), b = 3.862(2), c = 13.675(6)}$. This characterization was carried out by X-ray diffraction, a technique known to access the lattice parameters with high precision, superior to that obtained by electron diffraction in SAED mode. However, electron diffraction has a great advantage over X-ray diffraction; it directly allows access (imaging and diffraction) to the symmetry (point and space groups) characterizing the structure. Based on this observation, it is clear that BOC crystallizes in the centered tetragonal structure and belongs to the space group $I4/mmm$. This result is comforted by the theory of groups based on symmetry analysis of the morphology of the BOC nanosheet dictated by the point group $4/mmm$.

In a recent study, nanosecond-pulsed spark discharge between two lead electrodes in liquid nitrogen allowed to synthesize hexagonal lead nanosheets with the following characteristics: $6/mmm$ and $P6/mmm$ as point and space groups, hexagonal prism as morphology, ledge mechanism as process growth [Kabbara2019]. In the same way, the bismuth allowed the synthesis of pinacoid belonging to $4/mmm$ and $I4/mmm$ and the same ledge mechanism. Based on the similarities developed in these two studies, we can, instead of a single metal, use a binary alloy (Pb-Bi) or even a HEA.

Chapter 4

Photocatalytic performance of $Bi_2O_2CO_3$ nanosheets

4.1 Photocatalytic performance of $Bi_2O_2CO_3$ nanosheets

We assessed the photocatalytic performance of ultrathin $Bi_2O_2CO_3$ nanosheets, with thicknesses ranging from 5 to 20 nm. We evaluated their efficiency in the photodegradation of model pollutants, Rhodamine B and Methyl Orange, under both ultraviolet and visible light irradiation. We compared their performance with that of commercial Bi_2O_3 nanoparticles. Our findings align with those reported by Jia *et al.* [Colloids and Surfaces A, 653 (2002) 129915], who used 3D-peony flower-like nanostructures composed of nanosheets slightly thicker than ours.

The photoactivity of $Bi_2O_2CO_3$ nanosheets is on par with that of commercial Bi_2O_3 nanoparticles, which have diameters ranging from 80 to 200 nm. We found that oxygen vacancies have a limited influence on the dye degradation process. Trapping experiments confirmed that both holes and superoxide radicals played significant roles in the degradation of RhB, while hydroxyl radicals made a negligible contribution.

Furthermore, these $Bi_2O_2CO_3$ nanosheets exhibited excellent reusability over three cycles, indicating their substantial potential for further applications in environmental decontamination.

4.1.1 Introduction

Among the ternary bismuth compound phases, the bismuth oxycarbonate (BOC) $Bi_2O_2CO_3$ phase, also known as bismutite and bismuth subcarbonate $(BiO)_2CO_3$, is of particular interest [Ni2016]. $Bi_2O_2CO_3$ is one of the most extensively studied Aurivillius-related Layered Bismuth Based materials, characterized by its inherently layered structure composed of alternating $[Bi_2O_2]_2^+$ and $(CO_3)_2^-$ sub-layers. This unique structure promotes the growth of the crystal along a specific axis, resulting in anisotropic nanosheets. $Bi_2O_2CO_3$ is a semiconductor with a wide band gap of approximately 3.1–3.5 eV [Tian2022], which limits its application under solar light. To enhance the light absorption range of $Bi_2O_2CO_3$ materials, various approaches have been explored, including morphology regulation, metal deposition, metal/nonmetal ion doping,

and heterostructure formation [Madhusudan2011, Cheng2010, Zu2021, Tian2014, Yang2019b]. In nanostructured form, $Bi_2O_2CO_3$ has demonstrated useful properties, particularly in the fields of energy, catalysis, and photocatalysis [Ni2016], as well as supercapacitors [Wang2017].

$Bi_2O_2CO_3$ can be synthesized through various methods, such as hydrothermal [Zheng2010, Zha02011, Huang2014, Nguyen2022, He2022, Meng2022], solvothermal [Liu2010a, Sun2020, Zhang2022, Li2022b, Wu2023], gas-liquid interfacial synthesis [Wang2017], solution precipitation method [Yu2018], combining aqueous chemical approach with hydrothermal route [Dong2014], laser ablation in liquids (LAL) using a femtosecond laser and deionized water [Flores-Castaneda2023], and sonochemically assisted liquid-phase exfoliation of Bi [Gupta2022]. The resulting morphology of the synthesized $Bi_2O_2CO_3$ nanomaterials varies, but the predominant morphology observed is 3D flower-like spherical particles composed of plates or nanosheets [Zheng2010, Madhusudan2013, Zha02011, Meng2022, Wang2022, Jia2022], or 2D-like nanoobjects of different thicknesses [Liu2010b, Dong2014, Wang2017, Kar2017, Flores-Castaneda2023, Yu2018, Lopes2018, Sun2020, Li2022b, Wu2023].

Particularly in the context of photocatalysis, the 2D morphology can offer advantages due to its large surface area for catalytic reactions, efficient charge separation, reducing the probability of recombination of electron-hole pairs and efficient electron transfer to and from the electrolyte due to short migration lengths of photogenerated charge carriers to the reaction fronts on the surfaces of 2D materials. This characteristic reduces recombination losses and leads to higher activity of 2D forms of common materials [Luo2016].

The orientation of the reactive surface is another crucial factor that can impact the photocatalytic ability [Zheng2010, Huang2015]. Huang *et al.* demonstrated that single-crystal nanoplates predominantly exposing {001} facets exhibit significantly enhanced photocatalytic performance and photoelectrochemical properties. This improvement can be attributed to the high separation and rapid transfer of charge carriers originating from the {001} facets [Huang2015]. According to Zheng *et al.*, the photocatalytic activity of the flower-like hierarchically structured $Bi_2O_2CO_3$, composed of nanoflakes, is not solely attributed to its higher BET surface area (where BET stands for Brunauer–Emmett–Teller) but also to the presence of exposed reactive {001} planes [Zheng2010].

However, the synthesis of $Bi_2O_2CO_3$ in an atomically thin 2D morphology remains relatively underdeveloped, particularly concerning the precise control of lateral sizes and thicknesses [Ni2016]. Only a few reports [Gupta2022, Qin2021, Zhang2022] exist regarding BOC nanosheets (written BOCN hereinafter) thinner than 10 nm. Consequently, it is still unknown

whether transitioning $Bi_2O_2CO_3$ into a 2D form could unlock new fields of photocatalytic applications [Gupta2022]. To address this research gap, we present a new, versatile one-pot discharge-in-liquid method [Belmonte2023, Saito2019] for synthesizing laterally large, few-layer-thin {001}-exposed 2D $Bi_2O_2CO_3$ nanosheets. In the present work, the photocatalytic performance of these BOC nanomaterials is evaluated in the degradation of Rhodamine B (RhB) and Methyl Orange (MO), and a comparison is made with commercial Bi_2O_3 nanoparticles. Various scavengers are employed to investigate the contribution of different active species in the degradation of RhB, thereby studying their effects. Additionally, the stability of the photocatalysts is assessed, and a photocatalytic mechanism is proposed.

4.2.2 Experimental section

4.2.2.a Reagents and materials

Bismuth rods measuring 10 mm in diameter with a purity of 99.999% were acquired from Goodfellow. Bismuth oxide (Bi_2O_3) nanoparticles, with a purity of 99.9% and diameters ranging from 80 to 200 nm, were purchased from ThermoFisher Scientific Co., Ltd. Rhodamine B (RhB), methyl orange (MO), P-benzoquinone (p-BQ), tert-butyl alcohol (TBA), ethylenediaminetetraacetic acid (EDTA), and dimethyl sulfoxide (DMSO) were obtained from Sigma Aldrich Co., Ltd.

All chemicals used were of reagent grade or higher purity and were employed without additional purification. Ultra-pure MilliQ water was utilized throughout the experimental procedures.

4.2.2.b $Bi_2O_2CO_3$ nanosheets synthesis

BOCNs were synthesized using a straightforward process. Initially, bulk Bismuth rod electrodes were subjected to chemical etching, followed by erosion through nanosecond-pulsed discharges in MilliQ water, as illustrated in **Supplementary Material S4.1**. The procedure involved shaping the Bi rod into a conical form with a 10 mm base diameter, polishing the electrodes using 1200-grid paper, and rinsing them with tap water. Subsequently, the electrodes were immersed in a 5% Nital chemical etching solution for 20 minutes. After the etching process, the Bi electrodes were rinsed, secured in electrode holders, and submerged in a 100 ml Dewar flask filled with the chosen dielectric liquid, which, in this experiment, was ultra-pure water (conductivity: 0.055 $\mu S\ cm^{-1}$). The distance between the electrodes was maintained constant by adjusting it with micrometric screws. A high positive voltage was provided by a DC power supply

(Technix SR15-R-1200) to a solid-state switch (HTS-301-03-GSM), which was controlled02 by a function generator and generated high voltage pulses. The power electrode received the electrical signal, while the second electrode acted as the cathode and was grounded during the breakdown process. Pulses with a voltage of 5 kV, frequency of 10 Hz, and pulse width of 75 ns were applied to the power electrode for 90 minutes to achieve a concentration of 15 mg in a water volume of 30 ml. To characterize the products resulting from electrode erosion, carbon and holey carbon grids were employed as substrates for electron microscopy analysis. The nanosheets were collected by immersing a TEM grid in a solution containing the synthesized BOCNs.

4.2.2.c Characterization

The X-ray diffraction (XRD) patterns of the samples were obtained using a Bruker X-ray diffractometer (D8 Discover) with Co Kα radiation source (λ = 1.78897 Å). The surface morphology and thickness of the $Bi_2O_2CO_3$ samples were examined using a JEOL ARM 200 F cold FEG TEM/STEM operating at 200 kV. It was equipped with a spherical aberration (Cs) probe and image correctors, providing a point resolution of 0.12 nm in TEM mode and 0.078 nm in STEM mode. The camera used was a GIF quantum ER model 965. Additionally, a scanning electron microscope ZEISS GeminiSEM 500 and an atomic force microscope AFM SmartSPM 100 setup (AIST-NT) in semi-contact mode at ambient conditions were utilized for further examination. HQ:NSC16/Hard/Al BS (MicroMasch) cantilevers have been utilized with 190 kHz resonant frequency and 45 Nm-1 force constant. UV-visible diffuse reflectance spectra and absorption spectra were measured using an Agilent Cary 7000 UMS spectrophotometer.

4.2.2.d Electrochemical measurements

The photoelectrochemical measurements were performed on a potentiostat BioLogic SP150, employing a standard three-electrode configuration. A platinum coil served as the counter electrode and a commercial Ag/AgCl electrode in saturated KCl functioned as the reference electrode. The electrolyte utilized was a 0.5 M Na_2SO_4 aqueous solution with a pH of 7.

The as-prepared samples deposited on fluorine doped tin oxide (FTO) glass substrates were used as the working electrodes. Firstly, a fluorine-tin oxide (FTO) glass substrates with a 1.0 cm^2 surface area was thoroughly cleaned using an ultrasonic bath. Next, the prepared water solution containing catalyst - BOC nanomaterials or Bi_2O_3 nanoparticles (0.5 g L^{-1}) - was then drop-deposited onto the FTO glass surface, and finally dried at 80 °C overnight. Working electrodes were exposed to a 500 W Xe arc lamp fitted or not with a UV cutoff filter (λ > 380 nm) or an AM 1.5G filter (simulated solar light irradiation).

Photocurrent density was evaluated from chronoamperometric measurements by applying a constant potential of 0.15 V vs Ag/AgCl. Electrochemical impedance spectroscopy (EIS) measurements were performed by applying a sinusoidal AC perturbation of 10 mV. Nyquist plots were obtained within the frequency range of 500 kHz to 20 mHz at open circuit potential (OCP). Mott-Schottky plots were acquired at frequencies from 4 kHz to 10 kHz in the potential range of -0.8 V to 0.4 V vs Ag/AgCl in the dark.

4.2.2.e Photocatalytic experiments

A homemade photocatalytic reactor, equipped with a water cooling device and a 350 W Xenon lamp, was used to investigate the photocatalytic degradation of dyes, namely Rhodamine B and Methyl Orange. To prepare the photocatalyst solution, 10 mL of the dye solution (with a concentration of 40 mg L^{-1}) was mixed with 30 mL of a solution containing 14 mg of BOCN. The initial solution, therefore, consisted of a total volume of 40 mL, containing BOCN (14 mg) and the dye (10 mg L^{-1}). The photocatalyst solution was placed in a quartz beaker with dimensions of 33 mm in diameter and 60 mm in height. The beaker was positioned at a distance of 10 cm from the 350 W Xenon lamp. Before turning on the light source, the solution was stirred magnetically in the dark for 0.5 hours to establish the equilibrium of adsorption-desorption mechanisms. After that, the light source was activated to initiate the photocatalytic reaction.

At regular time intervals, approximately 2 mL of the solution was sampled and immediately centrifuged for 3 minutes at 15,000 rpm to separate the catalyst and analyzed by UV-Visible spectroscopy to estimate the dye concentration.

These measurements were then compared to a solution with the same concentration of Rhodamine B but without any catalysts. Furthermore, comparisons were made with a solution containing commercial Bi_2O_3 nanoparticles (30 mg).

The degradation efficiency (%) was calculated using the following formula:

$$\text{Degradation (\%)} = \frac{C_0 - C}{C_0} \times 100\%, \qquad \text{(Eq.4.1)}$$

where C_0 is the initial concentration of RhB; and C is the concentration of RhB at time t.

Additionally, the degradation procedure of MO was the same as that of RhB.

To assess the stability of the photocatalyst, three cycling runs for the degradation of Rhodamine B (RhB) were conducted. After each cycle, the reaction mixture was washed with

deionized water, and then the photocatalyst was used again with a fresh RhB solution for the next cycling.

4.2.2.f Active species trapping experiments

To identify the active species generated during the photocatalytic reaction, the following scavengers were added at specified concentrations:

- For superoxide radicals ($\bullet O_2^-$) – p-benzoquinone (p-BQ), 0.1 mM
- For holes (h^+) – ethylenediaminetetraacetic acid (EDTA), 10 mM
- For hydroxyl radicals ($\bullet OH$) – tert-butyl alcohol (TBA), 10 mM
- For electrons (e^-) – dimethyl sulfoxide (DMSO), 10 mM.

The method employed for investigating these active species was similar to the previous photocatalytic experiments. The scavengers were added separately to the reaction mixture, and the photocatalytic process was carried out as before, followed by analysis and measurements to identify the presence and effect of the active species.

4.2.3 Results and discussion

4.2.3.a Phase structure and morphology

The synthesis process of bismuth oxycarbonate nanosheets (BOCNs) is depicted in **Supplementary Material S4.1**. In this study, series of free-standing 2D BOCNs were successfully synthesized. **Figs. 4.1a** and **b** present typical transmission electron microscopy (TEM) images of the synthesized BOCNs, revealing the exposure of the (001) facet, as confirmed in **Figs 4.1c** and **d**. The high-resolution TEM (HRTEM) images in **Figs. 4.1c**-**h** showcase the excellent crystallinity of the BOCNs. **Fig. 4.1c**, which utilizes the atomic resolution scanning transmission electron microscopy (STEM) mode with high-angle annular dark-field (HAADF) imaging, reveals a measured lattice spacing of 0.276 nm. This spacing corresponds to the (110) plane of the tetragonal $Bi_2O_2CO_3$ crystal, which belongs to the I4/mmm 139 space group. The selective area electron diffraction (SAED) pattern shown in **Fig. 4.1d** demonstrates a well-ordered array of diffraction spots that can be indexed to the (110), (1-10), and (200) reflections, confirming that the $Bi_2O_2CO_3$ nanosheet possesses a single-crystal structure [Dong2014]. Furthermore, some weak diffraction spots are also observed (**Figs. 4.1d** and **Supplementary Material S4.2**). They can be attributed to local disorder-order transformations and multiple diffraction, as described in the previous Chapter.

The synthesis process of BOCN by nano-pulsed discharges in water involves the formation of metallic nanoparticles, followed by a series of transformations involving oxidation and carbonation. The initial step involves the synthesis of metallic nanoparticles from a metallic vapor during electrodes erosion by discharges. After the metallic nanoparticles are formed, they undergo oxidation when exposed to water or water vapor. The water molecules can react with the surface of the metallic nanoparticles, leading to the transformation into the metal oxide nanosheets. Subsequently, the metal oxide nanosheets are exposed to air containing carbon dioxide (CO_2). The carbon dioxide can react with the metal oxide nanosheets, leading to their carbonation.

We cannot exclude that this sequence of reactions introduces strain within the nanosheets due to the differences in lattice parameters between the metal oxide and carbonate phases. It is known that strained nanoparticles can serve as efficient catalysts due to their unique surface properties and reactivity [Feng2015]. However, we do not observe a significant shift of XRD peaks that could demonstrate a high level of stress within the nano-objects. Therefore, we will consider that stress, if any, has a limited role in the photocatalytic activity of the nanosheets.

To characterize the BOC nanosheets, we conducted elemental mapping measurements using HAADF STEM as shown in **Fig. 4.1e**. The results indicate a uniform distribution of Bi, O, and C throughout the entire sample. To further characterize the crystalline structure, we performed X-ray diffraction (XRD) analysis, presented in **Fig. 4.1f**. The excellent agreement between our measured XRD patterns and the JCPDS card data confirms that our synthesized samples consist of the $Bi_2O_2CO_3$ phase with a tetragonal I4/mmm structure. The diffraction peaks observed at 15.1°, 28.1°, 30.4°, 35.6°, 46.1°, 49.8°, 61.6°, and 66.9° can be indexed to the (002), (011), (004), (013), (006), (114), (116), and (123) planes of the tetragonal $Bi_2O_2CO_3$ phase, with lattice parameters of $a = b = 0.3865$ nm and $c = 1.377$ nm. These values are consistent with the PDF standard card of tetragonal $Bi_2O_2CO_3$ (JCPDS card no. 41-1488). The sharper and stronger diffraction peaks for the (002), (004), and (006) planes compared to other peaks indicate that the nanosheets are grown layer by layer, oriented along the [001] direction. **Fig. 4.1g** shows a typical atomic force microscopy (AFM) image of BOCN. The topographical profiles in **Fig. 4.1g** reveal that the thickness of BOCN is in the range of 6-9 nm. Considering the layer spacing of $Bi_2O_2CO_3$ (~0.68 nm), the layer number of $Bi_2O_2CO_3$ can be assigned to be 6-7 layers, which is consistent with the measurement from the lateral HAADF STEM micrograph shown in **Fig. 4.1h**. This observation provides further confirmation of the layered structure of the BOC nanosheets.

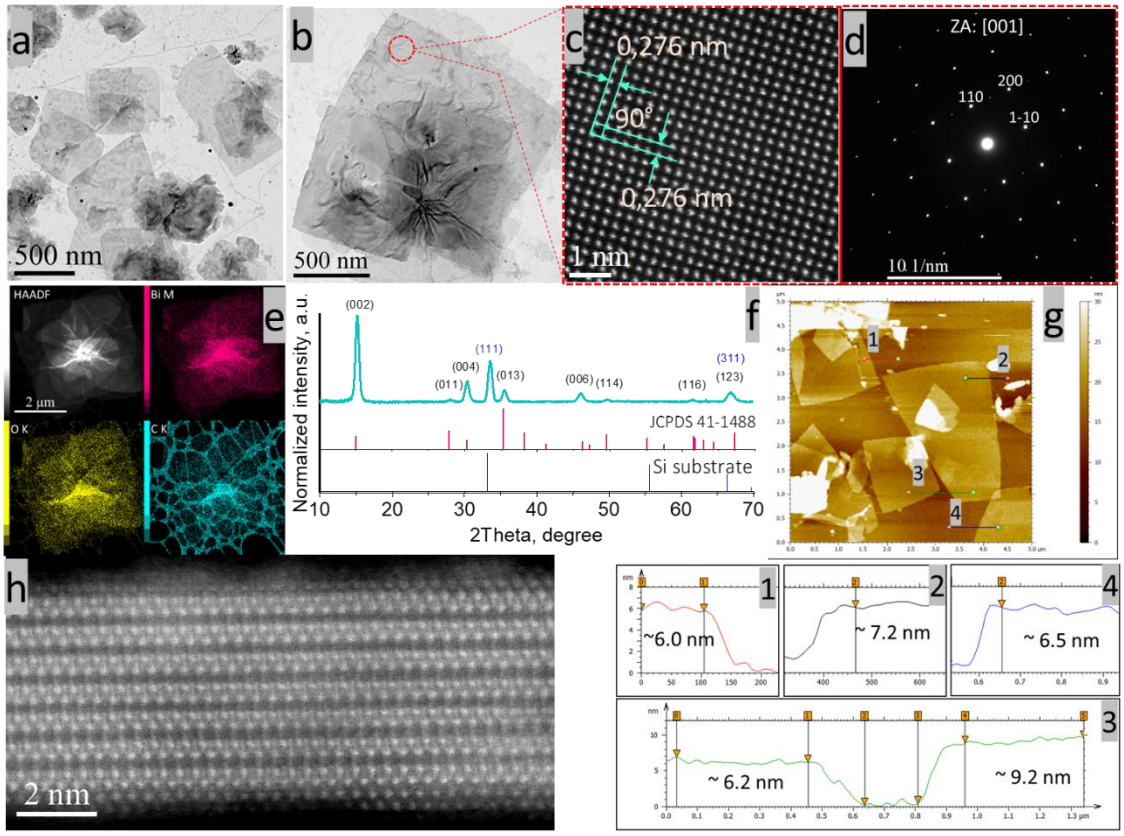

Fig. 4.1: Characterization of $Bi_2O_2CO_3$ nanosheets (BOCN). a, b) typical low magnification TEM images, c) typical high resolution HAADF STEM image, d) SAED of (b), e) HAADF STEM image of $Bi_2O_2CO_3$ nanosheet and elemental mapping measurements showing the distribution profiles of Bi (magenta), O (yellow), and C (cyan) elements, f) measured XRD patterns of the BOCN. The benchmark data from the JCPDS card (no. 41-1488, $Bi_2O_2CO_3$ in space group I4/mmm) is shown for comparison, g) typical atomic force microscopy (AFM) image with corresponding height profiles for four nanosheets, h) high resolution side view HAADF STEM image of $Bi_2O_2CO_3$ nanosheet. The cross-section of the multilayer stack was obtained using the focused ion beam (FIB) method, where the micro-area to be observed is protected before etching by gallium ions with a platinum coating.

4.2.3.b Light absorption, charge separation measurements

The optical absorption property of a semiconductor plays a crucial role in determining its photocatalytic activity [He2014]. To analyze the optical properties of the $Bi_2O_2CO_3$ sample, UV-Vis diffuse reflectance spectra (DRS) analysis was performed, and the results are presented in **Supplementary Material S4.3**. As depicted in the spectrum, the BOCN sample exhibits absorption of UV light (≤ 360 nm) only. The absorption peak is located at 360 nm, with a long tail extending beyond 800 nm. It is well-known that the UV-vis absorption edge is closely related to the energy band structure of the semiconductor catalyst, which is dependent on its electronic configuration [Wang2014, Lin2016]. The observed absorption in the UV range indicates the potential of BOCN as photocatalyst, as nanosheets are capable of absorbing UV light, which is crucial for initiating photocatalytic reactions.

The extended tail can be attributed to the energy increase of the charged carriers generated by the incident photons due to quantum confinement within the nanoparticles present in the solution. As proposed in previous reports [Kar2017, Lin2016], incident photons with lower energies than the optical gap can, via this mechanism, trigger reactions requiring at least this energy. The extended tail can also be explained by the presence of surface defects like oxygen vacancies [Yu2018]. Indeed, oxygen vacancies introduce defect states between the conduction band and the valence band, favoring the transition of electrons in the forbidden band, which causes tail absorption. However, we will show next that the role of oxygen vacancies is limited, if not inexistent.

To accurately determine the band gap energy of our semiconductor photocatalyst showing a significant absorption of sub-band gap energy photons, the Tauc method with a baseline approach was employed. The Tauc method relies on the assumption that the energy-dependent absorption coefficient α can be expressed by the following equation (1) [Makula2018]:

$$(\alpha h\nu)^{1/\gamma} = B(h\nu - E_g) \qquad \text{(Eq4.2)}$$

where α, h, ν, E_g and B are the absorption coefficient, the Plank constant, the photon's frequency, the band gap energy, and a constant. The γ factor depends on the nature of the electron transition and is equal to 0.5 or 2 for the direct and indirect allowed transition band gaps, respectively. Since $Bi_2O_2CO_3$ undergoes an indirect transition [Huang2015, Tian2014], the Tauc method with a baseline approach and γ value of 2 was applied to analyze the absorption data. By plotting $(\alpha h\nu)^{0.5}$ against photon energy ($h\nu$), a linear fit of the fundamental peak with a baseline in the sub-band gap region of the Tauc plot was used to estimate the band gap energy. The slope below the fundamental absorption in the linear fit was used as the abscissa. The intersection of the two fitting lines gives an estimation of the band gap energy, as illustrated in **Fig. 4.2**. According to the analysis, the estimated band gap energy of $Bi_2O_2CO_3$ is found to be 3.51 eV, in agreement with other works [Cheng2010, Yu2017]. Additionally, the collected spectra demonstrate a steep change in absorbance in the UV region, characteristic of wide band gap semiconductors.

The separation efficiency of photo-generated charges was also investigated by transient photocurrent responses (**Fig. 4.3**). A larger photocurrent density generally indicates higher charge separation efficiency for photocatalysts.

The photocurrent density measurements are conducted under cyclic illumination (light ON and OFF, with 30-second periods). The transient photocurrent response curves under Xe

lamp irradiation are shown in **Fig. 4.3a,** and the photocurrent density of BOCN is 1.5 times higher than that of Bi_2O_3 for the selected concentrations.

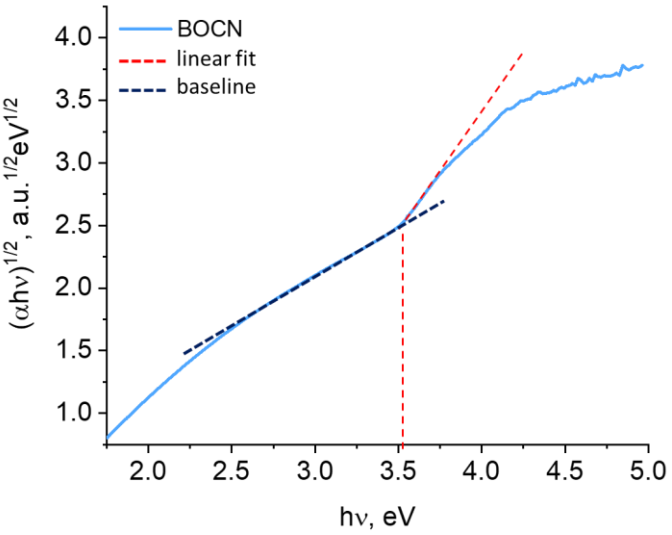

Fig. 4.2: Baseline approach of the Tauc method applied to DRS UV-vis data to determine the band gap value [Makula2018]

Additional valuable information was obtained by measuring the photocurrent responses of BOCN under various illumination conditions:

- Without filters at 350 W, 250 W, and 150 W.
- At 350 W with an air mass filter (to simulate the solar spectrum).
- At 350 W with a UV cutoff filter λ>380 nm (to eliminate the effect of UV radiation).

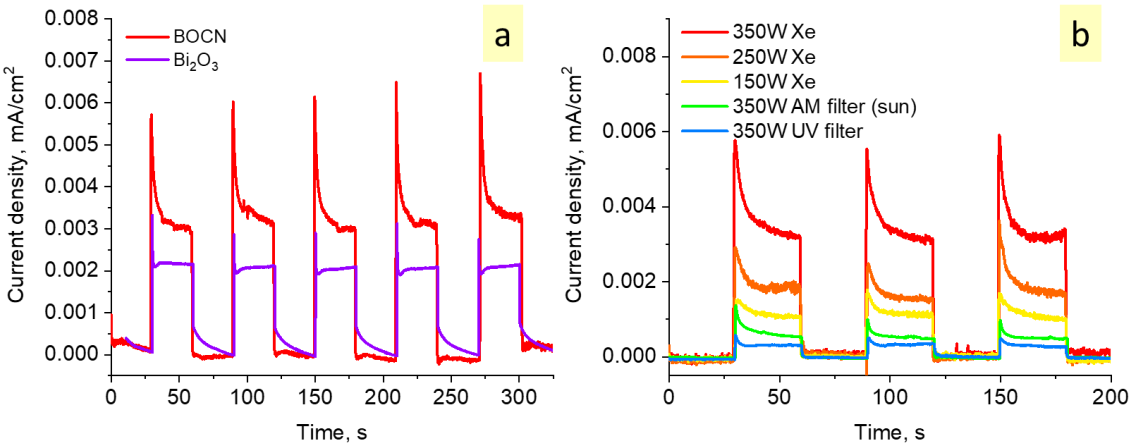

Fig. 4.3: a) Transient photocurrent response (0.15 V vs Ag/AgCl) of BOCN and commercial Bi_2O_3 under UV-visible illumination (Xe lamp at 350 W), b) photocurrent density of BOCN at 0.15 V vs Ag/AgCl as a function of the light source

The transient photocurrent response curves under illumination from different light sources are shown in **Fig. 4.3b**. The observed photocurrent density followed an expected trend: without a

filter, the highest photocurrent density was observed at 350 W, followed by 250 W and 150 W. When the filter was applied under 350 W illumination, the order changed to: No filter > Air mass filter (approximately 4% UV) > UV filter. The use of filters resulted in a significant decrease in photocurrent density. These findings align with the absorbance measurements conducted, as described below.

To estimate the charge transfer at the catalyst/electrolyte interface, we conducted electrochemical impedance spectroscopy (EIS) to measure the kinetics of charge transfer [Yu2017]. In **Supplementary Material S4.4**, the Nyquist plots of Bi_2O_3 and $Bi_2O_2CO_3$ under open-circuit potential at a steady state are presented. The arc radii Bi_2O_3 and $Bi_2O_2CO_3$ are pretty close, evidencing that the migration and transfer efficiencies of charge carriers were similar for both materials (moderate charge transfer resistance values of ~1800 and ~1300 Ω respectively). This conclusion is in line with the limited role of oxygen vacancies from the UV-Vis DRS analyses presented above.

4.2.3.c Photocatalytic performance of $Bi_2O_2CO_3$

The photocatalytic performance of the as-synthesized $Bi_2O_2CO_3$ material was evaluated through the photodegradation of model pollutants (RhB and MO) under both ultraviolet and visible light irradiation (**Fig. 4.4**) and compared with photocatalytic performance of commercial Bi_2O_3 nanoparticles. Before conducting the photocatalytic tests, the as-synthesized samples ($Bi_2O_2CO_3$ and Bi_2O_3) were allowed to come into contact with the RhB and MO dye solution for 30 minutes to reach adsorption/desorption equilibrium.

Figs. 4.4a and **d** show the time-dependent UV-vis spectra of RhB and MO respectively in aqueous solution after the photodegradation reaction with BOCN sample. As the irradiation time is increased, the absorption peak of RhB at 554 nm (abs. peak of MO at 464 nm) decreases dramatically and almost disappears in 180 min (330 min). In addition, the absorption peak of RhB shows a blue-shift during the degradation process, that can be due to de-ethylation of RhB as was shown in [Chen2016, Pei2023], suggesting its degradation through dye sensitization. In contrast, the photodegradation of MO does not follow the sensitization-degradation route, as shown in **Fig. 4.4d** [Arshad2022]. After 210 min of degradation, the RhB solution was observed to become colorless (**Supplementary Material S4.5**).

As shown in **Figs. 4.4b** and **4.4e**, in the absence of photocatalyst, a negligible removal of RhB and MO was observed. This indicated that single photolysis alone was insufficient to degrade these dyes, and their degradation was primarily photocatalytically driven.

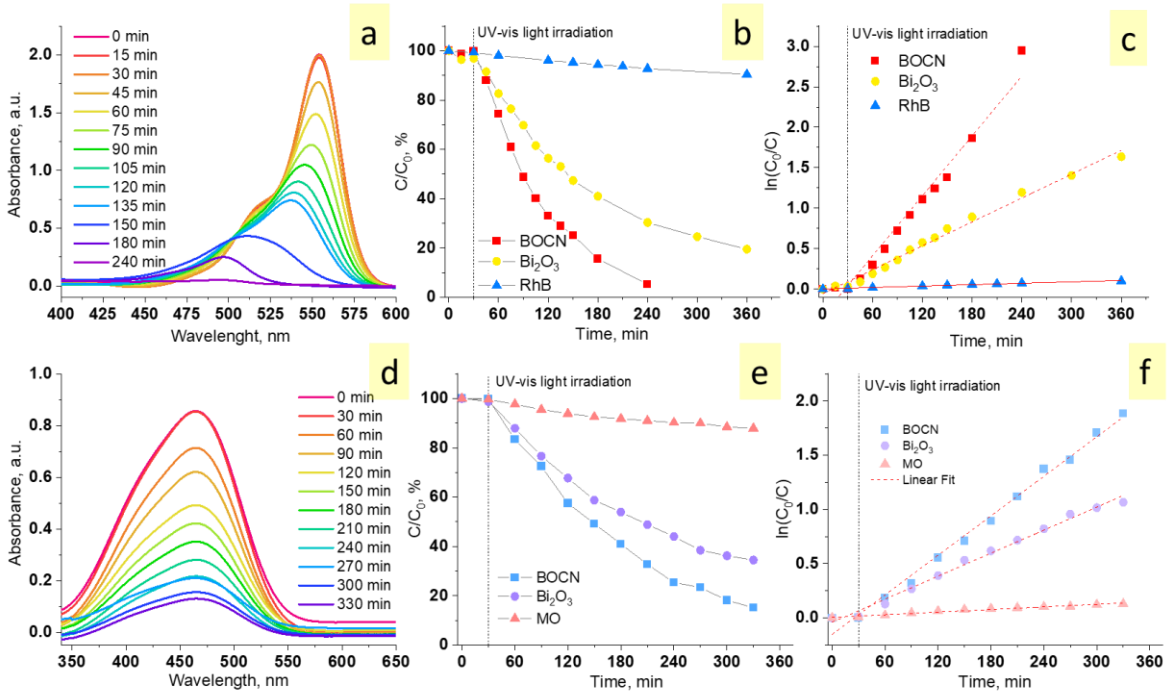

Fig. 4.4: a) Evolution of RhB absorbance as a function of exposure time to Xe lamp in presence of BOCN, b) Photocatalytic degradation of RhB as a function of the irradiation time, without a catalyst, in the presence of BOCN and commercial Bi_2O_3 nanoparticles, c) kinetic curves of the RhB degradation, d) Evolution of MO absorbance as a function of exposure time to Xe lamp in presence of BOCN, e) photodegradation efficiency of MO as a function of the irradiation time without a catalyst, in the presence of BOCN and commercial Bi_2O_3 nanoparticles, f) kinetic curves of the MO degradation

Upon exposure to BOCN, the degradation rates for RhB and MO were strikingly higher, reaching 94.7% and 84.8% respectively after 210 and 300 minutes of irradiation. However, the presence of the larger quantity of Bi_2O_3 catalyst (30 mg vs 14 mg for $Bi_2O_2CO_3$) still led to comparatively lower degradation rates, with only 80% and 65% degradation of RhB and MO respectively, even after a 300-minute irradiation. Moreover, it was observed that the photocatalytic degradation kinetics of RhB and MO followed a quasi-first-order reaction, with the corresponding kinetics expressed as $\ln(C_0 / C) = k \times t$ [Herrmann1997] (**Figs. 4.4c** and **4.4f**). The RhB photodegradation rate of $Bi_2O_2CO_3$ (0.0123 min^{-1}) was found to be higher than that of commercial Bi_2O_3 (0.0049 min^{-1}) by a factor of 2.5, and for MO, it was higher by a factor of 1.7. Those results indicates that the photocatalytic efficiency of $Bi_2O_2CO_3$ significantly outperforms that of Bi_2O_3 in degrading the RhB and MO dyes within the present conditions.

Yao *et al.* [Yao2004] demonstrated that the increase in BET areas (from 7.56 to 27.2 $m^2\ g^{-1}$) leads to a corresponding enhancement in the photocatalytic properties. Simultaneously, the presence of meso/macropores and the formation of an internal electric field between the $Bi_2O_2^{2+}$

layers and the CO_3^{2-} slabs in $Bi_2O_2CO_3$ facilitate the efficient transfer of photoinduced carriers, accelerating their reaction with organic pollutant molecules and reducing recombination.

For instance, Zheng *et al*. conducted the first study on the photocatalytic activity of $Bi_2O_2CO_3$ nanostructures and found that samples with exposed {001} planes exhibited the best photocatalytic performance due to numerous oxygen defects supplied by the distorted Bi–O polyhedron [Zheng2010]. If the presence of oxygen vacancies can extend the light absorption range, enhance charge separation, and improve the efficiency of charge transfer processes, it is not obvious in the case of the present material that this mechanism applies. In our case, {001} planes are also exposed. Yu *et al*. [Yu2018] could only illustrate the role of oxygen vacancies by creating them on purpose from $Bi_2O_2CO_3$ nanosheets with the assistance of glyoxal as reductant.

In the present experiments, if the overall efficiencies of the dye's degradation by the two photocatalysts are reassessed by taking into account their respective surface areas (see Estimation in **Supplementary Material S4.6**), it turns out that both Bi_2O_3 as $Bi_2O_2CO_3$ exhibit similar efficiencies.

Indeed, if we assume that efficiencies are the same, the ratios of the surface areas of the two materials would be 2.3 for experiments with RhB and 1.9 for experiments with MO. A simple estimate of this ratio for the two materials given in **Supplementary Material S4.6** lies roughly in the range from 1 to 5, which is compatible with the assumption made here of similar efficiencies for both materials.

When compared to other results, the present data obtained with $Bi_2O_2CO_3$ nanosheets are almost the same as those presented by Jia *et al*. [Jia2022] (**Table 4.1**). The only difference in the experimental parameters lies in the mean thickness of their nanosheets compared to ours: 20-50 nm versus 5-10 nm here. This comparison reinforces the idea that dye degradation is mainly controlled by volume processes (generation of electron-hole pairs) than by surface processes. Even though enhanced charge separation is known to be active in thin 2D nanomaterials, which can facilitate the separation of photogenerated electron-hole pairs more efficiently due to shorter diffusion distances, it does not seem to be efficient for the ultrathin nanosheets synthesized by the discharge-in-liquid process.

$Bi_2O_2CO_3$ morphology	Dimensions	S_{BET} m^2/g	Catalyst concentration	RhB concentration	Irradiation time	RhB Degradation efficiency	Refs
3D peony flower-like	1-5 µm	33-37	30 mg/100 mL	10 mg/L	180 min	92-96%	Jia2022
2D nanoplate	70-100 nm	10	100 mg/100 mL	20 mg/L	100 min	40%	Liu2010
	< 20 nm	32				97%	
3D Flower-like {001}	2 µm	20.43	80 mg/100mL	10^{-5} mol/L	40 min	~100%	Zheng2010
3D Sponge-like spheres	6–8 µm	50.60			50 min	92%	
Plate-like	500-800 nm	4.30			50 min	70%	
Nanoplate {001}	100-800 nm	10.6	50 mg/100mL	-	30 min	95%	Huang2015
Microspheric 3D {013}	1 µm	14.5		-	30 min	58%	
Thin 2D BOCN {001}	< 10 nm		35 mg/100mL	10 mg/L	210 min	97%	This work*

Table 4.1: Comparison of RhB photocatalytic degradation efficiency of $Bi_2O_2CO_3$ photocatalysts of different morphologies

4.2.3.d Possible photocatalytic mechanism

To identify the active species involved in the photocatalytic degradation of RhB over $Bi_2O_2CO_3$, trapping experiments were conducted by adding suitable radical scavengers (**Fig. 4.5a**). The principal contributors to the generation of active species are undoubtedly superoxide radicals ($\bullet O_2^-$) and holes (h^+), as also demonstrated by Tian *et al.* [Tian2014], and these radicals may consequently influence the degradation of organic pollutants. In the trapping experiments, p-BQ and EDTA were used as scavengers for holes and superoxide radicals, respectively. **Fig. 4.5b** illustrates that the removal efficiency of RhB decreased from 89.7% to 30.2% in the presence of EDTA. The addition of p-BQ also reduced the RhB removal efficiency to 45.4%. Additionally, TBA and DMSO were utilized as capture agents for hydroxyl radicals ($\bullet OH$) and electrons (e^-), respectively. As shown in **Fig. 4.5b**, the presence of the TBA scavenger only resulted in a minor loss of 3.9% in RhB degradation efficiency, whereas the DMSO scavenger led to a loss of 9.1% in RhB removal efficiency.

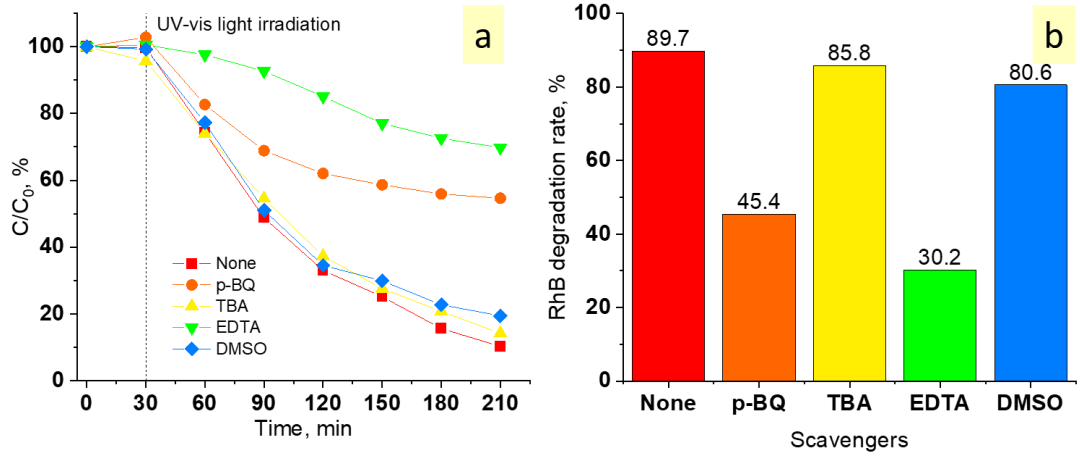

Fig. 4.5: Effects of radical scavengers on a) the RhB degradation using the $Bi_2O_2CO_3$ photocatalyst under UV-Vis light irradiation, b) conversion after 180 minutes of light exposure.

These findings demonstrate that the presence of superoxide radicals and holes in the system significantly impacted the photocatalytic degradation of RhB. On the other hand, hydroxyl radicals and electrons contributed the least to the RhB degradation, which is in good agreement with previous studies [Tian2014, Zhang2019b].

In **Fig. 4.6**, the Mott Schottky plot for $Bi_2O_2CO_3$ material is shown. The positive slope of the $1/C_{SC}^2(V)$ plot indicates n-type semiconductor behavior, *i.e.* electrons are the majority carriers. This observation aligns with previous studies [Ma2021, Huang2015]. The flatband potential was estimated using the Mott-Schottky equation [Gelderman2007]:

$$\frac{1}{C_{SC}^{\ 2}} = \frac{2}{e\varepsilon_r\varepsilon_0 A^2 N_d}\left(V - V_{fb} - \frac{k_B T}{e}\right) \qquad \text{(Eq4.3)}$$

where:

- C_{SC} is the capacitance of the space charge layer,
- e is the elementary charge (1.602×10^{-19} C),
- ε_r is the relative permittivity of the semiconductor material,
- ε_o is the vacuum permittivity (8.854×10^{-12} F/m),
- N_d is the free carrier density,
- V is the applied voltage with respect to the reference electrode,
- V_{fb} is the flat-band potential, representing the voltage at which the semiconductor is in equilibrium with the electrolyte and the net charge at the interface is zero,
- k_B is Boltzmann's constant,
- T is absolute temperature,
- A is surface area.

Therefore, the flatband potential can be obtained by extrapolating the linear portion of the MS curve to V axis.

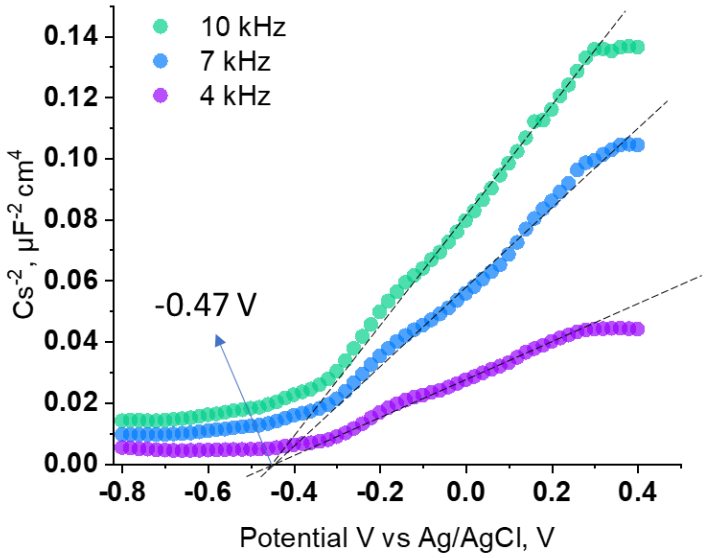

Fig. 4.6: Mott Schottky plots for BOCN at different frequencies.

The flat band potential of BOCN, calculated from the tangential intercept of the Mott Schottky diagram, is determined to be –0.47 V versus Ag/AgCl electrode (similar to Wu *et al.*'s data [Wu2023]). This potential is equivalent –0.27 V versus the normal hydrogen electrode (NHE), using Nernst equation: ($V_{NHE} = V_{Ag/AgCl} + V^{o}_{Ag/AgCl}$, where $V^{o}_{Ag/AgCl}$ = 0.1976 V). Usually, the flat band potential (quasi Fermi level) is slightly lower (~ 0.1 V) than the conduction band (CB) edge for n-type semiconductors [Liu2019, Man2020]. Therefore, the CB minimum of BOCN is –0.37 V vs NHE. Considering a band gap of 3.51 eV, the potential of the valence band (VB) edge can be estimated to be 3.14 V vs NHE. As a result, the energy band structure diagram of BOCN is proposed (**Fig. 4.7**). Due to its wide band gap of 3.51 eV, $Bi_2O_2CO_3$ cannot be effectively excited by visible light, leading to poor photocatalytic activity in the visible light range [Fan2019, Guo2018, Sun2017, Zerjav2018, Zheng2019].

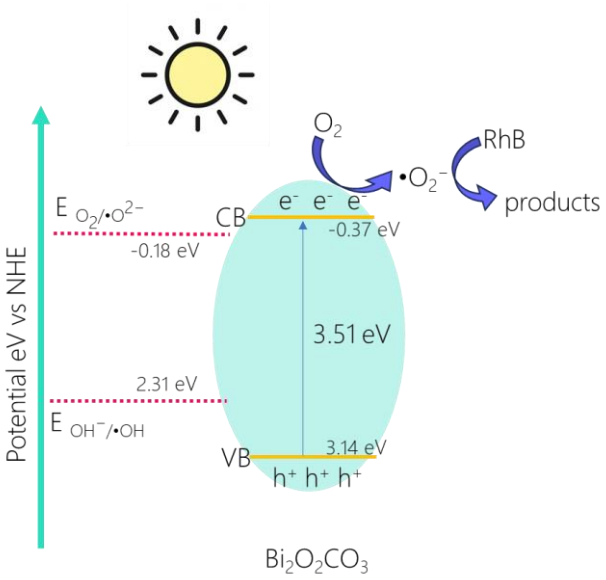

Fig. 4.7: Schematic band structure of BOCN

Based on the experimental findings that superoxide radicals ($•O_2^-$) and holes (h^+) are the main species responsible for the degradation of Rhodamine B (RhB) using $Bi_2O_2CO_3$ as a photocatalyst under Xe lamp irradiation, the following photocatalytic degradation mechanism can be proposed: $Bi_2O_2CO_3$ absorbs photons with energy equal to or greater than its band gap (3.51 eV), enabling it to absorb UV light ($\lambda < 360$ nm) and a portion of visible light (360 nm $< \lambda <$ 800 nm). Upon light absorption, $Bi_2O_2CO_3$ generates electron-hole pairs. Photons with sufficient energy promote electrons from the valence band to the conduction band, creating holes in the valence band. The photogenerated electrons (e^-) and holes (h^+) then undergo separation due to the internal electric field present in $Bi_2O_2CO_3$. The electrons are involved in reduction reactions, while the holes participate in oxidation reactions. Due to the CB of BOCN –0.37 V *vs* NHE) being more negative than that of $O_2/•O_2^-$ (-0.18 V *vs* NHE)[Koppenol2010], the photoexcited electrons

in the CB of BOCN can trap the O_2 adsorbed on the catalyst surface and reduce it to $\bullet O_2^-$. These superoxide radicals are highly reactive and play a crucial role in the degradation of Rhodamine B (RhB). Rhodamine B molecules in the solution can adsorb onto the surface of $Bi_2O_2CO_3$ through electrostatic interactions or other surface forces. The superoxide radicals ($\bullet O_2^-$) and holes (h^+) then react with the adsorbed RhB molecules, initiating oxidation and fragmentation reactions. During this process, superoxide radicals significantly contribute to the degradation, while the holes play a role in the oxidation of RhB. The degradation process continues until the RhB molecules are fully mineralized, resulting in discoloration (**Supplementary Material S4.5**) and the formation of smaller organic compounds, water, carbon dioxide, and other byproducts [Wang2014].

The VB potential of BOCN (3.14 V *vs* NHE) surpasses that of $\bullet OH/H_2O$ (2.31 V *vs* NHE) [Koppenol2010], theoretically enabling the generation of •OH radicals. However, as depicted in **Fig. 4.4**, their role appears to be negligible, if not nonexistent.

The identification of superoxide radicals and holes as the main species responsible for the degradation of Rhodamine B (RhB) suggests a mechanism in which the superoxide radicals initiate the oxidation reactions, while the holes contribute to the overall oxidation and degradation of RhB molecules.

Interestingly, surface structure-dependent oxygen activation abilities with UV light was shown [Zha02013]. The (001) face of BiOCl favors reducing O_2 to ($\bullet O_2^-$) via one-electron transfer pathway, but the (010) face prefers forming O_2^{2-} through two-electron transfer pathway, which is jointly controlled by facet exposure and in-situ induced OVs of the (001) and (010) plans under UV light [Tian2022, Zha02013].

The major reaction steps during the photocatalytic process in our experiment may be described by the following equations:

$$Bi_2O_2CO_3 + h\nu \rightarrow Bi_2O_2CO_3\,(e^-) + Bi_2O_2CO_3\,(h^+) \quad \text{(R4a)}$$

$$Bi_2O_2CO_3\,(e^-) + O_2 \rightarrow \bullet O_2^- \quad \text{(R4b)}$$

$$\bullet O_2^- + \text{RhB} \rightarrow \text{Degraded products} \quad \text{(R4c)}$$

$$h^+ + \text{RhB} \rightarrow \text{Degraded products} \quad \text{(R4d)}$$

As illustrated in **Fig. 4.7**, BOCN can be excited to generate photogenerated electron-hole pairs when exposed to UV-vis light irradiation.

4.2.3.f Stability

The reusability and the stability of a photocatalyst is crucial for evaluating its practical application potential. To assess this, three consecutive cycles were performed, and the results are presented in **Fig. 4.8**. After each cycle, the photocatalyst was recovered by centrifugation and reused without any treatment. The photocatalysis experiment was repeated with a Rhodamine B (RhB) concentration of 10 mg L^{-1} using the recycled catalyst. It can be observed that the $Bi_2O_2CO_3$ photocatalyst maintained a high photocatalytic activity even after the third cycle. No distinct deactivation was observed, as there was only a 10.5% reduction in the RhB degradation rate after the last cycle. A slight loss of the used catalyst was inevitable during the recovery process, which might be one of the reasons for the reduction in photocatalysis activity. However, these results clearly indicate that the $Bi_2O_2CO_3$ photocatalyst possesses good stability and reusability.

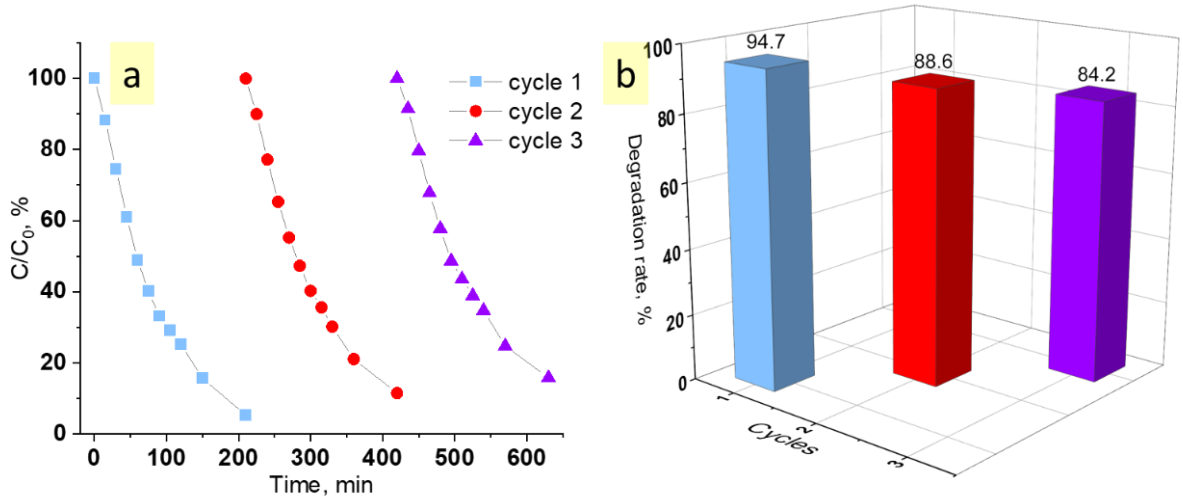

Fig. 4.8: a) Recyclability study of BOCN under UV-vis irradiation in RhB, b) conversion after 210 minutes of exposure for three cycles

4.2 Conclusion

Few-layer $Bi_2O_2CO_3$ nanosheets were successfully fabricated using a facile EDDL method followed by exposure to ambient conditions. To the best of our knowledge, this is the first report of BOCNs with thicknesses under 10 nm, produced by this method.

When compared to commercially available Bi_2O_3 nanoparticles, $Bi_2O_2CO_3$ exhibited comparable activity in the photocatalytic degradation of Rhodamine B (RhB) under UV-Vis light irradiation. We were unable to demonstrate any additional activity that could be attributed to the specific orientation of the exposed planes of our BOCNs. In comparison to other studies, the surface reactivity of the BOC nanosheets is shown to be independent of their thickness.

The stress induced by the carbonation of nanosheets appears to play a very limited role in catalytic activity, primarily because we have not observed a significant shift in XRD peaks that would indicate a high level of stress within the BOCN.

This observation is further supported by EIS measurements, which revealed remarkably similar arc radii for both Bi_2O_3 and $Bi_2O_2CO_3$, indicating similar migration and transfer efficiencies of charge carriers for both materials. This finding underscores the minimal influence of oxygen vacancies in the process. Consequently, it can be inferred that the extended tail observed in the DRS analysis is not a result of oxygen vacancies but is more likely attributed to the increase in energy of charged carriers generated by incident photons. This increase in energy is a consequence of quantum confinement effects within the nanoparticles present in the solution, providing a more comprehensive explanation for this phenomenon.

Trapping experiments confirmed that both holes and superoxide radicals were major contributors to the degradation of RhB, while hydroxyl radicals showed negligible contribution to RhB decomposition. Then, a plausible degradation pathway of RhB was proposed.

Additionally, these $Bi_2O_2CO_3$ nanosheets exhibited good reusability after three cycles, indicating their considerable potential for further applications in environmental decontamination.

General conclusion and perspectives

The synthesis of $Bi_2O_2CO_3$ nanosheets was achieved through nanosecond-pulsed discharges in both water and liquid nitrogen. To ensure successful synthesis, a low applied overvoltage slightly above the breakdown threshold is required, and the process is significantly enhanced by a suitable chemical etching pre-treatment. The selectivity of the process can be excellent, with nanosheets being the predominant nanoobjects produced without the presence of other types of nanostructures.

Nanosheets grow through localized deposition assisted by ions on the defects created by the chemical etching of the cathode electrode. Planes of combs, primarily found in trenches created by the polishing process but not limited to them, provide the necessary support for nanosheet growth. The nanosheets form flower-like structures that are randomly distributed along the trenches. The sweeping action of the bubble-liquid interface over the cathode surface collects the nanosheets, often leading to their fragmentation, and releases them into the liquid during the collapse of the bubble. This mechanism facilitates the transfer of nanoobjects to the liquid, where they can be subsequently collected.

Aging of electrodes in air after in-liquid discharge treatment makes nanosheets grow on both electrodes but with much slower rates than by discharges in liquids. Nanosheets grow by outward diffusion of bismuth from the electrode core but the way the discharge treatment activates this mechanism is still unclear. It should imply creation of defects on emerging plans in combs on both electrodes.

Through our crystallographic study, we have demonstrated that the synthesis of BOC nanosheets originates from nano-second pulsed discharges in water, followed by oxidation and carbonation in air. This BOC crystallizes in the body centred tetragonal Bravais lattice (a = 3.91 Å and c = 13.77 Å) nm and belongs to the $4/m2/m2m$ holosymmetric point group and to the $I4/mmm$ space group (or $I4/m2/m2/m$ in its full notation).

Based on the group theory (symmetry analysis), the BOC nanosheets exhibit a pinacoid shape, characterized by a pair of parallel planes parallel to (001). This particular shape is unique to the $4/m2/m2/m$ point group and is inherited from the bismuth nanosheets formed in water.

A mechanism, related to the ledge mechanism (kinks and jogs) initially proposed to explain the formation of thin plates in metallic matrix, was showed to be relevant in this work. However, unlike the plane coherency in the ledge mechanism, the plane compactness plays an important role in the development of the bismuth nanosheets in water, before their subsequent oxidation in the liquid and carbonation in air.

To the best of our knowledge, this study is the first instance of synthesizing BOC by the spark discharge, identifying its crystallographic structure, explaining its morphology, and proposing a mechanism for its growth.

Compared to commercially available Bi_2O_3 nanoparticles, $Bi_2O_2CO_3$ demonstrated similar activity in the photocatalytic degradation of Rhodamine B (RhB) under UV-Vis light irradiation. No marked improvement could be observed despite their ultrathin thickness or the specific main orientation of their faces exposed to light.

The stress due to carbonation of nanosheets seem to have very limited role in a catalytic activity mostly because we don't observe a significant shift of XRD peaks that could demonstrate a high level of stress within the BOCN.

As confirmed through EIS measurement, migration and transfer efficiencies of charge carriers were similar for Bi_2O_3 and $Bi_2O_2CO_3$. This, in turn, highlights the limited influence of oxygen vacancies in the process. Consequently, it can be concluded that the extended tail observed in DRS analysis isn't due to oxygen vacancies, but is more likely attributed to the energy increase of charged carriers generated by incident photons. This increase in energy results from quantum confinement effects within the nanoparticles present in the solution, offering a more comprehensive explanation for the phenomenon.

Trapping experiments confirmed that both holes and superoxide radicals were major contributors to the degradation of RhB, while hydroxyl radicals showed negligible contribution to RhB decomposition. A plausible degradation pathway of RhB was proposed. Additionally, these $Bi_2O_2CO_3$ nanosheets exhibited good reusability after three cycles, indicating their considerable potential for further applications in environmental decontamination.

Concerning **the perspectives** of the present study, creating new ultrathin nanosheets made of other metals, and eventually of alloys could lead to new properties. In a recent study, a nanosecond-pulsed spark discharge was employed between two lead electrodes immersed in liquid nitrogen, resulting in the synthesis of hexagonal lead nanosheets. These nanosheets exhibited the following characteristics: a point group of *6/mmm*, a space group of *P6/mmm*, a

hexagonal prism morphology, and growth through a ledge mechanism, as previously reported by Kabbara *et al.* in 2019 [Kabbara2019]. Similarly, bismuth was utilized in the synthesis process, yielding pinacoid structures with crystallographic characteristics belonging to point groups $4/mmm$ and $I4/mmm$, employing the same ledge mechanism. Building upon the insights gained from these two studies and their underlying similarities, there is potential to expand the range of applications and explore new properties. Instead of employing a single metal, the possibility arises to utilize a binary alloy, such as Pb-Bi, or even consider the use of a High Entropy Alloy (HEA). Some attempts was done in this direction yielding to interesting results with possibility to obtain mixed Bi-Pb nanosheets with rounded morphology (**Fig. 5.1**).

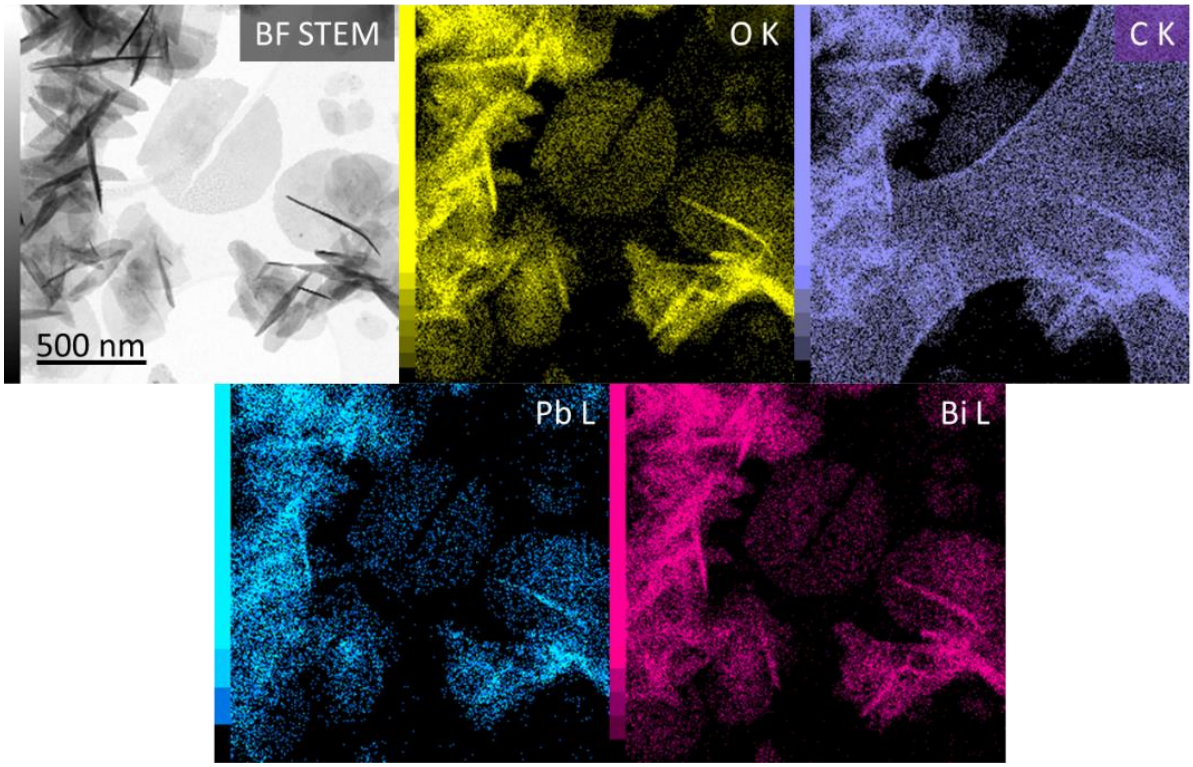

Fig. 5.1: BF STEM image of $Bi_2O_2CO_3$ nanosheet and elemental mapping measurements showing the distribution profiles of Bi (magenta), Pb (cyan), O (yellow), and C (purple) elements.

This dissertation study does not provide a clear explanation for why certain materials with low melting points like bismuth or lead (**Fig. 5.2**), such as tin (melting point = 505 K), or indium (melting point = 430 K), do not yield nanosheets, as depicted in. One plausible explanation for the hindered growth of nanosheets in these instances could be the absence of emerging defects. Further investigations are necessary to comprehensively understand these limitations and to broaden the scope of nanosheet synthesis to encompass a broader range of metals.

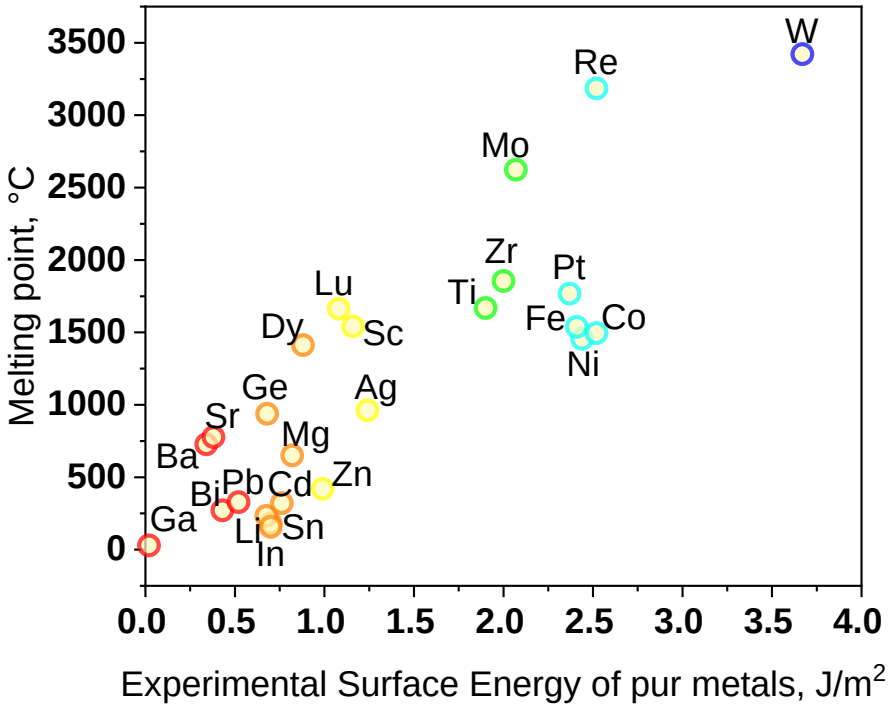

Fig. 5.2: Melting point vs surface energy for varying metals.

In previous studies, former PhD students employed a similar method to synthesize various nanomaterials, such as ZnO, PbO_2, CdO, and others, as detailed in references [Kabbara2018b, Kabbara2019, Trad2019, Trad2020]. Remarkably, each of these materials displayed unique morphologies, with some adopting the shape of nanosheets while others manifesting as spherical nanoparticles. To quantify this variation, we introduced a form factor, computed as the ratio of the length of these nanostructures to their thickness, as illustrated in **Fig. 5.3**.

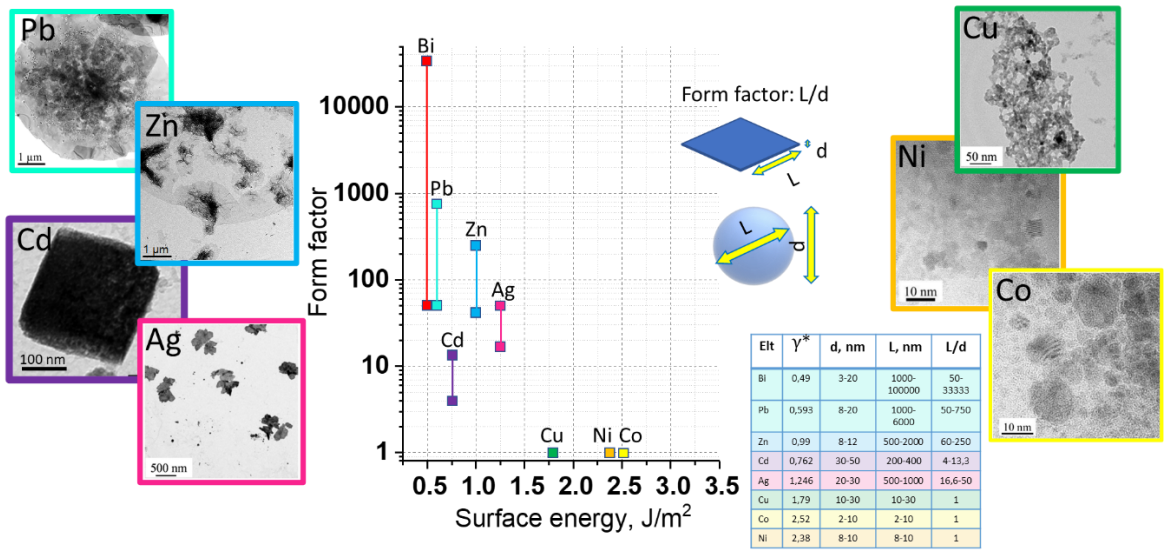

Elt	γ*	d, nm	L, nm	L/d
Bi	0,49	3-20	1000-100000	50-33333
Pb	0,593	8-20	1000-6000	50-750
Zn	0,99	8-12	500-2000	60-250
Cd	0,762	30-50	200-400	4-13,3
Ag	1,246	20-30	500-1000	16,6-50
Cu	1,79	10-30	10-30	1
Co	2,52	2-10	2-10	1
Ni	2,38	8-10	8-10	1

Fig. 5.3: Estimated form factor vs surface energy for various metals : Bi, Pb, Cd, Zn, Ag, Cu, Ni, Co. Insert table: form factor estimation. Insert images of nanoparticles with different morphologies. Surface energy values taken from [Vitos1998].

Upon thorough analysis of this data, an intriguing pattern began to emerge. It became evident that there might be a correlation between the surface energy of these materials and their resulting morphologies. It appears that materials with lower surface energy tend to yield nanostructures with higher form factors. In essence, lower surface energy appears to facilitate the growth of larger surface areas, providing valuable insights into the relationship between surface energy and nanomaterial morphology.

To explore this potential connection, more experiments can be carried out to confirm this observation.

In a recent study (please refer to the **Appendix**), BOC nanosheets were tested for their potential application in electronic devices. The results of these tests revealed that BOC exhibits competitive breakdown field values, approximately ranging between 12-14 MV/cm^2, possesses a bandgap of 3.5-4 eV, and remains stable up to 300°C. To assess the electrical characteristics of BOC, a vertical architecture Metal-Insulator-Metal (MIM) type device was developed. The resulting I-V plots displayed memristive-like behaviour. However, it is challenging to definitively attribute this behaviour solely to the BOC material itself, as some devices without nanosheets exhibited similar behaviour, suggesting that it may be a collective effect of the contacts and the BOC nanosheet. New experiments are now needed to clarify these unexpected results.

Supplementary Materials

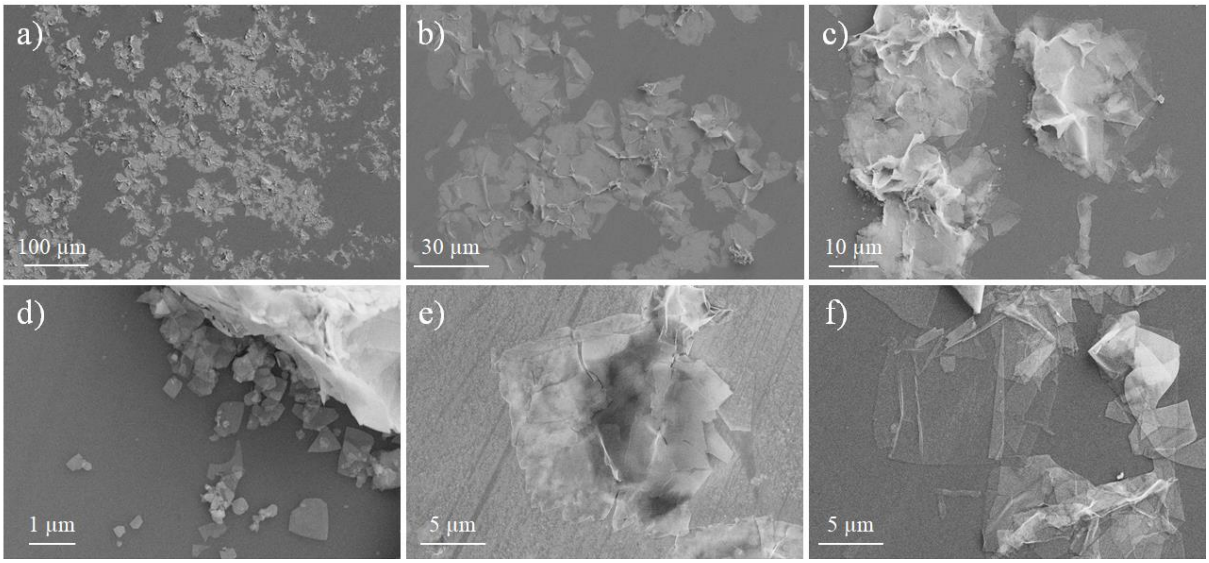

Supplementary Material S2.1: Scanning electron microscope (SEM) micrographs at different magnifications (**a**: x180, **b**:x700, **c**: x1400) of a silicon wafer covered in nanosheets (case of water but similar images are obtained with liquid nitrogen); **d)** small fragments around crumpled nanosheets; **e)** broken thick nanosheets; **f)** ultrathin nanosheets.

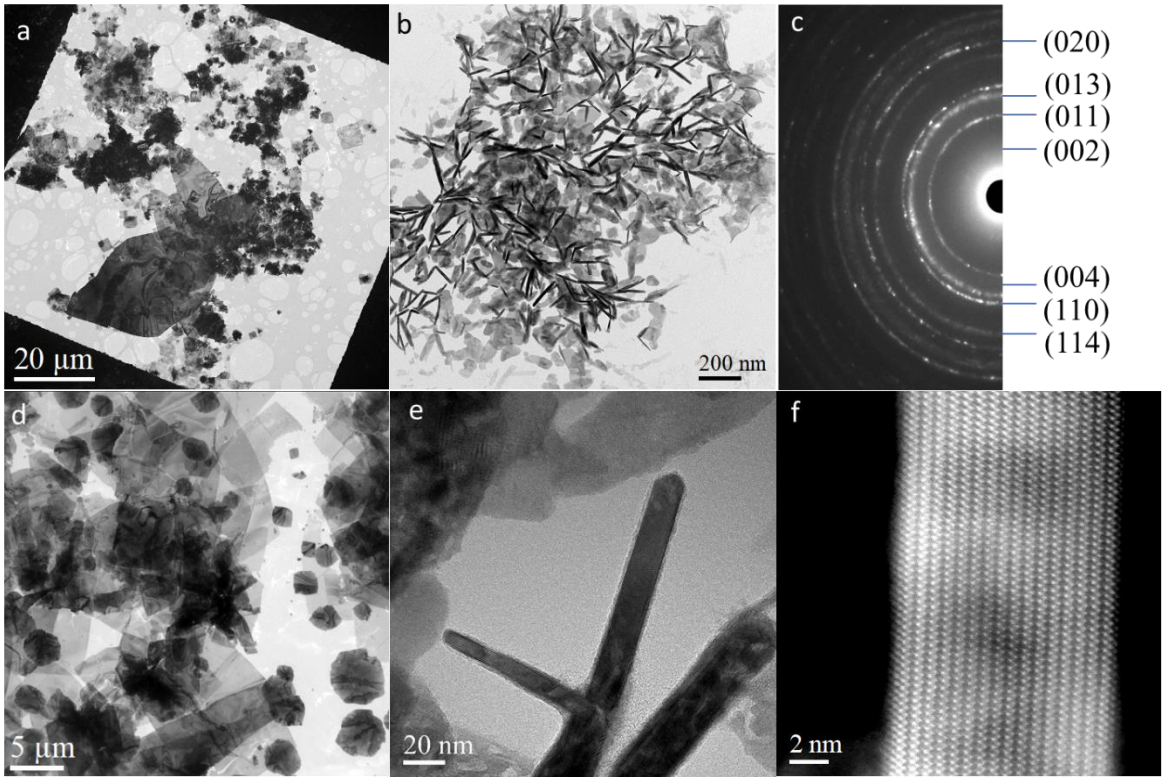

Supplementary Material S2.2: Set of nanosheets as in a) water and d) liquid nitrogen. b) Thin rolled nanosheets. c) Corresponding diffraction pattern and d-spacings corresponding to $Bi_2O_2CO_3$ (JCPDS card 41-1488). e) High magnification of a properly-oriented cross-section of a nanosheet. f) Atomic resolution of the corresponding structure showing the zig-zag structure of $Bi_2O_2CO_3$.

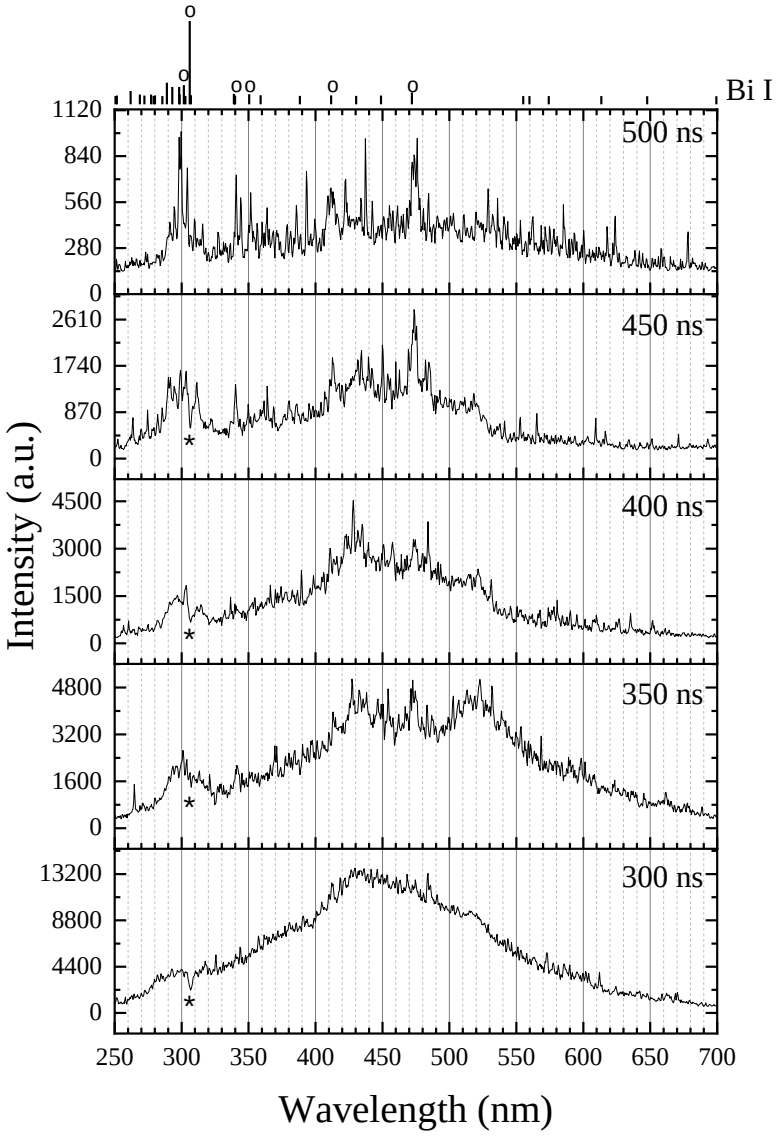

Supplementary Material S2.3: Time-resolved low-resolution optical emission spectra in the visible range of a nanosecond-pulsed discharge in water created between two pin electrodes. Before 300 ns, only continua are observed. Spectra are much noisier than in liquid nitrogen. For this reason, Bi I lines that are identified for certainty are depicted by an "o" above the expected wavelengths of the possible transitions showed by bars on the top of the graph. * show absorbed lines due to absorption of photons emitted by the continuum. Wavelengths of Bi I transitions are taken from NIST [NIST2023].

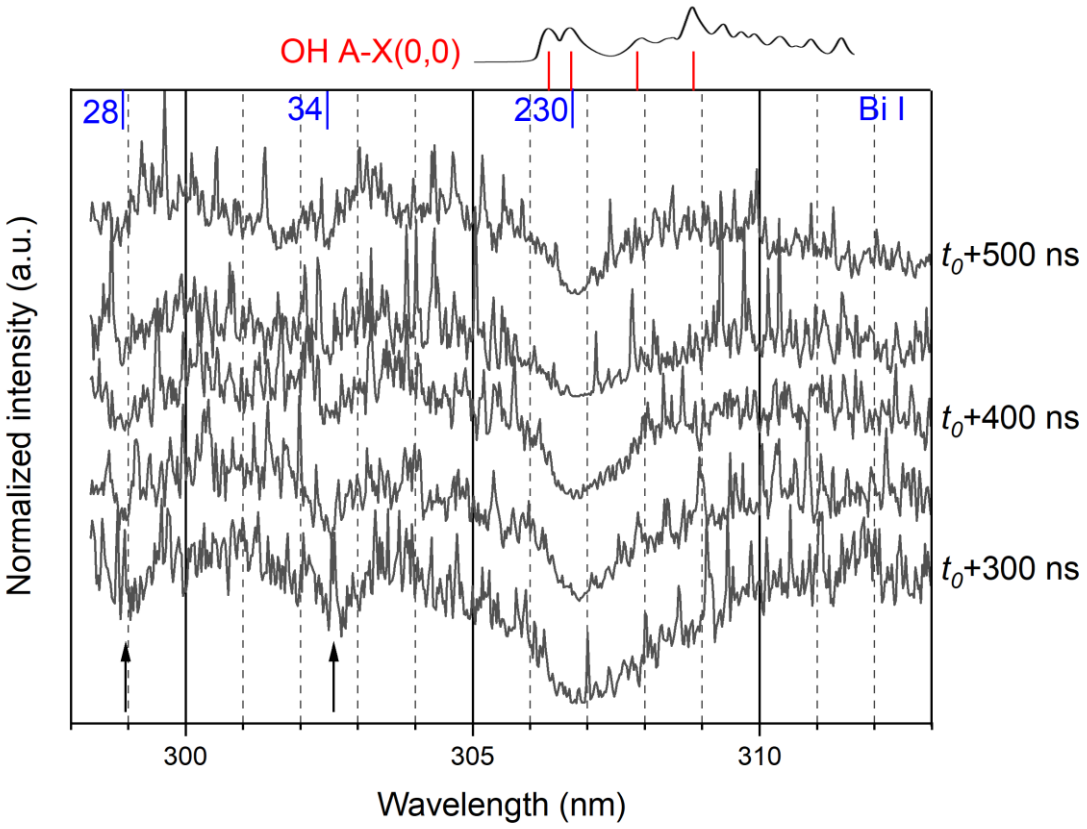

Supplementary Material S2.4: High-resolution optical emission spectrum of a nanosecond-pulsed discharge in water created between two pin-electrodes made of bismuth. Grating: 1800 mm^{-1}. Acquisition time: 50 ns. Same conditions as those given in the text. Holes present in the spectrum at 298.9, 302.6 and 306.8 are attributed to Bi I self-absorption, as explained in [Nominé2021]. 28, 34 and 230 are relative intensities from NIST database (divided by 10^3). OH emission spectrum is presented assuming a temperature of 2000 K, likely to correspond to temperature of the discharge in this period of time. If self-absorption of OH(A-X) lines was effective, other absorption bands should be visible at 307.8 and 308.9 nm. Then, it is possible to conclude that absorption is only due to bismuth and not to OH. Wavelengths of Bi I transitions are taken from NIST [NIST2023].

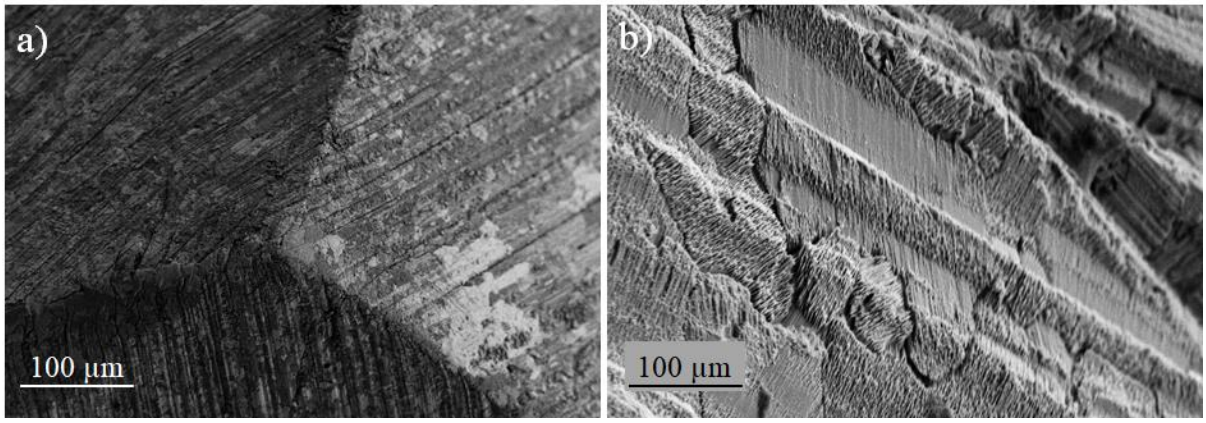

Supplementary Material S2.5: Surface state of one electrode left in the air 6 days after polishing and chemical etching. a) tip of the electrode, b) detail of trenches and combs. No nanosheets were observed.

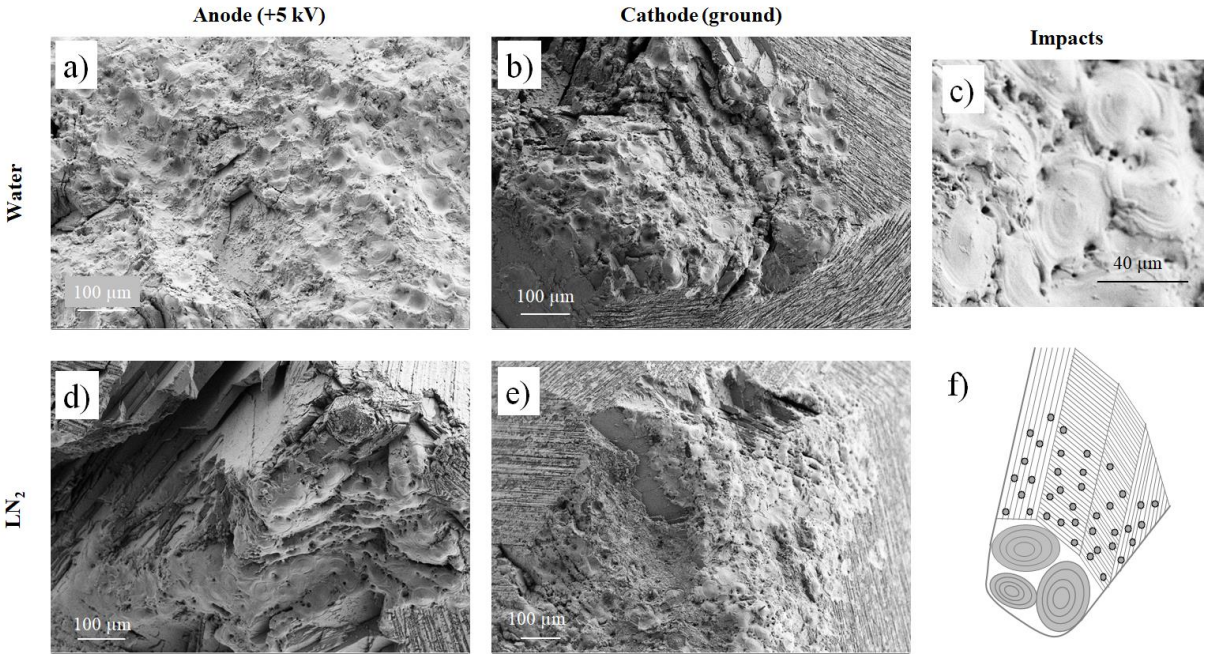

Supplementary Material S2.6: Comparison of the anode and cathode tips after treatment in water (a and b) and in liquid nitrogen (d and e). The transition between the area eroded by discharges and the area etched by the Nital solution is clearly visible in b, d and f. c) Magnification showing some impacts on electrodes. f) Schematic of the electrode state after treatment. Discharge impacts are present on the electrode tip, which is dull. Lateral faces are etched and flowers are found located in the trenches, but only on the cathode.

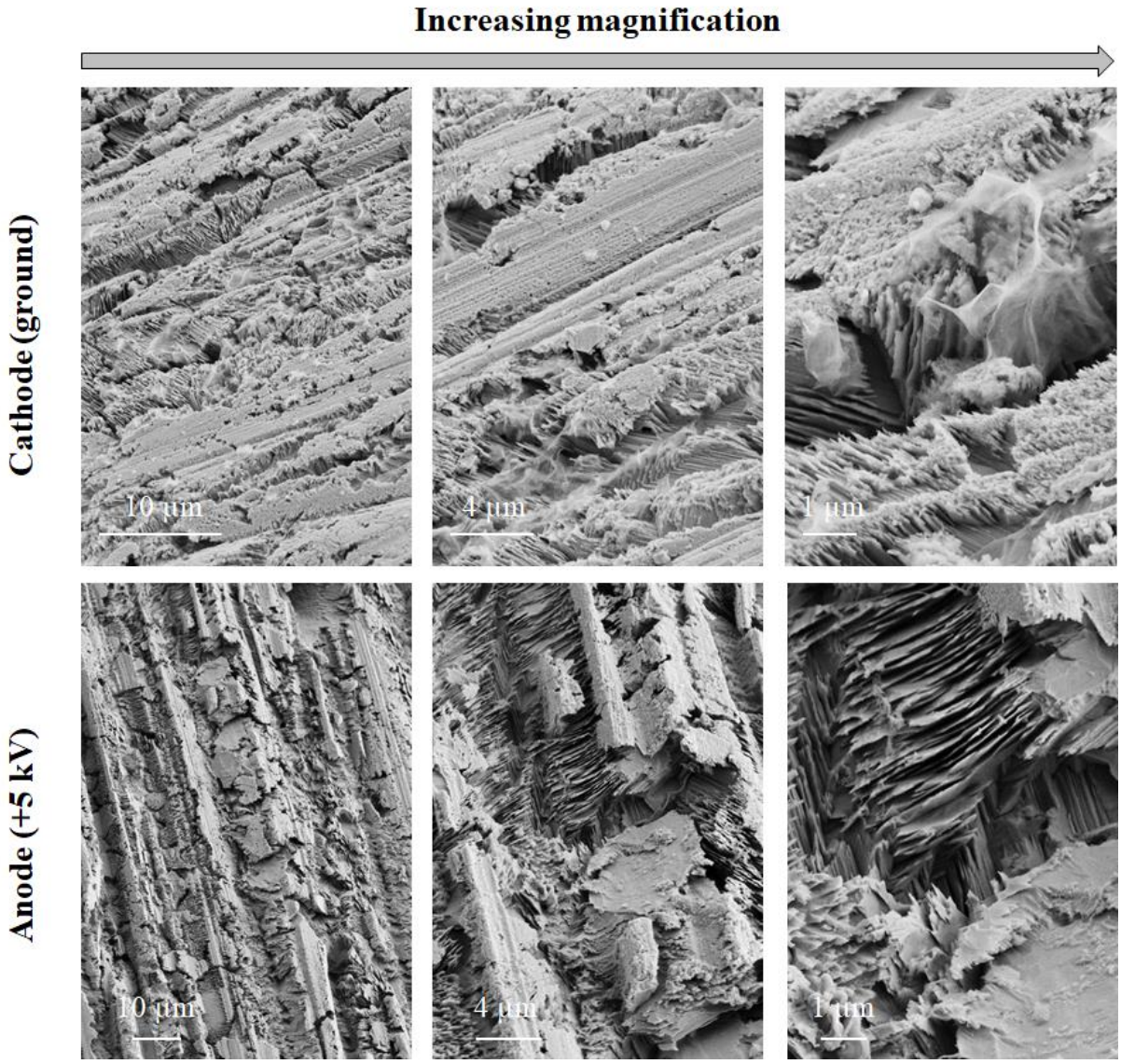

Supplementary Material S2.7: Comparison of the surfaces of anode and cathode after treatment in water. The same features (trenches and combs) are observed. Here again, nanosheets are only observed on the cathode, whichever the liquid.

Supplementary Material S2.8: Set of pictures showing the movement of the generated particles in the liquid between two discharges. The time scale is in second. Particles remain at the bottom of the beaker, settling by gravity.

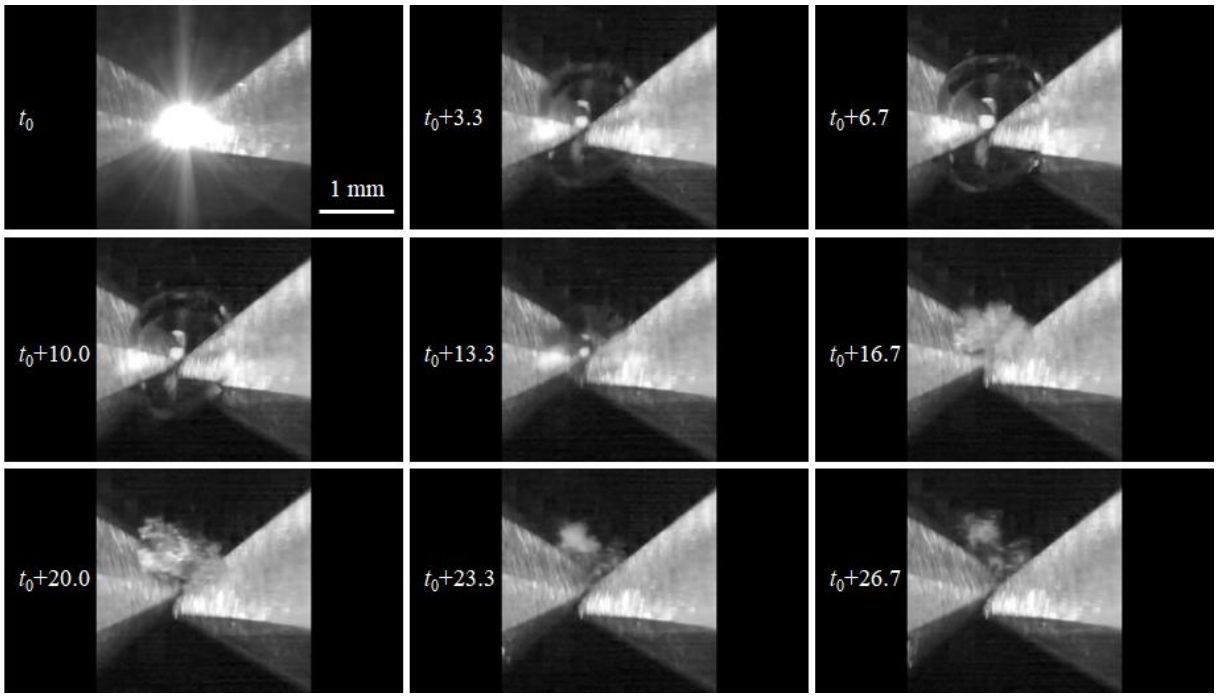

Supplementary Material S2.9: Set of pictures showing the transfer of nanosheets by mechanical sweeping of the surface by the bubble-liquid interface. The time scale is in µs. Discharge conditions are those reported in the experimental part. This event is characterized by the fact that the bubble expands and collapses one time only.

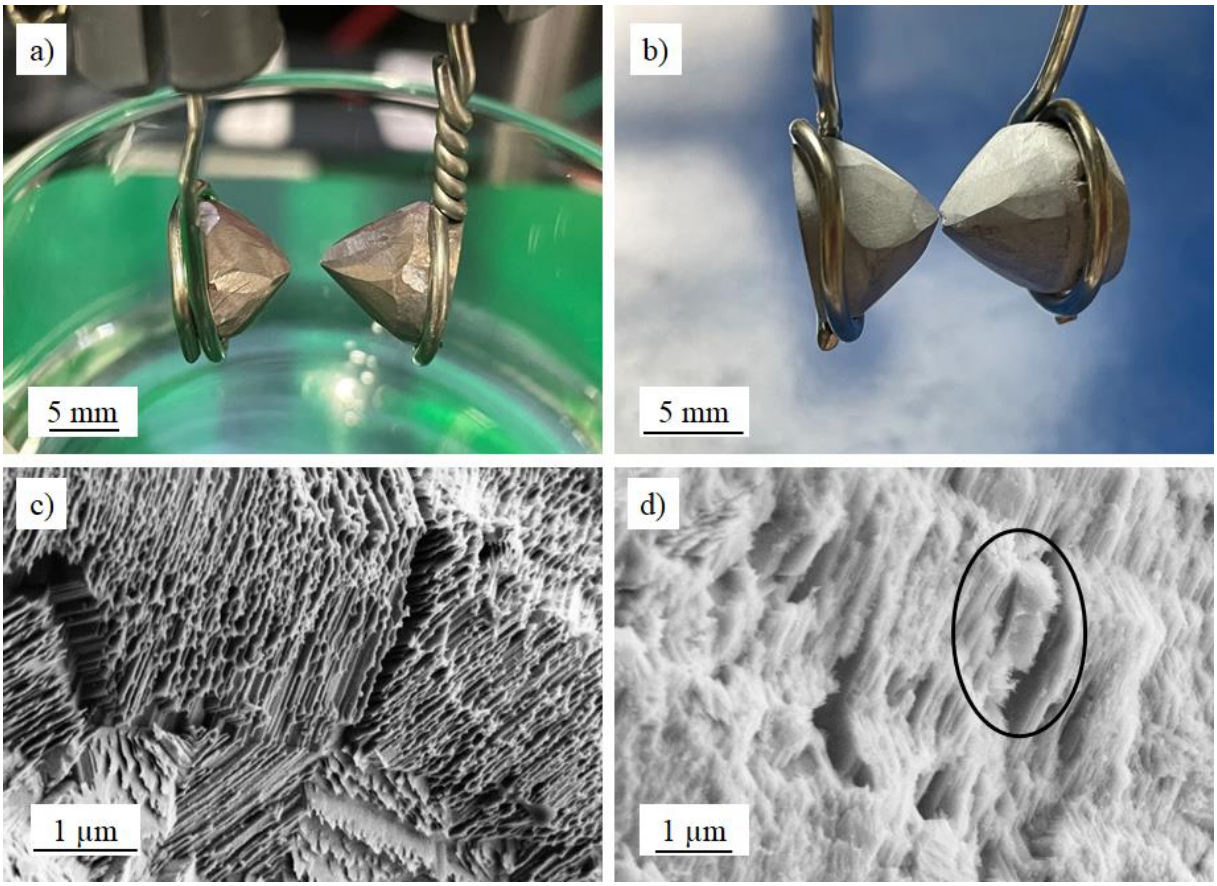

Supplementary Material S2.10: a) Overall view of bismuth electrodes after polishing, chemical etching and air exposure. The metallic aspect of the electrode surface is clear. b) Same as a) but with an additional 1-min plasma activation after chemical etching. The whitish color of both electrodes is patent. c) Comb structure after polishing, chemical etching and air exposure. d) Same as c) but with an additional 1-min plasma activation after chemical etching. The encircled area shows the early stage of nanosheet growth. Note that the entire surface appears fuzzier.

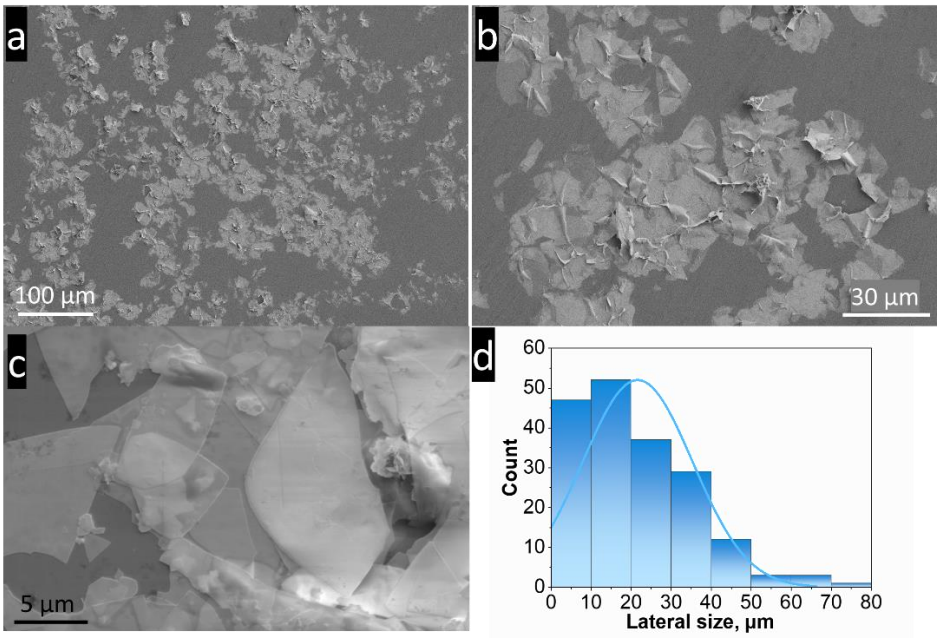

Supplementary Material S3.1: Low-magnification SEM images of a) nanosheets deposited on a Si substrate, b) magnified view of the nanosheets, c) magnified view of a bundle of nanosheets, d) lateral size distribution of synthesized nanosheets

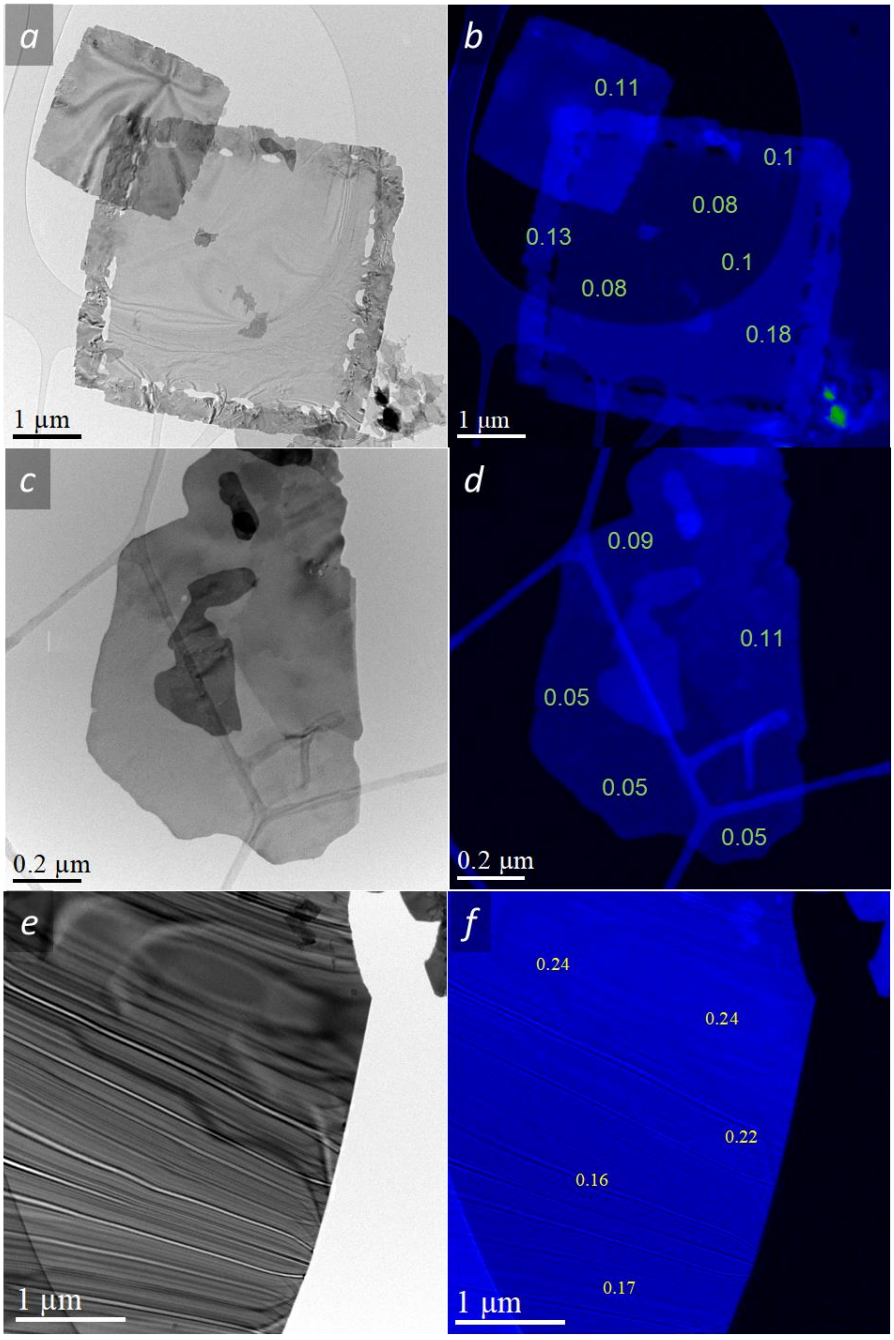

Supplementary Material S3.2: Examples of three nanosheets with different thicknesses: a,c,e) BF STEM micrograph of a BOC nanosheets deposited on a holey carbon TEM grid with b,d,f) corresponding EELS thickness mappings. Figs. 4a and 4c: examples of the thinnest nanosheets. Fig. 4e: example of the thickest nanosheet. These mappings indicate the values of the t / λ ratio needed for thickness estimation.

Crystal system ⟹		*Tetragonal*						
Crystal forms (11)	# Faces	Point groups						
		4	**$\bar{4}$**	**$4/m$**	**422**	**$4mm$**	**$\bar{4}2m$**	**$4/mmm$**
1. Pedion	**1**	$001, 00\bar{1}$				$001, 00\bar{1}$		
2. Pinacoid	**2**		001	001	001		001	001
3. Tetragonal prism	**4**	$hk0$	$hk0$	$hk0$	$100, 110$	$100, 110$	$100, 110$	$100, 110$
4. Ditetragonal Prism	**8**				$hk0$	$hk0$	$hk0$	$hk0$
5. Tetragonal pyramid	**4**	$\boldsymbol{hkl}$				$h0l, hhl$		
6. Tetragonal disphenoid	**4**		$\boldsymbol{hkl}$				$hhl, h\bar{h}l$	
7. Tetragonal bipyramid	**8**			$\boldsymbol{hkl}$	$h0l, hhl$		$h0l$	$h0l, hhl$
8. Tetragonal trapezohedron	**8**				$\boldsymbol{hkl}$			
9. Ditetragonal pyramid	**8**					$\boldsymbol{hkl}$		
10. Tetragonal scalonohedron	**8**						$\boldsymbol{hkl}$	
11. Ditetragonal bipyramid	**16**							$\boldsymbol{hkl}$
Class ⟹		**Tetragonal pyramidal**	**Tetragonal disphenoidal**	**Tetragonal dipyramidal**	**Tetragonal trapezohedral**	**Ditetragonl pyramidall**	**Tetragonal scalenohedral**	**Ditetragonal dipyramidal**

Supplementary Material S3.3: Crystal forms for the Tetragonal System dictated by the corresponding point Groups

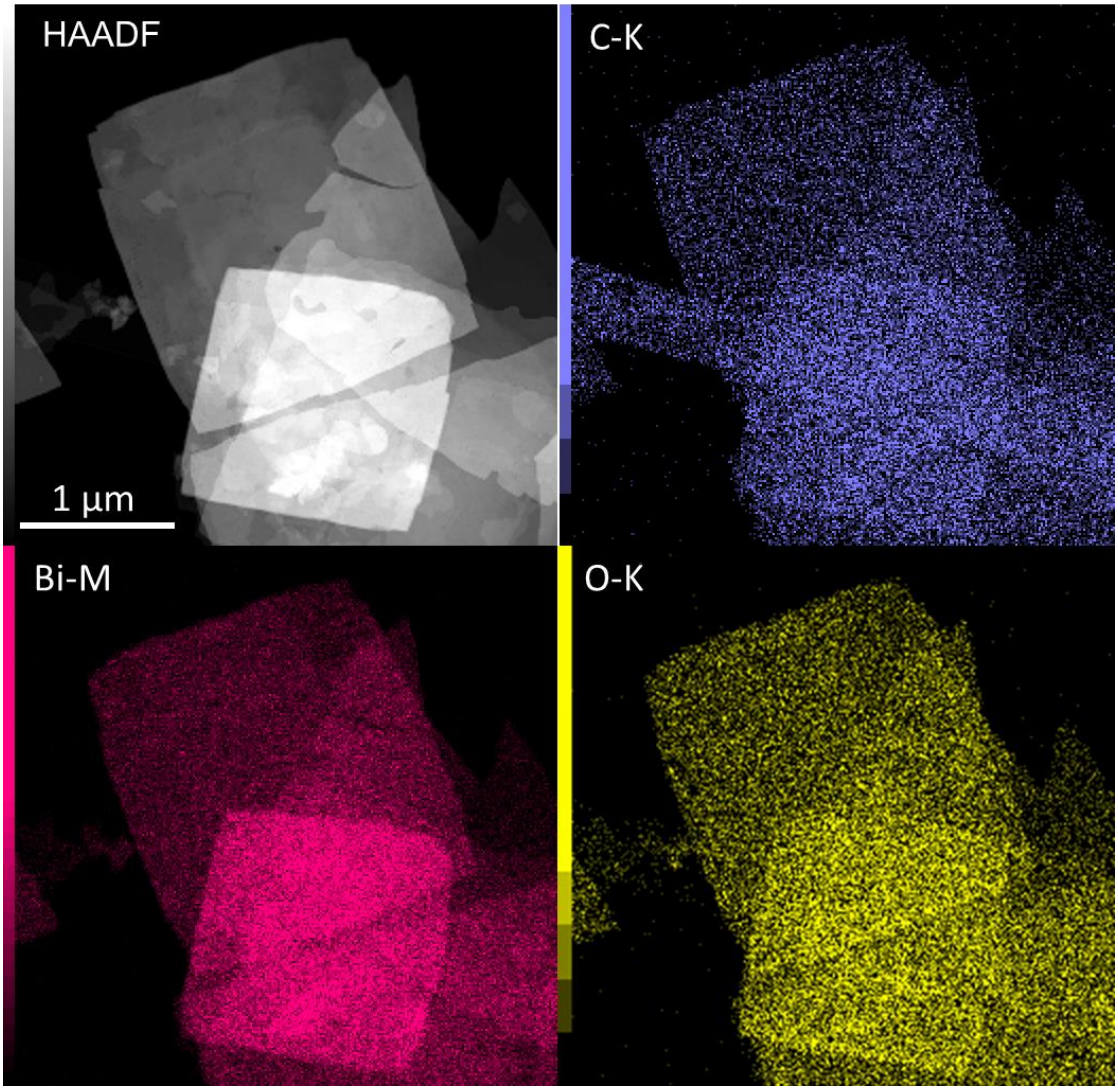

Supplementary Material S3.4: The STEM HAADF micrograph of a $Bi_2O_2CO_3$ nanosheet and corresponding EDS elemental mapping of C, Bi and O respectively

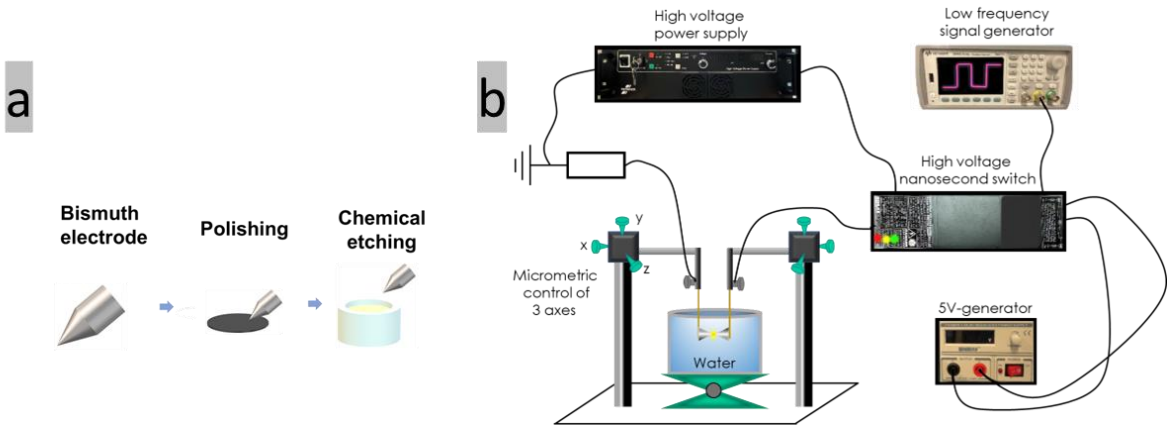

Supplementary Material S4.1: a) Pre-treatment of the electrodes leading to the cone-shaped pin etched in Nital 5%, b) Schematic representation of the experimental setup.

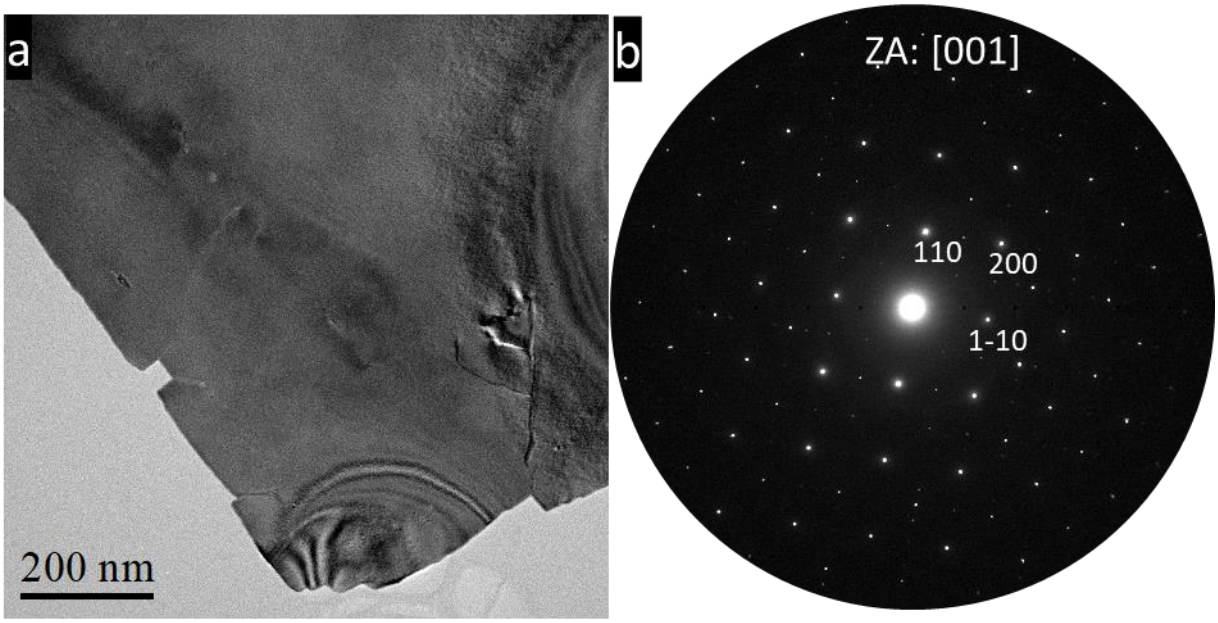

Supplementary Material S4.2: a) BF TEM micrograph of $Bi_2O_2CO_3$ nanosheet with b) corresponding SAED pattern indexed as tetragonal phase $Bi_2O_2CO_3$ PDF file 41-1488 in [001] zone axis

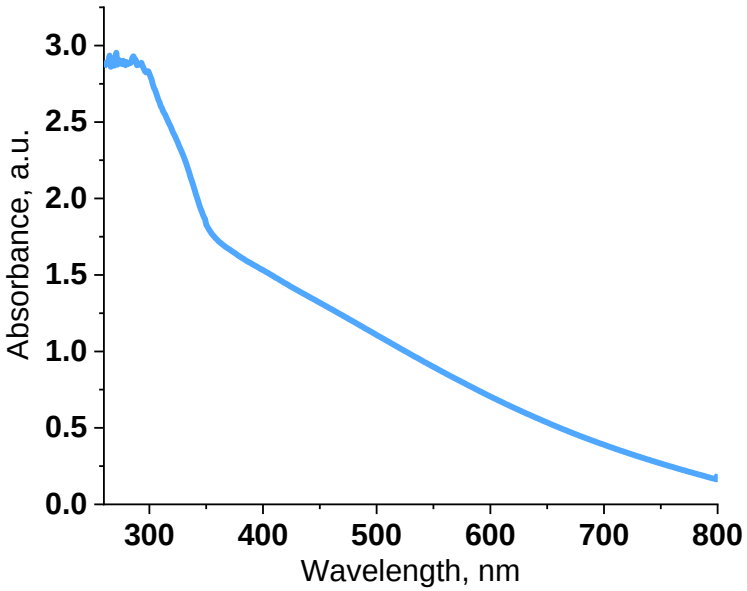

Supplementary Material S4.3: UV–Vis diffuse reflectance spectra (DRS) of $Bi_2O_2CO_3$. The absorption peak is located at 360 nm, with a long tail extending beyond 800 nm. This tail is attributed to the scattering of nanoparticles present in the solution.

a

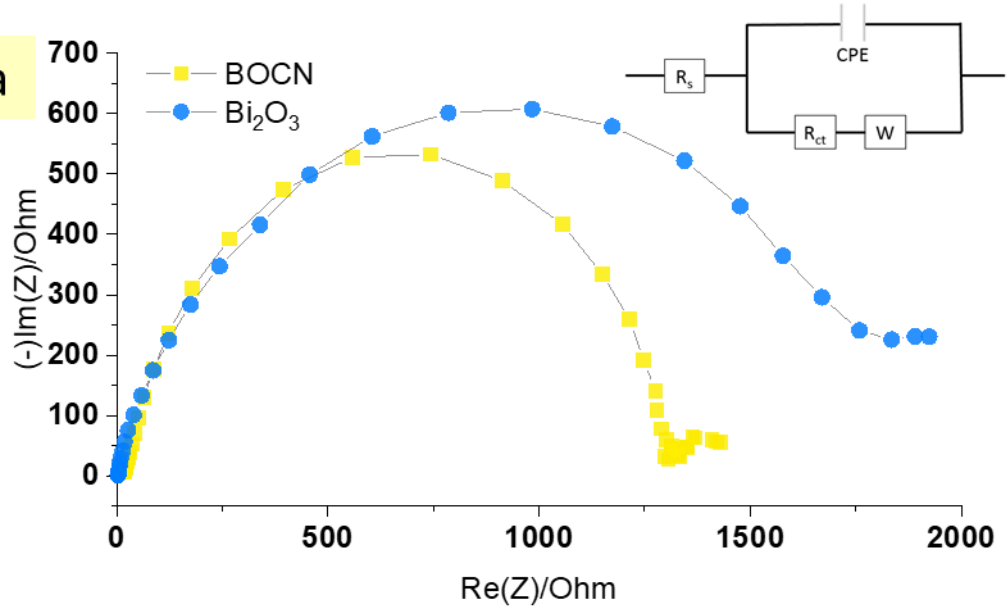

b

Sample	Rs (Ω)	Q ($F.s^{-1}$)	n	Rct (Ω)	σ ($Ω.s^{-1/2}$)
BOCN	23.59	$8.8*10^{-7}$	0.8735	1296	37.44
Bi_2O_3	23.94	$36.04*10^{-6}$	0.748	1857.7	22.41

Supplementary Material S4.4: a) Nyquist plots for $Bi_2O_2CO_3$ and Bi_2O_3 under open-circuit potential at a steady state in dark, insert : the Randles equivalent circuit used for fitting impedance spectra where *Rs* is the electrolyte resistance, *Rct* the charge transfer resistance, *W* the Warburg impedance and *CPE* the constant phase element; b) Table with Impedance parameters obtained after fitting the EIS curves with the Randles equivalent model, where *n* is the exponent of the constant phase element *Q* and σ is the Warburg coefficient.

Supplementary Material S4.5: Evolution of RhB solution after exposure duration of 0, 30, 60, 90, 120, 150, 180 and 210 min respectively

SUPPLEMENTARY MATERIAL S4.6

Estimation of the specific surface area of the BOC nanosheets (SSA_{2D}) in unit of $m^2\,g^{-1}$:

$$SSA_{2D} = \frac{S_{total}}{m_{total}}.$$

Denoting *w* and *t* as the width and thickness of a single nanosheet with surface S_{1NS}, one reads:

$S_{total} = S_{1NS} \times N \approx 2\,wt \times N$,

If we neglect the lateral surface areas of the nanosheets. Their number is simply:

$$N = \frac{m_{total}}{m_{1NS}}$$

with $m_{1NS} = V_{1NS}{}^* \rho_{1NS}$. Finally:

$$SSA_{2D} = \frac{2}{t \times \rho_{\mathrm{BOC}}}$$

In average, thicknesses of $Bi_2O_2CO_3$ nanosheets lie in range 5-10 nm and we choose $\rho_{BOC} = 8.27 \times 10^6\ g/m^3$ for BOC to get data given in **Table 1**. This value is deduced from the crystallographic assessment of the unit cell of BOC (see chapter 3). With 54 sites/unit cell and 0.0782 atoms/Å^3, the density is 8.27 g/cm^3.

Similarly, estimation of the specific surface area of the Bi_2O_3 commercial nanoparticles (SSA_{3D}) with radius *R* reads:

$$SSA_{3D} = \frac{3}{R \times \rho_{\mathrm{Bi_2O_3}}}$$

For the Bi_2O_3 commercial nanoparticles with sizes varying 40 and 100 nm in radius, we choose $\rho_{\mathrm{Bi_2O_3}} = 8.9 \times 10^6\ g/m^3$.

In experiments, the following quantities were used: 14 mg of $Bi_2O_2CO_3$ and 30 mg Bi_2O_3 (see Experimental section 2.5 Photocatalytic Experiments)

t	5 nm	10 nm	20 nm
SSA_{2D} ($Bi_2O_2CO_3$)	48.4 m² / g	24.2 m² / g	12.1 m² / g
$SSA_{2D} \times M(Bi_2O_2CO_3)$	0.678 m²	**0.339** m²	0.169 m²
R	50 nm	65 nm	80 nm
SSA_{3D} (Bi_2O_3)	6.7 m² / g	5.2 m² / g	4.2 m² / g
$SSA_{3D} \times M(Bi_2O_3)$	0.201 m²	**0.156** m²	0.126 m²

Table 1: Estimates of surface specific areas of BOC nanosheets and Bi_2O_3 nanoparticles.

If we select SSA_{2D} and SSA_{3D} values appearing in **Table 1**, one gets roughly:

$$1 \lesssim \frac{SSA_{2D} \times M(Bi_2O_2CO_3)}{SSA_{3D} \times M(Bi_2O_3)} \lesssim 5$$

with $SSA_{2D} = 2.2 \times SSA_{3D}$ for values in bold.

Appendix

$Bi_2O_2CO_3$ for nanoelectronics

A1 Introduction & objectives

Recently, BOC has garnered significant attention in the realm of electronic devices, as evidenced by studies such as [Zhang2021a], [Karaka2023], and [Chen2023]. The layered structure of bismuth oxycarbonate ($Bi_2O_2CO_3$) renders it not only suitable for photocatalysis but also for applications in supercapacitors, as indicated by research like [Wang2017], and sensors, as demonstrated in studies such as [Umar2016]. This versatility arises from its expansive active surface area and its unique semiconductor properties.

However, to the best of our knowledge, no prior studies have explored the potential of BOC in electronic devices. In order to assess the performance of our material and its viability for application in nanoelectronics, we conducted a comprehensive analysis. This included measurements of the breakdown field, evaluation of the band gap, assessment of operational temperature ranges, fabrication of devices with a vertical Metal-BOCN-Metal configuration, and subsequent measurements of their I-V characteristics.

With the same experimental setup as that described in chapter 2, we got the following results.

A2 Results

A2.1 Dielectric breakdown field

The nanoscale electrical properties of 2D materials play a significant role in the performance and/or mechanism of related microscopic or macroscopic electronic devices [Giannazz02019]. The operating electric fields of dielectric capacitors depend on their intended applications. Dielectric materials can undergo changes, when exposed to high electric fields above which their electrical resistance is drastically reduced. The maximum electric field strength that a material can withstand before experiencing electrical breakdown, which often results in an insulator-to-conductor transition or dielectric breakdown, is referred to as the “breakdown field”. This is also known as the dielectric breakdown strength ($\mathbf{E_{BD}}$).

The dielectric breakdown field ($\mathbf{E_{BD}}$) of a dielectric capacitor depends on factors, including the material's bandgap and permittivity. Additionally, it is influenced by various parameters, including the phase structure, grain size, defect chemistry, sample thickness, microstructural uniformity, and porosity of the dielectric material, as well as the configuration of

electrodes, and the operational conditions (voltage, frequency, temperature, pressure, and aging time), and environmental factors (radiation and humidity) [Palneedi2018]. In this context, the production of high-quality dielectric materials with dense microstructures holds significance in achieving enhanced capacitance sustainability under high electric fields, thereby increasing the EBD.

Conductive atomic force microscope (C-AFM) is a useful tool with high spatial resolution for investigating the electrical properties of 2D materials at the nanoscale, as highlighted in [Hui2019]. Following the transfer of 2D $Bi_2O_2CO_3$ nanosheets onto a conductive Si substrate coated by sputtered gold, C-AFM was used to study their breakdown characteristics. The C-AFM setup utilizes the Au substrate is one electrodes, with the AFM cantilever serving as the other to apply an electric field to the $Bi_2O_2CO_3$ samples.

Prior to C-AFM measurements, AFM scanning was performed to image the microscopic morphology and measure the thickness of one selected $Bi_2O_2CO_3$ flake (**Fig. A1b**).

Afterwards, four precise positions on the flake, as marked by yellow circles in **Fig. A1b**, were chosen and cyclic triangular wave electric field with different amplitudes was applied in the vertical direction by the C-AFM tip. **Fig. A1a** shows C-AFM signal as function of applied breakdown field for 4 zones depicted in **Fig. A1b**. It is evident that a more favorable breakdown field characteristic is achieved in the single-layer zone. Conversely, when the nanosheet is folded (forming double or triple layers) or exhibits defects, the breakdown field values gradually decrease.

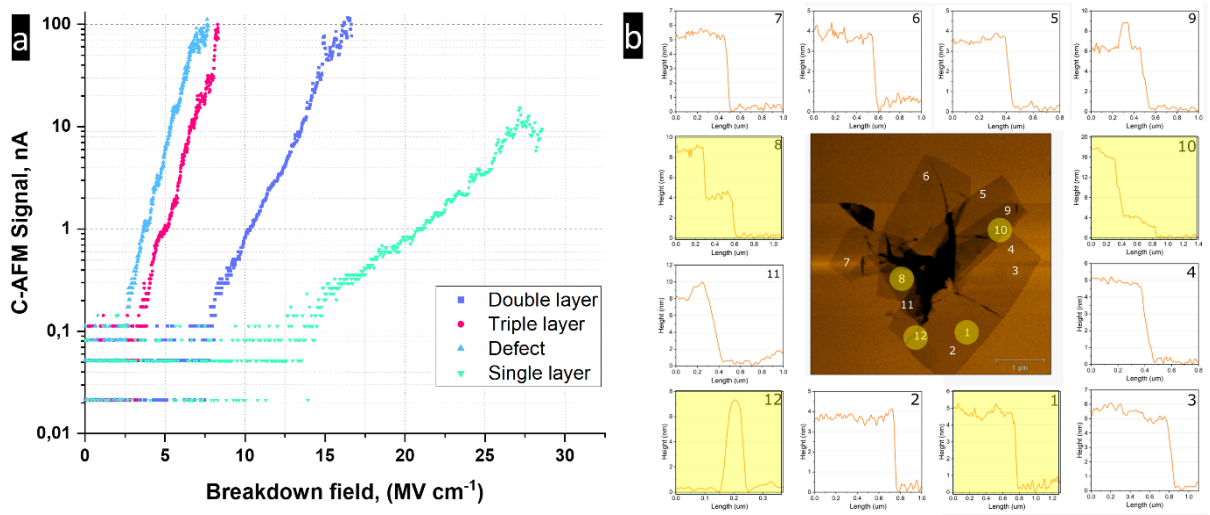

Fig. A1: a) C-AFM signal vs. breakdown field measured in four different zones corresponding to the 1st, 8th, 10th and 12th scans as shown in b) AFM scan of BOCN, with marked positions where height profiles are conducted; Scans 1 to 12: corresponding height profiles.

A2.2 Energy band gap

Energy band gap measurements were performed by valence EELS. The results are given in **Fig. A2a**.

Using the linear-fit method described for instance in [Park2009], we consistently measure a bandgap energy of 4 eV, clear spectroscopic evidence that our synthesized BOCN is a wide bandgap electrical insulator.

By this method, the band gap energy can be estimated from the intersection of a straight line originating from the background level with a linear fit to the onset of the loss signal spectrum.

The band gaps of the BOCN, alumina thin film and SiO_2 were determined to be 4 eV, 8.2 and 8.8 eV respectively. This determination involved performing two linear fits within a band gap energy range, and the cross point was estimated as the band gap, as shown in the bottom of **Fig. A2a**. The Full Width Half Maximum, presented in a **Fig. A2b**, provides information about the precision and resolution of the measurement.

This experimental value is in good agreement with the predicted bandgap energy of 3.51 eV for the BOC, as measured by the photocatalytic method described in previous chapter. To assess the reliability of this method, we also collected EELS spectra for well-known Al_2O_3 and SiO_2, and their experimentally measured band gaps align with the bandgap values found in the literature.

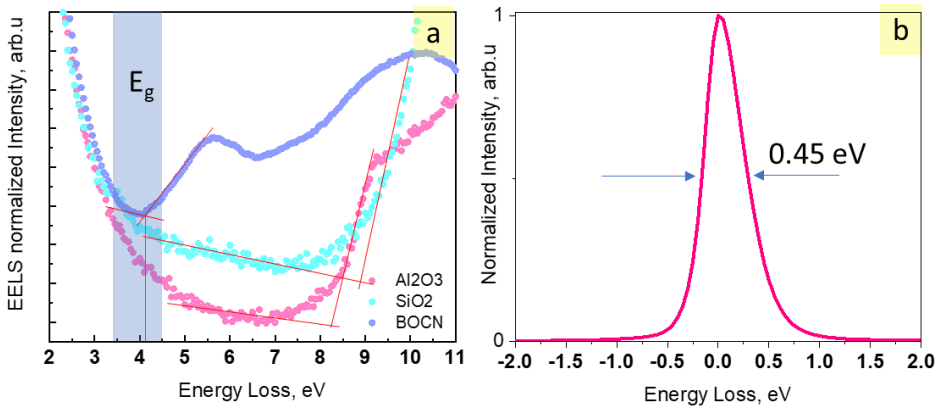

Fig. A2: a) STEM-EELS spectra (valence band excitations) collected with primary electron beam of 200 keV for BOCN, Al_2O_3 and SiO_2 with applied linear-fit method used to calculate a bandgap energy of ~ 4 eV for BOCN, compared to ~ 8 eV for Al_2O_3 and ~ 9 eV for SiO_2. b) Zero loss peak acquired from JEM - ARM 200F Cold FEG. Normalized intensity is shown on a linear scale. The full-widths at half-maximum is 0.45 eV.

An overview of dielectric breakdown properties and bandgap values for various materials with thicknesses under 25 nm is presented in **Fig. A3**. While specific dielectric constant (ε') data for our material is currently unavailable, literature reports suggest a range between 10 [Hao2022]

and 34 [Feng2021, Liu2021]. The determination of the dielectric constant for our BOCN is currently underway.

When considering the dielectric constant (ε') values reported in the literature for BOC, our BOC nanosheets exhibit comparable E_{BD} (electric breakdown field) values to widely used materials such as Al2O3 and HfO2. Moreover, they demonstrate higher effective permittivity and higher breakdown strength values compared to recently reported high-k perovskite SrTiO3 membranes [Huang2022]. However, further measurements are required to confirm these dielectric constant values for BOC nanosheets.

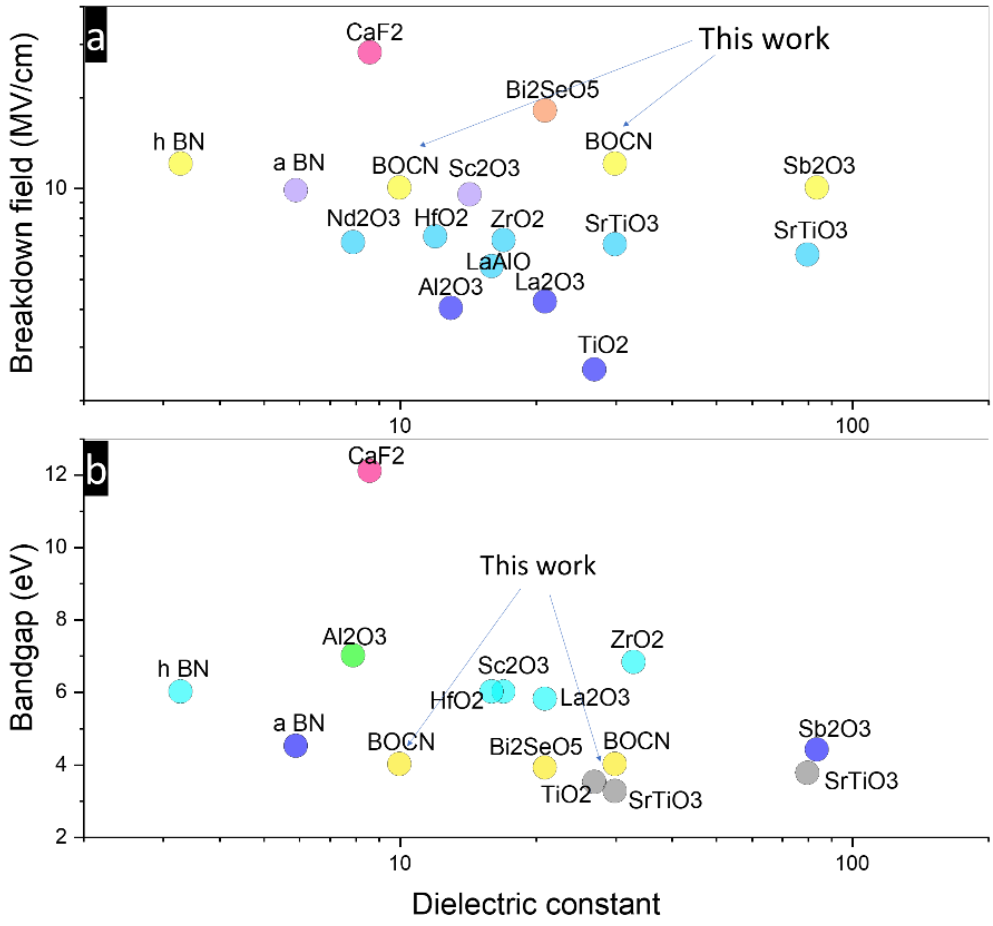

Fig. A3: Overview of dielectric properties and band gap values for various materials under 25 nm.

A2.3 Temperature stability

In situ heating experiments were conducted to ascertain the temperature stability range of Bismuth Oxycarbonate (BOC) nanosheets. The results, as depicted in **Fig. A4** through bright-field transmission electron microscopy (BF TEM) micrographs, unequivocally reveal that nanosheet degradation initiates at 300 °C. Additionally, the SAED pattern at 300°C exhibits the emergence of a diffused ring, possibly indicative of the onset of material amorphization.

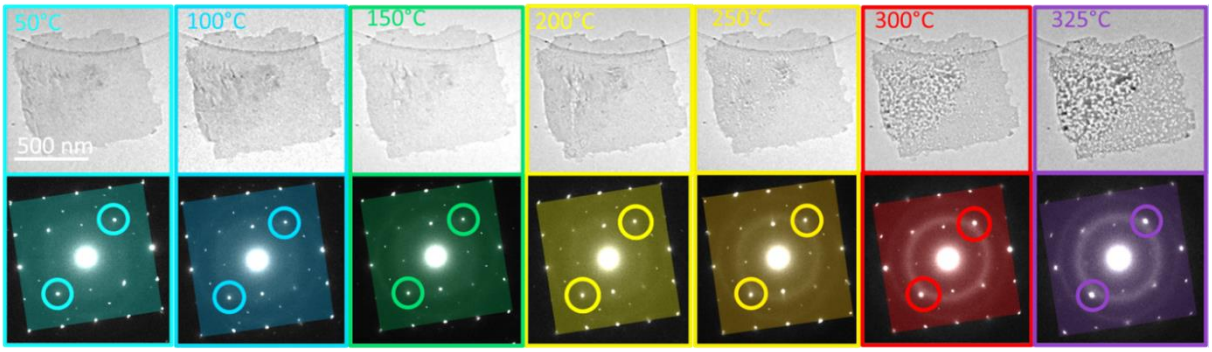

Fig. A4: (Top images) BF TEM micrographs of a random BOC nanosheet recorded during in-situ heating from 50 to 325°C with their corresponding SAED patterns. (Bottom images) one spot selected (in circle) to follow its evolution during heating. There is no major morphological modifications under 300°C.

A3 Electrical characterization of Metal-Insulator-Metal device

An optical image of as-fabricated Metal-Insulator-Metal (MIM) device with a vertical structure, which is used to perform I-V characterizations of the $Bi_2O_2CO_3$ nanosheets, is shown in **Fig. A5a**.

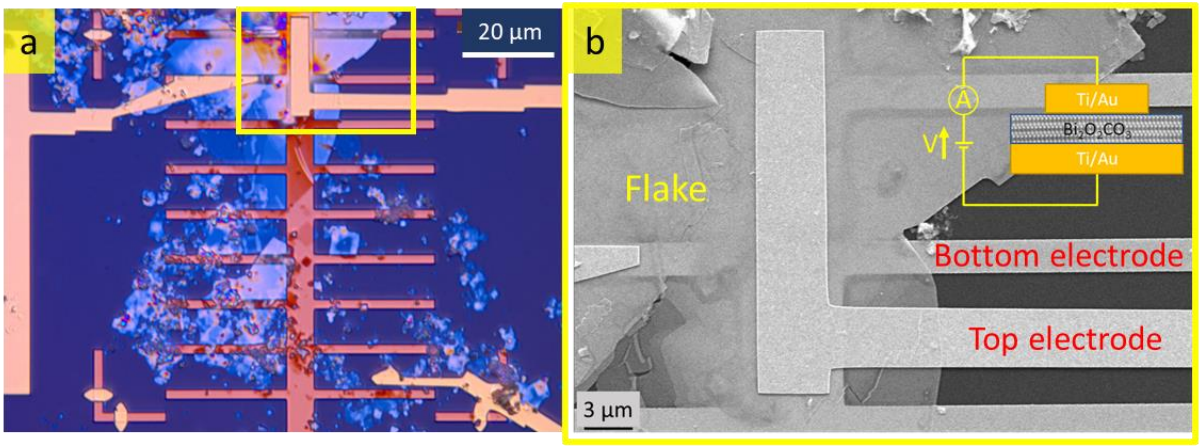

Fig. A5: The device structure. a) Optical image of the BOC based device on a Si/SiO2 wafer, b) SEM micrograph of the yellow area of the device, insert shows the schematic diagram of the MIM type vertical BOC device.

The first step of device fabrication involved employing e-beam lithography to create the bottom electrodes (BE) made of Ti (10 nm)/Au (100 nm) in a rake-like configuration on an SiO_2 (270 nm)/Si wafer substrate. The electrode are deposited by a classical evaporation technique (see part **A5** Device fabrication). The choice of the rake shape was made to increase the likelihood of a flake adequately covering one of the rake branches during the subsequent deposition step in the process. The second step entails depositing the BOC flake onto the substrate with pre-printed bottom electrodes. This is achieved by immersing the substrate in a water solution containing the as-synthesized BOC nanoflakes. After a thorough examination of the deposited flakes with SEM, suitable flakes are selected, and a second Ti (10 nm)/Au (100 nm) layer serving as the top electrode (TE) is deposited by e-beam lithography. **Fig. A5b** provides a close-up SEM image of the region

outlined by the yellow line. **Fig. A5b** provides a close-up SEM image of the region outlined by the yellow line. To assess the performance of the BOC device unit, we conducted various electrical characterizations.

The initial I(V) characterizations were performed on devices that had no prior electrical contacts, are illustrated on **Fig. A6**. Each I(V) measurement involved sweeping the voltage (V) from $+V_{max}$ to $-V_{max}$ and then from $-V_{max}$ to $+V_{max}$ at a constant sweep rate of 0.1 V/s. The results shown in **Fig. A6** represent typical outcomes obtained from our device. However, it is worth noting that the tested devices displayed qualitatively the same behavior but quantitative differences were observed from sample to sample. To account for this variability, we conducted statistical measurements on 30 devices. This variation can be attributed to the fact that we did not have information about the thickness of the contacted flake (which can be measured in future studies).

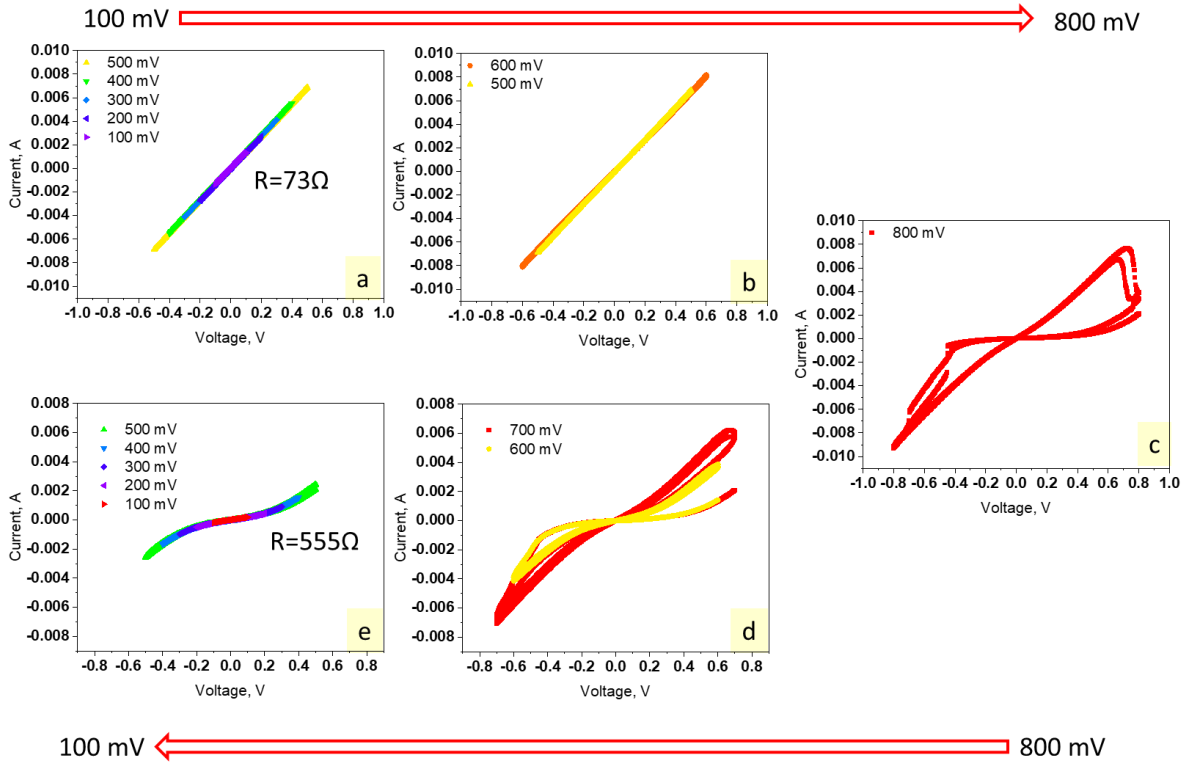

Fig. A6: I-V characteristics of a Ti/Au/BOC/Au/Ti device, demonstrating a) linear behavior from 100 to 500 mV, b) linear behavior with slight deviation at 500-600 mV and c) hysteresis loop at 800 mV, d) hysteric behavior at 700-600 mV, e) non-linear behavior from 500 to 100 mV.

The initial V_{max} was incremented in 100 mV steps, starting from 100 mV without any previously applied voltage, up to 800 mV (as shown in **Fig. A6a-c**). Up to V_{max} of 500 mV, the behavior remained purely linear, indicating ohmic behavior with a resistance of 73 Ohms (**Fig. A6a**). Beginning at V_{max} of 600 mV, a deviation from linear behavior becomes noticeable (**Fig.**

A6b). Beyond 600 mV, the behavior starts to exhibit hysteresis loop (**Fig. A6c**). To assess the reversibility of the system, we conducted the same set of measurements but with a decrease in V_{max} voltage from 800 mV to 100 mV (**Fig. A6c-e**). The hysteric behavior persists at V_{max} 600-700 mV (**Fig. A6d**). Below 600 mV, the behavior transit into a non-hysteric, but semiconducting (or metal/semiconductor interface) type behavior. Extracting the resistance around 0V (slope of I(V) characteristic taken between -50 mV and +50 mV) yields a value of approximately 555 Ohms, indicating that the system does not return to its initial state. This implies that the resistivity of the device around 0 bias can be controlled based on the history of previously applied voltages.

In a second time, we explored the properties of the hysteric I(V) loops at V_{max} voltage. As shown in **Fig. A7**, we conducted two consecutive IV cycles, starting from $+V_{max}$ = 800 mV (point **1** in **Fig. A7a**). From this curve, we can see that the resistance around 0V applied voltage can be adjusted between a low-resistance state (LRS) of 73 Ohms and a high-resistance state (HRS) of 555 Ohms (for that specific device).

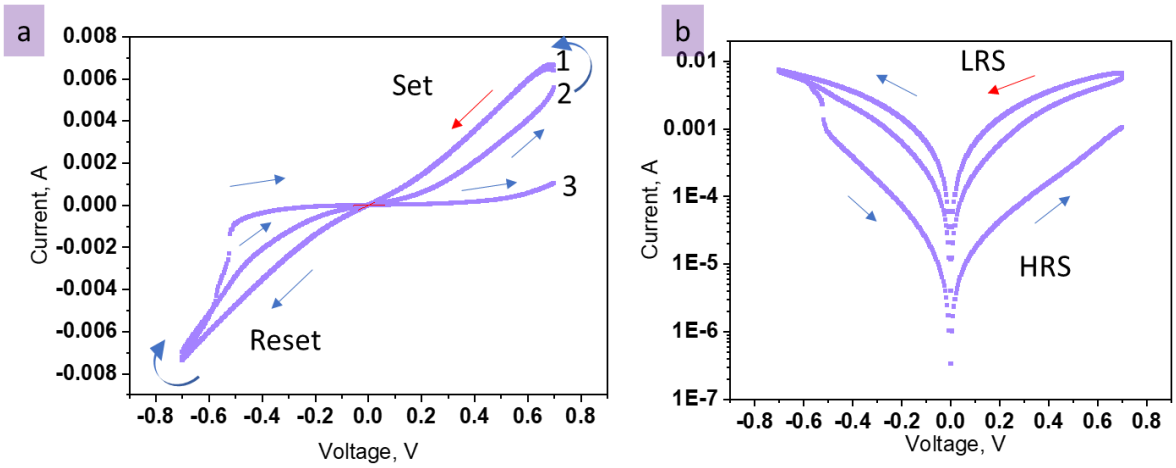

Fig. A7: Characteristic I-V curves of the MIM device based on a BOC material at Vmax 700 mV. a) and b) show the typical I-V curves of the device; the original curves in a) represent a 2 cycle switching process (1st cycle loop depicted 1-2, 2nd cycle loop 2-3) and a log scale curves in b) show obvious low and high resistance states (LRS and HRS).

In **Fig. A7b**, we have presented the same loop, but this time, the y-axis represents the logarithm of the absolute value of the measured current. The shape of the hysteric curve **in Fig. A7b** exhibits two cycles of resistance switching, a phenomenon observed in several 2D systems with vertical geometry [Ge2018, Zhang2019c, Zhu2019] as well. In all of these examples, the authors attribute this behavior to memristive phenomena.

To examine **Fig. A7a** more closely, we can see that in the first loop (depicted **1-2**) a small opening begin to appear and system come back close to initial state (point **2**). During the second loop the measured current follow the same path than in the first loop up to $-V_{max}$ but between

$-V_{max}$ and $+V_{max}$ the device undergo another modification (point **3**) and the system now finish in the point **3** with strong increase of the resistance with respect to point **1** and **2**. This means that the final state at V_{max} strongly depends on the history of the applied voltage, and/or on the time spent close to +800mV, indicating a potential low time scale diffusion process.

To access the timescale at which the state at V=800 mV evolves, we conducted the following measurements: First, we reset the system to -800 mV and held it for 20 minutes. Afterward, we checked the resistance around 0 bias at point A. Then, we applied +800 mV and recorded the resistance evolution at his applied voltage over time. At point B, after 10 minutes at +800 mV, we measured the resistance around 0V again. We repeated the process of going back to +800 mV and measured the resistance 10 minutes later. The measurements including resistance around 0V (**Fig. A8b**) and resistance evolution in time (**Fig. A8a**).

In **Fig. A8a**, we observe a rapid increase in resistance during the first 100 seconds at +800 mV, followed by a slower increase. The resistance measurements around 0V (points A and B) indicate that the resistance has varied from 90 Ohms (LRS) to 787 Ohms (HRS) during the 10 min at +800mV. Between points B and C, the evolution of the resistance in time at +800 mV is slow, and the resistance measurements at 0 bias between B and C remain unchanged, indicating that the system remains in the HRS. This implies that the timescale for transitioning from LRS to HRS in this device is approximately 100 seconds. We conducted these tests multiple times with the opposite voltage polarity and observed a reversed behavior, resetting from HRS to LRS.

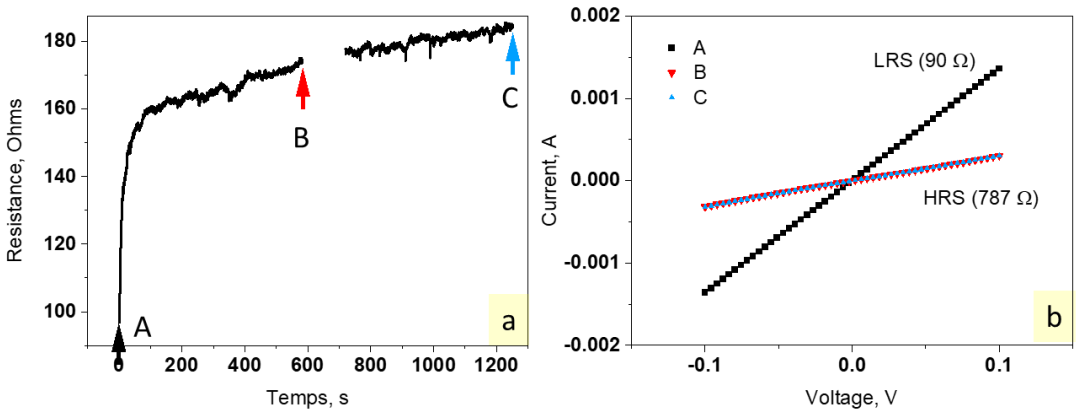

Fig. A8: a) Time evolution of resistance measured with a polarization voltage +800 mV after 20 min of resetting at V reset of -800 mV, b) IV log curves (Vmax=100 mV) taken at the time A, B and C indicated in a)

A3.1 Reproducibility of results

For statistical purposes, we performed the same sets of measurements on 30 devices. For each device SEM images has been taken before the electrical characterizations, and their I-V curves were recorded and subsequently compared to corresponding SEM images, some of which are presented in **Fig. A9**. All of those devices present similar behaviors. The voltage at which the

hysteretic behavior appears for the first time vary significantly device to device (**Fig. A9**). For the device depicted in **Fig.A9a** the hysteretic loop appears above 1.2 V and for the device of **Fig. A9b** it appears at 500 mV.

However, similar results were also obtained from devices where SEM imaging conducted before measurements indicated no visible flakes (**Fig. A10**). In some cases, nanosheets were absent, possibly removed during the deposition of top contacts using the lift-off step of the lithography process.

Fig. A10 illustrates that the majority of devices without nanosheets (ex. **Fig. A10a-b**) exhibit linear behavior without a hysteresis loop, even for V max up to 2V. Increasing the voltage in these cases results in electrode destruction. On the other hand, some devices (Fig. **A10c**) display behavior similar to that of MIM devices, exhibiting LRS and HRS states as shown in **Fig. A9**. To ensure that no hidden flakes are present between the two electrodes, we fabricated devices using the same process but without adding flakes to the water solution used in the second step of the process.

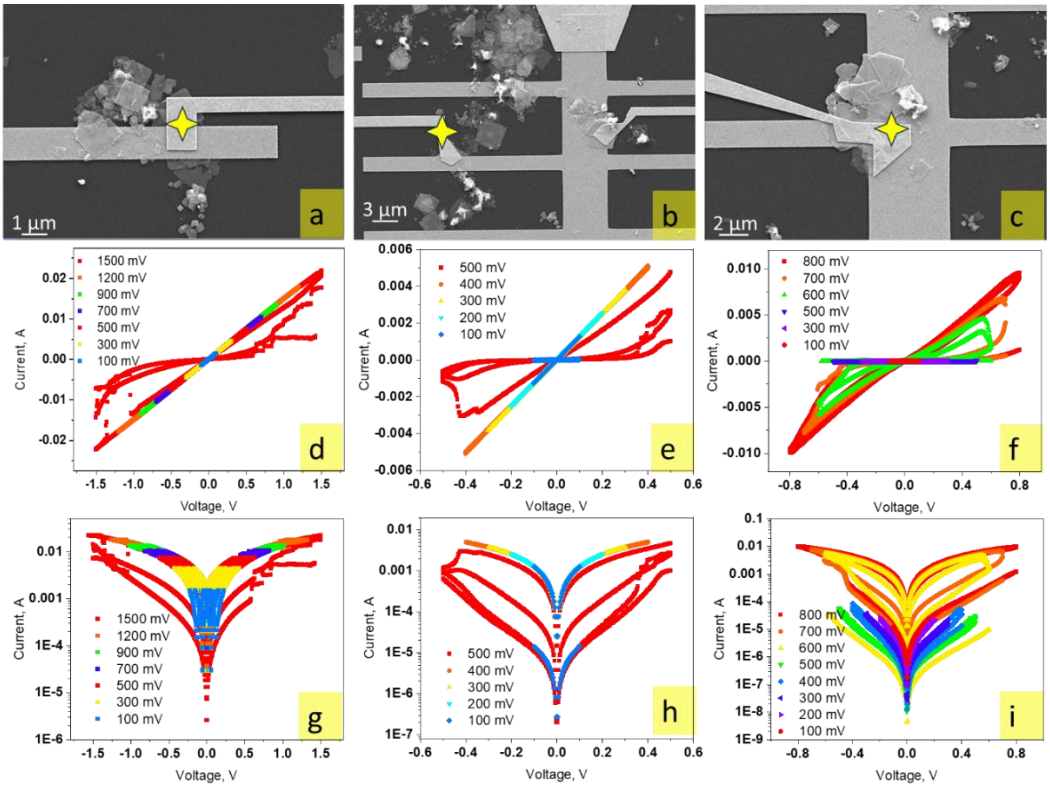

Fig. 9: a,b,c) SEM images of a three different Ti/Au/BOC/Au/Ti devices with d,e,f) their corresponding IV curves and log scale curves g,h,i).

Surprisingly, some of those reference devices displayed also MIM-like behavior, example shown on **Fig. A10c**. Since the top electrodes are composed of Ti/Au layers with thicknesses of 10/100 nm, with Ti being used to enhance the adhesion of the Au layer, we can't exclude oxidation

of the Ti sublayer or contamination at the interface between the bottom Au electrode and the Ti top electrode during the device fabrication. It remains challenging to ascertain whether the memristive-like effect originates solely from the BOC material itself or is a cumulative effect of the BOC material and other oxides (in the event that Ti undergoes oxidation) that can be formed during the device fabrication process. These results raise questions and doubts about the reliability of a vertical geometry for the study of 2D materials.

A4 Conclusion

In conclusion, this **Appendix** suggests the potential for a Metal-Insulator-Metal (MIM) behavior in BOC-based devices for the first time. While the current MIM-type BOC device results are promising, further investigation is needed to clarify the role played by the electrode. Additional tests, such as FIB cross-section analysis of the MIM device to detect any oxidation of Ti/Au electrodes during the lithography process, or considering changes to the electrode material or geometry (moving from a vertical to a planar configuration) to reduce the contribution of the electrode-BOC-electrode interface, should be conducted.

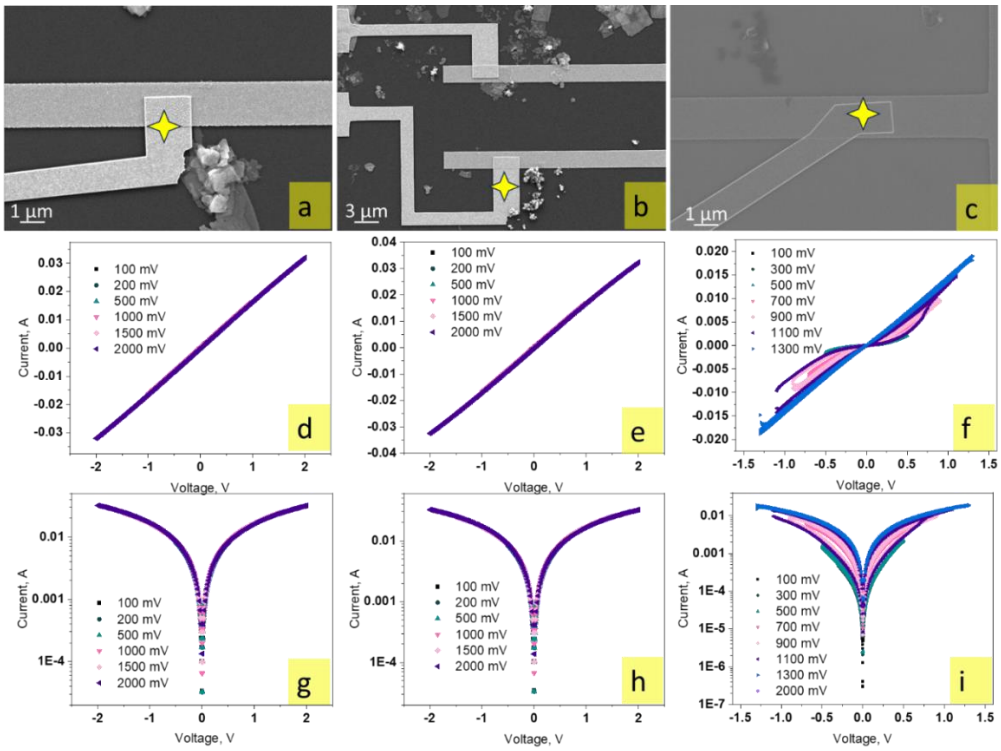

Fig. A10: a,b,c) SEM images of three different devices without BOC, with their corresponding typical IV switching curves d,e,f) and log scale curves in g,h,i).

While these challenges may pose intricate questions, they also underline the importance of this study. The absence of prior research on BOC's memristive behavior, coupled with our willingness to confront and document challenges, can be useful for further understanding and optimizing further device's architecture.

A5 Preparation of freestanding 2D BOCN nanosheets

BOC nanosheets were prepared via an ultra-facile and rapid procedure containing two steps: chemical etching of the electrodes and their successive erosion by nanosecond-pulsed discharges in water. A high voltage is delivered by a DC voltage power supply (Technix SR15-R-1200—15 kV— 80 mA) that feeds a high voltage solid-state switch (HTS-301-03-GSM). The switch is driven by a function generator and delivers a high voltage pulse. The electrical signal, defined by its frequency, amplitude and pulse width, is applied to the power electrode. The second electrode is connected to the ground and serves as cathode at breakdown. The two electrodes are immersed in a 100 ml Dewar filled with dielectric liquid (nitrogen or water). The inter-electrode gap distance that enables breakdown is kept constant during the process by continuously adjusting it with micrometric screws.

Initially, the Bi rod (10 mm in diameter, of high purity 99.999% purchased from Goodfellow) was cut out to get a conical form with a base diameter of 10 mm. Then, conical Bi electrodes were gently polished with 1200-grid paper and rinsed next with tap water. After that, they were immerged in Nital 5% chemical etching solution for 20 min.

After chemical etching, Bi electrodes were rinsed with distilled water, installed in electrode's holders, then immerged in dielectric liquid (water). Pulses of 5 kV, 10 Hz and 75 ns were applied to the power electrode during 20 minutes.

Carbon and holey carbon grids were used as substrates to collect the products from electrode erosion to be characterized by electron microscopy. Nanosheets were collected by immerging TEM grid in solution with synthesized Nps.

HRTEM (TEM, EDX, EELS, heating)

Microstructure and composition of the nanoparticles are characterized by high-resolution TEM (HRTEM). HRTEM investigation is performed using a JEOL ARM 200 F cold FEG TEM/STEM operating at 200 kV, equipped with a spherical aberration (Cs) probe and image correctors (point resolution 0.12 nm in TEM mode and 0.078 nm in STEM mode) and camera GIF quantum ER model 965.

High-angle dark-field imaging in scanning TEM (HAADF/STEM) and 2D elemental mapping using energy dispersive X-ray spectroscopy (EDX) are combined to obtain information about chemical composition of nanoparticles. In scanning mode (STEM), EDX analyses were obtained using a JEOL CENTURIO energy-dispersive X-ray spectrometer. EDX element distribution maps recorded over an area of 512 nm × 512 nm (one measurement point per nm),

were produced by using an acquisition time of 1 ms per measurement point and by repeating 20 scans over the same area.

In situ TEM heating experiments

The procedure for *in situ* TEM heating of BOCN involved preparing nanosheets as described above, transferring them onto Protochips Fusion thermal chips with holey carbon film, and inserting them into the TEM instrument. Heating experiments were performed using a Protochips Fusion heating holder, from room temperature up to 325°C, gradually increasing the temperature while continuously imaging and recording the nanosheets' behavior in real-time, allowing for the observation of structural or morphology changes, phase transitions, and other phenomena. The sample was heated in vacuum with a 5 ◦C/s ramp rate in the temperature range from 25-325 ◦C. The heating process was controlled by the corresponding Protochips software. The acquired data is then analyzed and compared at different temperatures to gain insights into the nanosheets' thermal response and behavior.

Post-Heating Analysis: Additional analyses and characterization techniques, such as electron diffraction, selected area electron diffraction (SAED), spectroscopy, were necessary to supplement the TEM observations.

AFM

The AFM scans have been done with the SmartSPM 1000 (AIST-NT microscope) in semi-contact mode at ambient conditions. Working cantilevers were HQ:NSC16/Hard/Al BS (MikroMasch), NSG01 (TipsNano), and PPP-NCSTAuD-10 (Nanosensors), differing in resonant working frequencies (190 kHz, 145 kHz, and 140 kHz, respectively) and force constant (45 N/m, 7.5 N/m, and 14 N/m, respectively).

Device fabrication & Lithography

Fabrication of BOCN device includes the following process steps involved in the nanofabrication cleanroom process:

The first step is cleaning the Si/SiO2 sample with acetone and isopropanol to ensure that it is free of any contaminant. Once the sample is clean, a bilayer PMMA-resin (thickness of 330 nm) is deposited using spin coating at 4000 rpm. The following specific types are used: PMMA/MA: AR-P 617.06 and PMMA: AR-P 672.02.

Next, the sample is exposed to an electron beam lithography process using the Raith 150 II tool. The exposure parameters include a voltage of 20 kV, a dose of 120 μC/cm², a current of 16 pA with a 10 μm diaphragm, and an exposure time of 6 hours.

After the exposure, the sample is developed with MIBK (4-methyl-2-pentanone) for 1 minute, followed by 30 seconds of isopropanol. A metal deposition process is then used to create a Ti/Au layer of 10/100 nm using an electron evaporator Plassys MEB400S.

The next step is a lift-off process using a remover called NMP 1165 (N-Methyl-2-Pyrrolidone) for 1 hour. This step removes any unwanted material and leaves behind the desired pattern. Finally, the sample is ready for the deposition of BOCN nanosheets.

To fabricate BOCN device, BOCN flakes are transferred from a solution onto a 270 nm thick SiO2/Si substrate by immersion of the substrate into the solution (as described in *Preparation of freestanding 2D BOCN nanosheets)* before drying.

On the transferred BOCN, a double electron resistor layers is spin-coated and a second electron beam lithography process is performed to align the contacts with the BOCN flakes.

I-V measurements

All the I-V characterizations are performed using a K2450 source-meter in a two wire geometry. The measurement have been made in a probe station (**Fig. A11**) in a static vacuum of 1 mbar at room temperature. Voltage is swept at constant rate of 0.1 V/s.

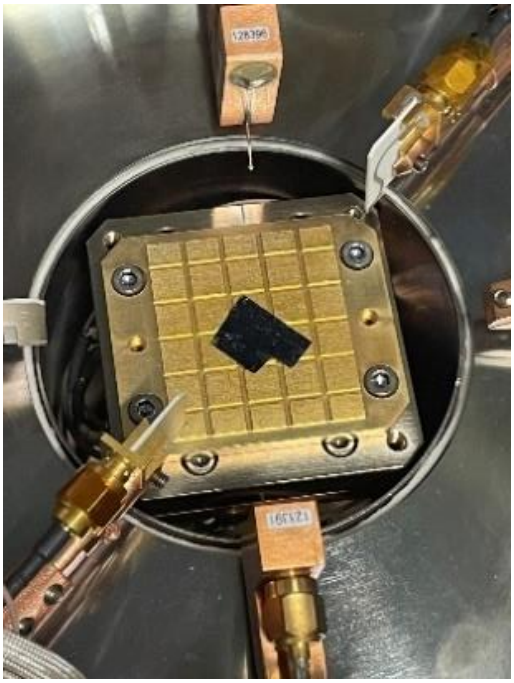

Fig. A11: Sample in LakeShore probe station.

Bibliography

[Abdullaeva2012] Abdullaeva, Z., Omurzak, E., Iwamoto, C., *et al.* (2012). Onion-like carbon-encapsulated Co, Ni, and Fe magnetic nanoparticles with low cytotoxicity synthesized by a pulsed plasma in a liquid. Carbon, 50(5), 1776-1785.

[Ahmed2016] Ahmed, G., Hanif, M., Zhao, L., *et al.* (2016). Defect engineering of ZnO nanoparticles by graphene oxide leading to enhanced visible light photocatalysis. Journal of Molecular Catalysis A: Chemical, 425, 310-321.

[Ajaev2003] Ajaev, V. S., Willis, D. A. (2003). Thermocapillary flow and rupture in films of molten metal on a substrate, Physics of Fluids, 15(10), 3144–3150.

[Amadu2021] Amadu, B. D., Xu, D., Zhang, Q., *et al*. (2021). Synthesis of ultrathin, porous and surface modified $Bi_2O_2CO_3$ nanosheets by Ni doping for photocatalytic organic pollutants degradation, Journal of the Taiwan Institute of Chemical Engineers, 125, 78–87.

[Ambrosetti2016] Ambrosetti, A., Ferri, N., DiStasio, R. A., *et al*. (2016). Wavelike charge density fluctuations and van der Waals interactions at the nanoscale. Science, 351(6278), 1171–1176.

[Arora2014] Arora, N., Sharma, N. N. (2014). Arc discharge synthesis of carbon nanotubes: Comprehensive review. Diamond and related materials, 50, 135–150.

[Arshad2022] Arshad, H., Tahir, M. U., Rehman, F., *et al*. (2022). Facile synthesis of bismuth oxide nanostructures derived from solvent-mediated oxalates and their visible-light-driven photocatalytic removal of organic pollutants. Applied Surface Science, 574, 151678.

[Ashkarran2009] Ashkarran, A. A., Mahdavi, S. M., Ahadian, M. M., *et al*. (2009). Rapid and efficient synthesis of colloidal gold nanoparticles by arc discharge method. Applied Physics A, 96(2), 423-428.

[Ashkarran2013] Ashkarran, A. A. (2013). Seed mediated growth of gold nanoparticles based on liquid arc discharge. Plasma Science and Technology, 15(4), 376-381.

[Atkinson1985] Atkinson, A. (1985). Transport processes during the growth of oxide films at elevated temperature. Reviews of Modern Physics, 57(2), 437-470.

[Averback1996] Averback, R. S., Zhu, H. L. (1996). Sintering of nanoparticle powders: Simulations and experiments. Philosophical Magazine Letters, 73, 27-31.

[Baerdemaeker2005] De Baerdemaeker, F., Monte, M., Leys, C. (2005). Capillary underwater discharges. IEEE Transactions on plasma science, 33(2), 492-493.

[Balden2013] Balden, M., Rohde, V., Lindig, S., *et al*. (2013). Blistering and re-deposition on tungsten exposed to ASDEX Upgrade divertor plasma. Journal of Nuclear Materials, 438, S220-S223.

[Bhattacharyya2009] Bhattacharyya, S., Staack, D., Vitol, E. A., Singhal, R., Fridman, A., Friedman, G., & Gogotsi, Y. (2009). Localized synthesis of metal nanoparticles using nanoscale corona discharge in aqueous solutions. Advanced Materials, 21(40), 4039-4044.

[Belmonte2014] Belmonte, T., Hamdan, A., Kosior, F., *et al*. (2014). Interaction of discharges with electrode surfaces in dielectric liquids: Application to nanoparticle synthesis. Journal of Physics D: Applied Physics, 47(22), 224016.

[Belmonte2023] Belmonte, T., Nominé, A. V., Noël, C., *et al*. (2023). Submerged Discharges in Liquids for Nanoobject Synthesis: Expectations and Capabilities. Plasma Chemistry and Plasma Processing, 1-56.

[Bera2005] Bera, D., Brinley, E., Kuiry, S. C., *et al.* (2005). Optoelectronically automated system for carbon nanotubes synthesis via arc-discharge in solution. Review of scientific instruments, 76(3).

[Bera2006] Bera, D., Johnston, G., Heinrich, H., *et al.* (2006). A parametric study on the synthesis of carbon nanotubes through arc-discharge in water. Nanotechnology, 17(6), 1722.

[Bird2010] Bird, J. C., De Ruiter, R., Courbin, L., *et al.* (2010). Daughter bubble cascades produced by folding of ruptured thin films. Nature, 465(7299), 759-762.

[Bonyár2018] Bonyár, A., Csarnovics, I., Veres, M., *et al.* (2018). Investigation of the performance of thermally generated gold nanoislands for LSPR and SERS applications. Sensors and Actuators B: Chemical, 255, 433-439.

[Buerger1978] Buerger, M. (1978). Elementary crystallography: an introduction to the fundamental features of crystals. Cambridge: Massachussetts Institute of Technology Press.

[Bulychev2016] Bulychev, N. A., Kazaryan, M. A., Lepnev, L. S., *et al.* (2016). The influence of ultrasonic cavitation on plasma discharge in a liquid medium and the properties of thus-produced nanoparticles. Instruments and Experimental Techniques, 59(6), 842-847.

[Bulychev2019] Bulychev, N. A., Kazaryan, M. A., Kirichenko, M. N., *et al.* (2019). Study of acoustoplasma discharge as a technique for synthesis of optically active materials. International Journal of Nanotechnology, 16(1-3), 34-41.

[Burakov2015] Burakov, V. S., Nevar, E. A., Nedel'Ko, M. I., *et al.* (2015). Synthesis and modification of molecular nanoparticles in electrical discharge plasma in liquids. Russian Journal of General Chemistry, 85(5), 1222-1237.

[Butler2013] Butler, S. Z., Hollen, S. M., Cao L., *et al.* (2013). Progress, challenges, and opportunities in two-dimensional materials beyond graphene. ACS Nano, 7(4), 2898-2926

[Buxton1976] Buxton, B.F., Eades, J.A., Steeds, J.W., *et al*. (1976). The symmetry of electron diffraction zone axis patterns. Philosophical Transaction of the Royal Society of London. Serie A, 281(1301), 171-194.

[Cabrera1949] Cabrera, N. F. M. N., Mott, N. F. (1949). Theory of the oxidation of metals. Reports on progress in physics, 12(1), 163-184.

[Cahn1982] Cahn, J. W., Kalonji, G., Aaronson, H., *et al*. (1982). Solid-solid phase transformations. Proceedings of the International Conference on Solid-Solid Phase Transformations, edited by Aaronson, H. I., Laughlin, D. E., Skerka, R. F., Marvin Wayman, C.M. Washington: The Metallurgical Society of AIME, 3-14.

[Carter2009] Williams D B., Barry Carter, C. Transmission Electron Microscopy A Textbook for Materials Science. Springer publication, New York, 2009.

[Cataldo2004] Cataldo, F. (2004). Polyynes and cyanopolyynes synthesis from the submerged electric arc: about the role played by the electrodes and solvents in polyynes formation. Tetrahedron, 60(19), 4265-4274.

[Chen2004] Chen, L. C., Pai, S. H. (2004). In-situ measurement and control of electric discharge on submerged arc synthesis process for continuous TiO2 nanoparticle fabrication. Materials transactions, 45(10), 3071-3078.

[Chen2005] Chen, C. H., Yamaguchi, T., Sugawara, K. I., *et al.* (2005). Role of stress in the self-limiting oxidation of copper nanoparticles. The Journal of Physical Chemistry B, 109(44), 20669-20672.

[Chen2010] Chen, R. H., Phuoc, T. X., Martello, D. (2010). Effects of nanoparticles on nanofluid droplet evaporation. International Journal of Heat and Mass Transfer, 53(19-20), 3677-3682.

[Chen2012a] Chen, X., Zhou, Y., Liu, Q., *et al.* (2012). Ultrathin, single-crystal WO3 nanosheets by two-dimensional oriented attachment toward enhanced photocatalystic reduction of CO2 into hydrocarbon fuels under visible light. ACS applied materials & interfaces, 4(7), 3372-3377.

[Chen2012b] Chen, L., Huang, R., Yin, S. F., *et al.* (2012). Flower-like $Bi_2O_2CO_3$: Facile synthesis and their photocatalytic application in treatment of dye-containing wastewater. Chemical engineering journal, 193, 123-130.

[Chen2015] Chen, Q., Li, J., Li, Y. (2015). A review of plasma–liquid interactions for nanomaterial synthesis. Journal of Physics D: Applied Physics, 48(42), 424005.

[Chen2016] Chen, J., Mei, W., Huang, Q., *et al.* (2016). Highly efficient three-dimensional flower-like AgI/ $Bi_2O_2CO_3$ heterojunction with enhanced photocatalytic performance. Journal of Alloys and Compounds, 688, 225-234.

[Cheng2010] Cheng, H., Huang, B., Yang, K., *et al.* (2010). Facile Template-Free Synthesis of $Bi_2O_2CO_3$ Hierarchical Microflowers and Their Associated Photocatalytic Activity. ChemPhysChem, 11(10), 2167-2173.

[Cho2011] Cho, S. P., Bratescu, M. A., Saito, N., *et al.* (2011). Microstructural characterization of gold nanoparticles synthesized by solution plasma processing. Nanotechnology, 22(45), 455701.

[Choi2009] Choi, S. U. (2009). Nanofluids: from vision to reality through research. Journal of Heat transfer, 131(3), 033106.

[Chon2007] Chon, C. H., Paik, S., Tipton, J. B., *et al.* (2007). Effect of nanoparticle sizes and number densities on the evaporation and dryout characteristics for strongly pinned nanofluid droplets. Langmuir, 23(6), 2953-2960.

[Cosgrove2005] Cosgrove, T. (2005). Colloid science: Principles, Methods and Applications. Blackwell publishing limited. 2nd edition. Wiley.

[Coughlan2018] Coughlan, C., Guo, Y., Singh, S., *et al.* (2018). Synthesis of Curved $CuIn_{1-x}Ga_x(S_{1-y}\ Se_y)_2$ Nanocrystals and Complete Characterization of Their Diffraction Contrast Effects. Chemistry of Materials, 30(23), 8679-8689.

[CrystalMaker2023] CrystalMaker software® (http://crystalmaker.com) version 9 (2023).

[DebRoy1991] DebRoy, T., Basu, S., Mundra, K. (1991). Probing laser induced metal vaporization by gas dynamics and liquid pool transport phenomena. Journal of Applied Physics, 70(3), 1313-1319.

[Derjaguin1941] Derjaguin, B., Landau, L. D. (1941) Theory of the Stability of Strongly Charged Lyophobic Sols and of the Adhesion of Strongly Charged Particles in Solutions of Electrolytes. Acta Physicochimica U.R.S.S., 14, 633-662.

[Ding2020] Ding, J., Wang, H., Luo, Y., *et al.* (2020). (002) Oriented $Bi_2O_2CO_3$ nanosheets with enhanced photocatalytic performance for toluene removal in air. Catalysts, 10(4), 389.

[Dong2011] Dong, F., Ho, W. K., Lee, S. C., *et al.* (2011). Template-free fabrication and growth mechanism of uniform (BiO)2CO3 hierarchical hollow microspheres with outstanding photocatalytic activities under both UV and visible light irradiation. Journal of materials chemistry, 21(33), 12428-12436.

[Dong2012] Dong, F., Sun, Y., Fu, M., *et al.* (2012). Novel in situ N-doped (BiO) 2CO3 hierarchical microspheres self-assembled by nanosheets as efficient and durable visible light driven photocatalyst. Langmuir, 28(1), 766-773.

[Dong2014] Dong, F., Bian, J., Sun, Y., *et al.* (2014). The rapid synthesis of photocatalytic $Bi_2O_2CO_3$ single-crystal nanosheets via an eco-friendly approach. CrystEngComm, 16(17), 3592-3604.

[Eckert2021] Eckert, T., Schmidt, M., de Las Heras, D. (2021). Gravity-induced phase phenomena in plate-rod colloidal mixtures. Communications Physics, 4(1), 202.

[Eskizeybek2011] Eskizeybek, V., Demir, O., Avci, A., & Chhowalla, M. (2011). Synthesis and characterization of cadmium hydroxide nanowires by arc discharge method in de-ionized water. Journal of Nanoparticle Research, 13(10), 4673-4680.

[Everett2007] Everett, D. H. (2007). Basic principles of colloid science. Published by the Royal society of chemistry. London.

[Fan2004a] Fan, H. G., Kovacevic, R. (2004). A unified model of transport phenomena in gas metal arc welding including electrode, arc plasma and molten pool. Journal of Physics D: Applied Physics, 37(18), 2531.

[Fan2004b] Fan, H. J., Scholz, R., Kolb, F. M., *et al.* (2004). On the growth mechanism and optical properties of ZnO multi-layer nanosheets. Applied Physics A, 79, 1895-1900.

[Fan2019] Fan, H., Zhou, H., Li, H., *et al.* (2019). Novel Ag2CrO4/ $Bi_2O_2CO_3$ heterojunction: Simple preparation, wide visible-light absorption band and excellent photocatalytic activity. Chemical Physics, 517, 60-66.

[Feng2015] Feng, H., Xu, Z., Wang, L., *et al.* (2015). Modulation of photocatalytic properties by strain in 2D BiOBr nanosheets. ACS applied materials & interfaces, 7(50), 27592-27596.

[Feng2021] Feng, Y., Zhang, Z., Zhao, K., *et al.* (2021). Photocatalytic nitrogen fixation: Oxygen vacancy modified novel micro-nanosheet structure $Bi_2O_2CO_3$ with band gap engineering. Journal of Colloid and Interface Science, 583, 499-509.

[Flores-Castaneda2023] Flores-Castañeda, M., Camacho-Lopez, S. (2023). Si nanoparticle decorated $Bi_2O_2CO_3$ 2D nanocomposite synthesized by femtosecond laser ablation of solids in liquids and aging. Optics & Laser Technology, 158, 108891.

[Font2013] Font, F., Myers, T. G. (2013). Spherically symmetric nanoparticle melting with a variable phase change temperature. Journal of nanoparticle research, 15(12), 2086.

[Fromhold1980] Fromhold, A.T. Jr. (1980). Theory of metal oxidation Vol 2. Netherlands: North-Holland Publ Co.

[Fromhold1988] Fromhold, A. T. Jr. (1988). Growth rate of low-space-charge oxides on spherical metal particles. Journal of Physics and Chemistry of Solids, 49(10), 1159-1166.

[Furuya2007] Furuya, K., Hirowatari, Y., Ishioka, T., *et al.* (2007). Protective agent-free preparation of gold nanoplates and nanorods in aqueous HAuCl4 solutions using gas–liquid interface discharge. Chemistry letters, 36(9), 1088-1089.

[Ge2018] Ge, R., Wu, X., Kim, M., Shi, J., Sonde, S., Tao, L., Zhang, Y., Lee, J.C. and Akinwande, D. (2018). Atomristor: nonvolatile resistance switching in atomic sheets of transition metal dichalcogenides. Nano letters, 18(1), pp.434-441.

[Gebauer2014] Gebauer, D., Kellermeier, M., Gale, J. D., *et al.* (2014). Pre-nucleation clusters as solute precursors in crystallisation. Chemical Society Reviews, 43(7), 2348-2371.

[Geim2013] Geim, A. K., Grigorieva, I. V. (2013). Van der Waals heterostructures, Nature 499(7459) 419–425

[Gelderman2007] Gelderman, K., Lee, L., Donne, S. W. (2007). Flat-band potential of a semiconductor: using the Mott–Schottky equation. Journal of chemical education, 84(4), 685.

[Geng2018] Geng, D., Yang, H. Y. (2018). Recent advances in growth of novel 2D materials: beyond graphene and transition metal dichalcogenides. Advanced Materials, 30(45), 1800865.

[George1986] George, J., Pradeep, B., Joseph, K. S. (1986). Oxidation of bismuth films in air and superheated steam. Thin solid films, 144(2), 255-264.

[Georgiev2013] Georgiev, P., Bojinova, A., Kostova, B., *et al.* (2013). Implementing atomic force microscopy (AFM) for studying kinetics of gold nanoparticle's growth. Colloids and Surfaces A: Physicochemical and Engineering Aspects, 434, 154-163.

[Germain2003] Germain, V., Li, J., Ingert, D., *et al*. (2003). Stacking faults in formation of silver nanodisks. The Journal of Physical Chemistry B, 107(34), 8717-8720.

[Giammanco2010] Giammanco, F., Giorgetti, E., Marsili, P., *et al*. (2010). Experimental and theoretical analysis of photofragmentation of Au nanoparticles by picosecond laser radiation. The Journal of Physical Chemistry C, 114(8), 3354-3363.

[Giannazzo2019] Giannazzo, F., Greco, G., Roccaforte, F., *et al*. (2019). Conductive AFM of 2D materials and heterostructures for nanoelectronics. Electrical Atomic Force Microscopy for Nanoelectronics, 303-350.

[Ghomi2013] Ghomi, H., Yousefi, M., Shahabi, N., & Khoramabadi, M. (2013). Ultrasonic-assisted spark plasma discharge for gold nanoparticles synthesis. Radiation effects and defects in solids, 168(11-12), 881-891.

[Gonzalez2009] Gonzalez, J. J., Cayla, F., Freton, P., *et al*. (2009). Two-dimensional self-consistent modelling of the arc/cathode interaction. Journal of Physics D: Applied Physics, 42(14), 145204.

[Gouriet2009] Gouriet, K., Sentis, M., Itina, T. E. (2009). Molecular dynamics study of nanoparticle evaporation and condensation in a gas. The Journal of Physical Chemistry C, 113(43), 18462-18467.

[Grammatikopoulos2014] Grammatikopoulos, P., Cassidy, C., Singh, V., *et al*. (2014). Coalescence-induced crystallisation wave in Pd nanoparticles. Scientific reports, 4, 5779.

[Grammatikopoulos2019] Grammatikopoulos, P., Sowwan, M., Kioseoglou, J. (2019). Computational modeling of nanoparticle coalescence. Advanced Theory and Simulations, 2(6), 1900013.

[Grice2002] Grice J. D., (2002). A Solution to the crystal structures of the Bismutite and Beyerite. The Canadian Mineralogist, 40, 693-698

[Guo2018] Guo, Y., Dai, Y., Zhao, W., *et al*. (2018). Highly efficient photocatalytic degradation of naphthalene by $Co_3O_4/Bi_2O_2CO_3$ under visible light: A novel p–n heterojunction nanocomposite with nanocrystals/lotus-leaf-like nanosheets structure. Applied Catalysis B: Environmental, 237, 273-287.

[Gupta2022] Gupta, T., Rosza, N., Sauer, M., *et al*. (2022). Sonochemical Synthesis of Large Two-Dimensional $Bi_2O_2CO_3$ Nanosheets for Hydrogen Evolution in Photocatalytic Water Splitting. Advanced Sustainable Systems, 6(11), 2100326.

[Hamdan2013a] Hamdan, A., Audinot, J. N., Migot-Choux, S., *et al*. (2013). Interaction of discharges in heptane with silicon covered by a carpet of carbon nanotubes. Advanced Engineering Materials, 15(10), 885-892.

[Hamdan2013b] Hamdan, A., Kosior, F., Noel, C., *et al.* (2013). Plasma-surface interaction in heptane. Journal of Applied Physics, 113(21), 213303.

[Hamdan2013c] Hamdan, A., Noel, C., Kosior, F., *et al.* (2013). Impacts created on various materials by micro-discharges in heptane: Influence of the dissipated charge. Journal of Applied Physics, 113(4), 043301.

[Hamdan2013d] Hamdan, A., Noel, C., Ghanbaja, J., *et al.* (2013). Synthesis of platinum embedded in amorphous carbon by micro-gap discharge in heptane. Materials Chemistry and Physics, 142(1), 199-206.

[Hamdan2014] Hamdan, A., Marinov, I., Rousseau, A., *et al.* (2014). Time-resolved imaging of nanosecond-pulsed micro-discharges in heptane. Journal of Physics D: Applied Physics, 47(5), 055203.

[Hamdan2018] Hamdan, A., Kabbara, H., Noel, C., *et al.* (2018). Synthesis of two-dimensional lead sheets by spark discharge in liquid nitrogen. Particuology, 40, 152-159.

[Hamdan2021] Hamdan, A., Agati, M., Boninelli, S. (2021). Selective synthesis of 2D mesoporous CuO agglomerates by pulsed spark discharge in water. Plasma Chemistry and Plasma Processing, 41, 433-445.

[Han2023] Han, M., Qian, Y., Li, X., *et al.* (2023). Ni-doped $Bi_2O_2CO_3$ nanosheet with H+/Zn2+ co-insertion for "rocking chair" zinc-ion battery. Journal of Colloid and Interface Science, 645, 483-492.

[Hao2022] Hao, X., Fu, Q., Hou, Y., *et al.* (2022). Enhancement of Energy Storage Performances in PMMA/PVDF Nanocomposites with Low Dielectric Bismuth Carbonate Nanosheets. ACS Applied Energy Materials, 5(12), pp.15939-15947.

[Hassanein1997] Hassanein, A., Belan, V., Konkashbaev, I., *et al.* (1997). Modeling and simulation of melt-layer erosion during plasma disruption. Journal of nuclear materials, 241, 288-293.

[He2022] He, Q., Liu, X., Li, F., *et al.* (2022). Effect of Light and Heavy Rare Earth Doping on the Physical Structure of $Bi_2O_2CO_3$ and Their Performance in Photocatalytic Degradation of Dimethyl Phthalate. Catalysts, 12(11), 1295.

[Henry2011] Henry, A. I., Bingham, J. M., Ringe, E., *et al.* (2011). Correlated structure and optical property studies of plasmonic nanoparticles. The Journal of Physical Chemistry C, 115(19), 9291-9305.

[Heo2010] Heo, Y. K., Kim, S. M., Lee, S. Y. (2010). Effects of discharge duration on the size and shape of gold nanoparticles synthesized using solution plasma processing. Physica Scripta, 2010(T139), 014025.

[Herrmann1997] Herrmann, J. M., Tahiri, H., Ait-Ichou, Y., *et al.* (1997). Characterization and photocatalytic activity in aqueous medium of TiO2 and Ag-TiO2 coatings on quartz. Applied Catalysis B: Environmental, 13(3-4), 219-228.

[Hieda2008] Hieda, J., Saito, N., Takai, O. (2008). Exotic shapes of gold nanoparticles synthesized using plasma in aqueous solution. Journal of Vacuum Science & Technology A: Vacuum, Surfaces, and Films, 26(4), 854-856.

[Holgate2019] Holgate, J. T., Coppins, M. (2019). Enhancement of droplet ejection from molten and liquid plasma-facing surfaces by the electric field of the sheath. Journal of Physics D: Applied Physics, 53(10), 105204.

[Holse2015] Holse, C., Elkjær, C. F., Nierhoff, A., *et al*. (2015). Dynamic behavior of CuZn nanoparticles under oxidizing and reducing conditions. The Journal of Physical Chemistry C, 119(5), 2804-2812.

[Hori2011] Hori, M., Kondo, H., & Hiramatsu, M. (2011). Radical-controlled plasma processing for nanofabrication. Journal of Physics D: Applied Physics, 44(17), 174027.

[Horikoshi2017] Horikoshi, S., Serpone, N. (2017). In-liquid plasma: a novel tool in the fabrication of nanomaterials and in the treatment of wastewaters. RSC advances, 7(75), 47196-47218.

[Horváth2006] Horváth, Z. E., Kertész, K., Pethő, L., *et al*. (2006). Inexpensive, upscalable nanotube growth methods. Current Applied Physics, 6(2), 135-140.

[Hu2014] Hu, D., Zhang, K., Yang, Q., *et al*. (2014). Super-high photocatalytic activity of Fe2O3 nanoparticles anchored on $Bi_2O_2CO_3$ nanosheets with exposed {0 0 1} active facets. Applied surface science, 316, 93-101.

[Hu2016] Hu, Y., Li, Y., Fan, C., *et al.* (2016). Simple hydrolysis route to synthesize $Bi_2O_2CO_3$ nanoplate from Bi nanopowder and its photocatalytic application. Materials Letters, 170, 72-75.

[Hu2018] Hu, J., Chen, D., Li, N., *et al*. (2018). Recyclable carbon nanofibers@ hierarchical I-doped $Bi_2O_2CO_3$–MoS2 membranes for highly efficient water remediation under visible-light irradiation. ACS Sustain Chem Eng 6: 2676–2683.

[Hu2021] Hu, X., Zhao, H., Liang, Y., *et al*. (2021). Broad-spectrum response NCQDs/$Bi_2O_2CO_3$ heterojunction nanosheets for ciprofloxacin photodegradation: Unraveling the unique roles of NCQDs upon different light irradiation. Chemosphere, 264, 128434.

[Huang2014] Huang, H., Tian, N., Jin, S., *et al*. (2014). Syntheses, characterization and nonlinear optical properties of a bismuth subcarbonate $Bi_2O_2CO_3$. Solid State Sciences, 30, 1-5.

[Huang2015] Huang, H., Wang, J., Dong, F., *et al*. (2015). Highly efficient $Bi_2O_2CO_3$ single-crystal lamellas with dominantly exposed {001} facets. Crystal Growth & Design, 15(2), 534-537.

[Huang2021] Huang, H., Zhigilei, L. V. (2021). Atomistic view of laser fragmentation of gold nanoparticles in a liquid environment. The Journal of Physical Chemistry C, 125(24), 13413-13432.

[Huang2022] Huang, J.K., Wan, Y., Shi, J., *et al*. (2022). High-κ perovskite membranes as insulators for two-dimensional transistors. Nature, 605(7909), pp.262-267.

[Huh2020] Huh, W., Lee, D., Lee, C. H. (2020). Memristors based on 2D materials as an artificial synapse for neuromorphic electronics. Advanced Materials, 32(51), 2002092.

[Hui2019] Hui, F., Lanza, M. (2019). Scanning probe microscopy for advanced nanoelectronics. Nature electronics, 2(6), 221-229.

[Isikawa2021] Isikawa, M. M., Assuncao, A. C. A., Baffa, O., *et al.* (2021). Enhanced optical cross-section of radiation induced defect centers under plasmon resonance conditions: Shifting stimulation wavelength of optically stimulated luminescence dosimeters. Journal of Luminescence, 231, 117841.

[Jedsukontorn2018] Jedsukontorn, T., Ueno, T., Saito, N., *et al.* (2018). Narrowing band gap energy of defective black TiO2 fabricated by solution plasma process and its photocatalytic activity on glycerol transformation. Journal of Alloys and Compounds, 757, 188-199.

[Jia2022] Jia, S., Wang, B., Liu, J., *et al.* (2022). Morphology normalization of peony flower-like $Bi_2O_2CO_3$ boosts photocatalytic seawater purification. Colloids and Surfaces A: Physicochemical and Engineering Aspects, 653, 129915.

[Jungblut2019] Jungblut, S., Eychmüller, A. (2019). Modeling nanoparticle aggregation. Chemical Modelling: Volume 15, Editors: Michael Springborg, Jan-Ole Joswig, pp. 1-27

[Kabbara2015] Kabbara, H., Noel, C., Ghanbaja, J., *et al.* (2015). Synthesis of nanocrystals by discharges in liquid nitrogen from Si–Sn sintered electrode. Scientific reports, 5(1), 1-8.

[Kabbara2017] Kabbara, H., Ghanbaja, J., Noël, C., *et al.* (2017). Synthesis of Cu@ ZnO core–shell nanoparticles by spark discharges in liquid nitrogen. Nano-Structures & Nano-Objects, 10, 22-29.

[Kabbara2018a] Kabbara, H., Ghanbaja, J., Noël, C., *et al.* (2018). Nano-objects synthesized from Cu, Ag and Cu28Ag72 electrodes by submerged discharges in liquid nitrogen. Materials Chemistry and Physics, 217, 371-378.

[Kabbara2018b] Kabbara, H., Ghanbaja, J., Noël, C., & Belmonte, T. (2018). Synthesis of copper and zinc nanostructures by discharges in liquid nitrogen. Materials Chemistry and Physics, 207, 350-358.

[Kabbara2019] Kabbara, H., Ghanbaja, J., Redjaïmia, A., *et al.* (2019). Crystal structure, morphology and formation mechanism of a novel polymorph of lead dioxide, γ-PbO2. Journal of Applied Crystallography, 52(2), 304-311.

[Kang2019] Kang, W., Lin, B., Jiang, Z., *et al.* (2019). $Bi_2O_2CO_3$ microspheres anchored on reduced graphene oxide nanosheets as electrode material for lithium ion batteries and supercapacitors. Materials Letters, 240, 299-302.

[Kanitz2019] Kanitz, A., Kalus, M. R., Gurevich, E. L., *et al.* (2019). Review on experimental and theoretical investigations of the early stage, femtoseconds to microseconds processes during laser ablation in liquid-phase for the synthesis of colloidal nanoparticles. Plasma Sources Science and Technology, 28(10), 103001.

[Kar2017] Kar, P., Maji, T. K., Nandi, R., *et al.* (2017). In-situ hydrothermal synthesis of Bi–$Bi_2O_2CO_3$ heterojunction photocatalyst with enhanced visible light photocatalytic activity. Nano-Micro Letters, 9, 1-10.

[Karahaliou2012] Karahaliou, P. K., Svarnas, P., Georga, S. N., *et al*. (2012). CuO/Ta_2O_5 core/shell nanoparticles synthesized in immersed arc-discharge: production conditions and dielectric response. Journal of Nanoparticle Research, 14(12), 1297.

[Ke2011] Ke, Z., Huang, Q., Zhang, H., *et al*. (2011). Reduction and removal of aqueous Cr (VI) by glow discharge plasma at the gas–solution interface. Environmental science & technology, 45(18), 7841-7847.

[Khezri2012] Khezri, S. H., Yazdani, A., Khordad, R. (2012). Pure iron nanoparticles prepared by electric arc discharge method in ethylene glycol. The European Physical Journal Applied Physics, 59(3), 30401.

[Khezri2013] Khezri, S. H., Yazdani, A., Khordad, R., *et al*. (2013). Preparation of pure cobalt nanoparticles by electric arc discharge method in ethylene glycol. Modern Physics Letters B, 27(09), 1350057.

[Kim2006] Kim, H. Y., Sofo, J. O., Velegol, D., *et al*. (2006). van der Waals forces between nanoclusters: Importance of many-body effects. The Journal of chemical physics, 124(7), 074504.

[Kim2014] Kim, S. M., Lee, Y. J., Kim, J. W., *et al.* (2014). Facile synthesis of Pt–Pd bimetallic nanoparticles by plasma discharge in liquid and their electrocatalytic activity toward methanol oxidation in alkaline media. Thin Solid Films, 572, 260-265.

[Knotek2013] Knotek, P., Tichy, L. (2013). Explosive boiling of Ge35Sb10S55 glass induced by a CW laser. Materials Research Bulletin, 48(9), 3268-3273.

[Kolb1983] Kolb, M., Botet, R., Jullien, R. (1983). Scaling of kinetically growing clusters. Physical Review Letters, 51(13), 1123.

[Kolb1984] Kolb, M. (1984). Unified description of static and dynamic scaling for kinetic cluster formation. Physical review letters, 53(17), 1653.

[Koppenol2010] Koppenol, W. H., Stanbury, D. M., Bounds, P. L. (2010). Electrode potentials of partially reduced oxygen species, from dioxygen to water. Free Radical Biology and Medicine, 49(3), 317-322.

[Kottmann2001] Kottmann, J. P., Martin, O. J., Smith, D. R., *et al*. (2001). Plasmon resonances of silver nanowires with a nonregular cross section. Physical Review B, 64(23), 235402.

[Kozáková2019] Kozáková, Z., Krčma, F., Čechová, L., Simic, S., *et al*. (2019). Generation of Silver Nanoparticles by the Pin-Hole DC Plasma Source with and without Gas Bubbling. Plasma Physics and Technology, 6(2), 180-183.

[Kuchmizhak2017] Kuchmizhak, A. A., Nepomnyashchii, A. V., Vitrik, O. B., *et al*. (2017). Plasmon-mediated enhancement of rhodamine 6g spontaneous emission on laser-spalled nanotextures. Physics Procedia, 86, 66-71.

[Larin2020] Larin, A. O., Nominé, A., Ageev, E. I., *et al*. (2020). Plasmonic nanosponges filled with silicon for enhanced white light emission. Nanoscale, 12(2), 1013-1021.

[Lebedev2018] Lebedev, Y. A. (2018). Microwave discharges in liquids: fields of applications. High Temperature, 56(5), 811-820.

[Lee2014] Lee, D. J., Kim, S. J., Lee, J., *et al.* (2014). Bipolar pulsed electrical discharge for synthesis of tungsten nanoparticles in the aqueous solutions. Science of Advanced Materials, 6(7), 1599-1604.

[Lehtinen2002] Lehtinen, K. E., Zachariah, M. R. (2002). Energy accumulation in nanoparticle collision and coalescence processes. Journal of Aerosol Science, 33(2), 357-368.

[Leong2010] Leong, K. Y., Saidur, R., Kazi, S. N., *et al.* (2010). Performance investigation of an automotive car radiator operated with nanofluid-based coolants (nanofluid as a coolant in a radiator). Applied Thermal Engineering, 30(17-18), 2685-2692.

[Letzel2017] Letzel, A., Gökce, B., Wagener, P., *et al.* (2017). Size quenching during laser synthesis of colloids happens already in the vapor phase of the cavitation bubble. The Journal of Physical Chemistry C, 121(9), 5356-5365.

[Letzel2018] Letzel, A., Gökce, B., Menzel, A., *et al.* (2018). Primary particle diameter differentiation and bimodality identification by five analytical methods using gold nanoparticle size distributions synthesized by pulsed laser ablation in liquids. Applied Surface Science, 435, 743-751.

[Levchenko2007] Levchenko, I., Ostrikov, K. (2007). Nanostructures of various dimensionalities from plasma and neutral fluxes. Journal of Physics D: Applied Physics, 40(8), 2308.

[Lewis1997] Lewis, L. J., Jensen, P., Barrat, J. L. (1997). Melting, freezing, and coalescence of gold nanoclusters. Physical Review B, 56(4), 2248.

[Li2014] Li, R., Wu, Y., Xiao, J. (2014). The nucleation process and the roles of structure and density fluctuations in supercooled liquid Fe. The Journal of chemical physics, 140(3).

[Li2016] Li, T., Hu, X., Liu, C., *et al.* (2016). Efficient photocatalytic degradation of organic dyes and reaction mechanism with $Ag_2CO_3/Bi_2O_2CO_3$ photocatalyst under visible light irradiation. Journal of Molecular Catalysis A: Chemical, 425, 124-135.

[Li2017] Li, J. F., Li, C. Y., Aroca, R. F. (2017). Plasmon-enhanced fluorescence spectroscopy. Chemical Society Reviews, 46(13), 3962-3979.

[Li2022a] Li, J., Li, M., Li, Y., *et al.* (2022). Lotus-leaf-like $Bi_2O_2CO_3$ nanosheet combined with Mo2S3 for higher photocatalytic hydrogen evolution. Separation and Purification Technology, 288, 120588.

[Li2022b] Li, J., Wu, Z., Zhang, S., *et al.* (2022). Hydroxyl-assisted iodine ions intercalating $Bi_2O_2CO_3$ nanosheets to construct an interlayered bridge for enhanced photocatalytic degradation of phenols. CrystEngComm, 24(7), 1377-1386.

[Liang2023] Liang, X. D., Zheng, Q. Z., Wei, N., *et al.* (2023). In-situ constructing Bi@$Bi_2O_2CO_3$ nanosheet catalyst for ampere-level CO2 electroreduction to formate. Nano Energy, 114, 108638.

[Lin2016] Lin, S., Liu, L., Liang, Y., *et al.* (2016). Oil-in-water self-assembled synthesis of Ag@ AgCl nano-particles on flower-like $Bi_2O_2CO_3$ with enhanced visible-light-driven photocatalytic activity. Materials, 9(6), 486.

[Liu2010a] Liu, P., Cui, H., Wang, C. X., *et al.* (2010). From nanocrystal synthesis to functional nanostructure fabrication: laser ablation in liquid. Physical Chemistry Chemical Physics, 12(16), 3942-3952.

[Liu2010b] Liu, Y., Wang, Z., Huang, B., *et al.* (2010). Preparation, electronic structure, and photocatalytic properties of $Bi_2O_2CO_3$ nanosheet. Applied Surface Science, 257(1), 172-175.

[Liu2018] Liu, J., Li, Y., Li, Z., *et al.* (2018). In situ growing of Bi/ $Bi_2O_2CO_3$ on Bi2WO6 nanosheets for improved photocatalytic performance. Catalysis Today, 314, 2-9.

[Liu2019] Liu, H., Chen, P., Yuan, X., *et al.* (2019). Pivotal roles of artificial oxygen vacancies in enhancing photocatalytic activity and selectivity on $Bi_2O_2CO_3$ nanosheets. Chinese Journal of Catalysis, 40(5), 620-630.

[Liu2021] Liu, Z., Yuan, C., Hao, W., *et al.* (2021). In-situ conversion of $Bi_2O_2CO_3$ to $Bi_2O_2CO_3$/Fe_2O_3/BiOCl, Fe_2O_3/BiOCl heterojunctions and boosted photodegradation activity. Inorganic Chemistry Communications, 134, 109066.

[Lo2005] Lo, C. H., Tsung, T. T., Chen, L. C. (2005). Shape-controlled synthesis of Cu-based nanofluid using submerged arc nanoparticle synthesis system (SANSS). Journal of Crystal Growth, 277(1-4), 636-642.

[Lopes2018] Lopes, O. F., Carvalho, K. T., Avansi, W., *et al.* (2018). Insights into the photocatalytic performance of $Bi_2O_2CO_3$/$BiVO_4$ heterostructures prepared by one-step hydrothermal method. RSC advances, 8(20), 10889-10897.

[López2018] López, L. H., Monzonís, L. M., Vicente, L. B., *et al.* (Eds.). (2018). Report about nanofluid's health, safety and environmental impact. Int. J. Therm. Sci, 129, 504-531.

[Lukes2012] Lukes, P., Locke, B. R., Brisset, J. L. (2012). Aqueous-phase chemistry of electrical discharge plasma in water and in gas-liquid environments. Plasma chemistry and catalysis in gases and liquids, 1, 243-308.

[Lukes2014] Lukes, P., Dolezalova, E., Sisrova, I., *et al.* (2014). Aqueous-phase chemistry and bactericidal effects from an air discharge plasma in contact with water: evidence for the formation of peroxynitrite through a pseudo-second-order post-discharge reaction of H2O2 and HNO2. Plasma Sources Science and Technology, 23(1), 015019.

[Lung2007] Lung, J. K., Huang, J. C., Tien, D. C., Liao, C. Y., Tseng, K. H., Tsung, T. T., Kao, W. S., Tsai, T. H., Jwo, C. S., Lin, H. M., & Stobinski, L. (2007). Preparation of gold nanoparticles by arc discharge in water. Journal of alloys and compounds, 434, 655-658.

[Luo2016] Luo, B., Liu, G., Wang, L. (2016). Recent advances in 2D materials for photocatalysis. Nanoscale, 8(13), 6904-6920.

[Lv2017] Lv, W., Bei, J., Zhang, R., *et al*. (2017). $Bi_2O_2CO_3$ nanosheets as electrocatalysts for selective reduction of CO2 to formate at low overpotential. ACS omega, 2(6), 2561-2567.

[Ma2021] Ma, J., Liang, C., Li, H., *et al*. (2021). A novel composite material based on hydroxylated g-C3N4 and oxygen-vacant TiO2 for improvement of photocatalytic performance. Applied Surface Science, 546, 149085.

[Madhusudan2011] Madhusudan, P., Ran, J., Zhang, J., *et al*. (2011). Novel urea assisted hydrothermal synthesis of hierarchical $BiVO4/Bi_2O_2CO_3$ nanocomposites with enhanced visible-light photocatalytic activity. Applied Catalysis B: Environmental, 110, 286-295.

[Madhusudan2013] Madhusudan, P., Zhang, J., Cheng, B., *et al*. (2013). Photocatalytic degradation of organic dyes with hierarchical $Bi_2O_2CO_3$ microstructures under visible-light. CrystEngComm, 15(2), 231-240.

[Makula2018] Makuła, P., Pacia, M., Macyk, W. (2018). How to correctly determine the band gap energy of modified semiconductor photocatalysts based on UV–Vis spectra. The journal of physical chemistry letters, 9(23), 6814-6817.

[Man2020] Man, L., Xu, Q., Li, W., *et al*. (2020). Oxygen vacancy engineering of $Bi_2O_2CO_3$ hierarchical microspheres for enhanced adsorption of Cd2+ ions and photocatalytic degradation of Rodamine B. Applied Surface Science, 512, 145647.

[Marczewska2010] Marczewska, B., Marczewski, K. (2010). First Glass Electrode and its Creators F. Haber and Z. Klemensiewicz–On 100th Anniversary. Zeitschrift für Physikalische Chemie, 224(05), 795-799.

[Mardanian2013] Mardanian, M., Nevar, A. A., Nedel'ko, M., *et al*. (2013). Synthesis of colloidal CuInSe 2 nanoparticles by electrical spark discharge in liquid. The European Physical Journal D, 67(10), 208.

[Mardanian2014] Mardanian, M., Tarasenko, N. V., Nevar, A. A. (2014). Influence of liquid medium on optical characteristics of the Si nanoparticles prepared by submerged electrical spark discharge. Brazilian Journal of Physics, 44(2-3), 240-246.

[Markutsya2010] Markutsya, S. (2010). Modeling and simulation of nanoparticle aggregation in colloidal systems. Retrospective Theses and Dissertations. 15299. Iowa State University Ames, Iowa, USA.

[Matijevic2012] Matijevic, E., Good, R. J. (Eds.). (2012). Surface and colloid science (Vol. 12). Springer Science & Business Media.

[Meakin1983] Meakin, P. (1983). Formation of fractal clusters and networks by irreversible diffusion-limited aggregation. Physical Review Letters, 51(13), 1119.

[Meakin1988] Meakin, P., Family, F. (1988). Structure and kinetics of reaction-limited aggregation. Physical Review A, 38(4), 2110.

[Meng2013] Meng, F. E. I., Morin, S. A., Forticaux, A., *et al*. (2013). Screw dislocation driven growth of nanomaterials. Accounts of chemical research, 46(7), 1616-1626.

[Meng2022] Meng, L., Chang, L., Hou, J. (2022). Degradation of methyl green from wastewater with ultrasound synergized with $Bi_2O_2CO_3$ catalysis: Kinetics, products, and pathways. Journal of Cleaner Production, 342, 130976.

[Menon1998] Menon, S., Lal, M. (1998). On the dynamics and instability of bubbles formed during underwater explosions. Experimental thermal and fluid science, 16(4), 305-321.

[Mizukoshi2017] Mizukoshi, Y., Hori, F., Okitsu, K. (2017). Comparison of reductive nanoparticle preparation using plasma and ultrasound irradiation in aqueous solution. Japanese Journal of Applied Physics, 57(1), 0102A5.

[Morin2011] Morin, S. A., Forticaux, A., Bierman, M. J., *et al*. (2011). Screw dislocation-driven growth of two-dimensional nanoplates. Nano letters, 11(10), 4449-4455.

[Muniz-Miranda2011] Muniz-Miranda, M., Del Rosso, T., Giorgetti, E., *et al*. (2011). Surface-enhanced fluorescence and surface-enhanced Raman scattering of push–pull molecules: sulfur-functionalized 4-amino-7-nitrobenzofurazan adsorbed on Ag and Au nanostructured substrates. Analytical and bioanalytical chemistry, 400, 361-367.

[Nguyen2022] Nguyen, T. T., Le, T. T., Nguyen, T. B. T., *et al*. (2022). Effect of pH on the Performance of $Bi_2O_2CO_3$ Nanoplates for Methylene Blue Removal in Water by Adsorption and Photocatalysis. Bulletin of Chemical Reaction Engineering & Catalysis, 17(2), 331-339.

[Ni2016] Ni, Z., Sun, Y., Zhang, Y., *et al*. (2016). Fabrication, modification and application of $(BiO)_2CO_3$-based photocatalysts: a review. Applied Surface Science, 365, 314-335.

[NIST2023] Kramida A., Ralchenko Yu., Reader J. and NIST ASD Team (2022). NIST Atomic Spectra Database (ver. 5.10), [Online]. Available: https://physics.nist.gov/asd [2023, July 3]. National Institute of Standards and Technology, Gaithersburg, MD.

[Nominé2021] Nominé, A. V., Noel, C., Gries, T., *et al*. (2021). Study by Optical Spectroscopy of Bismuth Emission in a Nanosecond-Pulsed Discharge Created in Liquid Nitrogen. Molecules, 26(23), 7403.

[Oh-Ishi2020] Oh-Ishi, K., Ohsuna, T. (2020). Inelastic mean free path measurement by STEM-EELS technique using needle-shaped specimen. Ultramicroscopy, 212, 112955.

[Ortiz2019] Ortiz-Medina, J., Wang, Z., Cruz-Silva, R., *et al*. (2019). Defect Engineering and Surface Functionalization of Nanocarbons for Metal-Free Catalysis. Advanced Materials, 31(13), 1805717.

[Oshima2012] Oshima, F., Stauss, S., Ishii, C., *et al*. (2012). Plasma microreactor in supercritical xenon and its application to diamondoid synthesis. Journal of Physics D: Applied Physics, 45(40), 402003.

[Ou2008] Ou, D. R., Mori, T., Ye, F., *et al*. (2008). Oxygen-vacancy ordering in lanthanide-doped ceria: Dopant-type dependence and structure model. Physical review B, 77(2), 024108.

[Ozturk2020] Ozturk,U., Cabrera, J-M., Calvo, J., *et al*. (2020), High-Temperature Deformation Behavior of 718Plus: Consideration of γ' Effects Materials Performance and Characterization 9, no. 2 (2020), 57–74

[Palneedi2018] Palneedi, H., Peddigari, M., Hwang, G. T., *et al*. (2018). High-performance dielectric ceramic films for energy storage capacitors: progress and outlook. Advanced Functional Materials, 28(42), 1803665.

[Park2009] Park, J., Heo, S., Chung, J. G., *et al*. (2009). Bandgap measurement of thin dielectric films using monochromated STEM-EELS. Ultramicroscopy, 109(9), 1183-1188.

[Parkansky2005] Parkansky, N., Alterkop, B., Boxman, R. L., Goldsmith, S., Barkay, Z., & Lereah, Y. (2005). Pulsed discharge production of nano-and microparticles in ethanol and their characterization. Powder Technology, 150(1), 36-41.

[Parkansky2008] Parkansky, N., Alterkop, B. A., Boxman, R. L., *et al*. (2008). Submerged arc breakdown of sulfadimethoxine (SDM) in aqueous solutions. Plasma Chemistry and Plasma Processing, 28(5), 583-592.

[Pei2023] Pei, X., An, W., Zhao, H., *et al*. (2023). Enhancing visible-light degradation performance of g-C3N4 on organic pollutants by constructing heterojunctions via combining tubular g-C3N4 with Bi2O3 nanosheets. Journal of Alloys and Compounds, 934, 167928.

[Phillips1971] Phillips, F. C. (1971). An introduction to crystallography, 4th ed. Singapore: Longman.

[Pootawang2012] Pootawang, P., Saito, N., Takai, O., *et al*. (2012). Synthesis and characteristics of Ag/Pt bimetallic nanocomposites by arc-discharge solution plasma processing. Nanotechnology, 23(39), 395602.

[Pootawang2013] Pootawang, P., Saito, N., & Lee, S. Y. (2013). Discharge time dependence of a solution plasma process for colloidal copper nanoparticle synthesis and particle characteristics. Nanotechnology, 24(5), 055604.

[Porter2009] Porter D. A., Easterling K. E., Sherif M.Y ., (2009). Chap. 3: Crystal Interfaces and Microstructures. In: Phase Transformations in Metals and Alloys, 3rd ed. Boca Raton: CRC Press. pp. 113-198.

[Povarnitsyn2013] Povarnitsyn, M. E., Itina, T. E., Levashov, P. R., *et al*. (2013). Mechanisms of nanoparticle formation by ultra-short laser ablation of metals in liquid environment. Physical Chemistry Chemical Physics, 15(9), 3108-3114.

[Qin2021] Qin, H., Yang, Y., Shi, W., *et al*. (2021). Few-layer Bi 2 O 2 CO 3 nanosheets derived from electrochemically exfoliated bismuthene for the enhanced photocatalytic degradation of ciprofloxacin antibiotic. RSC advances, 11(23), 13731-13738.

[Qotba2005] Qotba, R., Aitken, F., Denat, A. (2005, June). Experimental investigation of the behavior of microscopic bubbles in insulating liquids: influence of pressure and temperature. In IEEE International Conference on Dielectric Liquids, 2005. ICDL 2005. (pp. 115-118). IEEE.

[Rahaghi2015] Rahaghi, S. H., Poursalehi, R., Miresmaeili, R. (2015). Optical properties of Ag-Cu alloy nanoparticles synthesized by DC arc discharge in liquid. Procedia Materials Science, 11, 738-742.

[Rao2014] Rao, S. V., Podagatlapalli, G. K., Hamad, S. (2014). Ultrafast laser ablation in liquids for nanomaterials and applications. Journal of nanoscience and nanotechnology, 14(2), 1364-1388.

[Rebollo2014] Rebollo-Plata, B., Sampedro, M. P., Gallardo-Gómez, G., Ortega-Miranda, N., Bravo-Barrera, C. F., Daniel-Pérez, G., ... & Jiménez-Sandoval, S. (2014). Growth of metal micro and/or nanoparticles utilizing arc-discharge immersed in liquid. Revista mexicana de física, 60(3), 227-232.

[Redjaïmia1993] Redjaïmia, A., Ruterana, P., Metauer, G., *et al.* (1993). Identification and characterization of a novel intermetallic compound in a Fe-22 wt% Cr-5 wt% Ni-3 wt% Mo-0.03 wt% C duplex stainless steel. Philosophical Magazine A, 67(5), 1277-1286.

[Reich2017] Reich, S., Schönfeld, P., Wagener, P., *et al.* (2017). Pulsed laser ablation in liquids: Impact of the bubble dynamics on particle formation. Journal of colloid and interface science, 489, 106-113.

[Rodríguez-González2006] Rodríguez-González, B., Pastoriza-Santos, I., Liz-Marzán, L. M. (2006). Bend contours in silver nanoprisms. The Journal of Physical Chemistry B, 110(24), 11796-11799.

[Saito2012] Saito, G., Hosokai, S., Tsubota, M., *et al.* (2012). Influence of solution temperature and surfactants on morphologies of tin oxide produced using a solution plasma technique. Crystal growth & design, 12(5), 2455-2459.

[Saito2015] Saito G., Akiyama T. (2015).Nanomaterial synthesis using plasma generation in liquid. Journal of Nanomaterials, 2015, 123696.

[Saito2018] Saito, N., Bratescu, M. A., Hashimi, K. (2018). Solution plasma: A new reaction field for nanomaterials synthesis. Japanese Journal of Applied Physics, 57(1), 0102A4.

[Saito2019] Saito, N., Ueno, T., Bratescu, M. A., *et al.* (2019). Synthesis of Nanomaterials Using Solution Plasma Process. Novel Structured Metallic and Inorganic Materials. Setsuhara Y. *et al.* (eds.). Springer Nature Singapore Pte Ltd. Chap 23, 343-355.

[Sambles1970] Sambles, J. R., Skinner, L. M., Lisgarten, N. D. (1970). An electron microscope study of evaporating small particles: the Kelvin equation for liquid lead and the mean surface energy of solid silver. Proceedings of the Royal Society of London. A. Mathematical and Physical Sciences, 318(1535), 507-522.

[Sambles1971] Sambles, J. R. (1971). An electron microscope study of evaporating gold particles: the Kelvin equation for liquid gold and the lowering of the melting point of solid gold particles. Proceedings of the Royal Society of London. A. Mathematical and Physical Sciences, 324(1558), 339-351.

[Sano2001] Sano, N., Wang, H., Chhowalla, M., *et al.* (2001). Synthesis of carbon'onions' in water. Nature, 414(6863), 506-507.

[Sano2002] Sano, N., Wang, H., Alexandrou, I., *et al*. (2002). Properties of carbon onions produced by an arc discharge in water. Journal of Applied Physics, 92(5), 2783-2788.

[Sano2004] Sano N., Kikuchi T., Wang H., *et al.* (2004). Carbon nanohorns hybridized with a metal-included nanocapsule. Carbon, 42, 95–99.

[Sano2008] Sano, N., Kawanami, O., Charinpanitkul, T., *et al*. (2008). Study on reaction field in arc-in-water to produce carbon nano-materials. Thin Solid Films, 516(19), 6694-6698.

[Sarou-Kanian2003] Sarou-Kanian, V., Millot, F., Rifflet, J. C. (2003). Surface tension and density of oxygen-free liquid aluminum at high temperature. International journal of Thermophysics, 24(1), 277-286.

[Sato1992] Sato, T., Usuki, K., Okuwaki, A., & Goto, Y. (1992). Synthesis of metal nitrides and carbide powders by a spark discharge method in liquid media. Journal of materials science, 27(14), 3879-3882.

[Senthilnathan2013] Senthilnathan, J., Weng, C. C., Liao, J. D., *et al*. (2013). Submerged liquid plasma for the synthesis of unconventional nitrogen polymers. Scientific reports, 3, 2414.

[Sergiienko2007] Sergiienko, R., Shibata, E., Zentaro, A., *et al*. (2007). Formation and characterization of graphite-encapsulated cobalt nanoparticles synthesized by electric discharge in an ultrasonic cavitation field of liquid ethanol. Acta Materialia, 55(11), 3671-3680.

[Sergiienko2010] Sergiienko, R., Kim, S., Shibata, E., *et al*. (2010). Structure of Fe–Pt alloy included carbon nanocapsules synthesized by an electric plasma discharge in an ultrasonic cavitation field of liquid ethanol. Journal of Nanoparticle Research, 12(2), 481-491.

[Shi2019] Shi, H. L., Zou, B., Li, Z. A., *et al*. (2019). Direct observation of oxygen-vacancy formation and structural changes in Bi2WO6 nanoflakes induced by electron irradiation. Beilstein Journal of Nanotechnology, 10(1), 1434-1442.

[Shih2017] Shih, C. Y., Shugaev, M. V., Wu, C., *et al*. (2017). Generation of subsurface voids, incubation effect, and formation of nanoparticles in short pulse laser interactions with bulk metal targets in liquid: Molecular dynamics study. The Journal of Physical Chemistry C, 121(30), 16549-16567.

[Shih2018] Shih, C.-Y., Streubel, R., Heberle, J., *et al*. (2018). Two mechanisms of nanoparticle generation in picosecond laser ablation in liquids: the origin of the bimodal size distribution. Nanoscale, 10, 6900-6910.

[Shih2020] Shih, C. Y., Shugaev, M. V., Wu, C., *et al*. (2020). The effect of pulse duration on nanoparticle generation in pulsed laser ablation in liquids: Insights from large-scale atomistic simulations. Physical Chemistry Chemical Physics, 22(13), 7077-7099.

[Shiyan2015] Shiyan, L. N., Yavorovskii, N. A., Pustovalov, A. V., *et al*. (2015, April). Influence of the type of electric discharge on the properties of the produced aluminium nanoparticles. In IOP Conference Series: Materials Science and Engineering. Vol. 81: Radiation-Thermal Effects and Processes in Inorganic Materials.—United Kingdom, 2015. (Vol. 81, p. 120775). IOP Publishing.

[Shizuno2011] Shizuno, T., Miyazoe, H., Saito, K., *et al.* (2011). Synthesis of diamondoids by supercritical xenon discharge plasma. Japanese Journal of Applied Physics, 50(3R), 030207.

[Skiba2018] Skiba O., Redjaïmia, A., Dulcy, J., *et al.* (2018), A proper assessment of TEM diffraction patterns originating from CrN nitrides in a ferritic matrix, Materials Characterization, 144, 671–677

[Starikovskiy2011] Starikovskiy, A., Yang, Y., Cho, Y. I., *et al.* (2011). Non-equilibrium plasma in liquid water: dynamics of generation and quenching. Plasma Sources Science and Technology, 20(2), 024003.

[Stoldt1999] Stoldt, C. R., Jenks, C. J., Thiel, P. A., *et al.* (1999). Smoluchowski ripening of Ag islands on Ag (100). The Journal of chemical physics, 111(11), 5157-5166.

[Suito1965] Suito, E., Uyeda, N. (1965). Electron microscopy and diffraction studies on the growth and structure of laminar single crystals of colloidal gold (Special Issue on Electron Microscopy). Bulletin of the Institute for Chemical Research, Kyoto University, 42(6), 511-541.

[Sulaimankulova2019] Sulaimankulova, S., Mametova, A., Abdullaeva, Z. (2019). Fusiform gold nanoparticles by pulsed plasma in liquid method. SN Applied Sciences, 1(11), 1427.

[Sun2016] Sun, S. H., Jung, S. C. (2016). Facile synthesis of bimetallic Ni-Cu nanoparticles using liquid phase plasma method. Korean Journal of Chemical Engineering, 33(3), 1075-1079.

[Sun2017] Sun, M., Yan, T., Zhang, Y., *et al.* (2018). Rod-like Bi4O7 decorated $Bi_2O_2CO_3$ plates: Facile synthesis, promoted charge separation, and highly efficient photocatalytic degradation of organic contaminants. Journal of colloid and interface science, 514, 240-249.

[Sun2020] Sun, D., Huang, L., Li, L., *et al.* (2020). Plasma enhanced Bi/ $Bi_2O_2CO_3$ heterojunction photocatalyst via a novel in-situ method. Journal of colloid and interface science, 571, 80-89.

[Swiatkowska2015] Swiatkowska-Warkocka, Z., Pyatenko, A., Krok, F., *et al.* (2015). Synthesis of new metastable nanoalloys of immiscible metals with a pulse laser technique. Scientific reports, 5, 9849.

[Tahboub1979] Tahboub, R. M., El Guindy, M., Merchant, H. D. (1979). Oxidation kinetics of bismuth and its dilute alloys. Oxidation of metals, 13, 545-556.

[Tamaddon2011] Tamaddon, F., Aboee, F., Nasiri, A. (2011). ZnO nanofluid as a structure base catalyst for chemoselective amidation of aliphatic carboxylic acids. Catalysis Communications, 16(1), 194-197.

[Tarasenka2020] Tarasenka, N., Nominé, A., Nevar, A., *et al.* (2020). Synergistic effect of plasma and laser processes in liquid for alloyed-nanoparticle synthesis. Physical Review Applied, 13(1), 014021.

[Teijlingen2020] van Teijlingen, A., Davis, S. A., Hall, S. R. (2020). Size-dependent melting point depression of nickel nanoparticles. Nanoscale Advances, 2, 2347–2351.

[Thiele2009] Thiele, U., Vancea, I., Archer, A. J., *et al.* (2009). Modelling approaches to the dewetting of evaporating thin films of nanoparticle suspensions. Journal of Physics: Condensed Matter, 21(26), 264016.

[Thomas1979] Thomas, G., Goringe, M. J. (1979). Transmission electron microscopy of materials. New York, Chichester, Brisbane, Toronto: John Wiley and Sons.

[Tian2014] Tian, N., Huang, H., Guo, Y., *et al.* (2014). A g-C_3N_4/$Bi_2O_2CO_3$ composite with high visible-light-driven photocatalytic activity for rhodamine B degradation. Applied surface science, 322, 249-254.

[Tian2022] Tian, N., Hu, C., Wang, J., *et al.* (2022). Layered bismuth-based photocatalysts. Coordination Chemistry Reviews, 463, 214515.

[Tien2010] Tien, D. C., Chen, L. C., Van Thai, N., & Ashraf, S. (2010). Study of Ag and Au nanoparticles synthesized by Arc discharge in deionized water. Journal of nanomaterials, 2010.

[Tomaszewska2013] Tomaszewska, E., Soliwoda, K., Kadziola, K., *et al.* (2013). Detection limits of DLS and UV-Vis spectroscopy in characterization of polydisperse nanoparticles colloids. Journal of Nanomaterials, 2013, 60-60.

[Trad2019] Trad, M., Nominé, A., Tarasenka, N., *et al.* (2019). Synthesis of Ag and Cd nanoparticles by nanosecond-pulsed discharge in liquid nitrogen. Frontiers of Chemical Science and Engineering, 13(2), 360-368.

[Trad2020] Trad, M., Nominé, A., Noël, C., *et al.* (2020). Evidence of alloy formation in CoNi nanoparticles synthesized by nanosecond-pulsed discharges in liquid nitrogen. Plasma Processes and Polymers, 17(5), 1900255.

[Tseng2009] Tseng, K. H., Huang, J. C., Liao, C. Y., Tien, D. C., & Tsung, T. T. (2009). Preparation of gold ethanol colloid by the arc discharge method. Journal of alloys and compounds, 472(1-2), 446-450.

[Tseng2013] Tseng, K. H., Lee, H. L., Liao, C. Y., *et al.* (2013). Rapid and efficient synthesis of silver nanofluid using electrical discharge machining. Journal of Nanomaterials, 2013.

[Tsukanov2019] Tsukanov, A. A., Lozhkomoev, A. S., Lerner, M. I., *et al.* (2019). Molecular dynamics study of bimetallic Fe–Cu Janus nanoparticles formation by electrical explosion of wires. Philosophical Magazine, 99(9), 1121-1138.

[Umar2016] Umar, A., Ahmad, R., Kumar, R., *et al.* (2016). $Bi_2O_2CO_3$ nanoplates: Fabrication and characterization of highly sensitive and selective cholesterol biosensor. Journal of Alloys and Compounds, 683, 433-438.

[Ushio2004] Ushio, M., Tanaka, M., Lowke, J. J. (2004). Anode melting from free-burning argon arcs. IEEE transactions on Plasma Science, 32(1), 108-117.

[Van Landeghem2015] Van Landeghem, H.P., Gouné M., Bordère, L.S., *et al.* (2015), Competitive precipitation of amorphous and crystalline silicon nitride in ferrite: Interaction between structure, morphology, and stress relaxation, Acta Materialia 93 (2015) 218–234

[Vanraes2016] Vanraes, P., Nikiforov, A. Y., Leys, C. (2016). Electrical discharge in water treatment technology for micropollutant decomposition. Plasma science and technology—progress in physical states and chemical reactions, 429.

[Varón2013] Varón, M., Ojea-Jimenez, I., Arbiol, J., *et al*. (2013). Spontaneous formation of hollow cobalt oxide nanoparticles by the Kirkendall effect at room temperature at the water–air interface. Nanoscale, 5(6), 2429-2436.

[Verwey1955] Verwey, E. J. W., Overbeek, J. T. G. (1955). Theory of the stability of lyophobic colloids. Journal of Colloid Science, 10(2), 224-225.

[Vesta2011] Momma, K., Izumi, F., (2011) VESTA 3 for three-dimensional visualization of crystal, volumetric and morphology data. Journal of Applied Crystallography, 44, 1272-1276.

[Viswanath2008] Viswanath, B., Kundu, P., Mukherjee, B., *et al*. (2008). Predicting the growth of two-dimensional nanostructures. Nanotechnology, 19(19), 195603.

[Vitos1998] Vitos, L., Ruban, A. V., Skriver, H. L., *et al*. (1998). The surface energy of metals. Surface science, 411(1-2), 186-202.

[Volkov2017] Volkov, A. N., Zhigilei, L. V. (2017). Melt dynamics and melt-through time in continuous wave laser heating of metal films: Contributions of the recoil vapor pressure and Marangoni effects. International Journal of Heat and Mass Transfer, 112, 300-317.

[Wagner1933] Wagner, C. (1933). Beitrag zur theorie des anlaufvorgangs. Zeitschrift für physikalische Chemie, 21(1), 25-41.

[Wang2005] Wang, C. M., Baer, D. R., Thomas, L. E., *et al*. (2005). Void formation during early stages of passivation: Initial oxidation of iron nanoparticles at room temperature. Journal of Applied Physics, 98(9), 094308.

[Wang2008] Wang, L., Jiang, X. (2008). Plasma-induced reduction of chromium (VI) in an aqueous solution. Environmental science & technology, 42(22), 8492-8497.

[Wang2014] Wang, Q., Yun, G., Bai, Y., *et al*. (2014). Photodegradation of rhodamine B with MoS_2/ $Bi_2O_2CO_3$ composites under UV light irradiation. Applied surface science, 313, 537-544.

[Wang2017] Wang, B., Wang, J., Zhang, Y., *et al*. (2017). Electrochemical performance of $Bi_2O_2CO_3$ nanosheets as negative electrode material for supercapacitors. Ceramics International, 43(12), 9310-9316.

[Wang2022] Wang, X., Chen, L., Li, C., *et al*. (2022). Enhanced Photocatalytic Performance of $Bi_2O_2CO_3$ Loaded Activated Carbon for Toluene Removal in Air. Applied Sciences, 12(23), 12500.

[Wiley2006] Wiley, B. J., Im, S. H., Li, Z. Y., *et al*. (2006). Maneuvering the surface plasmon resonance of silver nanostructures through shape-controlled synthesis.

[Willis2000] Willis, D. A., Xu, X. (2000). Transport phenomena and droplet formation during pulsed laser interaction with thin films. J. Heat Transfer, 122(4), 763-770.

[Witten1981] Witten Jr, T. A., Sander, L. M. (1981). Diffusion-limited aggregation, a kinetic critical phenomenon. Physical review letters, 47(19), 1400.

[Wu2014] Wu, C., Zhigilei, L. V. (2014). Microscopic mechanisms of laser spallation and ablation of metal targets from large-scale molecular dynamics simulations. Applied Physics A, 114(1), 11-32.

[Wu2016] Wu, C., Zhigilei, L. V. (2016). Nanocrystalline and polyicosahedral structure of a nanospike generated on metal surface irradiated by a single femtosecond laser pulse. The Journal of Physical Chemistry C, 120(8), 4438-4447.

[Wu2023] Wu, C., Zuo, H., Zhao, S., *et al*. (2023). Br-doping mediated band-gap engineering contributed Bi/$Bi_2O_2CO_3$ nano-platelets with enhanced photocatalytic performance. Chemical Engineering Journal, 454, 140157.

[Xia2009] Xia, Y., Xiong, Y., Lim, B., *et al*. (2009). Shape-controlled synthesis of metal nanocrystals: simple chemistry meets complex physics?. Angewandte Chemie International Edition, 48(1), 60-103.

[Xiu2023] Xiu, M., Cao, X., Lu, Y., *et al*. (2023). Electric-field oriented self-assembly of Mn3O4 nanostructures driven by liquid plasma discharge for super capacitor. Electrochimica Acta, 439, 141620

[Xu2002] Xu, X., Willis, D. A. (2002). Non-equilibrium phase change in metal induced by nanosecond pulsed laser irradiation. J. Heat Transfer, 124(2), 293-298.

[Xu2006] Xu, B., Guo, J., Wang, X., *et al*. (2006). Synthesis of carbon nanocapsules containing Fe, Ni or Co by arc discharge in aqueous solution. Carbon, 44(13), 2631-2634.

[Xu2013] Xu, Y. S., Zhang, W. D. (2013). Anion exchange strategy for construction of sesame-biscuit-like $Bi_2O_2CO_3$/Bi_2MoO_6 nanocomposites with enhanced photocatalytic activity. Applied Catalysis B: Environmental, 140, 306-316.

[Yang2005] Yang, D. Q., Gillet, J. N., Meunier, M., *et al*. (2005). Room temperature oxidation kinetics of Si nanoparticles in air, determined by x-ray photoelectron spectroscopy. Journal of Applied Physics, 97(2), 024303.

[Yang2019a] Yang, L., Chen, L., Chen, Y. C., *et al*. (2019). Homogeneously alloyed nanoparticles of immiscible Ag–Cu with ultrahigh antibacterial activity. Colloids and Surfaces B: Biointerfaces, 180, 466-472.

[Yang2019b] Yang, C., Xue, Z., Qin, J., *et al*. (2019). Visible light-driven photocatalytic H2 generation and mechanism insights into $Bi_2O_2CO_3$/G-C_3N_4 Z-scheme photocatalyst. The Journal of Physical Chemistry C, 123(8), 4795-4804.

[Yang2020] Yang, F., Elnabawy, A. O., Schimmenti, R., *et al*. (2020). Bismuthene for highly efficient carbon dioxide electroreduction reaction. Nature communications, 11(1), 1088.

[Yao2004] Yao, W. F., Xu, X. H., Wang, H., *et al*. (2004). Photocatalytic property of perovskite bismuth titanate. Applied Catalysis B: Environmental, 52(2), 109-116.

[Yao2005] Yao, W. T., Yu, S. H., Zhou, Y., *et al.* (2005). Formation of uniform CuO nanorods by spontaneous aggregation: Selective synthesis of CuO, Cu2O, and Cu nanoparticles by a solid– liquid phase arc discharge process. The Journal of Physical Chemistry B, 109(29), 14011-14016.

[Yu2017] Yu, S., Zhang, Y., Dong, F., *et al.* (2017). Readily achieving concentration-tunable oxygen vacancies in $Bi_2O_2CO_3$: Triple-functional role for efficient visible-light photocatalytic redox performance. Applied Catalysis B: Environmental, 226, 441-450.

[Yu2018] Yu, S., Zhang, Y., Dong, F., *et al.* (2018). Readily achieving concentration-tunable oxygen vacancies in $Bi_2O_2CO_3$: Triple-functional role for efficient visible-light photocatalytic redox performance. Applied Catalysis B: Environmental, 226, 441-450.

[Zaman2019] Zaman, Q., Souza, J., Pandoli, O., *et al.* (2019). Two-color surface plasmon resonance nanosizer for gold nanoparticles. Optics express, 27(3), 3200-3216.

[Zerjav2018] Žerjav, G., Djinović, P., Pintar, A. (2018). TiO2-Bi2O3/(BiO)2CO3-reduced graphene oxide composite as an effective visible light photocatalyst for degradation of aqueous bisphenol A solutions. Catalysis Today, 315, 237-246.

[Zhang2014] Zhang, X., Guo, T., Wang, X., *et al.* (2014). Facile composition-controlled preparation and photocatalytic application of $BiOCl/Bi_2O_2CO_3$ nanosheets. Applied Catalysis B: Environmental, 150, 486-495.

[Zhang2017] Zhang, Q., Xu, B., Yuan, S., *et al.* (2017). Improving g-C_3N_4 photocatalytic performance by hybridizing with $Bi_2O_2CO_3$ nanosheets. Catalysis Today, 284, 27-36.

[Zhang2018] Zhang, D., Zhang, C., Liu, J., *et al.* (2018). Carbon-encapsulated metal/metal carbide/metal oxide core–shell nanostructures generated by laser ablation of metals in organic solvents. ACS Applied Nano Materials, 2(1), 28-39.

[Zhang2019a] Zhang, G. Y., Wang, J. J., Shen, X. Q., *et al.* (2019). Br-doped $Bi_2O_2CO_3$ nanosheets with improved electronic structure and accelerated charge migration for outstanding photocatalytic behavior. Applied Surface Science, 470, 63-73.

[Zhang2019b] Zhang, J., Liu, Z., Ma, Z. (2019). Facile formation of $Bi_2O_2CO_3/Bi_2MoO_6$ nanosheets for visible light-driven photocatalysis. ACS omega, 4(2), 3871-3880.

[Zhang2019c] Zhang, F., Zhang, H., Krylyuk, S., Milligan, C.A., Zhu, Y., Zemlyanov, D.Y., Bendersky, L.A., Burton, B.P., Davydov, A.V. and Appenzeller, J. (2019). Electric-field induced structural transition in vertical MoTe2-and Mo1–x W x Te2-based resistive memories. Nature materials, 18(1), pp.55-61.

[Zhang2021a] Zhang, W., Wang, Y., Guo, X., *et al.* (2021). High performance $Bi_2O_2CO_3$/rGO electrode material for asymmetric solid-state supercapacitor application. Journal of Alloys and Compounds, 855, 157394.

[Zhang2021b] Zhang, W., Gao, H., Deng, C., *et al.* (2021). An ultrathin memristor based on a two-dimensional WS 2/MoS 2 heterojunction. Nanoscale, 13(26), pp.11497-11504.

[Zhang2022] Zhang, Y., Chen, Y., Liu, R., *et al.* (2023). Oxygen vacancy stabilized Bi2O2CO3 nanosheet for CO2 electroreduction at low overpotential enables energy efficient CO-production of formate. InfoMat, 5(3), e12375.

[Zhang2023] Zhang, Y., Chen, Y., Liu, R., *et al.* (2023). Oxygen vacancy stabilized $Bi_2O_2CO_3$ nanosheet for CO2 electroreduction at low overpotential enables energy efficient CO-production of formate. InfoMat, 5(3), e12375.

[Zhao2011] Zhao, T., Zai, J., Xu, M., *et al.* (2011). Hierarchical $Bi_2O_2CO_3$ microspheres with improved visible-light-driven photocatalytic activity. CrystEngComm, 13(12), 4010-4017.

[Zhao2013] Zhao, K., Zhang, L., Wang, J., *et al.* (2013). Surface structure-dependent molecular oxygen activation of BiOCl single-crystalline nanosheets. Journal of the American Chemical Society, 135(42), 15750-15753.

[Zhao2015] Zhao, Z., Zhou, Y., Wang, F., *et al.* (2015). Polyaniline-decorated {001} facets of $Bi_2O_2CO_3$ nanosheets: in situ oxygen vacancy formation and enhanced visible light photocatalytic activity. ACS applied materials & interfaces, 7(1), 730-737.

[Zheng2010] Zheng, Y., Duan, F., Chen, M., *et al.* (2010). Synthetic $Bi_2O_2CO_3$ nanostructures: novel photocatalyst with controlled special surface exposed. Journal of Molecular Catalysis A: Chemical, 317(1-2), 34-40.

[Zheng2019] Zheng, X., Yuan, J., Shen, J., *et al.* (2019). A carnation-like rGO/$Bi_2O_2CO_3$/BiOCl composite: Efficient photocatalyst for the degradation of ciprofloxacin. Journal of Materials Science: Materials in Electronics, 30, 5986-5994.

[Zhou2010] Zhou, L., Yu, M., Yang, J., *et al.* (2010). Nanosheet-based $Bi_2Mo_xW_{1-x}O_6$ solid solutions with adjustable band gaps and enhanced visible-light-driven photocatalytic activities. The Journal of Physical Chemistry C, 114(44), 18812-18818.

[Zhu2019] Zhu, K., Liang, X., Yuan, B., Villena, M.A., Wen, C., Wang, T., Chen, S., Hui, F., Shi, Y. and Lanza, M. (2019). Graphene–boron nitride–graphene cross-point memristors with three stable resistive states. ACS applied materials & interfaces, 11(41), pp.37999-38005.

[Zhuang2013] Zhuang, H., Zhang, L., Fuchs, R., *et al.* (2013). When epitaxy meets plasma: a path to ordered nanosheets arrays. Scientific Reports, 3(1), 2427.

[Ziashahabi2017] Ziashahabi, A., Poursalehi, R., Naseri, N. (2017). Formation mechanism of bead-chain-like ZnO nanostructures from oriented attachment of Zn/ZnO nanocomposites prepared via DC arc discharge in liquid. Materials Science in Semiconductor Processing, 72, 128-133.

[Zu2021] Zu, X., Zhao, Y., Li, X., *et al.* (2021). Ultrastable and efficient visible-light-driven CO_2 reduction triggered by regenerative oxygen-vacancies in $Bi_2O_2CO_3$ nanosheets. Angewandte Chemie International Edition, 60(25), 13840-13846.

Résumé

Synthèse de nanofeuillets de $Bi_2O_2CO_3$ par décharges électriques dans des liquides pour des applications photocatalytiques et nanoélectroniques

Ce travail porte sur la synthèse de feuillets nanométriques ultraminces composés de Bi2O2CO3, ci-après dénommé BOC. La synthèse est réalisée par une technique rapide et simple connue sous le sigle EDDL correspondant au procédé de décharges électriques dans les liquides diélectriques. Pour assurer la reproductibilité de la synthèse, une méthode de prétraitement impliquant la gravure d'électrodes de bismuth avec du Nital a été employée. Le procédé choisi consiste à initier des décharges électriques entre ces électrodes alors qu'elles sont immergées soit dans l'azote liquide, soit dans l'eau (voir Figure 1).

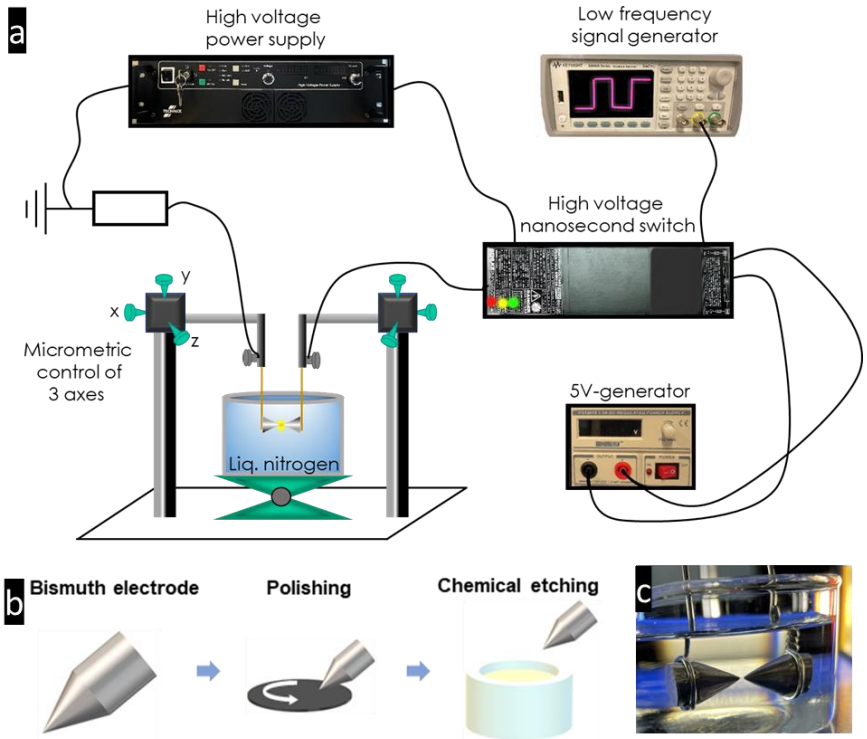

d

Solution	Composition
Nital 4%	96 ml C_2H_5OH + 4 ml HNO_3 (>70 wt.%)
Nital 5%	95 ml C_2H_5OH + 5 ml HNO_3 (>70 wt.%)
Chloric-based solution	30 ml HCL + 2 g $FeCl_3$ + 100 ml H_2O

Fig. 1 : a) Schéma de l'installation expérimentale, ici présentée dans le cas de l'azote liquide. b) Prétraitement des électrodes gravée dans l'une des solutions chimiques présentées en d). c) Image des électrodes dans de l'eau Milli-Q. d) Composition des quatre solutions chimiques testées dans cette étude.

Brièvement, la configuration expérimentale utilisée (Fig. 1a) comporte un commutateur à semi-conducteurs (Behlke HTS-301-03-GSM) connecté à une électrode pointe, tandis que l'autre électrode pointe est mise à la masse. Le commutateur est alimenté par un générateur de puissance à haute tension continue (Technix SR15-R-1200-15 kV-80 mA). Le temps de montée en tension est d'environ 20 ns. Des impulsions de tension positives, d'une durée de 75 ns, sont appliquées à une fréquence de 10 Hz à l'électrode d'alimentation (anode) pendant une durée de 30 minutes. L'influence de la tension appliquée a été étudiée dans la plage de +4 à +10 kV. Les nanofeuillets sont formés uniquement lorsque la tension est légèrement supérieure à la tension de claquage, environ +4 kV pour l'azote liquide et l'eau Milli-Q ultrapure. Plus précisément, les nanofeuillets sont synthétisées entre +4 kV et +5 kV, la production la plus élevée étant observée à +5 kV. Au-delà de cette tension, des nanoparticules sont synthétisées et d'autant plus nombreuses que la tension augmente. À +10 kV, les nanofeuillets ne sont plus synthétisés. Tous les résultats présentés dans cette étude ont été obtenus à +5 kV.

On a pu observer que les deux liquides utilisés (l'azote liquide et l'eau) conduisent à des nanostructures identiques (Figure 2), une similitude validée par spectroscopie d'émission optique, technique qui a permis de confirmer la nature métallique de la décharge dans les deux milieux. Après cette étape, les nanofeuillets subissent une oxydation et une carbonatation rapide lorsqu'ils sont exposés à l'air.

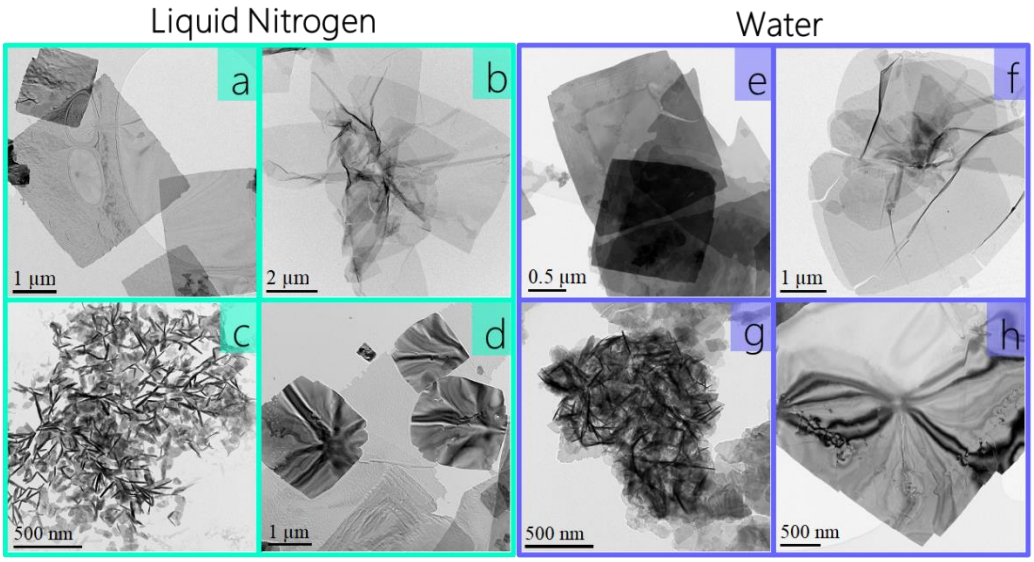

Fig. 2 : Micrographies TEM en champ clair montrant les différentes formes de nanofeuillets synthétisés dans l'azote liquide et dans l'eau. a) et e) nanofeuillets minces et plats. b) et f) nanofeuillets minces froissés. c) et g) nanofeuillets minces enroulés. d) et h) nanofeuillets épais et plats.

Le mécanisme de croissance proposé est étroitement lié au mécanisme connu sous le nom de « ledge mechanism », en raison de la présence de « kinks » et de « jogs » clairement visibles le long des bords des nanofeuillets (Figure 3). Ces nanostructures bidimensionnelles émergent d'abord à la surface de la cathode et croissent ensuite verticalement (Figure 4). Cette croissance anisotrope est rendue possible par l'assistance ionique dans les régions qui ressemblent à des motifs en forme de peigne formés pendant l'étape de gravure chimique, condition préalable nécessaire à une forte reproductibilité du processus de croissance.

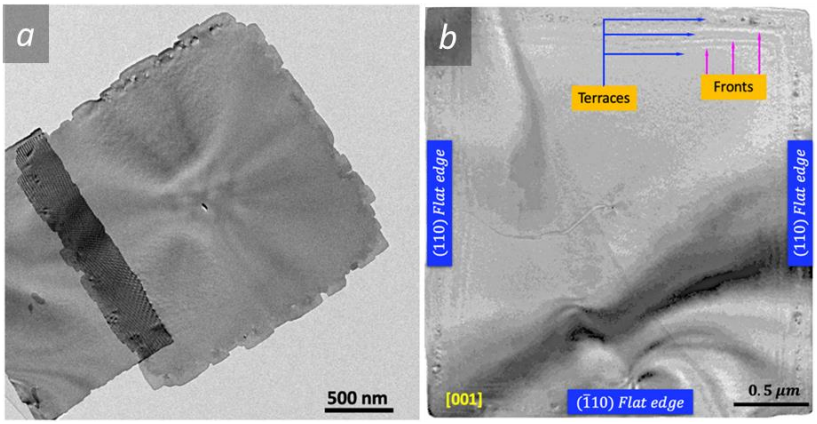

Fig. 3: Images TEM en champ clair montrant la forme carrée des nanofeuillets de BOC avec a) des bords dentelés par des coins (terrasses et fronts) et b) des bords plats (sans coins apparents). On peut remarquer la présence de terrasses et de fronts sur la surface projetée.

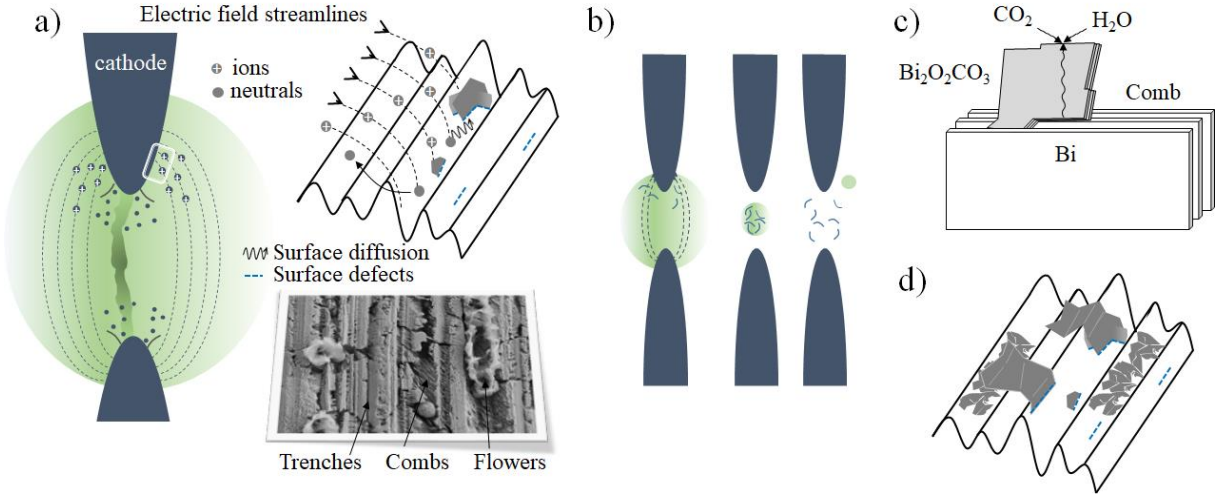

Fig. 4: Schéma des mécanismes de croissance déduits des résultats actuels. Dans le liquide : a) Lorsque les ions sont neutralisés au niveau de la cathode, ils peuvent diffuser à la surface et se désorber s'ils n'entrent en contact avec aucun défaut. Sinon, ils contribuent à la croissance des nanofeuillets. Les espèces neutres émises vers l'extérieur depuis l'extrémité de l'électrode ne contribuent pas à la croissance. b) La collecte et l'éjection des nanofeuillets sont provoquées par le mouvement de l'interface gaz-liquide de la bulle de décharge. Dans l'air : c) Les atomes de Bi du noyau de l'électrode diffusent vers l'extérieur et atteignent la surface où ils réagissent avec H2O et CO2 pour former Bi2O2CO3. d) Ce processus est activé à température ambiante et cinétiquement lent, mais les nanofeuillets peuvent croître significativement pour recouvrir les tranchées.

La caractérisation cristallographique détaillée des nanofeuillets de BOC a été réalisée à l'aide d'une série de techniques, notamment la microscopie électronique en transmission (TEM), la microscopie électronique en transmission à balayage (STEM), la microscopie électronique en transmission à haute résolution (HRTEM), la spectroscopie de rayons X à dispersion d'énergie (EDX), la diffraction d'électrons en aire sélectionnée (SAED), la diffraction d'électrons en faisceau convergent (CBED), la microscopie électronique en transmission filtrée en énergie (EFTEM) et la spectroscopie de perte d'énergie des électrons (EELS). L'étude révèle que la structure cristallographique du BOC est conforme au groupe spatial I4/mmm, avec des paramètres de maille a=3,91 Å et c=13,77 Å, une détermination qui a été confirmée par diffraction des rayons X (DRX).

L'étude clarifie également l'origine potentielle des taches satellites qui sont régulièrement observées dans les motifs SAED le long de l'axe de zone [001]. Dans cette étude, ces taches ont été principalement attribuées à deux phénomènes : la diffraction multiple et les transformations locales ordre-désordre qui se produisent dans la structure cristalline du BOC. Cette transformation implique une transition d'une structure quadratique centrée vers un réseau primitif de Bravais (Figure 5).

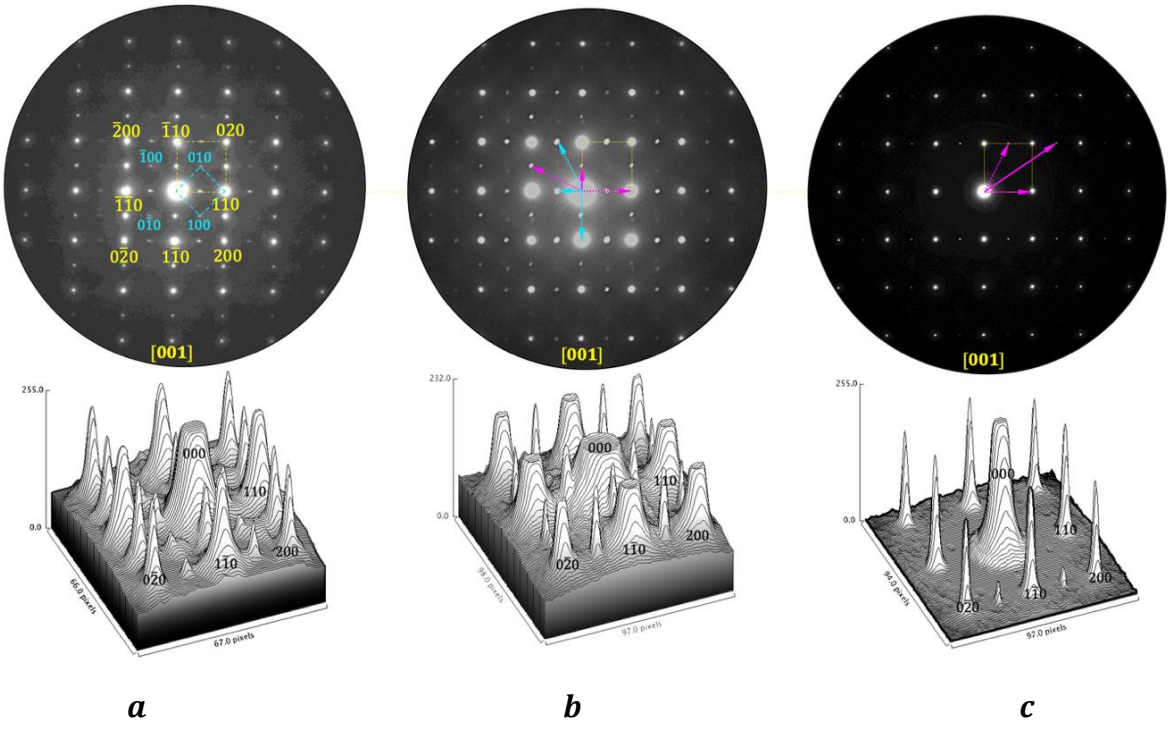

Fig. 5 : Origine des réflexions supplémentaires sur le motif de diffraction électronique enregistré le long de [001] sur différentes zones sous le faisceau électronique : a) transformation ordre-désordre (maille unitaire en cyan), b) et c) diffraction multiple mise en évidence par des vecteurs colorés en cyan et/ou en magenta.

Afin d'évaluer leur utilité pratique, nous avons mesuré la performance photocatalytique des nanofeuillets de BOC synthétisés à l'aide de la méthode EDDL (Figure 6). Lorsqu'ils sont comparés aux nanoparticules commerciales de Bi2O3, les nanofeuillets de BOC montrent une efficacité globale de la dégradation des deux colorants choisis (Rhodamine B et Méthyl Orange – données non fournies ici –) comparable si l'on tient compte des surfaces actives respectives des deux catalyseurs. Nous n'avons pas pu démontrer d'activité supplémentaire qui pourrait être attribuée à l'orientation spécifique des plans exposés des nanofeuillets de BOC. En comparaison avec d'autres études, la réactivité de surface des nanofeuillets de BOC s'est révélée être indépendante de leur épaisseur.

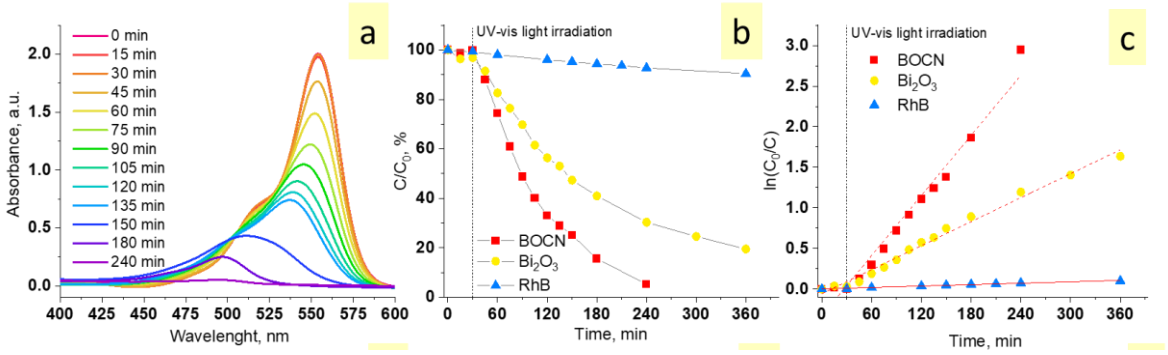

Fig. 6 : a) Évolution de l'absorbance de la Rhodamine B en fonction du temps d'exposition à la lampe Xe en présence de BOCN, b) Dégradation photocatalytique de la Rhodamine B en fonction du temps d'irradiation, sans catalyseur, en présence de BOCN et de nanoparticules commerciales de Bi2O3, c) Courbes cinétiques de la dégradation de la Rhodamine B.

En outre, les nanofeuillets de BOC ont été testés pour leur potentiel d'application dans les dispositifs électroniques. Les résultats de ces tests ont révélé que le BOC présente des valeurs de champ de claquage remarquables, se situant approximativement entre 12 et 14 MV/cm². Les nanofeuillets possèdent une largeur de bande de 3,5 à 4 eV, et reste stable jusqu'à 300°C. Pour évaluer les caractéristiques électriques du BOC, un dispositif de type architecture verticale métal-isolant-métal (MIM) a été développé. Les courbes I-V obtenues sont présentées Figure 7. La forme de la courbe d'hystérésis présente deux cycles de commutation de résistance, un phénomène observé dans plusieurs systèmes 2D avec une géométrie verticale où les auteurs attribuent ce comportement à des phénomènes memristifs.

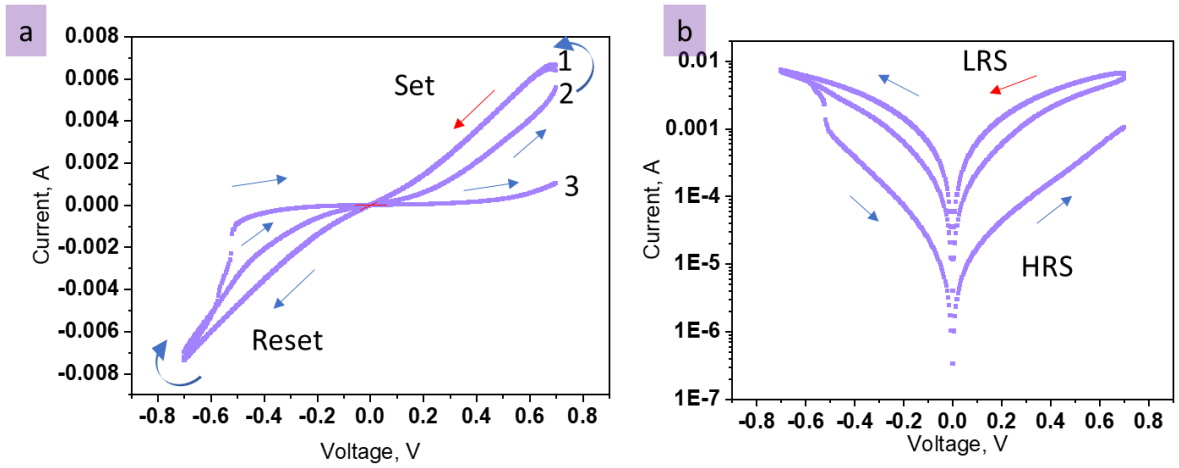

Fig. A7: Courbes I-V caractéristiques du dispositif MIM basé sur un matériau BOC à Vmax 700 mV. a) et b) courbes I-V typiques du dispositif ; les courbes originales en a) représentent un processus de commutation à 2 cycles (boucle du 1er cycle représentée par 1-2, boucle du 2ème cycle par 2-3. Les mêmes courbes sont présentées en échelle logarithmique en b). Elles montrent des états évidents de résistance faible et élevée (notés LRS et HRS).

Cependant, il est difficile d'attribuer définitivement ce comportement uniquement au matériau BOC lui-même, car certains dispositifs sans nanofeuillets présentent un comportement similaire, suggérant qu'il pourrait s'agir d'un effet collectif des contacts et du nanofeuillet de BOC. L'absence de données disponibles sur le comportement memristif du BOC requiert de devoir reprendre ces mesures de manière plus approfondie.

Synthesis of $Bi_2O_2CO_3$ nanosheets by electrical discharges in liquids for photocatalytic and nanoelectronic applications

Abstract:

This work reports on the synthesis of $Bi_2O_2CO_3$ (BOC) ultrathin nanosheets by electrical discharges in liquids, involving the initiation of electrical discharges between two Bi electrodes submerged in either liquid nitrogen or water, resulting in identical nanostructures. Optical Emission Spectroscopy confirms the metallic nature of the discharge in both environments. Subsequently, nanosheets undergo rapid oxidation and carbonation upon exposure to air. The growth mechanism, related to the ledge mechanism, was proposed. Detailed crystallographic characterization of BOC nanosheets confirms their structure in space group I4/mmm (a=3.91 Å, c=13.77 Å). The study also elucidates the potential nature of satellite spots consistently observed in SAED patterns along the [001] zone axis, which primarily arises from multiple diffraction and local disorder-to-order transformations within the BOC crystal structure. Catalytic performance of BOC nanosheets is found to be consistent with BOC obtained through alternative methods. Additionally, the electronic performance was explored, aiming to uncover their potential in nanodevice applications.

Keywords: discharges in liquids; $Bi_2O_2CO_3$ nanosheets ; ledge mechanism ; satellite spots ; carbonation in air

Synthèse de nanofeuillets de $Bi_2O_2CO_3$ par décharges électriques dans des liquides pour des applications photocatalytiques et nanoélectroniques

Résumé :

Ce travail rend compte de la synthèse de nanofeuillets ultrafins de $Bi_2O_2CO_3$ (BOC) par décharges électriques dans les liquides, impliquant l'amorçage de décharges électriques entre deux électrodes de bismuth immergées dans de l'azote liquide ou de l'eau, ce qui donne lieu à des nanostructures identiques. La spectroscopie d'émission optique confirme la nature métallique de la décharge dans les deux milieux. Par la suite, les nanofeuillets subissent une oxydation rapide puis une carbonatation lorsqu'ils sont exposés à l'air. Un mécanisme de croissance, lié au mécanisme dit « ledge », a été proposé. La caractérisation cristallographique détaillée de BOC confirme leur structure appartenant au groupe spatial I4/mmm (a=3,91 Å, c=13,77 Å). L'étude clarifie également la nature potentielle des taches satellites constamment observées dans les diagrammes SAED le long de l'axe [001], taches qui proviennent principalement de la diffraction multiple et des transformations locales ordre-désordre au sein de la structure cristalline du BOC. Les performances catalytiques des nanofeuillets de BOC sont cohérentes avec celles obtenues par d'autres procédés. De plus, les performances électroniques des BOC ont été explorées dans le but de révéler leur potentiel dans des nanodispositifs.

Mots-clés : décharges dans les liquides; nanofeuillets de $Bi_2O_2CO_3$; ledge mécanisme; taches satellites ; carbonatation à l'air